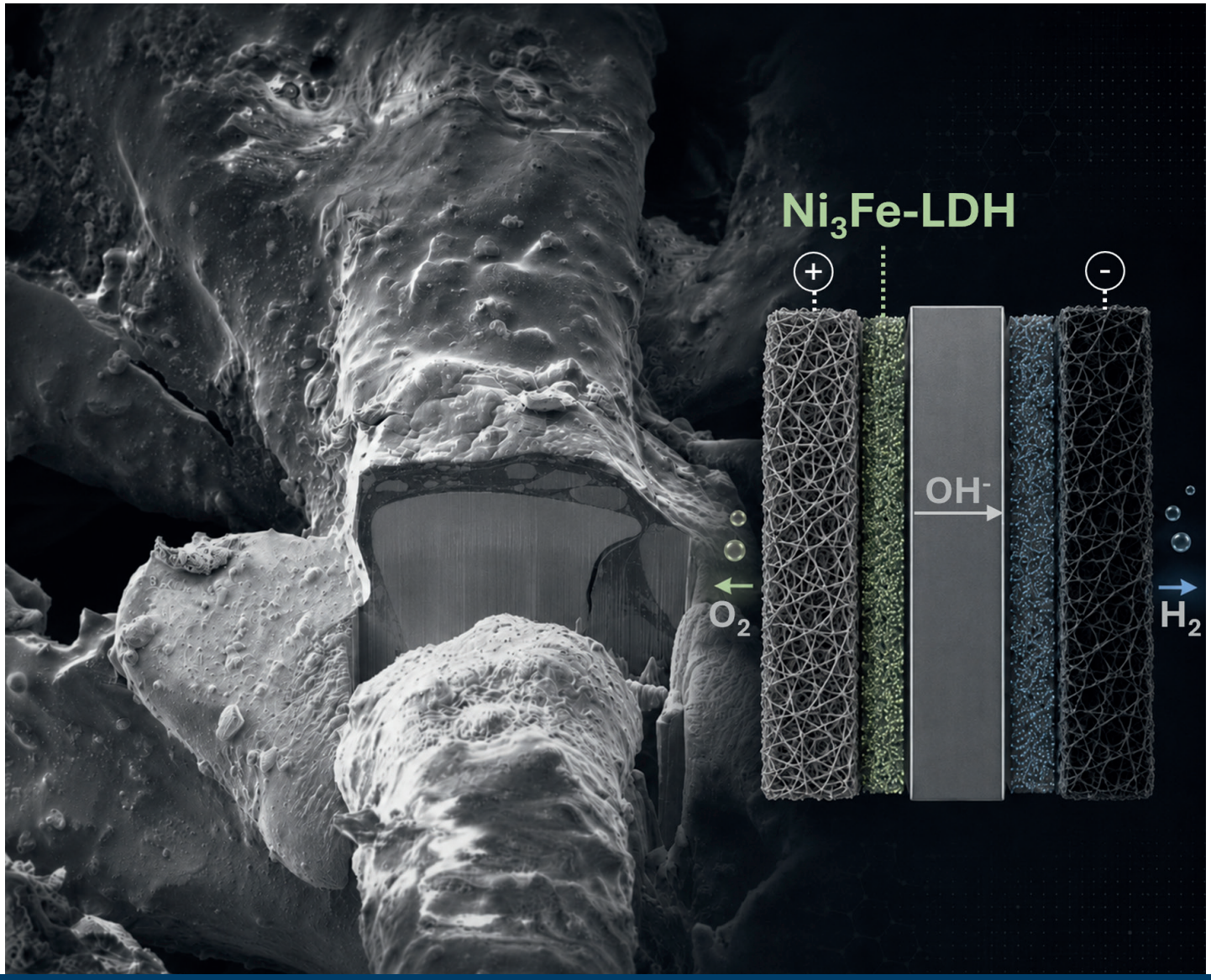

Development and Characterization of Ni_3Fe Layered Double Hydroxide-Based Oxygen-Evolution Electrodes for Anion Exchange Membrane Water Electrolysis

Irina Galkina

Energie & Umwelt / Energy & Environment
Band / Volume 726
ISBN 978-3-95806-967-1

Mitglied der Helmholtz-Gemeinschaft

JÜLICH
Forschungszentrum

Development and Characterization of Ni_3Fe Layered Double Hydroxide-Based Oxygen-Evolution Electrodes for Anion Exchange Membrane Water Electrolysis

Entwicklung und Charakterisierung von Sauerstoffentwicklungselektroden auf Basis von Ni_3Fe-Schichtdoppelhydroxiden für die Anionenaustauschmembran-Wasserelektrolyse

Von der Fakultät für Maschinenwesen der Rheinisch-Westfälischen Technischen Hochschule Aachen zur Erlangung des akademischen Grades einer Doktorin der Naturwissenschaften genehmigte Dissertation

vorgelegt von

Irina Galkina

Berichter/in:	Univ.-Prof. Dr. rer. nat. Anna Mechler Univ.-Prof. Dr.-Ing. Ralf Peters
Tag der mündlichen Prüfung:	28.05.2026

Forschungszentrum Jülich GmbH
Institute of Energy Technologies (IET)
Elektrochemische Verfahrenstechnik (IET-4)

Development and Characterization of Ni_3Fe Layered Double Hydroxide-Based Oxygen-Evolution Electrodes for Anion Exchange Membrane Water Electrolysis

Irina Galkina

Schriften des Forschungszentrums Jülich
Reihe Energie & Umwelt / Energy & Environment Band / Volume 726

ISSN 1866-1793 ISBN 978-3-95806-967-1

Bibliografische Information der Deutschen Nationalbibliothek.
Die Deutsche Nationalbibliothek verzeichnet diese Publikation in der Deutschen Nationalbibliografie; detaillierte Bibliografische Daten sind im Internet über http://dnb.d-nb.de abrufbar.

Herausgeber und Vertrieb:	Forschungszentrum Jülich GmbH Zentralbibliothek, Verlag 52425 Jülich Tel.: +49 2461 61-5368 Fax: +49 2461 61-6103 zb-publikation@fz-juelich.de www.fz-juelich.de/zb
Umschlaggestaltung:	Grafische Medien, Forschungszentrum Jülich GmbH
Druck:	Grafische Medien, Forschungszentrum Jülich GmbH
Copyright:	Forschungszentrum Jülich 2026

Schriften des Forschungszentrums Jülich
Reihe Energie & Umwelt / Energy & Environment, Band / Volume 726

D 82 (Diss., RWTH Aachen, Univ., 2026)

ISSN 1866-1793
ISBN 978-3-95806-966-4 (Print)
ISBN 978-3-95806-967-1 (E-Book)

Vollständig frei verfügbar über das Publikationsportal des Forschungszentrums Jülich (JuSER) unter www.fz-juelich.de/zb/openaccess.

ABSTRACT

Anion exchange membrane water electrolysis (AEMWE) is a promising technology for sustainable hydrogen production, combining the prospect of high current-density operation with the potential for reduced reliance on scarce materials. This thesis investigates the integration of nickel–iron layered double hydroxide (Ni_3Fe-LDH) as an oxygen evolution reaction (OER) catalyst into AEMWE systems, with the goal of developing and validating membrane electrode assemblies (MEAs) suitable for scalable fabrication and future stack integration.

The work establishes a translation pathway from catalyst powder to realistic device operation by focusing on catalyst implementation and quality control during MEA fabrication, followed by systematic single-cell testing under industrially relevant conditions. It clarifies how electrode design parameters, such as catalyst loading, binder content, ink formulation, and catalyst layer microstructure, together with operating conditions such as temperature and electrolyte concentration, govern performance and stability, highlighting the significant role of catalyst utilization and transport within the catalyst layer.

Long-term operation is investigated through extended electrochemical testing coupled with time-resolved post-mortem electrode analysis, enabling separation of conditioning effects from subsequent degradation and providing insight into time-dependent anode evolution, including chemical reconstruction of the active state and microstructural changes of the catalyst layer. To improve manufacturability and reproducibility, electrode engineering is introduced through catalyst powder post-treatment and systematic dispersion control, linking processing to ink stability, catalyst layer homogeneity, and accessibility of active sites.

The thesis further assesses MEA architecture by comparing catalyst-coated substrate and catalyst-coated membrane configurations and shows that architecture-specific optimization depends on balancing ionic, electronic and mass transport, and interface integrity. Robustness is strengthened by evaluating both pre-commercial and commercial anion-conducting materials, while material variability and batch effects are treated explicitly through repeat testing and complementary characterization. Overall, the work provides validated strategies for electrode engineering, durability assessment, architecture selection, and reproducible testing to support the development of robust, scalable Ni_3Fe-LDH-based AEMWE MEAs.

ZUSAMMENFASSUNG

Die Anionenaustauschmembran-Wasserelektrolyse (AEMWE) ist eine vielversprechende Technologie für die nachhaltige Wasserstofferzeugung, da sie den Betrieb bei hohen Stromdichten ermöglicht und zugleich das Potenzial bietet, die Abhängigkeit von kritischen ressourcenintensiven Materialien zu verringern. Diese Arbeit untersucht die Integration von Nickel–Eisen-Schichtdoppelhydroxid (Ni_3Fe-LDH) als Katalysator für die Sauerstoffentwicklungsreaktion (OER) in AEMWE-Systeme mit dem Ziel, Membran-Elektroden-Einheiten (MEA) zu entwickeln und zu validieren, die für eine skalierbare Herstellung und eine spätere Stack-Integration geeignet sind.

Die Arbeit etabliert einen Übertragungsweg vom Katalysatorpulver hin zum realistischen Gerätebetrieb, indem sie die Katalysatorimplementierung und Qualitätskontrolle während der MEA-Herstellung in den Mittelpunkt stellt und diese durch systematische Einzelzellentests unter industrienahen Bedingungen ergänzt. Sie zeigt, wie Elektroden-Designparameter wie Katalysatorbeladung, Binderanteil, Tintenformulierung und Mikrostruktur der Katalysatorschicht zusammen mit Betriebsbedingungen wie Temperatur und Elektrolytkonzentration die Performanz bzw. Leistung und Stabilität bestimmen, und hebt die entscheidende Rolle der Katalysatorausnutzung sowie des Stoff- und Ionentransports innerhalb der Katalysatorschicht hervor.

Die Langzeitstabilität wird durch elektrochemische Tests in Kombination mit zeitaufgelöster Post-mortem-Analyse untersucht. Dadurch lassen sich Konditionierungseffekte von der anschließenden Degradation trennen und die zeitabhängige Entwicklung der Anode nachvollziehen, einschließlich der chemischen Rekonstruktion des aktiven Zustands und mikrostruktureller Veränderungen der Katalysatorschicht. Zur Verbesserung von Herstellbarkeit und Reproduzierbarkeit werden Maßnahmen des Elektroden-Engineerings eingeführt, insbesondere durch Nachbehandlung des Katalysatorpulvers mittels Mahlen und systematische Kontrolle der Dispersion, wobei der Zusammenhang zwischen Prozessführung, Tintenstabilität, Homogenität der Katalysatorschicht und Zugänglichkeit aktiver Zentren herausgearbeitet wird.

Darüber hinaus untersucht die Arbeit den Einfluss der MEA-Architektur durch den Vergleich von katalysatorbeschichtetem Substrat (CCS, engl. catalyst-coated substrate) und katalysatorbeschichteter Membran (CCM, engl. catalyst-coated membrane) und zeigt, dass eine architekturspezifische Optimierung vom Zusammenspiel aus Ionen- und Elektronenleitung, Stofftransport und Grenzflächenintegrität abhängt. Die Aussagekraft wird durch die Betrachtung sowohl vorkommerzieller als auch kommerzieller anionenleitender Materialplattformen gestärkt; zugleich werden Materialvariabilität und Batch-Effekte explizit als methodische Herausforderung behandelt und durch Wiederholungstests sowie ergänzende Charakterisierung abgesichert. Insgesamt liefert diese Arbeit validierte Strategien für Elektroden-Engineering, Dauerhaftigkeitsbewertung, Architekturauswahl und reproduzierbares Testen und unterstützt damit die Entwicklung robuster, skalierbarer Ni_3Fe-LDH-basierter AEMWE-MEAs.

CONTRIBUTIONS

The contributions to the thesis chapter, including the related experimental work and publications, are detailed below.

1 General experimental and analytical contributions

The Ni_3Fe-LDH OER catalyst synthesis was supported by Dr. Wulyu Jiang. Most SEM and EDX analyses were performed by Andreas Everwand at IET-4, Forschungszentrum Jülich, who also carried out the XRD measurements. Additional SEM images used in Chapter 5.3. and 5.4 were recorded by Dr. Nikita Grigorev at the Institute of Mineral Engineering, RWTH Aachen University. FIB-SEM analysis was conducted by Lea Risters at the Ernst Ruska-Centrum (ER-C), Forschungszentrum Jülich. TEM and STEM images were recorded by Dr. Meital Shviro at Forschungszentrum Jülich. XPS analysis was performed by Heinrich Hartmann at ZEA-3, Forschungszentrum Jülich, and partly by Dr. Alaa Y. Faid at the Norwegian University of Science and Technology (NTNU), Trondheim, Norway. BET analysis was supported by Dr. Nikolai Utsch at IET-4, Forschungszentrum Jülich. Raman spectroscopy measurements were partly supported by Dr. Alaa Y. Faid at NTNU. ICP-MS/ICP-OES analyses were supported by Volker Nischwitz (former ZEA-3, Forschungszentrum Jülich), and ToF-SIMS analysis was assisted by Uwe Breuer at ZEA-3, Forschungszentrum Jülich.

2 Chapter-specific contributions and publication context

Chapter 5.2: A significant part of this chapter has been published as “Stability of Ni–Fe-layered double hydroxide under long-term operation in AEM water electrolysis” in *Small* (DOI: 10.1002/smll.202311047). While the overall structure and key sections remain unchanged, selected figures and text were adapted to the thesis context, and additional results and discussion were included to complete the study.

The work presented in Chapter 5.2 was supported by Dr. Alaa Y. Faid (mentoring, scientific support, and execution of Raman spectroscopy measurements), Dr. Wulyu Jiang (Ni_3Fe-LDH synthesis), and Dr. Fabian Scheepers (supervision and scientific support). Patrick Borowski (Evonik) served as the contact person responsible for AEM and binder provision. Further scientific support and supervision were provided by Prof. Svein Sunde, Prof. Werner Lehnert, and Prof. Anna K. Mechler. Dr. Meital Shviro contributed TEM imaging and scientific support.

Chapter 5.3: This chapter is based on the paper entitled “Optimized NiFe-LDH catalyst layers boost anion exchange membrane water electrolyzer performance and durability,” published in the *International Journal of Hydrogen Energy* (DOI: 10.1016/j.ijhydene.2026.155383). In addition to the published results, a third milling method using a roller bench was investigated, and the discussion was expanded to provide a deeper interpretation of its effects on electrolyzer performance. The chapter was supported by the same key collaborators as for Chapter 5.2: Additionally, Dr. Nikita Grigorev supported SEM analysis and catalyst milling.

CONTENTS

1 INTRODUCTION AND MOTIVATION

The rising demand for energy, environmental challenges, including climate change coupled with the simultaneously increasing lack in traditional fossil fuel resources (coal, oil, and natural gas), present significant challenges to the modern society.[1] In response to these developments, strategies for renewable energy production have gained importance in the past decades. Among these, hydrogen has emerged as a promising large-scale energy carrier, enabling the conversion, storage, and distribution of renewable energy across various sectors, including transportation, industry and power generation.[2]

Currently, the proportion of hydrogen produced from fossil compounds is considerable, contributing to substantial pollution and greenhouse gas emissions,[3,4] which does not align with global initiatives to reduce CO_2 emissions and other greenhouse gases.[5,6] Thus, the development and implementation of efficient technologies to produce green hydrogen are necessary and meaningful. Among different techniques for producing hydrogen, water electrolysis (WE, or water splitting) stands out as a promising method, utilizing renewable energy sources such as solar and wind energy.[7,8] However, hydrogen produced via water electrolysis remains costly across the entire value chain, from production and storage to distribution and end use, and it is not yet available at the scales necessary to facilitate a direct transition to a hydrogen-based energy system.[9] Moreover, electrolyzers require improvements in both efficiency and durability to become economically competitive with conventional hydrogen production processes like steam methane reforming or coal gasification.[10]

Anion exchange membrane water electrolyzers (AEMWE) has emerged as a promising hybrid concept, aiming to combine the cost-effective materials of alkaline electrolysis (AEL) with the high efficiency and compact design of proton exchange membrane electrolysis (PEMWE).[11] Operating in a mildly alkaline environment and at moderate temperatures (<80 °C), AEMWE enables the use of non-noble metal catalysts and polymer membranes, reducing system costs and reliance on scarce materials. Unlike AEL, AEMWE supports a zero-gap cell design without the need for bulk liquid electrolytes or porous diaphragms, which significantly reduces ohmic resistance (introduced in Chapter 2.1), gas crossover, and startup times. This design not only enhances efficiency and safety but also enables a compact and modular stack architecture that is better suited for dynamic operation with fluctuating renewable electricity sources.[11]

According to the key performance indicators from the Clean Hydrogen Report of 2022,[12] AEMWE is projected to achieve capital costs of 600 €/kg(H_2) and 300 €/kW by 2030, surpassing both AEL and PEMWE in cost targets. The use of critical raw materials in AEMWE catalysts is expected to fall from 1.7 mg/W in 2020 to zero, compared to 2.5 mg/W (2030 target: 0.25 mg/W) for PEMWE. Operational and maintenance costs are also forecasted to decrease to 21 €/(kg/day)/year, matching PEMWE and outperforming AEL. Additionally, AEMWE systems demonstrate superior dynamic response

characteristics, with hot and cold start ramp times of 5 and 150 s, respectively, far outperforming AEL and approaching PEMWE performance.

Despite these promising developments, several critical challenges remain, which currently limit AEMWE to the research and development stage. The membrane-electrode assembly (MEA) continues to be a key bottleneck due to the high price and limited maturity of anion-conducting materials (membranes and ionomers). Moreover, the lack of efficient, durable, and scalable non-noble metal catalysts remains a major obstacle. The oxygen evolution reaction (OER) at the anode remains the kinetic bottleneck, requiring effective electrocatalysts to reduce overpotentials and energy losses.

Among different non-noble metal-based OER catalysts, Ni-Fe-based catalysts, specifically, Ni-Fe layered double hydroxides (LDH) have emerged as some of the most promising candidates.[13–15] However, their evaluation has often been limited to simplified three-electrode setups (e.g., rotating disk electrode, RDE), which do not accurately reflect performance in membrane-integrated single-cell systems.[16] The translation of these materials into full AEMWE cells, along with long-term durability studies and degradation pathway analysis, remains underexplored.[17–19] Furthermore, the integration of such catalysts into practical MEAs involves complex and fine-tuned engineering challenges, such as ink formulation and dispersion, electrode or catalyst layer architecture and contact layer configurations. Long-term stability and degradation tracking studies of entire electrodes, including post-mortem analysis, and investigation on best performing and durable system parameters should be examined under realistic electrolyzer conditions. These steps are particularly challenging but crucial for the development and relevance of AEMWE technology.

This work builds on these challenges and aims to address critical research gaps in catalyst integration, system operation, and long-term performance of AEMWEs. The performance and degradation behavior of Ni_3Fe-LDH-based anodes are investigated under realistic AEMWE operating conditions. Through systematic evaluation of ink formulation, catalyst layer composition, and MEA configuration, strategies to enhance electrochemical performance and improve reproducibility are developed. Post-operational analyses provide insights into anode degradation pathways during extended single-cell operation. By addressing both material- and system-level challenges, the work bridges the gap between catalyst development and practical application.

2 WATER ELECTROLYSIS: THEORY AND STATE-OF-THE-ART

This chapter provides the theoretical basis and state-of-the-art overview required to place this thesis in its scientific and technological context. It first summarizes the fundamental electrochemical principles of water electrolysis and introduces the key definitions. Building on this basis, Chapter 2.2 outlines electrolysis for hydrogen production and compares the established technologies, thereby motivating the relevance of AEMWE as the focus of this work. Finally, Chapter 2.3 reviews the current research state of AEMWE, describing the roles, requirements, and limitations of core components and summarizing key bottlenecks and recent developments aimed at improving efficiency and long-term stability.

2.1 FUNDAMENTALS OF WATER ELECTROLYSIS

Thermodynamics

Water electrolysis is a fundamental process, where electrical energy is used to decompose water into hydrogen and oxygen. The energy required for this reaction is dictated by thermodynamic principles, which determine the minimum energy input, the efficiency of conversion, and how temperature and pressure influence the system. A typical low temperature electrolyzer is shown in Figure 2.1:

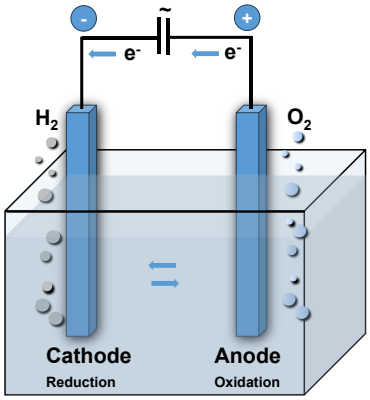

Figure 2.1. General schematic of a typical low-temperature water electrolyzer, showing cathode (negative pole) and anode (positive pole) immersed in liquid electrolyte and connected via an external electric circuit.

At the cathode, the hydrogen evolution reaction occurs, where water molecules (in alkaline media) gain electrons to form hydrogen gas. The half-cell reaction is as follows:

$$4\mathrm{H_2O} + 4\mathrm{e^-} \rightarrow 2\mathrm{H_2} + 4\mathrm{OH^-} \qquad \text{Equation 2.1}$$

Simultaneously, at the anode, the oxygen evolution reaction takes place, where hydroxide molecules are oxidized to oxygen gas under the release of electrons:

$$4\mathrm{OH^-} \rightarrow \mathrm{O_2} + 2\mathrm{H_2O} + 4e^- \qquad \text{Equation 2.2}$$

The overall water splitting reaction can be summarized as follows:

$$2\mathrm{H_2O} \rightarrow 2\mathrm{H_2} + \mathrm{O_2} \qquad \text{Equation 2.3}$$

This reaction is thermodynamically non-spontaneous, meaning external energy input is required to drive it. The minimal work required to split water is determined by the Gibbs free energy ($\Delta G°$), which under standard conditions (298.15 K, 1 bar) is given by the Gibbs-Helmholtz Equation 2.4:[20]

$$\Delta G^0 = \Delta H^0 - T \cdot \Delta S^0 \qquad \text{Equation 2.4}$$

where enthalpy $\Delta H^0 = -285.84\ \mathrm{kJ\ mol^{-1}}$, entropy $\Delta S^0 = 163.15\ \mathrm{J\ mol^{-1}K^{-1}}$, resulting in Gibbs free energy $\Delta G^0 = 237.22\ \mathrm{kJ\ mol^{-1}}$ for liquid water. If water is considered to be in evaporated state, $\Delta G^0 = 228.66\ \mathrm{kJ\ mol^{-1}}$ (with $\Delta H^0_{\mathrm{vap}} = 241.80\ \mathrm{kJ\ mol^{-1}}$, $\Delta S^0{}_{\mathrm{vap}} = 44.10\ \mathrm{J\ mol^{-1}K^{-1}}$.[21]

As ΔG^0>0, the reaction is non-spontaneous and requires additional external energy input. The Gibbs free energy is highly dependent on temperature and decreases as the operation temperature of the electrolyzer increases. The electrical energy required to drive the reaction is related to ΔG^0 by the equation:

$$\Delta G^0 = -nFE^0_{\mathrm{rev}} \qquad \text{Equation 2.5}$$

where the number of electrons converted per water molecule $n = 2$, Faradey constant $F = 96485\ \mathrm{C\ mol^{-1}}$ and the reversible equilibrium potential $E^0_{\mathrm{rev}} = 1.23\ \mathrm{V}$. With $\Delta G^0_{\mathrm{vap}} = 228.66\ \mathrm{kJ\ mol^{-1}}$, when the lowest heating value of hydrogen is considered, assuming water remains in vapor form and neglecting the condensation energy, the reversible potential is $E^0_{\mathrm{vap}} = 1.18\ \mathrm{V}$.

Water electrolysis is endothermic under standard conditions, meaning it absorbs heat from the surrounding environment. The total energy required corresponds to the ΔH rather than just ΔG. The voltage required to provide this energy is known as the thermoneutral potential (E^0_{th}):[22]

$$\Delta H^0 = -nFE^0_{\mathrm{th}} \qquad \text{Equation 2.6}$$

At standard conditions, and for liquid water, $E^0_{\mathrm{th}} = 1.48\ \mathrm{V}$, meaning that electrolysis becomes exothermic if the applied voltage exceeds this value. If the reacting water is in vapor form, $E^0_{\mathrm{th_{vap}}} = 1.25\ \mathrm{V}$ due to the absence of condensation energy.

As described above, the change in ΔH, ΔS and ΔG are temperature and pressure dependent, so is the E^0_{rev}. Considering the reversible electrode potential as a function of temperature, the gas constant and the activities of the gas species, the fundamental Nernst equation can be used (Equation 2.7).[23,24]

$$E_{\mathrm{rev}} = E^0_{\mathrm{rev}} - \frac{\mathrm{R}T}{nF}\ln\left(\frac{a_{\mathrm{Red}}}{a_{\mathrm{Ox}}}\right) = \qquad \text{Equation 2.7}$$

$$= E^0_{\mathrm{rev}} - \frac{\mathrm{R}T}{2F}\ln\left(\frac{a_{\mathrm{H_2O}}}{a_{\mathrm{H_2}}\, a_{\mathrm{O_2}}^{0.5}}\right) \qquad \text{Equation 2.8}$$

where the gas constant $R = 8.31441\ \mathrm{J\ mol^{-1}\ K}$, number of transferred electrons $n = 2$, and the relative activities of the reactants a_{reactant}. The Nernst equation describes how the cell potential depends on reactant and product activities, temperature, and the number of electrons transferred. It can predict potential in strongly diluted solutions, where it simplifies to a concentration-dependent form. At standard conditions, as the relative activity coefficients are set to one, $E_{\mathrm{rev}} = E^0_{\mathrm{rev}}$. In strongly diluted conditions, the molar concentrations can be used instead of relative reactant activities, making it useful for practical electrochemical systems operating under dilute conditions.

The temperature dependence of E^0_{rev} can be calculated as explained by Bratsch:[25]

$$E^0_{\mathrm{rev}} = 1.2291\ \mathrm{V} - 0.0008456\ \mathrm{V}\ (T - 298.15\ \mathrm{K}) \qquad \text{Equation 2.9}$$

As for liquid water the activity $a_{\mathrm{H_2O}} = 1$, and the activities of gaseous species ($a_{\mathrm{H_2}}$, $a_{\mathrm{O_2}}$) are represented by the partial pressures, the reversible cell potentials can be expressed as follows:

$$E_{\mathrm{rev}} = E^0_{\mathrm{rev}} - \frac{\mathrm{R}T}{n\mathrm{F}} \ln\left[\left(\frac{1\ \mathrm{bar}}{p_{\mathrm{H_2}}}\right)\left(\frac{1\ \mathrm{bar}}{p^{0.5}_{\mathrm{O_2}}}\right)\right] \qquad \text{Equation 2.10}$$

where $p_{\mathrm{H_2}}$and $p_{\mathrm{O_2}}$are the partial pressures of H_2 and O_2, respectively.

At typical experimental conditions in this work (60 °C, ambient pressure), the saturation pressure of water is 0.197 atm or 0.199 bar, resulting in $p_{\mathrm{H_2}}$=$p_{\mathrm{O_2}}$=0.80 bar, and leading to an adjusted reversible potential of $E_{\mathrm{rev}} = 1.19\ \mathrm{V}$.

Efficiency and Voltage Losses of a Water Electrolyzer

In real electrolyzers, the cell voltage exceeds the theoretical voltage due to various overpotentials, as outlined later in this chapter. To calculate the voltage efficiency (η_{v}) of an electrolyzer, one must divide the theoretical energy needed for the reaction (the reaction enthalpy) by the actual electrical energy input, derived from the operating cell potential E_{cell}:

$$\eta_{\mathrm{v}} = \frac{\Delta H^0}{nFE_{\mathrm{cell}}} \qquad \text{Equation 2.11}$$

η_{v} depends on whether the higher heating value (HHV) or lower heating value (LHV) of hydrogen is used.

The HHV includes total reaction enthalpy, accounting for the condensation enthalpy of water vapor. It is typically used to calculate η_{HHV} when hydrogen is utilized for chemical applications or when evaluating the overall heat balance of the electrolyzer. The LHV excludes condensation enthalpy and is more relevant when hydrogen is used as an energy carrier (in fuel cells or combustion processes), where water remains in vapor form and condensation energy is not recovered.

In addition to voltage efficiency, the overall system efficiency includes the faradaic efficiency (η_{F}), which quantifies the fraction of the total charge that is effectively used to produce the desired electrochemical reaction product, accounting for losses such side reactions. The faradaic efficiency

further considers the losses due to the used materials and their parameters (e.g. membrane and its thickness or catalyst and its selectivity), the operating conditions (temperature, pressure, electrolyte), the currents, at which the electrolyzer is operated. This estimation would be out of the work's scope but are considered in commercial stack systems. In this work, the voltage efficiency is referred to an electrolyzer single-cell, and η_{HHV} is used, calculated as follows:

$$\eta_{\mathrm{HHV}} = \frac{E_0}{E_{\mathrm{cell}}} \qquad \text{Equation 2.12}$$

Voltage losses

The actual cell voltage (E_{cell}) in an electrolyzer deviates significantly from the theoretical reversible cell voltage (E_{rev}). As current increases, the E_{cell} experiences an incline due to various voltage losses (Equation 2.13). In this context, current, potential, and overpotential are all considered as positive values.

$$E_{\mathrm{cell}}(i) = E_{\mathrm{rev}} + iR_{\mathrm{Ohm}} + \eta_{\mathrm{kin}} + \eta_{\mathrm{mt}} \qquad \text{Equation 2.13}$$

Here, i is the current of the electrolyzer, R_{Ohm} is the ohmic resistance, η_{kin} is the kinetic overpotential of both OER and HER (losses due to electrochemical reactions in the electrodes, highly dependent on the used catalysts),[26] η_{mt} presents the mass transport losses, which arises from limitations in reactant supply and product gases removal.

The ohmic resistance (R_{Ohm}) originates from both ionic and electronic resistances in the electrolyzer. Ionic resistance (R_{mem}) comes from anion transport resistance through the membrane, including the contributions of the anion-conducting binder. The electronic resistance (R_{el}) is a sum of contact resistances between the bipolar plates, PTLs, electrodes, and the internal resistance of the PTL bulk material. Electrolyte resistivity also contributes to the ohmic losses though it remains constant if the electrolyte composition is fixed. In zero-gap electrolyzers, the electrode separation distance is effectively equal to the membrane thickness, making membrane resistance a key design parameter.

Due to the described voltage losses, WEs do not follow a linear input current and resulting voltage relationship (or vice versa). Instead, their performance is typically assessed using polarization curves, obtained in a two-electrode configuration, as described further in Figure 2.4 and Figure 4.6. A typical polarization curve, as shown in Figure 2.2, can be divided into three main distinct regions, the kinetic, the ohmic and the mass transport regions.[27,28]

At low currents i (Figure 2.2, red zone) activation losses, denoted as kinetic overpotential η_{kin}, dominate the cell voltage. As i increase (Figure 2.2, yellow zone), electronic and ionic resistances within the cell become increasingly significant and contribute to the ohmic overpotential ($\eta_{\mathrm{Ohm}} = i \cdot R_{\mathrm{Ohm}}$). At high i (Figure 2.2, blue zone), mass transport overpotentials η_{mt} become relevant, typically due to insufficient reactant supply or inefficient product removal at the reaction sites. Accurate identification and minimization of these voltage loss contributions are essential for improving MEA performance and overall electrolyzer efficiency.

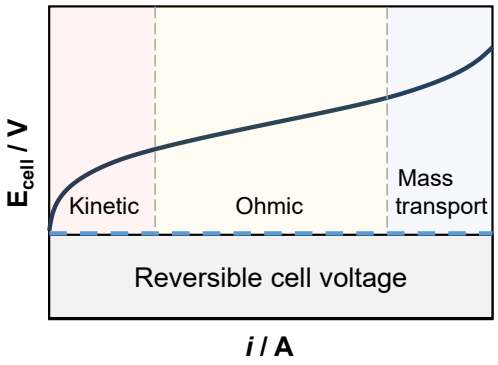

Figure 2.2. Schematic representation of a polarization curve for water electrolysis, indicating the contribution of different voltage losses. The three main zones are the kinetic (red), the ohmic (yellow) and the mass transport zone (blue).

Kinetics of Electrochemical Reactions

Electrochemical reactions involve reduction-oxidation processes, where the oxidation states and charges of reactants change as electrons are transferred. These reactions occur at electrode-electrolyte interfaces and are fundamental to the operation of water electrolyzers. For simplicity, a general redox reaction can be expressed as a one-electron reversible process:

$$\mathrm{Ox} + \mathrm{e}^- \rightleftharpoons \mathrm{Red} \qquad \text{Equation 2.14}$$

where Ox represents the oxidized species and Red the reduced one. The equilibrium potential (E_0) depends on the concentration (activity) of reactants and products, following the Nernst equation.

The kinetics of electrochemical reactions are strongly influenced by catalysts, electrode materials, and reaction conditions. In the absence of mass transport limitations, the charge-transfer kinetics at the metal/electrolyte interface follow the Butler-Volmer equation (Equation 2.15):[29]

$$j = j_0 \left[\exp\left(\frac{\beta F \eta}{RT}\right) - \exp\left(\frac{(1-\beta) F \eta}{RT}\right) \right] \qquad \text{Equation 2.15}$$

Where j is the total current density, j_0 is the exchange current density of the half-cell reaction, which quantifies the intrinsic reaction rate at equilibrium, β is the symmetry factor or transfer coefficient, which describes the level of decreased activation barrier of the electron transfer the specific catalyst induces (typically between 0 and 1). At high overpotentials, one exponential term dominates, allowing the Butler-Volmer equation to be simplified (Equation 2.16):[30]

$$j = j_0 \left(\exp\left(\frac{\beta F \eta}{\mathrm{RT}}\right)\right) \qquad \text{Equation 2.16}$$

Equation 2.16 can be rearranged into the Tafel form, expressing the kinetic overpotential:

$$\eta = \frac{\mathrm{R}T}{\beta F} \log\left|\frac{j}{j_0}\right| = b \log|j| + \mathrm{const} \qquad \text{Equation 2.17}$$

where *b* is the Tafel slope. The Tafel slope is a critical parameter for comparing the kinetics of different electrocatalysts, as it describes the overpotential required for a tenfold increase in current density.

The Tafel slope is typically extracted from polarization curves by plotting the ohmic loss-corrected cell voltage versus the logarithm of the current density over a defined low-current density region, typically up to 0.1 A cm^{-2}. The narrow region of, e.g. 0.03 to 0.1 A cm^{-2}, is usually chosen to account for primarily kinetic effects, avoiding possible effects of saturation of surface coverage of adsorbates and mass transport limitations.

Here, the ohmic loss correction refers to subtraction of the ohmic voltage drop ($i \cdot R_{\mathrm{Ohm}}$) from the measured cell voltage. In the following, polarization curves treated in this way are referred to as iR-corrected polarization curves (meaning $R = R_{\mathrm{Ohm}}$). A more detailed description of the impedance spectroscopy analysis is provided in Chapter 4.5.1.

Both hydrogen[31–33] and oxygen[34,35] evolution mechanisms and kinetics have been thoroughly examined in alkaline media. HER typically exhibits fast kinetics, meaning it requires lower overpotential and can proceed efficiently on a variety of electrode surfaces. OER, in contrast, is much slower, necessitating a higher overpotential at the anode. This large OER overpotential is one of the primary sources of inefficiency in water electrolysis cells. Since OER is the more sluggish reaction, it is often considered as the rate-determining step, leading the overall kinetic behavior of a MEA or a single-cell electrolyzer. When an electrolyzer system is tested in a complete MEA setup, the observed overpotential is affected by multiple factors beyond pure OER kinetics. Consequently, the apparent Tafel slope is often higher than the intrinsic Tafel slope obtained from idealized single-electrode measurements. (This observation has been discussed specifically for PEM water electrolyzers by researchers such as Bernt[27] and Suermann[36]). To avoid misinterpretations, in this work, the term *dE*/*d*log*j* is used instead of "Tafel slope" to describe the observed current increase rate in polarization curves. This specifically refers to the slope of the iR-corrected cell voltage vs. logarithm of current density. Further discussion on this definition will be given in Chapter 5.

2.2 ELECTROLYSIS TECHNOLOGIES FOR HYDROGEN PRODUCTION

Today hydrogen is considered as one of the most promising energy carriers. As such, hydrogen is not a direct energy source itself but can be derived from other energy sources and stored afterwards. The main challenge to step into the so-called hydrogen economy, where hydrogen in employed into an energy infrastructure to supply different economics sectors instead of fossil fuels, is the hydrogen production phase.[37] The main production methods are those, where hydrogen is produced from fossil fuels, biomass or water. Steam reforming and thermal cracking of natural gas, the partial oxidation of heavy hydrocarbon fuel fractions, coal gasification, biomass burning and fermenting, thermochemical routes, photolysis, thermolysis and combinations of former[38,39] are the main technologies for hydrogen production today. Water electrolysis is the electrochemical splitting of water into H_2 and O_2

driven by an external power supply. Ideally, for the green hydrogen economy, the current used should originate from renewable energy sources such as solar or wind.

The two leading commercial technologies, which represent the low-temperature WE sector are the acidic PEM and the traditional AWE (Figure 2.3a–b).

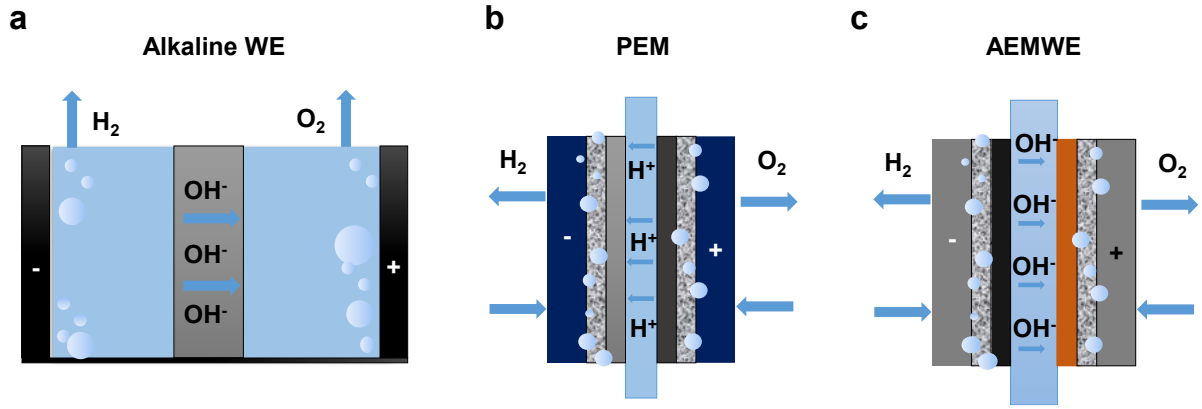

Figure 2.3. Schematic illustration of three water electrolysis (WE) technologies: (a) traditional alkaline WE operated in aqueous KOH electrolyte; (b) zero-gap proton exchange membrane water electrolysis (PEMWE) using a H^+ conductive polymer membrane in acidic environment; (c) zero-gap anion exchange membrane water electrolysis (AEMWE) employing a OH^- conductive membrane in alkaline conditions.

PEMWE

To date, PEMWE shows highest current densities and efficiency, based on higher heating value of hydrogen. Moreover, high purity of the produced hydrogen, the agile dynamic range of operation, a compact design and the feasibility to be operated under high partial pressures are the main advantages of the PEMWEs.[40–42] PEMWEs use a solid proton-conducting membrane as the electrolyte and operate with pure water. The presence of protons creates an acidic environment, so the technology depends on noble metal materials that can withstand low pH conditions and resist acid-induced degradation.[43,44] On the anode side, iridium (and its oxides) is typically used due to its stability and high intrinsic activity, whereas the cathode side often utilizes Pt supported on carbon. The two half-cell reactions, the hydrogen and oxygen evolution reactions, are defined in Equation 2.18 and Equation 2.19. Due to exposure to high oxidative potentials, the anode-side PTLs typically use high-cost Pt- or Au-coated Ti-based materials for durability and stability.

$$\textbf{Cathode}: 2\,H^+ + 2\,e^- \rightarrow H_2 \left(E^\circ = 0\ \text{V vs. SHE}\right) \qquad \text{Equation 2.18}$$

$$\textbf{Anode}: H_2O \rightarrow \frac{1}{2}\,O_2 + 2\,e^- + 2\,H^+ \left(E^\circ = +1.229\ \text{V vs. SHE}\right) \qquad \text{Equation 2.19}$$

State-of-the-art membranes are perfluorinated sulphonic acid copolymers (as Nafion® by DuPont de Nemours), which are used due to the high ionic conductivity and chemical and mechanical stability. These are considered to have a significant negative environmental effect during production, use and disposal or recycling[45,46] and might be restricted in the future.[47] Combined with the high-cost noble metal components (Ir, Pt, Ru, Ti), the PEMWE technology faces the challenge of high capital costs and limited scalability due to the scarcity of critical raw materials.

AWE

Hydrogen production via traditional AWEs is a well-established commercially proven method, operating in the lower temperature region (60–80 °C) and in aqueous KOH electrolytes (20–40 wt%, pH>14). The strong alkaline environment allows the use of non-noble metals, such as Ni or its alloys, which would degrade under acidic conditions.[48] The general, AWE configuration consists of two electrodes immersed in the electrolyte and divided by a porous separator, the diaphragm (Figure 2.3a). Depending on the configuration, the system can be zero-gap, where the electrodes are in direct contact with the separator for improved efficiency, or gap-based, an earlier design with a physical separation between the electrodes. The water reduction takes place at the cathode side (Equation 2.20), the oxidation of hydroxyl ion occurs on the anode side (Equation 2.21):

$$\textbf{Cathode}: 2\,H_2O + 2\,e^- \rightarrow H_2 + 2\,OH^- \left(E^\circ = -0.828\ \text{V vs. SHE}\right) \quad \text{Equation 2.20}$$

$$\textbf{Anode}: 2\,OH^- \rightarrow \frac{1}{2}\,O_2 + H_2O + 2\,e^- \left(E^\circ = +0.401\ \text{V vs. SHE}\right) \quad \text{Equation 2.21}$$

As the AWE utilizes low-cost materials, usually based on transition-metals (Ni- and Co-based, stainless steel)[49,50] the technology greatly reduces the overall costs compared to PEMWE. However, despite economic advantages, AWE faces several drawbacks that hinder its applicability in modern, dynamic energy systems. The primary limitation lies in the use of porous diaphragm (e.g., Zirfon) as the use of these separators leads to product gas cross-over. Gas intermixing not only reduces efficiency, as oxygen diffusing to the cathode side leads to parasitic reactions, but also causes safety risks and lowers hydrogen purity.[51–53] The use of a diaphragm further results longer equilibration times to achieve steady-state in terms of temperature and electrolyte flow.[54,55] Another drawback come from the use of a highly alkaline electrolyte, which, while enabling inexpensive materials, also introduces challenges in safety and long-term system stability. A supporting limitation is the relatively lower catalytic activity of the non-precious metal electrodes in AWE compared to the platinum group metal (PGM) catalysts used in PEMWE, which contributes to higher overpotentials and limits the achievable current density. These factors along with the use of the porous diaphragms hinders the AWE partly to be operated in agile regime, when coupled to unstable electricity donors as wind or solar technologies.[42]

Introducing AEMWE

AEMWEs (Figure 2.3c) bridge AWE and PEMWE, aiming to combine the cost advantages of AWE, largely enabled by using non-PGM catalysts and less expensive balance-of-plant components, with the high current-density and compact cell design typically associated with PEMWE. As a result, AEMWE is widely viewed as a promising next-generation platform for scalable, sustainable hydrogen production.

The key characteristics and operating parameters of the three technologies are summarized in Table 2.1.[37,43,56–58]

Table 2.1. Comparison of the main characteristics and parameters of the alkaline, PEM and AEM water electrolysis types (modified from IRENA).[59]

	PEMWE	Alkaline WE	AEMWE
Electrolyte	Perfluorosulfonic acid polymer membrane (Nafion®) in pure water	Aqueous KOH (20–40 wt%)	Anion conducting polymer with added aqueous KOH or in pure water
Operation temperature	50–80 °C	60–90 °C	50–60 °C
Operation pressure	<70 bar	1–30 bar	<35 bar
Separator	Solid electrolyte PEM (see above)	polysulfone-bonded polyantimonic acid, ZrO_2 on polyphenylsulfone (Diaphragm Zirfon®), asbestos, NiO,	Solid electrolyte AEM (see above)
Charge carrier	H^+	OH^-	OH^-
Electrodes/catalysts	Anode: Ir/IrO_2 Cathode: Pt/C	Anode and cathode: Ni-based	Anode and cathode: Transition-metal-based, preferable Ni-based
Bipolar plates	Anode: Pt-coated titanium Cathode: Au-coated titanium	Anode and cathode: full Ni or Ni-coated stainless steel	
Frame, sealing materials	Polytetrafluorethylen (PTFE), polysulfone (PSU), poly (ethylene-co-tetrafluoroethylene) (ETFE)	PSU, PTFE, ethylene propylene diene monomer (EPDM)	PTFE, EPDM, silicone
System lifetime / h	>60000	>100000	<10000
Technology progress	Commercial	Commercial	Research and development, commercial

2.3 PERFORMANCE AND COMPONENTS OF AEMWE

A deep understanding of the materials and properties involved in the AEMWE system can fast-track the evolution of efficient, affordable, and reliable energy storage solutions. In this chapter, the main components of the AEMWE system and their current state of development are described. While the hydrogen evolution reaction (HER) catalysts, the AEM, and the porous transport layers (PTLs) are not the central focus of this work, a brief overview of these materials will be provided. Even small Fe amounts can lead the OER catalyst, particularly as it relates to Ni-Fe-LDHs, as well as the MEA configurations, performance and durability studies of AEM water electrolyzers, and challenges that the technology face, will be described in greater detail. A schematic representation of the AEMWE cell and components is shown in Figure 2.4.

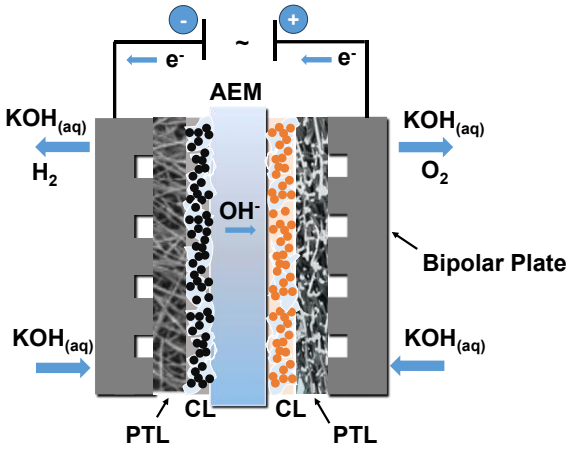

Figure 2.4. Schematic cross-sectional view of the main components in a single-cell AEMWE, illustrating the membrane, catalyst layers, porous transport layers, and bipolar plates.

2.3.1 SYSTEM PERFORMANCE AND OPERATION CONDITIONS

The AEMWE is a young technology, still under research and development. A quick survey of academic article databases reveals the massively growing attention to this technology and its research progress. Due to the massive support by US DOE[60] and Europe with its FCH-JU funding programs,[61] the technology progress experienced a strong boosting effect.

The first commercial AEMWE was launched by Enapter in 2020. Currently, Enapter offers a modular electrolyzer system with an estimated lifetime of up to 35,000 h, along with a multicore AEM system, capable of producing 450 kg of pure H_2 in one day.[62] On the experimentally proven level, however, long-term operation of around 10,000 h was achieved only once.[63] On laboratory scale, Bouzek et al. presented a study using a 3-cell stack with 25 cm^2 nickel foam electrodes (uncatalyzed) and a commercial anion-conducting membrane Ralex (MEGA, Czech Republic), reinforced with polypropylene mesh, achieving around 400 mA cm^{-2} at 6.4 V_{stack} in 20 wt% KOH electrolyte at 25 °C.[64] Further, Park et al. demonstrated a 5-cell stack with an active area of 64 cm^2, achieving ≈740 mA cm^{-2}

at 9.25 V_{stack} and a stability of 150 h,[65] while Jang et at. reported a 2000 h stability of a 3-cell stack with an active area of 63.6 cm^2, operated at 45 °C in 0.1 M KOH.[66]

A great comprehensive overview of the water electrolysis technologies, with focus on the AEMWEs, is provided in several review papers.[19,41,63,67–80] The following chapters will explore the performance and the key components of AEMWE and the main challenges associated with its current state of development. A precise comparison of AEMWE performance remains challenging due to the absence of standardized testing protocols and materials.[81]

Temperature effect

Elevated temperatures generally boost system efficiency by increasing the electrode reaction kinetics and enhancing the transport of electrons, ions, and mass. Simultaneously, the thermodynamic potential for the water splitting reaction decreases by roughly 8.5 mV for every 10 °C increase.[82] Park et al. tracked the AEMWE performance in dependence of the operating temperatures 1 M KOH from 50 to 70 °C, discovering enhanced performance at higher temperatures and achieving a high current density of 1.5 A cm^{-2} at 1.9 V.[83] All similar works reveal the positive effect of elevated operating temperatures.[17,82–84]

Electrolyte effect

The type and concentration of the electrolyte greatly influence the performance of AEMWEs. For AEMWE to be cost-competitive, electrolytes like pure water, KOH, and K_2CO_3 have been thoroughly studied, but their varying advantages and limitations have led to debates on the most suitable choice for future development.[85,86] While pure water electrolysis lowers capital costs, it suffers from low ionic conductivity within the AEM and ionomer, as well as instability of anion-conducting components, leading to higher cell voltages and reduced system durability.[87] But positively, operation in pure water can eliminate occurring shunt currents inside an AEMWE, which are parasitic currents that flow through unintended pathways within the electrolyzer, rather than through the main intended circuit. Those can complicate the design of stacks and cause loss in efficiency, corrosion and safety concerns of gas mixing. In contrast, alkaline electrolytes of higher pH like $KOH_{aq.}$, or $K_2CO_{3\,aq.}$, enhance ion transfer and reaction kinetics, yet increase costs due to their alkaline harshness.[80] As a results, to date a mild alkaline electrolyte is a preferable compromise for balancing activity and cost,[88] while ongoing research, particularly in the academic field, is exploring the transition to pure water. The main motivation for using only the membrane as electrolyte is to simplify the stack designs and balance-of-plant configurations, reduce maintenance, eliminate corrosive environments, and improve safety concerns related to electrolyte handling and leakage.[37,80] However, the pure water operation leads to strong decrease in electrolyzer performance. Only few studies presented adequate performance of around 1 A cm^{-2} below 2 V in pure water operation.[85,89–92]

Beyond concentration, electrolyte purity is another key factor affecting AEMWE performance and the comparability of reported results. Trace Fe species can alter the apparent activity of Ni-based electrodes via surface deposition and incorporation processes during operation. As OER strongly

influences the overall cell voltage, even small Fe amounts can lead to measurable changes in anodic overpotential and thus reported single-cell performance.[93] Therefore, Fe should not be treated solely as an impurity risk, but as an operational variable that can affect intrinsic catalyst performance and complicate benchmarking across studies. For meaningful comparisons, Fe concentration, electrolyte pretreatment or purification, and potential Fe sources from system hardware should be reported consistently. [93–96]

The impact of Fe impurities on HER performance is not consistent across studies. Depending on electrode material, potential history, and electrolyte composition, Fe deposition has been reported both to block active sites and to overlap with partial performance recovery, which highlights that impurity driven effects can be system specific. Specifically, it was reported that holding a Ni electrode at reducing potential in 30 wt% KOH containing 0.5 ppm Fe led to a continuous increase in overpotential over time, attributed to Fe deposition blocking active Ni sites.[97] Another study comparing 0.03 and 3 ppm Fe found no difference in degradation rates; notably, the 3 ppm sample showed performance recovery over time, likely due to increased surface area from Fe adsorption.[98] Not Fe adsorption is considered as the primary cathode degradation mechanism, but the surface hydride formation, acting as a hydrogen diffusion barrier[99], also observed in Raney-Ni cathodes.[100] Interestingly, Fe adsorption has been reported to suppress hydride formation, and in Ni–Fe catalysts, Fe impurities were found to enhance HER activity, with a maximum at ~90% Fe content.

While Fe or Ni ion contaminations can support the OER and HER activity, in contrast, Zn^{2+}, Cd^{2+}, Pb^{2+} are widely recognized as poisons for both electrodes and can cause pronounced performance losses.[101] Further discussion of Fe induced activity enhancements in Ni-based OER catalysts is provided in Chapter 2.4.3. The effect of electrolyte impurities on the AEM is rarely reported in the literature. Among the few identified concerns, CO_2 contamination is particularly critical (more in 2.3.5).

Durability

In AEMWE literature, durability is commonly reported either as stable operation time at fixed current density or as a voltage degradation rate at constant current. Operational tests are typically limited to hundred hours, and in some cases, even less.[84,102–106] In the literature, there are only a handful of extended durability tests with documented operational durations of 500 h,[107] 1000 h,[108] or 2000 h.[66,109]

The large-scale deployment of AEMWE is limited by its durability. Still, Motealleh et al. achieved significant stability, with their electrolyzer running effectively in 1 M KOH at 1 A cm^{-2} for around 10,000 h, exhibiting a low degradation rate of 0.7 µV h^{-1}, best stability reported so far.[63] Apart from this work, the usually reported AEMWE durability does not exceed 2000 h. For comparison, established AWE systems can operate up to 100,000 h, a timeframe that is believed to be economically favorable for hydrogen production, as supported by various references.[76,110,111]

Numerous further studies offer detailed evaluation of the AEMWE system using transition metal electrocatalysts, covering test conditions, and examining both the activity and stability of these systems.[11,19,41,63,67–80,112]

Considering all components and testing parameters collectively, there has been notable progress in the performance of AEMWEs. Between 2011 and 2015, the performance in pure water improved from ≈0.2 to ≈0.9 A cm^{-2} at 2 V using a non-PGM anode and a PGM cathode. By 2020, performances of 2 A cm^{-2} at 2 V were achieved.[90,92,113–116] For single-cells fed with aqueous KOH, there has been a comparable improvement in performance. Currently, these cells can achieve up to 3 A cm^{-2} below 2 V, a result of using progressively thinner membranes and advanced catalysts that enable higher potential efficiencies.[117,118] Overall, the non-PGM electrodes, particularly anodes, still perform better in diluted alkaline electrolytes rather than pure water.[63,119–122] The reported performance of AEMWEs using pure water is usually attributed to high operating temperatures (>60 °C), while advanced ionomeric binders that maintain a high pH at the catalyst-electrolyte interface.

As described earlier, the difficulties in comparing performance among reports arises from the strong dependence of AEMWE behavior not only on operational parameters but its components, such as membrane type, catalyst composition and loading, electrode design. Those aspects are described further.

2.3.2 MEMBRANE-ELECTRODE ASSEMBLIES

The MEA is the core functional unit of a water electrolyzer, integrating the membrane with both electrodes, the cathode and the anode. The AEMWEs adopt the so-called zero-gap configuration, the same as known from PEMWEs, where the membrane is sandwiched directly between the electrodes. This design minimizes interelectrode distance, significantly reducing resistive losses and improving overall cell efficiency.[123]

MEA fabrication is typically based on two approaches: the catalyst-coated substrate (CCS) and the catalyst-coated membrane (CCM).[124,125] Each method offers advantages and challenges, with their suitability depending on system characteristics and scalability requirements. The possible MEA architectures are summarized in Figure 2.5.

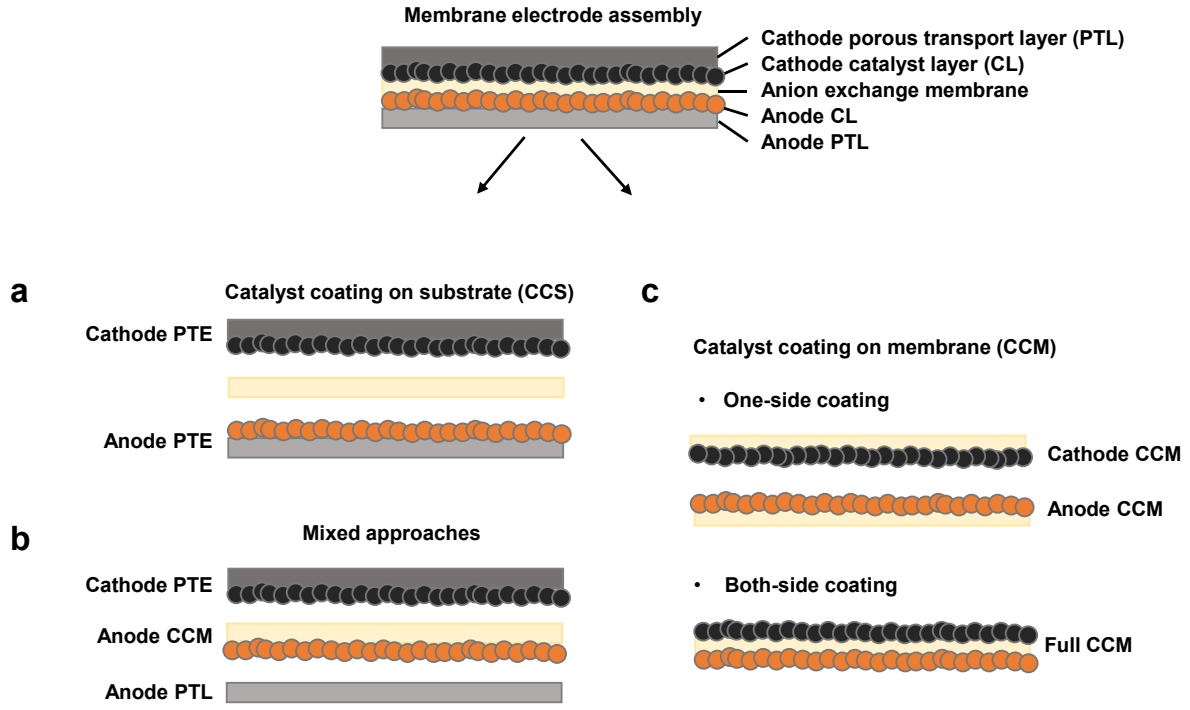

Figure 2.5. Concepts of membrane-electrode assemblies (MEAs): (a) catalyst coated on substrate (CCS); (b) mixed CCS/CCM approach as applied in this work, (c) catalyst-coated membrane (CCM), one or two side coated.

In the CCS method, the catalyst layer (CL) is deposited directly onto the substrate (usually, PTL), and the membrane is later placed between the two electrodes during MEA assembly (Figure 2.5a). In contrast, the CCM approach involves the CL being in direct contact with the membrane, forming a CCM-MEA, with the PTLs later added in mechanical contact only (Figure 2.5c). The CL is not always directly applied on the membrane; there are mixed possibilities to fabricate the MEA (Figure 2.5b). Hybrid configurations can combine the mechanical robustness of CCS type electrodes with improved ionic contact at the membrane interface. CCMs can achieve high performance with lower catalyst loadings[126] and offer improved uniformity in large-area electrodes.[127]

The CCS approach is widely used in AEMWE research due to its straightforward and relatively simple fabrication process, offering mechanical stability and flexibility in handling.[128] During fabrication, such as doctor blade, slot die coating or spraying deposition, the catalyst dispersion can penetrate multiple layers of the PTL, creating a multidimensional CL structure with high electrochemical surface area and enhanced accessibility. The direct contact between the conductive substrate and CL ensures efficient electron transport and strong adhesion, while the PTL provides mechanical support to withstand stress during cell assembly and operation.[129,130] An additional advantage of CCS-MEAs is the possibility of membrane and electrode lifetimes separation. If membrane degradation occurs, the membrane can be replaced separately. This is not possible in CCM-type MEAs, where the catalyst layers are permanently integrated into the membrane.[123] However, the lack of continuous contact between the membrane and the CCS-electrode is at the same time a drawback of the CCS approach. The missing CL-membrane contact can lead to increased interfacial resistance and reduced ionic conductivity.

These shortcomings can become more significant in low-conductivity environments, i.e., during pure water operation, where efficient ionic transport is essential.

Historically, the CCS configuration also dominated early PEM fuel cell (FC) development. Pt nanoparticles were deposited onto carbon-based gas diffusion layers to form gas diffusion electrodes, which were mechanically pressed against the membrane. Although suitable for initial lab-scale fabrication, this approach lacked the reproducibility and precision needed for large-scale production.[127] To address these limitations, the field shifted toward the CCM method, wherein the catalyst is applied directly onto the membrane surface, forming a monolithic structure. This change was driven in part by the mechanical flexibility of PEM materials like Nafion®, which enabled continuous coating using automated roll-to-roll processes. However, direct wet-coating of the membrane introduced new challenges. Exposure to solvent-rich catalyst dispersions could cause swelling, wrinkling, or shrinkage of the membrane, resulting in mechanical distortion or catalyst layer delamination.

To mitigate the issues occurring on the membrane in direct contact with a dispersion, the decal transfer method was introduced.[127] The decal method exploits the difference in glass transition temperature (T_g) between the ionomer and the substrate, allowing the catalyst layer to be transferred onto the membrane upon heating and pressing above the ionomer's T_g.[42,43] In this process, the CL is first cast onto a so-called transfer sheet (typically a PTFE-based film), dried to remove solvents, and then hot-pressed onto the membrane. This method reduces membrane exposure to solvents, allows better control over catalyst loading, and improves CL adhesion. It has since become the standard for CCM fabrication in PEMWEs and PEMFCs, offering enhanced reproducibility and compatibility with industrial manufacturing.[127]

However, the transfer of the decal method to AEMs remains technically challenging. Most polyaromatic-based AEMs exhibit poor thermal stability or T_g above 200 °C, making them unsuitable for the hot-pressing steps required in decal transfer. As a result, AEMWE research still predominantly relies on direct deposition methods like spray, bar, and slot-die coating, with potential for scale-up via roll-to-roll processing.[91,131–133] In this work, for instance, a direct ultrasonic spray-coating technique was employed to fabricate CCMs without the need for post-treatment or hot-pressing. While this method demands careful control to avoid membrane damage, it offers a practical approach for AEM-based MEA fabrication.

Establishing a universal preference between CCS and CCM configurations is not straightforward. Their relative performance depends on factors such as electrode composition, electrolyte concentration, and membrane properties.[78,81,128,134] In alkaline electrolytes like 1 M KOH, CCS electrodes often perform well due to their integrated, porous structure and effective electron transport via the PTL. However, if AEMWE technology develops toward operation with lower electrolyte concentrations or pure water, the more compact and well-integrated CL structure of CCMs may become increasingly advantageous.

2.3.3 ELECTRODES AND CATALYST LAYERS

Enhancing catalytic activity and utilization across the electrode involves more than catalyst development; it also requires morphological and structural enhancements to the electrode and the CL to increase accessible active sites. While the focus is more often on catalyst powder preparation,[92,135–139] the development of CLs is crucial yet frequently underestimated.

In AEMWE, the OER proceeds efficiently only at catalyst sides that simultaneously provide electronic conductivity, ionic connectivity, and access of liquid water as reactant with continuous pathways for oxygen removal. This co-located interaction is usually described as the triple-phase boundary (TPB), Figure 2.6, defined as the interfacial region where an electronic conductor (catalyst or PTL), an anion-conducting phase (ionomer or membrane, that enable OH^- transport) and the liquid reactant medium (water) meet at.[19,140–142] The illustration 2.6 is specifically valid in pure water operation. In KOH-fed AEMWE operation, the OER reaction zone can be described as a four-phase environment, because ionic transport may occur through both the anion-conducting ionomer and the aqueous KOH electrolyte, while electron transport is provided by the catalyst support and oxygen evolves into a distinct gas phase.

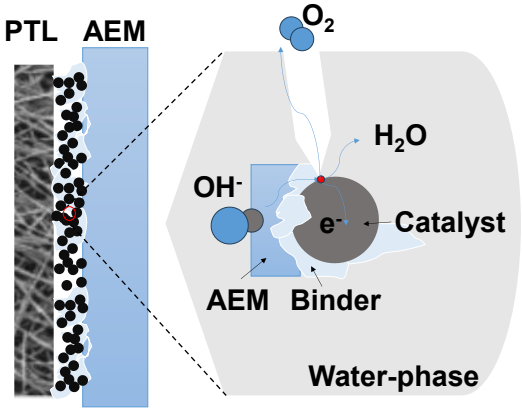

Figure 2.6. Schematic illustration of the TPB at the anode in a pure water operating AEMWE. The red point emphasizes the effective TPB region of electronically conductive network (catalyst), an ion-conducting phase (binder), connected to the AEM, and liquid water, enabling OER with additional water and oxygen gas release into the pore space.

So catalyst utilization is governed by the effective TPB density, which depends on ionomer coverage and film thickness on catalyst particles, the percolation of both electronic and ionic pathways, and the pore network connectivity and wetting state governing water supply and oxygen removal.[19,142] To achieve this, systematic research on catalyst inks and electrode fabrication is essential to maximize catalyst utilization. In particular, careful selection and evaluation of ink dispersions is critical to ensure a balanced catalyst-binder distribution and to increase the density and effectiveness of TPB.[18,143]

The amount of ionomer inside the CL should be carefully investigated; a low level of ionomer can cause increased ionic resistance, whereas too much ionomer might result in electrode blocking and hinder mass diffusion.[144,145] Numerous studies have explored the impact of ionomer content, aiming to find a balance between those two factors. The suited content of binder varies depending on the material,

leading to studies typically reporting system-specific optimal values based on the specific setup being investigated.[146–148] Usually, the ionomer content in the anodic CL of AEMWEs ranges from 7 to 25 wt%.[146,148–152]

Recently, there have been reports on the strategic design of the CL structure, focusing on optimizing the advantages of diverse MEA fabrication techniques.[128,130,153] In CCM, the CL is deposited directly onto the membrane, typically improving ionic contact at the CL-AEM interface. In CCS, the CL is deposited on or within the PTL, which can promote a more three dimensional catalyst distribution and favorable gas and liquid transport pathways, but can suffer from insufficient CL-membrane contact that limits the ionically connected catalyst fraction and thus reduces effective TPB density.[154,155] The efficiency of either the CCS or the CCM is further influenced by the preparation of the electrode.[156,157] The configuration of the electrode, particularly in terms of catalyst loading and ionomer content, also plays a crucial role in ensuring efficient electronic conductivity, optimal utilization of the catalyst, and effective mass transport of reactants and conductive ions.

The primary obstacle in achieving high performance in AEMWEs is the kinetically slow OER. Expectingly, an increased catalyst loading in the anode would lead to a higher number of active sites and would so boost the single-cell performance. Yet, after a specific loading, a performance-plateau may be reached, when further increase in catalyst content will not lead to further performance improvements.[152] Further, excessive catalyst loading leads to a thicker catalyst layer, which in turn raises mass transport and electronic resistances.[83,152] Therefore, achieving the optimal catalyst loading is essential for maximizing performance. For Ni-Fe-LDH anodes, reported loadings typically range from 2 to 3 mg cm^{-2}.[104,158–160] These loadings are comparable to other non-PGM catalyst loadings reported in literature.[84,152,161,162]

Not only the catalyst loading, but the catalyst distribution and the structural characteristics of the electrode are important. Wang et al. described that a uniform catalyst distribution enhances the electrochemically active surface area and improves mass transport, leading to increased efficiency. Conversely, uneven catalyst dispersion can result in performance losses due to poor electron conductivity and hindered ion transport pathways. Additionally, thinner anode CLs are shown to maintain good performance even with lower catalyst loading.[130]

Beyond the electrode structure, the adhesion of the CL to the substrate (AEM or PTL) is critical. Numerous studies, including the herein presented results, have highlighted issues with insufficient contact between the CL and AEM.[82,128,163,164] The proper adhesion of CL to the AEM and the PTL is important for several reasons. It ensures efficient electron and ion transfer for optimal functionality, enhances catalyst utilization, and contributes to the system's durability. Additionally, strong adhesion reduces overpotentials and ensures a uniform reaction distribution across the electrode by improving interfacial contact and lowering local current-density inhomogeneities.[165]

2.3.4 POROUS TRANSPORT LAYERS

The PTL serves as the intermediator between the catalyst layers and the current collectors, facilitating various transport processes essential for efficient electrolysis (Figure 2.4). Usually, the PTL is a fiber-felt, a foam-sheet or a woven metal network. The main functions of the PTL are: electronic conductivity, gas diffusion and mass transport, heat distribution, mechanical support for the CL and the MEA, pressure distribution, and creation of contact surface. Consequently, and correspondingly, the PTL exhibits pathways from external electric circuit to the electrode surface, distributes evolved product gases away from the CL while supporting the water or electrolyte supply and its homogenous distribution within the system. It further equalizes the pressure throughout the electrode and increases the effective contact surface area between the CL and the AEM.

Due to the need to transport electrons, the PTLs must be highly electrically conductive. To distribute reactants and products, a suitable porosity is further required. Usually, for these aims, Ti felts, well-known as the components of PEMWEs, were implemented as a PTL for AEMWEs.[17,161,166] However, the obtained performance was poor due to the surface passivation of the Ti.[167,168] For alkaline environment, Ni foams and Ni felts, recently used more often in the AEMWE system, have been successfully employed as an alternative to the Ti fiber felt PTL.[92,131,152,169,170] The advantage to use Ni-based PTLs is the initial catalytic activity and the thermodynamic stability of such PTLs.[84,170] Further, stainless steel (SS) PTLs were implemented into AEMWEs.[171,172] The steel alloy should be carefully chosen as not every material can stand the required conditions. Conventional SS 316 can release Fe-ions into the alkaline electrolyte at elevated temperatures and after longer exposure.[162,173] The choice of the optimal PTL is not straightforward and a benchmark does not exist yet for the AEMWEs. Which of the Ni-based PTL types, the fiber or the foam PTL, results in higher single-cell performance is still controversy discussed. The debate over whether SS-based or Ni-based PTLs, foam or fiber felt, exhibit greater catalytic activity for the OER and should be employed on the anode side is still under discussion.[166,170,171]

Based on the existing literature at the start of this work, preliminary experiments and project objectives, Ni-felt was selected as PTL for the anode side in this study. On the cathode side, facing lower potentials compared to the anode side, the use of carbon felts is possible.[174]

2.3.5 ANION EXCHANGE MEMBRANES AND IONOMERS

The AEM is the key component of the AEMWE MEA, primarily enabling ion conductivity by facilitating hydroxide ion transport from the cathode to the anode. Additionally, it acts as a physical separator, preventing direct hydrogen-oxygen mixing, which is essential for ensuring both system safety and efficiency. The membrane also serves as an electrical insulator, directing electron flow through the external circuit. Despite its critical role, low ionic conductivity and limited durability are hindering the large-scale adoption of AEMWEs. However, recent advancements in OH^- conductivity and alkaline stability are accelerating AEMWE development, making it a more viable alternative for sustainable hydrogen production.[162,175–178]

The AEM structure consists of a polymeric backbone, primarily providing thermal and mechanical stability, and functional groups (typically cationic) that electrostatically compensate OH^- ions. The functional groups are responsible for ion exchange and directly influence the ionic conductivity of the membrane. The most commonly cited backbone materials in the literature include PSU,[179] polyetherketone (PEEK),[180] poly(p-phenylene oxide) (PPO),[181] polybenzimidazole (PBI),[182] polyaryletherketone (PAEK), polyethylene (PE), polystyrene (PS),[182] polyethylenepyrrole-co-polyethyleneketone,[183] ETFE,[183] poly(carbazole),[184] polyphenylenes, perfluorinated types, and poly(vinylbenzyl chloride)-based varieties, among others. Typically, nitrogen-based functional groups are attached the backbone, including quaternary ammoniums (QA) like benzyltrialkylammoniums and those without benzyl rings. Heterocyclic systems such as imidazolium, benzimidazoles, and pyridinium-based types are also used. Less commonly, guanidinium-based,[185] phosphonium-based, and sulfonium-based[186] systems are incorporated. Additionally, metal-containing groups featuring complexes of Ru(II), Ni(II), and Au(II) have been documented.[187]

The ionic conductivity of the AEM is strongly influenced by its nanostructure as well as the ambient relative humidity. Exposure to air can result in deactivation (diminished ionic conductivity) due to the reaction of hydroxide ions with carbon dioxide (CO_2). Therefore, it is important to maintain full hydration of the AEM using a CO_2-free aqueous electrolyte.

Several AEMs are already available on the commercial level. Among these, the most popular are Fumasep® (Fumatech), Aemion™ (Ionomr), A201 (Tokuyama), Sustanion® (Dioxide Materials), Durion™ TM1 (Orion Polymer), PiperION (Versogen).[11,96,188–192] The literature provides a comprehensive overview of commercial AEMs, specifying their various properties.[11,67] Comparative tests of single-cell performances under identical conditions using commercial AEMs revealed that Sustanion® exhibited enhanced results over Aemion™ and A-201.[163] Among the available Aemion™ membranes, those with higher ion-exchange capacity and decreased thickness (up to 25 µm) achieved higher performances, especially in low electrolyte concentrations.[17]

As binding additives, or so-called binders or ionomers, which connect the catalyst particles within the catalyst layer, anion-exchange ionomers (AEIs) are used in AEMWEs. Like AEMs, those materials conduct negatively charged hydroxide ions through the positively charged cationic functional groups attached to the backbone of the polymer chain.[193] Besides the use as a binding agent, the AEIs create ion conducting pathways inside the catalyst layer being in charge of the ionic conductivity inside. The latter is controlled by the number of available anion-exchange functional groups. The drawback of a high conductivity is the increased water uptake, or swelling, of the AEIs and so shortcomings as ionomer dissolution upon increased operation temperature and degradation at higher operation voltages.

Overall, further progress in AEMWE depends strongly on simultaneously improving the AEM and AEI chemical and mechanical stability, intrinsic ionic conductivity, and interfacial compatibility of AEMs and AEI-containing CLs under realistic operating conditions. In addition to ion-transport materials,

catalyst selection critically defines the achievable performance; the next section therefore outlines state-of-the-art HER and OER catalysts and highlights the most promising candidates.

2.4 Catalysts for AEMWE: Overview and Mechanisms

A catalyst is a material that accelerates a chemical reaction without being permanently changed. In AEMWE, catalysts promote efficient water-splitting to produce hydrogen and oxygen, thereby reducing overpotentials and improving overall efficiency. Developing durable, non-precious HER and OER catalysts is therefore central to enabling cost-effective AEM electrolysis.

2.4.1 HER IN AEMWE

In alkaline conditions, the kinetic pathway of the HER unfolds in two phases: the initial dissociation of the water molecule to form hydrogen intermediates, known as the Volmer step, followed by either the electrochemical Heyrovsky step or the chemical Tafel recombination (as shown in Figure 2.7).[194] By **M** the active side for the reaction on the surface of a metal-based catalyst is indicated. The Volmer step is associated with the water oxidation to adsorbed hydrogen, which afterwards can be combined with molecular hydrogen (Tafel step) or with the hydrogen from another water oxidation step (Heyrovsky step).[195] The catalytic activity of HER decreases with increasing pH. In alkaline media, protons are not readily available, and hydrogen formation proceeds via water dissociation (Volmer step), which introduces an additional kinetic barrier and can be further hindered by OH^- adsorption that partially blocks active sides. This is critical for alkaline water electrolysis, where HER occurs at more negative potentials than OER. Consequently, the cathode operates under less oxidative (and less material-restrictive) conditions, meaning a broader range of materials can be considered for HER. Although in alkaline environment non-PGM metals can be used, Pt is still most active for HER and still serves as the benchmark catalyst,[196,197] even though its activity is over two orders of magnitude lower in alkaline than in acidic environments.[194,197,198] Still, the cheaper transition metal electrocatalysts can compensate their decreased activity and performance by higher surface area and catalyst loading on the electrode.[199]

Efforts to minimize the use of precious metals have led to the investigation of Ni and Pt composite catalysts, taking advantage of the synergistic effect between the two elements.[200–203] Studies on various combinations, such as Pt on $Ni(OH)_2$[204,205] or PtNi(N),[206] have shown similar or even superior catalytic activity compared to pure Pt.[75,207] Palladium (Pd) has also been examined as a viable alternative to Pt, with promising results observed in Pd-Ir/C nanoparticles, Pd_3Ru,[208] and Pd-Cu alloys[209] among others. Due to the aimed shift to completely PGM-free catalysts, many Ni-based HER catalysts were developed and investigated for alkaline environment. Pure commercial Ni nanopowder usually shows low electrochemical performance, as the intrinsic catalytic activity of Ni is relatively poor. To overcome the low activity, strategies to combine Ni with transition metals or other chemical compounds as oxides, selenides, nitrides, phosphides (Ni_2P, Ni_3P),[210] sulfides[211,212] were conducted. Ni_3N nanoparticles,[213] Ni-CeO_2/CNTs,[214] Ni-Cu alloys, Ni supported on mixed oxide and carbon

materials (CeO_2-La_2O_3/C),[161] Ni-NiO nanostructures supported on CNTs presented promising activities, but still did not reach the Pt-based catalyst performance.[215] Furthermore, oxides based on Mo and W have been utilized.[216] Even with the characteristic low electronic conductivity of these transition metal oxides, MoO_2 demonstrated both high stability and activity in an alkaline environment. Among a broad range of Ni-based binary and ternary alloys featuring elements like Fe, Co, Mo, Ce, Cu, and Zn, Ni-Mo alloys[217] have stood out for their superior catalytic performance[81] and have been extensively investigated.[91,218] However, in the context of AEMWE, achieving durable HER performance and translating promising catalysts into robust cathodes remain challenging, since alkaline HER relies on water dissociation and is highly sensitive to surface blocking and restructuring, impurity-driven deposition (e.g., Fe-ion deposition), and electrode architecture effects such as catalyst-layer wetting, bubble removal, and stable ionomer pathways. All these are factors that can cause performance drift even when intrinsic catalyst activity is high.

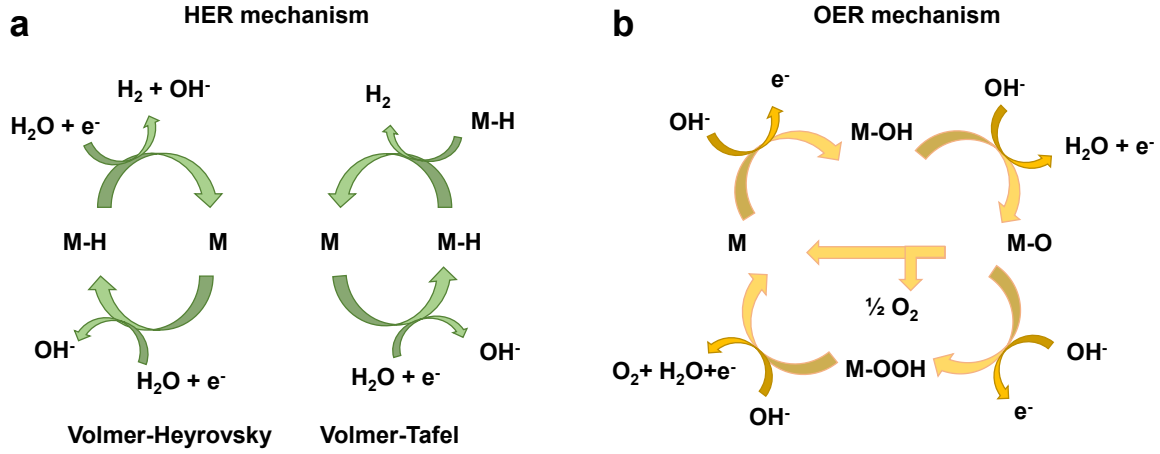

Figure 2.7. Schematic overview of the electrochemical mechanisms: (a) hydrogen evolution reaction (HER) and (b) oxygen evolution reaction (OER) pathways, highlighting intermediate steps.

2.4.2 OER IN AEMWE

In alkaline environment, the OER strongly contributes to the overall system overpotential because it remains a kinetically demanding four-electron process, that involves adsorption of OH^- intermediates, electron transfer, oxygen desorption.[219,220] The OER mechanism is still debated but commonly assumed as presented in Figure 2.7b.[13,221–223] Here, **M** denotes an active site on the metal-based catalyst surface. In alkaline media, OER is commonly described by a sequence of proton-coupled electron-transfer steps involving adsorbed oxygenated intermediates. First, hydroxide adsorption and oxidation form a surface hydroxyl species ($M + OH^- \rightarrow M–OH_{ads.} + e^-$). In the second step, further oxidation yields a surface oxo-species ($M–OH + OH^- \rightarrow M–O_{ads.} + H_2O + e^-$) or a hydroxide ($M–OH + OH^- \rightarrow M(OH)_2 + e^-$).[224] In the third step, nucleophilic attack of OH^- on M–O produces a hydroperoxo intermediate ($M–O/M(OH)_2 + OH^- \rightarrow M–OOH + e^-$). Finally, oxygen is released and the active site is regenerated ($M–OOH + OH^- \rightarrow M + O_2 + H_2O + e^-$). Overall, O_2 formation proceeds via four electron

transfers and involves hydroxide as the oxygen source, while the exact identity of the active site and the dominant pathway may depend on catalyst composition and operating conditions.[225,226]

Due to this complexity of the OER, the anodic overpotential becomes the dominant factor in a two-electrode cell configuration. Under standard conditions, the OER free-energy diagram indicates a step height of 1.23 eV and a total free energy change of 4.96 eV to transfer all four electrons.[227] Are the electrode potentials higher than 1.23 V, the OER becomes thermodynamically possible. The difference between the free energy change a catalyst causes and the value 1.23 V is called overpotential. As previously noted, the OER is kinetically inherently slow. Adjustments in the binding energy between the catalyst and reaction intermediates can change the overpotential. The minimum overpotential, for a catalyst that has a strong bond with a reaction intermediate, is determined by the energy required to break that bond between the intermediate and the catalyst surface. Strong binds between the catalyst and the intermediate predicts the overall catalyst activity (and resulted overpotential) and the suitability for being exposed in the OER. Mn, Co, Ir, and Ru oxides[228] are great examples of catalysts forming strong bonds with reaction intermediates and exhibiting high intrinsic OER activity, but poor long-term stability in alkaline conditions.[19] Those catalysts were the main anodes in concentrated alkaline environment for a long time.[7,42,229,230] Non-PGM catalysts such as those based on Ni, Co, Fe, and Cu are gaining attention for their cost-effectiveness and suitability for alkaline environments. Bimetallic catalysts like Ni-Fe outperform their single-metal counterparts in catalytic activity. For AEM water electrolyzers, Ni alloys and CoCu-based catalysts show high performance, with Ni-Fe-LDH standing out as the most effective, even surpassing Ir-based alternatives.[75,76]

2.4.3 NI AND NIFE-BASED OER CATALYSTS

Advanced density functional theory (DFT) calculations offer atomic-level understanding of catalysts.[231,232] Specifically, volcano-type plots can serve as activity trend guides for catalyst surfaces, assisting in the identification of high-activity catalysts through correlations with surface adsorption properties and electronic structure.[232,233] Theoretical examinations of various non-PGM catalysts showed that Ni- and Ni-Fe-based, and especially Ni-Fe-LDH with a hydroxide interfacial layer, demonstrate improved OER activity.

Electrochemistry of Ni

Understanding the electrochemical fundamentals of Ni is crucial for properly analyzing the outcomes and challenges of AEMWE systems (and the results of this work), given that Ni-based catalysts are commonly investigated for OER (and HER) in these contexts. Knowing the Ni cyclic voltammetry (CV) results (Figure 2.8),[234–236] prediction of the oxidation state and the formed Ni species can be made.

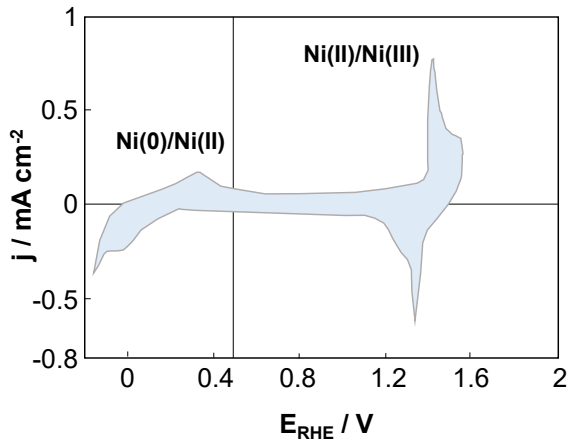

Figure 2.8. Cyclic voltammogram for Ni electrodes, scanned at 100 mV s^{-1} (0.5 M KOH, 293 K), based on literature.[234–236]

For Ni-based electrodes, under cathodic polarization in the HER region, surface oxides/hydroxides are reduced and the Ni surface becomes metallic; pre-formed NiO_x and $Ni(OH)_2$ species are converted back to Ni. Under sufficiently negative potentials, hydrogen absorption can occur, leading to the formation of α- and β-NiH_x phases.[235,237] When the potential is swept in the positive direction from the cathodic region towards more anodic potentials, the metallic Ni surface is progressively oxidized, forming the reversible surface hydroxide species α-$Ni(OH)_2$, according to the Ni(0)/Ni(II) transition, from −0.15 to 0.5 V vs RHE (Figure 2.8):

$$\mathrm{Ni} + 2\mathrm{OH}^- \rightleftharpoons \alpha\text{-}\mathrm{Ni(OH)_2} + 2e^- \qquad \text{(Equation 2.22)}$$

Nickel hydroxide may also form during storage in humid air. In this case, Ni is initially covered by a thin native NiO film, which can partially transform by hydration and oxidation into a layered surface consisting of metallic Ni beneath an oxide/hydroxide overlayer (often represented as $Ni/NiO/Ni(OH)_2$).[238][239] Further, according to Bode et al.'s work[240] (Figure 2.9), raising slowly the applied positive potential in the window of -0.15–1.55 V facilitates the irreversible aging of α-$Ni(OH)_2$ to β-$Ni(OH)_2$.

Further potential rise towards 1.55 V transforms both α- and β-$Ni(OH)_2$ into Ni oxyhydroxides, γ-NiOOH and β-NiOOH, respectively. To mention, α-$Ni(OH)_2$ and γ-NiOOH are hydrated phases, having intercalated water molecules in the structure.[241,242] The anodic peak around 1.2–1.55 V (Figure 2.8) corresponds to the Ni(II)/Ni(III) transition:

$$\mathrm{Ni(OH)_2} + \mathrm{OH}^- \rightleftharpoons \mathrm{NiOOH} + \mathrm{H_2O} + e^- \qquad \text{(Equation 2.23)}$$

Above 1.5 V, only the OER dominates. All these transformations can be observed by in situ Raman spectroscopy.[243]

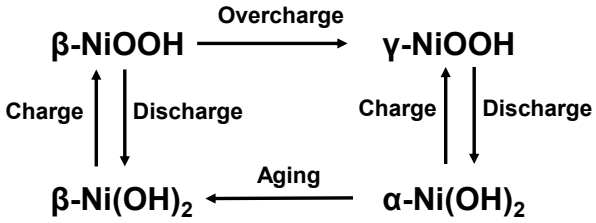

Figure 2.9. Bode's diagram for $Ni(OH)_2$-NiOOH reduction-oxidation transformations, adapted from reference.[240]

Fe effect

In the context of Ni-based OER catalysts, Fe plays two distinct roles that should be clearly separated. First, Fe can be intentionally introduced as a compositional element of the catalyst, for example in Ni-Fe-OOH and or Ni-Fe-LDH structures, to enhance OER activity through electronic and structural effects.[244–246] Second, Fe can be unintentionally incorporated during operation from trace impurities in alkaline electrolytes or from Fe containing system components, which can artificially improve anode performance.[94,247–249]

Because Ni-based catalysts alone exhibit limited OER activity, incorporating Fe into the Ni lattice has been intensively studied and is widely recognized to significantly enhance performance.[93,250] The role of Fe compounds in enhancing the performance was previously addressed in 1987.[251] The observation revealed that even trace amounts of Fe impurities in the KOH electrolytes increased the OER activity of Ni-based catalysts.

When the catalytically active NiOOH phase forms, Fe is incorporated into the Ni lattice by substituting Ni^{2+} sites; a similar process has also been observed for the α-$Ni(OH)_2$ phase.[252,253] In line with many previous studies,[93,242,252,254] Fe supports the oxidative shift in the Ni(II)/Ni(III) redox peaks and significantly improves OER activity. Prior research suggests that these changes may be attributed to Ni-to-Fe charge-transfer[254] and Fe's influence on the trigonal distortion of Ni centers.[255] Incorporating Fe into NiO_xH_y catalysts has been reported to increase catalytic activity by up to 1000 times,[256] while in NiO_xH_y films, Fe enhances catalytic activity up to 50 at%, but beyond 30–50 at%, it transforms into Fe_2O_3 and unstable FeOOH, diminishing the catalytic effect.[257] In NiFeOOH and Ni-Fe-LDH, Fe is considered as the active side as well.[244,253,257,258] However, the actual Fe influence on the Ni-based catalyst performance is surrounded by significant uncertainty and the debate regarding the role of Ni and Fe and the true active site continues, primarily due to the oxyhydroxide's complex structure.[15,242,244,253,259] Still, it remains essential to maintain a considerable number of active sites for both metals. This is because both Fe and Ni sites undergo oxidation to form active NiOOH and FeOOH compounds, which collectively contribute to enhanced OER performance, particularly at elevated current densities. These findings have stimulated the development of highly efficient Ni-Fe-based oxyhydroxide catalysts.[13,242,260]

2.4.4 NI-FE-LDH OER CATALYSTS

As discussed in previous chapters, Ni-Fe-LDH catalysts are among the most active OER materials and, consequently, are among the most widely developed. This strong interest stems from their chemically tunable structure, high activity under anodic polarization, and cost effectiveness enabled by the use of earth abundant elements.

Structure and active phase

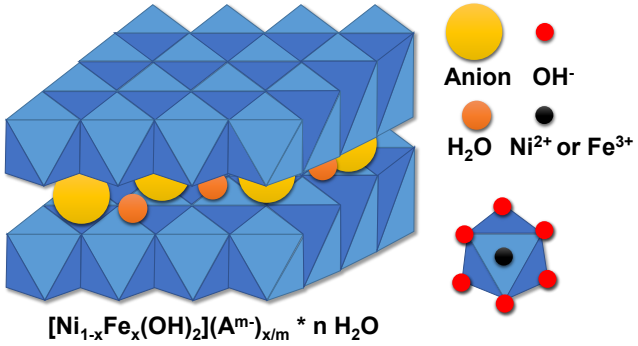

Figure 2.10 Schematic structure of the catalyst nickel-iron layered double hydroxide (Ni-Fe-LDH), highlighting the brucite-like layers and intercalated anions.

The Ni-Fe-LDH structure (Figure 2.10), also known as hydrotalcite-like clays, consists of positively charged well-defined layers composed of divalent Ni^{2+} and trivalent metal cations (e.g. Fe^{3+}), which are coordinated with OH^- anions (blue octahedra in Figure 2.10). Within the interlayer spaces of these layers, charge-balancing anions like CO_3^{2-} are intercalated. Those can be replaced by other anions like NO_3^-, SO_4^{2-}, Cl^- or Br^- or even organic anions (like short monomers or extended polymer chains).

Within the interlayer spaces of LDHs, intercalated water molecules form a dense hydrogen-bonding network, simultaneously bonding to hydroxyl groups on the LDH sheets and coordinating with the interlayer anionic species.[261,262] This interlayer hydration is not only a structural feature, it is directly linked to ion accessibility, anion exchange behavior, and stability under electrochemical operation.[263]

Under anodic potentials, Ni-Fe-LDH catalysts are reported to undergo surface reconstruction toward oxyhydroxide type phases, while the bulk layered structure can remain partially intact depending on operating conditions.[264] As a result, the catalytically active state can differ from the as-synthesized material, and both activity and degradation behavior may depend on the extent of reconstruction, Fe distribution, and the local chemical environment within the catalyst layer.[264] This aspect is particularly relevant when transferring Ni-Fe-LDH catalysts from three-electrode testing to MEA operation, where chemical environment, hydration, ionomer interactions, and local pH can differ.

Strategies for activity and conductivity improvement

Within the last years, many approaches to further improve the electrochemical activity of Ni-Fe-LDH catalysts have been reported. The main strategies can be grouped into four categories.

The first approach is increasing the density or number of active sites, e.g., by reducing particle size, creating defects or exfoliating layered structures. Exfoliation is often reported to increase electrochemically active surface area and to improve OER activity relative to bulk layered catalysts.[265-267]

Second, OER performance can be improved by increasing the electronic conductivity of the catalyst, for example by introducing conductive support. Specifically, one of the approaches is to dope Ni-Fe-LDH with carbon composites, graphene oxide or Co-N carbon nanoframes[95,268,269] to increase the structural disorder (from amorphous to distorted), number of active sites and conductivity. Conductivity is discussed as a requirement particularly when CL become thicker with higher catalyst loading of when ionomer content is increased for ionic connectivity or mechanical membrane stability.[19]

Third, OER activity can be tuned by interlayer chemistry, specifically, anion exchange and so adjustment in interlayer spacing.[270] This can influence water uptake, ion accessibility, and mass transport. Increasing the interlayer spacing provides greater diffusion space for reactants and facilitates bubble removal, while also exposing additional internal active sites for the reaction.[271]

Fourth, it is feasible to modify the local coordination environment through heteroatom doping or engineered reconstruction, aiming to stabilize highly active oxyhydroxide phases during OER.[272,273]

While these approaches can enhance intrinsic activity in half-cell tests, their relevance under AEMWE MEA conditions additionally depends on catalyst-layer formation, ionomer distribution, and stable interfacial contact to the membrane and porous transport layer.

Ni-Fe-LDH in single-cells

The incorporation of Ni-Fe-LDH into practical single-cell is the main challenge of the catalyst to be system relevant. At the start of this thesis and up to 2021, a limited number of studies had reported AEM electrolyzer performance using Ni-Fe-LDH catalysts.[17-19] Usually, the catalyst performance was analyzed in a three-electrode setup, however several single-cell performance reports exist.

Early implementations included the work of Chi et al., who integrated FeOOH/NiFe-LDH based anodes and reported a cell voltage of 1.71 V at 200 mA cm^{-2} in 1 M KOH. A further relevant milestone was reported by Koshikawa et al. in 2020, who demonstrated a Ni-Fe-LDH-based MEA and reported an energy conversion efficiency of 74.7% at 1.0 A cm^{-2}, and a stability of 6 h (1 M KOH, 80 °C).[158] More recently, a 50 h single-cell operation using bulk, monolayer structured and carbon-based Ni-Fe-LDH on Ni foam PTL was presented by Jeon et. al.[159] Only in 2023, Xing et al. presented the first 1000 h of single-cell operation in seawater, using Ni-Fe-LDH on the anode side, where the catalyst proved OER activity but partial component dissolution.[274]

To sum up, the single-cell literature considered up to the active phase of this thesis demonstrates that performance and durability are strongly constrained by MEA architecture, interfaces, and operating environment, and further compounded by the lack of harmonized benchmarking. Notably, the number

of related studies increased markedly in the subsequent years, highlighting both growing interest and the continuing need for structured assessment of the remaining challenges and research gaps in AEMWE discussed in the following chapter.

2.5 CHALLENGES, BOTTLENECKS AND RESEARCH GAPS

While this work focuses on incorporating the Ni_3Fe-LDH catalyst and addressing MEA and electrode-architecture questions such as anode stability (research questions presented in Chapter 2), AEMWE research more broadly still faces numerous unresolved questions and system-level challenges.

Benchmarking and standardization gaps

Currently, there are few established and standardized benchmark materials and testing procedures for AEMWE. Testing protocols are sometimes provided by material developers, particularly for AEMs, or adapted from the EU harmonized polarization curve test method for low-temperature water electrolysis developed by the Joint Research Centre (JRC).[275] However, these protocols still require optimization and adaptation to accommodate the specific characteristics of different AEMWE systems.

Pt/C and Ir (or IrO_2) remain the benchmark catalysts for HER and OER, respectively.[142] However, direct comparisons of catalyst activity and single-cell durability are challenging due to significant variations in experimental conditions, including catalyst loading, ionomer content, surface area, testing methods, applied current densities (200–1500 mA cm^{-2}), temperature (50–80 °C), and electrolyte composition ($K_2CO_{3(aq)}$, $KOH_{(aq)}$, pure water), as well as impurity levels, particularly Fe contamination. These inconsistencies make meaningful data comparisons difficult. Consequently, defining the optimal MEA components remains a challenge due to the diversity of experimental variables and the lack of standardized evaluation protocols.

AEM and catalyst bottlenecks

The AEM is the major component of the AEMWE considered to determine the electrolyzer performance, durability and so possible failure.[69,193] The chemical stability of AEMs is still a huge drawback. When operation temperatures exceed 80 °C, chemical degradation of AEM starts.[276] The thermal stability limitations of AEMs becomes more severe at higher pH.[277,278] Membranes based on poly(oxy-2,6-dimethyl-1,4-phenylene) or PPO were shown to have a good stability in 0.5 M KOH, while a higher concentration of 1 M led to accelerated backbone degradation leading to overall AEM weight loss. Not only PPO-based materials suffer from backbone degradation, but most of the employed polyethersulfone or ketone-derived materials do.[279] In polybenzimidazole membranes, which have gained increasing attention in recent years, an excessive presence of OH^- ions can also be harmful. OH^- ions may attack the C2 position of the imidazolium moieties, while bulky protective groups can enhance polymer stability and shield the vulnerable site from OH^- attack.[280] QA-based AEMs degradation is concerning, as their ammonium groups are prone to be attacked by hydroxide ions, which decreases the ionic conductivity of such AEMs rapidly. Chemical instability is mostly caused by the so-called Hoffmann elimination, the nucleophilic attack of hydroxides on N-alkyl groups

(S_N2 mechanism),[278] and ylide intermediate formation, while phenyl oxidations and radical induced reactions are critical too. Strategies like adding bulky or electron-donating functional groups have been suggested to mitigate these stability issues. Mechanical limitations of AEMs become critical under interrupted electrolyte feed conditions, leading to membrane dehydration. Generally, AEMs should possess a high Young's modulus, substantial tensile strength, and significant elongation at break. Further, local changes in temperature and humidity, which affect the swelling behavior of the AEM, can lead to structural damages such as cracks and ruptures not only within the membrane but at the AEM-electrode interface. As the ionic exchange capacity directly affects the water uptake and swelling, as well as the chemical stability of the AEM, achieving a great mechanical robustness by AEM synthesis is a challenge. There is generally an inverse relationship between mechanical strength and ionic conductivity, both of which are crucial for optimal AEM performance. A key limitation of AEMs is their sensitivity to CO_2 contamination, leading to a carbonation reaction between the ion-conducting OH^- group and CO_2. This reaction produces low-conductive HCO_3^- and, with additional OH^-, CO_3^{2-} ions, reduces the AEM's overall conductivity. The resultant local pH gradient can accelerate oxidation and lead to localized AEM degradation. Furthermore, the discussion on AEM durability is not complete without addressing ionomer degradation, particularly in pure water operation. In such conditions, the ionomer tends to detach from catalyst particles and undergo electrochemical oxidation of adsorbed phenyl groups within the electrode.[90,281]

Catalyst stability is a critical requirement for practical water electrolysis systems and remains a major challenge. In general, stability limitations are more pronounced for OER catalysts because they operate under highly oxidative anodic potentials, whereas HER catalysts often fail through comparatively less severe mechanisms, including physical degradation such as catalyst detachment during long-term operation. Anodic dissolution is commonly identified as the primary cause of metal degradation during OER. Although this is usually a continuous process, Speck et al. recently demonstrated that catalysts could experience instability during both start-up and shut-down periods.[282] A further known effect is the elemental composition change of the catalyst among metal dissolution and a possible redeposition or incorporation.[283]

Further, the activity of a catalyst can decrease due to various factors such as catalyst dissolution (or components of it, as elemental leaching), particle agglomeration, Ostwald ripening,[284] corrosion of the supporting material, ionomer moiety adsorption, and chemical breakdown of the ionomer.[285] The catalyst also suffers in neutral electrolyte, undergoing dissolution, reformation, or degradation.[286,287] According to the Pourbaix diagram, Ni-based materials exhibit greater stability in environments with a pH above 9. This is particularly relevant for Ni-Fe-based catalysts, which suffer from severe degradation in near-neutral conditions, primarily due to Fe leaching.[287] Assessing catalytic activity in thin-layer electrode setups is typically a short-term evaluation. To gain a comprehensive understanding, it is essential to further examine promising catalysts in full AEMWE cells.

Challenges of Ni-Fe-LDH cell incorporation

Despite the high intrinsic OER activity reported for Ni-Fe-LDH catalysts in three-electrode setups, transferring these materials into AEMWE single-cells remains non-trivial and is often limited by implementation rather than intrinsic activity.

Beyond the initial requirement of a simple, scalable, and reproducible catalyst synthesis at technically relevant scale, a central bottleneck is CL fabrication. Reliable electrode fabrication approaches must include the preparation of stable catalyst inks, preventing agglomeration not only in dispersions but final layers, and guarantee in that way homogeneous catalyst-binder distributions within the CL. This is directly linked to maximizing the effective TPB and maintaining balanced ionic and electronic connectivity, and mass transport. CL preparation must be reproducible both in processing and resulting electrode properties across scales to ensure consistent performance and enable technically relevant operation. In addition, durable CL adhesion to both PTL and AEM is critical, as local detachment, cracking, or delamination under compression, bubble evolution, and hydration changes can drive voltage drift and accelerate apparent degradation. Beyond mechanical effects, Ni-Fe-LDH catalysts may also undergo in-operando reconstruction and compositional changes, including Fe redistribution or leaching, which can alter activity over time and complicate durability assessment. Therefore, detailed electrochemical and physico-chemical analyses before and after single-cell testing are essential, ideally complemented by monitoring chemical and morphological electrode evolution under high current densities and cell voltages to track catalyst changes under true electrolyzer conditions.[19,67,142,148]

3 RESEARCH QUESTIONS AND APPROACH

Based on the background and motivation outlined in the previous chapters, this thesis aims to transfer the highly promising Ni_3Fe-LDH catalyst into a realistic AEMWE operating environment and assess its industrial relevance for future deployment.[19,288] The primary objective is the *development, optimization and evaluation of Ni_3Fe-LDH-based anode electrodes*, or catalyst layers, with the final goal to reach *high current densities* and *long-term operational stability* in a single-cell. To achieve this, the research is structured around five central questions (Q1–Q5), and one additional (Q6), that guide the experimental investigations and shape the scope of the work.

QUESTIONS

Q1. Is Ni_3Fe-LDH a suitable and durable OER catalyst for application in AEMWE anodes under realistic full-cell conditions?[1]

Q2. Which electrode design parameters, specifically catalyst loading and ionomer content, and which operating conditions, such as temperature and KOH concentration, are most critical for achieving high-performance Ni_3Fe-LDH anodes in AEMWE while maintaining stable operation and compatibility with anion-conducting components?

Q3. Can Ni_3Fe-LDH-based single-cells achieve sufficient stability that is competitive with existing water electrolysis technologies, how does the performance evolve during extended operation, and which time-dependent structural, morphological, and what are the primary degradation mechanisms limiting electrode longevity?

Q4. How can directed electrode engineering, specifically catalyst treatment and ink dispersion control, improve the technical relevance of Ni_3Fe-LDH anodes by manufacturability, reproducibility, and long-term stability under realistic AEMWE operation?

[1] At the start of this research project in late 2020, a central question was whether the Ni_3Fe-LDH catalyst is suitable for OER electrodes in AEMWEs. Since then, multiple studies, including this thesis and the associated publications, have provided clear evidence of its general suitability. However, the more important issue concerns the aspects of the optimal implementation strategies and long-term stability under realistic operating conditions. These points are covered by the remaining four research questions (Q2–Q6) and topics.

Q5. How do MEA or electrode architectures (CCS vs. CCM configuration) affect performance, and can an optimized design enable efficient operation at low electrolyte concentration, including sensitivity to residual KOH and interface integrity?

Q6. How do material variability and evolving pre-commercial components affect reproducibility (across work packages), and how can data validity be ensured despite these constraints?

Question 1 forms the foundation of the study and is addressed in Chapter 5.1. The primary objective is to assess the electrochemical performance of Ni_3Fe-LDH-based anodes. Once feasibility is established, Question 2 is explored, also within Chapter 5.1, through variation of key electrode and operational parameters to identify optimal performance conditions. To evaluate long-term viability, Question 3 is tackled in Chapter 5.2, which presents degradation studies under extended operation and the associated anode characterization. Question 4 is addressed in Chapter 5.3, where further electrode optimization strategies are investigated to improve reproducibility and technical readiness. Finally, Question 5 is answered in Chapter 5.4, which analyzes the effect of MEA architecture in varied electrolyte concentration on performance. Chapter 5.5 complements these studies by assessing experimental reproducibility (Question 6) and material variability to ensure robustness of the findings.

To systematically address these six research questions, the following experimental and analytical approaches were pursued throughout this thesis.

APPROACH

A1. To establish Ni_3Fe-LDH as an OER catalyst for AEMWE establish feasibility under realistic AEMWE conditions (and answer Q1–Q2), the work begins with reproducible catalyst synthesis and quality control at powder level. Each Ni_3Fe-LDH batch is verified by physicochemical analysis to ensure structural and compositional consistency. The catalyst is then benchmarked against an Ir-based OER reference in single-cell. The translation from powder to functional CLs is treated as a central integration task: the development of CL includes a parameter study on catalyst loading (1–5 mg cm^{-2}) and ionomer content (10–20 wt%) to balance catalyst utilization, ionic and electronic conduction, and mechanical integrity. The performance is assessed across a relevant operational window by varying temperature (30–80 °C) and KOH concentration (0.01–1 M), identifying conditions that increase performance while maintaining compatibility with anion-conducting components.

A2. Catalyst durability (Q3) is evaluated via single-cell operation over 1000 h, complemented by a time-resolved degradation analysis of the anode catalyst layer. Rather than interrupting a single running cell, the study employs multiple identical single-cells fabricated from the same anode batch and operated under the same conditions, which are stopped after defined runtime durations. Specifically, single-cells are stopped after 15, 100, 200, and 500 h, and compared against the initial beginning-of-test sample (BoT or 0 h) and the end-of-test condition (EoT or 1000 h). This yields a controlled electrode set representing 0-15-100-200-500-1000 h of operation. This design of experiments provides two advantages: it enables time-resolved post-mortem characterization of electrode evolution, and it strengthens interpretation by revealing the reproducibility of degradation trends across repeats, allowing degradation to be discussed as a consistent function of time rather than as a single-cell artifact. Electrochemical characterization results are correlated with morphological and elemental analysis to identify the major degradation sources and the structural changes responsible for performance change within 1000 h.

A3. Technical relevance (Q1) of Ni_3Fe-LDH is further strengthened through directed electrode engineering steps that address both performance and manufacturability (Q4). Aiming to tailor initial catalyst cluster (or agglomerate) size, improve accessibility of active sites, and increase homogeneity of the catalyst layer, the key approach is catalyst milling combined with systematic dispersion control. The further includes analyses of the catalyst powder to attain possible intrinsic changes induced by milling, CL morphology to quantify structural improvements, and electrochemical performance and reproducibility characterization to demonstrate whether catalyst processing translates to single-cell improvements. To directly link the processing strategy to durability, an additional long-term stability test is performed and compared against the earlier baseline, enabling assessment of whether improved microstructure and fabrication consistency also result in improved degradation behavior.

A4. To investigate the advantageous configuration for catalyst integration (Q5), a comparison of MEA architectures is performed. A key element is the systematic evaluation of ionomer content in CCM-based MEAs, recognizing that CCM performance depends strongly on achieving sufficient ionic pathways without blocking transport or weakening interfaces. To improve reliability and reduce uncertainty arising from material variability, the thesis intentionally works with two binder-AEM pairs: one pre-commercial pair and one commercial pair (as a reproducible baseline). This enables conclusions to be drawn with higher confidence and clarifies which observations are architecture-driven rather than batch-driven. In addition, the work develops and validates a procedure for in situ electrolyte concentration switching, allowing comparative performance assessment across electrolyte conditions without repeated cell disassembly. This is complemented by a dedicated analysis of ion transport differences between CCS- and CCM-based cells, interpreting the observed trends in terms of interface quality, ionic conduction pathways, and architecture-specific limitations.

A5. Because AEMWE components, especially membranes and ionomers, remain under rapid development, this thesis explicitly treats material variability as a methodological challenge. Over the project duration, multiple batches of catalysts and anion-conducting materials were used, and not all chapters are strictly comparable in terms of performance due to evolving materials. The work therefore distinguishes repeatability within each work package (typically ensured by selecting and benchmarking materials for that specific study period) from reproducibility across the thesis, which can be affected by batch-to-batch variation between work packages. Within this framework, externally supplied anion-conducting materials are used as received or according to recommended procedures, whereas in-house synthesized components (catalyst, electrodes) and hardware are subject to internal quality control. To address material variability, the relevant batch context is outlined, chapter-to-chapter inconsistencies are identified, and the validity of the fundamental research conclusions is justified despite changes in absolute performance, thereby improving the reliability and interpretation of the thesis results.

4 MATERIALS AND METHODS

This chapter presents a comprehensive overview of the experimental work conducted in this thesis. It details all materials and chemicals used, outlines the preparation and fabrication procedures and introduces characterization methods employed to evaluate both material properties and electrochemical single-cell performance. The following subchapters define so the methodological framework that ensures reproducibility and provides the basis for the results and discussion in the subsequent chapters.

4.1 CHEMICALS AND MATERIALS

Solvents and Aqueous Solutions

All aqueous solutions were prepared using deionized water (DI H_2O, 19.2 MΩ, EMD Millipore), obtained from a Millipore Q-POD® purification system (Merck KGaA). For preparation of alkaline electrolytes, KOH pellets (EMSURE®, 85 % purity, VWR) were dissolved in DI H_2O. Further solvents used are summarized in Table 4.1.

Table 4.1 Solvents used in the present work, incl. their brand and purity.

Solvent	Brand	Purity
1-propanol (1-PrOH)	Merck KGaA	>99.5 %
2-propanol (2-PrOH)	Th. Geyer-Labor	>99.8 %
Acetone	VWR Chemicals	>99.8 %
Ethanol (EtOH)	VWR Chemicals	>99.8 %
Dimethyl sulfoxide (DMSO)	Emplura®	>99.9 %
Methanol (MeOH)	Merck KGaA	>99.9 %
Ultrapure deionized water (DI H_2O)[2]	Merck KGaA (Q-POD®)	19.2 MΩ, EMD Millipore

Catalysts

As catalyst for the cathode, commercial Pt/C (60 % on high surface area carbon, Alfa Aesar™) was used. For PGM-based anodes, commercial Ir black powder (99.8 % metals basis, Alfa Aesar™) was used. The primary OER catalyst was Ni_3Fe-LDH.

[2] Throughout this work, DI H_2O refers specifically to ultrapure deionized water, unless indicated otherwise.

Ni_3Fe-LDH Synthesis and Milling

The OER catalyst Ni_3Fe-LDH synthesized via co-precipitation method based on the low solubility product of metal ions (Ni^{2+} and Fe^{3+}) in alkaline solution, following Jiang et.al.[131] Nickel(II) nitrate hexahydrate ($Ni(NO_3)_2{\cdot}6H_2O$, ACS reagent, ≥98.5%, Sigma Aldrich; 3.0 mmol) and iron(III) nitrate hexahydrate ($Fe(NO_3)_3{\cdot}9H_2O$, ACS reagent, ≥98%, Sigma Aldrich; 0.75 mmol) were dissolved separately in DI H_2O and then combined under vigorous stirring (1000 rpm) at room temperature (RT). In parallel, sodium hydroxide (NaOH, gradient grade, ≥99.9%, Honeywell; 7.5 mmol) was dissolved in DI H_2O and added dropwise to the mixed nitrate solution under continuous stirring (target 9–11 pH). After completion of base addition, the suspension was stirred vigorously to promote complete precipitation and homogenization. The precipitate was isolated by centrifugation (4500 rpm, 5 min) and washed thoroughly before drying. For washing, the solid was repeatedly re-dispersed in DI H_2O and separated again (three cycles), followed by an additional rinse with EtOH, to remove residual soluble impurities (especially Na^+ and NO_3^-) and facilitate drying. Finally, the cleaned solid was vacuum-dried overnight at RT.

For Ni_3Fe-LDH wet-milling, the powder was either treated on a roller shaker (roller bench, IKA™) or in a tumbler mixer Turbula® T2F (WAB) (Figure 4.1a and b). Pure EtOH was employed as the grinding medium. A 250 mL polyethylene (PE) bottle was filled to 1/3 of volume with zirconia grinding balls (type ZY-S, >99.79%, SiLibeads, ball diameter 1.3 mm). The weight ratio of catalyst to grinding balls was chosen as 1:25 wt%. The slurry was filled to 2/3 of the bottle volume. For the tumbler ball milling a duration of 15 hours and rotation speed of 67 was determined to be optimal for achieving a unimodal size distribution of the catalyst particles. On the roller shaker, the bottles were rotated for 24 or 48 h at the maximum rotation speed of 30 rpm.

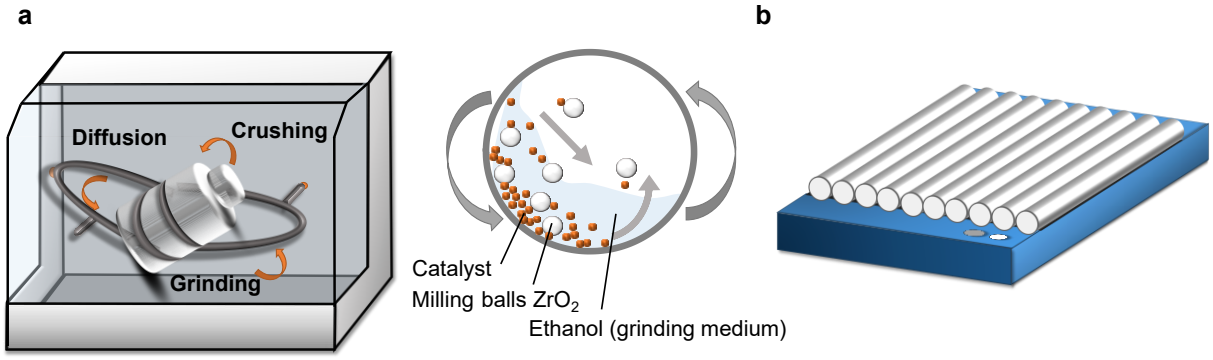

Figure 4.1. Illustration of two catalyst milling methods: (a) tumbler mixer showing the 3D movements with powder tumbling under gravity-driven forces, including shear forces; (b) roller shaker where a one-direction rotation movement takes place.

To distinguish the discussed powders, in Chapter 5.3, the Ni_3Fe-LDH catalyst are named according to Table 4.2.

Table 4.2. Names for the initial and milled Ni_3Fe-LDH catalysts, including the corresponding treatment description.

Catalyst name	Treatment
i-NiFe-LDH	As-synthetized Ni_3Fe-LDH powder
mTM-NiFe-LDH	Ni_3Fe-LDH powder, milled in tumbler mixer (Figure 4.1a)
mRB-NiFe-LDH	Ni_3Fe-LDH powder, milled on a roller bench (Figure 4.1b)

AEMs and Ionomers

For most experiments, the pre-commercial anion exchange membrane (≈70 µm wet thickness) DURAION® and its corresponding preliminary anion-conducting binder supplied by Evonik were used. For a 5 wt% anion-conducting binder solution, the solid binder was dissolved in 16 wt% EtOH and 84 wt% DMSO, followed by 2 h stirring at 60 °C. Since these materials are pre-commercial, different batches were used throughout this work. The specific batches used, along with some of the challenges associated with them, will be highlighted in Chapter 4.5.

The studies of Chapter 5.4 included the use of the 75 µm Aemion+™ membrane with a polyolefin reinforcement (AF2-HWP8-75-X, with ion exchange capacity of 2.1-2.5 meq g^{-1}) with the corresponding anion-conducting binder Aemion+™ Polymer Resin (AP2-HNN8-00-X) supplied by Ionomr Innovations Inc. Here, for a final 5 wt% ionomer dispersion, the solid ionomer was dissolved in 50 wt% MeOH and 50 wt% acetone under strong stirring over night at RT.

Porous Transport Layers and Gaskets

A Ni fiber-based felt with a fiber diameter of 22 µm and a porosity of 66 % (Ni 2GDL30-0.50, 500 µm thick, Bekaert) was used as the PTL at the anode side, while carbon fiber composite paper (TGP-H-120, 370 µm thick, Toray) was used as cathode PTL. Prio to use, both PTLs were cleaned in acetone, then 2-propanol and finally in DI H_2O for 10 min each at ambient temperature under sonication.

As single-cell gaskets around the electrodes, 250 and 500 µm PTFE foils (RCT Reichelt Chemietechnik) were used. For electrical isolation between the end plates and the flow-fields, 1 mm glass fiber reinforced PTFE foils (RCT Reichelt Chemietechnik) were used.

4.2 CATALYST DISPERSION PREPARATION

All catalyst dispersions used for electrode fabrication had a final solid content of 2 wt%. During each dispersion preparation, those were continuously cooled inside an ice bath. Figure 4.2 presents the main steps of catalyst dispersion preparation.

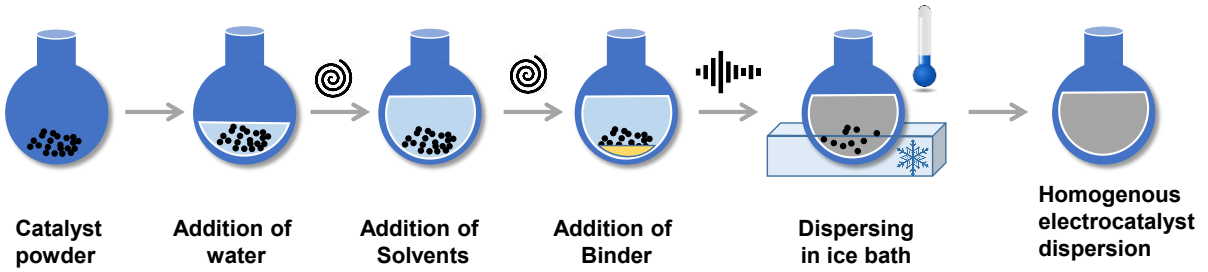

Figure 4.2. Schematic illustration of the electrocatalyst dispersion preparation process, from catalyst powder to final ink formulation for electrode fabrication.

Cathode Dispersion

The Pt/C contained ink contained catalyst powder, anion-conducting binder, EtOH and DI H_2O, in a 1:1 mass ratio (Table 4.3). First, the catalyst powder was weighed into a 250 mL glass bottle (Schott AG), DI H_2O was added, and the mixture was dispersed for 5 min at 4000 rpm (IKA® Ultra-Turrax® type T25). After adding the binder solution and EtOH, the dispersion was mixed for another 5 min (4000 rpm, IKA® Ultra-Turrax® type T25) and finally homogenized by ultrasonic horn treatment for 10 min (BANDELIN electronic GmbH & Co. KG SONOPULS, sonotrode MS73, 50% power).

Table 4.3. Composition and component quantity in the Pt/C ink formulations.

Catalyst, quantity	Ionomer, quantity	Solvent 1, quantity	Solvent 2, quantity
Pt/C, 500 mg	5 wt% DURAION®, 3333.33 mg	DI H_2O, 40.08 mL	EtOH, 50.8 mL

For Aemion+™-based dispersions, the same component weights and volumes were used. Final homogenization was achieved by additional overnight stirring on a magnetic plate. In all cathode inks, the binder content was fixed at 25 wt% of total solids.

Anode Dispersion

For the Ir-based inks (Table 4.4), the catalyst powder was mixed with DI H_2O, and dispersed for 5 min at 4000 rpm (IKA® Ultra-Turrax® type T25). After adding the binder solution and EtOH, the mixture was dispersed for another 5 min and finally ultrasonically homogenized for 30 min of ultrasonic horn homogenization finalized the dispersing process.

Table 4.4 Composition and component quantity in the Ir ink formulations.

Catalyst, quantity	Ionomer, quantity	Solvent 1, quantity	Solvent 2, quantity
Ir, 500 mg	5 wt% DURAION®, 2626.05 mg	DI H_2O, 40.42 mL	EtOH, 51.22 mL

For Ni_3Fe-LDH-based ink formulations, the homogenization procedure is analogous to the one with Ir catalyst. In Chapter 5.3, the final dispersion homogenization was set to 10 or 30 min of ultrasonic horn treatment, remaining steps remained unchanged.

The baseline Ni_3Fe-LDH dispersion used up to Chapter 5.2 contained the catalyst, DURAION® binder solution, EtOH and DI H_2O (1:1). The final ultrasonic homogenization was fixed to 30 min. In Chapter 5.3, six additional dispersion media (DM) were used for Ni_3Fe-LDH-based inks (Table 4.5, Table 4.7). The DM were chosen based on multiple factors, including the need for fast evaporation during electrode manufacturing at 80 °C,[289] limited selection to low hazardous solvents commonly used in fuel cell or electrolyzers production[102] and the previous optimization outcomes[290,291] for Ni-Fe-based catalysts.

Table 4.5. Composition and component quantity in the Ni_3Fe-LDH ink formulations, using DURAION® materials.

Dispersion Description	**Ni_3Fe-LDH quantity**	**5 wt% DURAION® solution quantity**	**H_2O quantity**	**EtOH quantity**
20 wt% ionomer content[3]	500 mg	2500 mg	15.5 mL	19.6 mL
15 wt% ionomer content		1764.7 mg	15.8 mL	20.1 mL
10 wt% ionomer content		1111.1 mg	16.1 mL	20.5 mL
7 wt% ionomer content (for anode-CCMs)		752.7 mg	16.3 mL	20.7 mL
5 wt% ionomer content (for anode-CCMs)		526.3 mg	15.5 mL	19.62 mL
Varied formulations for Chapter 5.3				
Dispersions based on further DM	**Ni_3Fe-LDH quantity**	**5 wt% DURAION® solution quantity**	**H_2O quantity**	**Solvent, quantity**
EtOH pure	500 mg	2500 mg	-	EtOH, 39.2 mL
EtOH:H_2O 3:1			7.7 mL	EtOH, 29.4 mL
2-PrOH:H_2O 1:1			15.5 mL	2-PrOH, 19.7 mL
2-PrOH:H_2O 3:1			7.7 mL	2-PrOH, 29.6 mL
1-PrOH:H_2O 1:1			15.5 mL	1-PrOH, 19.3 mL
1-PrOH:H_2O 3:1			7.7 mL	1-PrOH, 28.9 mL

The dispersions with the ionomer Aemion+™ are presented in Table 4.6.

[3] This is the "baseline" ink formulation based on EtOH and H_2O with a mass ratio of 1:1.

Table 4.6. Composition and component quantity in the Ni_3Fe-LDH ink formulations, using Aemion+™ materials.

Dispersion Description	Ni_3Fe-LDH quantity	5 wt% Aemion+™ binder solution quantity	H_2O quantity	2-PrOH quantity
20 wt% ionomer content	500 mg	2500 mg	15.5 mL	19.3 mL
15 wt% ionomer content		1764.7 mg	15.8 mL	19.8 mL
10 wt% ionomer content		1111.1 mg	16.1 mL	20.1 mL
7 wt% ionomer content		752.7 mg	16.3 mL	20.3 mL
5 wt% ionomer content		526.3 mg	16.4 mL	20.4 mL
3 wt% ionomer content		309.3 mg	16.5 mL	20.6 mL

Dispersions for Electrophoretic and Dynamic Light Scattering Analysis

For baseline electrophoretic dynamic light scattering analysis (ELS, *ζ*-potential measurements) of Ni_3Fe-LDH in DI H_2O, dispersions were prepared at 2 wt% solids by sonicating 10 mg powder in 490 mg DI H_2O for 30 min (ultrasonic sonotrode MS73, 50% power) while cooling in an ice bath. Baseline measurements of the anion-conducting binder DURAION® were performed at 0.4 wt% (matching the binder fraction in the final catalyst dispersions) immediately after dilution and after 30 min ultrasonic homogenization. For solvent comparisons, the catalyst concentration was kept at 2 wt%. *ζ* -Potential of the final catalyst inks was measured as prepared, following Chapter 4.2, without further dilution.

For the catalyst cluster size[4] characterization by dynamic light scattering (DLS) analysis of catalyst dispersions, either with or without binder, the samples underwent a 50-fold dilution. This procedure resulted in a final solid concentration of 0.04 wt%. While diluted catalyst inks might not perfectly mimic actual dispersions due to reduced agglomeration kinetics as shown before (increased dispersion dilution led to decreased carbon agglomerate sizes; although the effect of dilution was less than 20%[292]),[293] maintaining the same dilution across samples ensured comparability of results. For the analysis of the bare milled and initial powders, the DI H_2O-based dispersions were mixed for 1 min by a vortex mixer.

In all analyses the properties of the solvents used were either obtained from external measurements or derived from values found in the literature. Refractive indices and dielectric constants for the

[4] By catalyst agglomerate or catalyst cluster size the intensity-weighted hydrodynamic equivalent diameter, D_H, is described.

analysis were determined following literature guidelines.[294–299] These values for all used solvents and mixtures are detailed in Table 4.7.

Table 4.7. Properties of the dispersion mediums (solvents and solvents mixtures) for ELS and DLS analysis (at λ=660 nm) at given temperatures.

Solvent or solvent mixture	Refractive Index	Dynamic viscosity / mPa s	Rel. Permittivity* (Dielectric constant) ε
DI H_2O	1.333 (20 °C)[294]	0.89[296]	78.37 (25 °C)[295]
EtOH pure	1.361(20 °C)[294]	1.1[296]	24.28 (25 °C)[295]
EtOH:H_2O 1:1	1.351	2.5	53.44 (25 °C)[295]
EtOH:H_2O 3:1	1.338	1.7	35.72 (25 °C)[295]
2-PrOH pure	1.378 (20 °C)[294]	2.38[299]	18.20
2-PrOH:H_2O 1:1	1.361	3.5	52.00
2-PrOH:H_2O 3:1	1.346	2.1	30.00
1-PrOH pure	1.385 (20 °C)[294]	1.96[296]	20.18
1-PrOH: H_2O 1:1	1.360	2.6	27.70
1-PrOH: H_2O 3:1	1.369	2.52	22.10

4.3 CATALYST LAYERS AND MEAS

4.3.1 CATALYST LAYER FABRICATION BY ULTRASONIC SPRAY-COATING

Each electrode or CL was fabricated by ultrasonic spray coating using an Exactacoat system (Sono-Tek, Figure 4.3). Prior to coating, PTLs or membranes were placed at a defined position on a porous vacuum plate, continuously heated to 80 °C, and clamped with a stainless-steel frame featuring a 5 cm^2 cut-out (matching the electrode active area) to prevent movement.

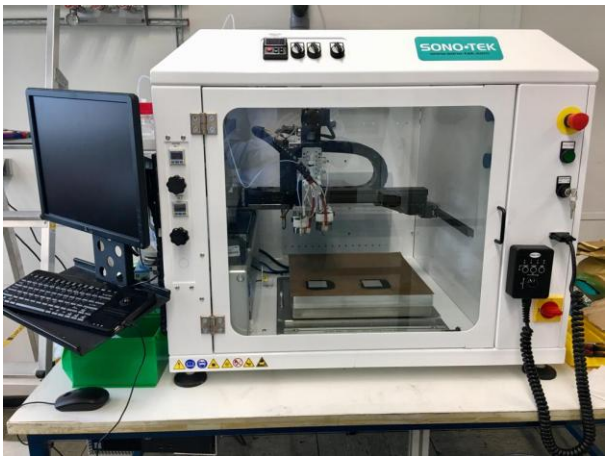

Figure 4.3. Photographic image of the ultrasonic spray-coating device (ExactaCoat, Sono-Tek) used for electrode fabrication.

The electrode fabrication process is schematically shown in Figure 4.4. The electrocatalyst inks (Chapter 4.2) were filled into a 25 mL Hamilton Gas Tight 1000 Series syringe and delivered by a syringe pump (Sono-Tek) mounted externally on the spray coater. To maintain homogeneous dispersion, the ink was continuously agitated by a magnetic stirrer inside the syringe. For spraying, the ink was fed to the ultrasonic nozzle (AccuMist) at a volumetric flow rate of 0.3 mL min^{-1}. The nozzle generated a fine aerosol at 48 kHz and a power level of 3 W. For spray cone shaping and to provide an inert shroud for the flammable alcohol-containing inks (especially Pt/C), nitrogen was supplied through an annular outlet around the nozzle at 1.5 kPa.

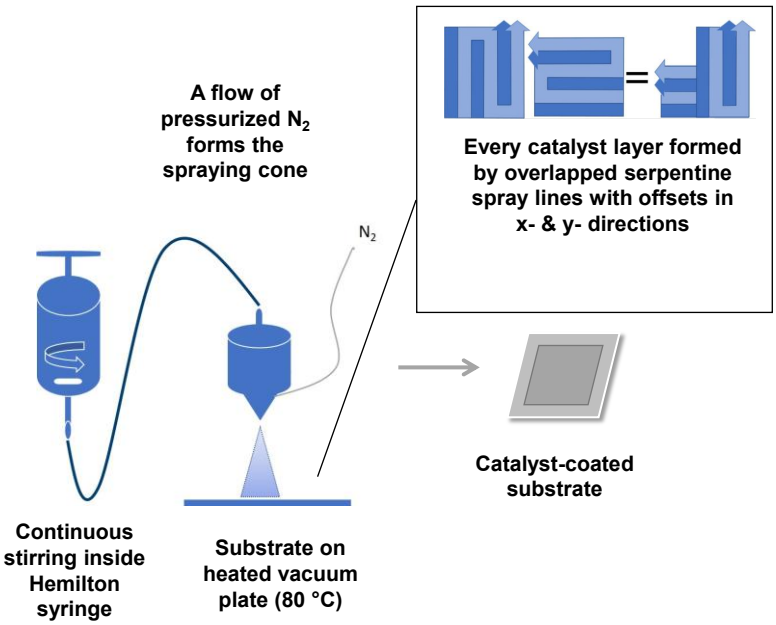

Figure 4.4. Schematic illustration of electrode fabrication by ultrasonic spray deposition, showing the spraying pattern in the zoom-in box.

The catalyst ink was deposited onto the substrate (PTL or membrane) in layer-by-layer meander pattern. To improve uniformity, each pass was sprayed in both x- and y-directions using alternating positive and negative offsets (± one third of the spray-line width, shown in Figure 4.5). Six such loops constituted one sprayed layer, and the catalyst loading was set by the number of layers. Loadings were determined gravimetrically by weighing the substrate before and after coating (AG204, Mettler Toledo).

For all cathodes, 0.6 mg cm^{-2} of Pt/C with 25 wt% binder was applied. The catalyst and binder loading on the anode side varied depending on the experiment and are detailed in the figure captions or discussed in the text where relevant. Unless specified otherwise, the loading was set at 2 mg cm^{-2} with a binder content of 20 wt%.

In this work, mostly the CCS approach was used (Figure 2.5a), with the catalyst ink sprayed directly onto the PTL to form a porous transport electrode (PTE). From Chapter 5.4, additionally, the CCM method was introduced (Figure 2.5b) by spray-coating the catalyst dispersions onto the as-received DURAION® or Aemion+™ membranes. The anode-CCM was formed by applying Ni_3Fe-LDH catalyst dispersion onto one side of the AEM only, as shown in Figure 2.5b.

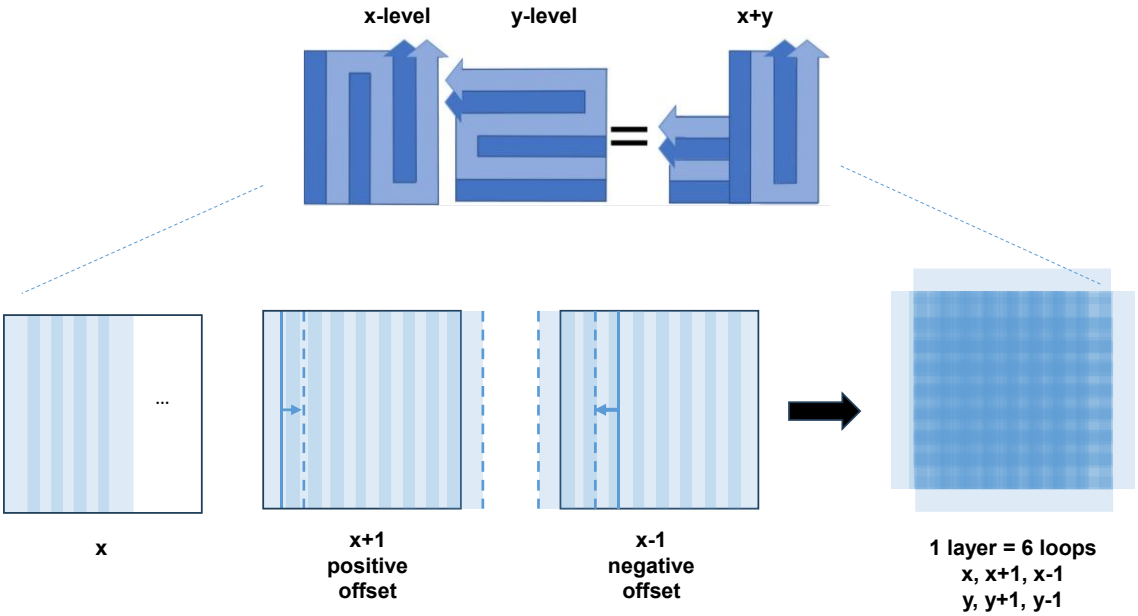

Figure 4.5. Schematic overview of the spraying pattern during electrode fabrication: one sprayed layer consists of 6 loops with 3 passes along the x-axis and 3 along the y-axis, each with a positive and negative offset of one-third of the sprayed line width, enabling the formation of a uniform thin film.

4.3.2 ASSEMBLY AND PRE-TREATMENT OF MEMBRANE-ELECTRODE ASSEMBLIES

For PTE-based MEAs, the AEM was sandwiched between anode and cathode PTEs without applying any additional pressure (Figure 2.5a). For the mixed configuration, a Ni PTL, an anode-CCM (fabricated by method shown in Figure 2.5b) and the cathode-PTE were combined to form the MEA (Figure 2.5c). In both cases, components were assembled wet at RT after pre-soaking in the electrolyte used for subsequent testing.

For DURAION®-based PTEs and membranes, all components were immersed in alkaline electrolyte for 3 h prior to assembly to promote binder swelling and complete ion exchange.

Aemion+™ membranes and ionomer-containing PTEs were conditioned in 1 M KOH for 48 h, with electrolyte replacement after 24 h. The initial yellow membranes became nearly colorless upon KOH exposure, indicating substantial ion exchange; however. In addition, exposure to air can promote carbonate formation.[182,300] For this reason, the components were stored in a liquid medium, and their exposure to air was minimized as much as possible during handling.

4.4 SINGLE-CELL CONFIGURATION AND TEST STATION SETUP

The electrochemical measurements were conducted using an in-house cell hardware (Figure 4.6a and b), which included integrated voltage sense ports, heater ports, and electrolyte flow inlets and outlets within the nickel flow fields, covering an active area of 5 cm^2.[301] MEA compression was defined by PTFE sealing foils (250 µm on cathode side, 500 µm on anode side). Glass-fiber-reinforced PTFE foils electrically insulated the stainless-steel endplates from the flow fields. The cell was tightened with eight bolts (each with 10 Nm), resulting in an applied pressure of up to 3 N mm^{-2} on the active area.

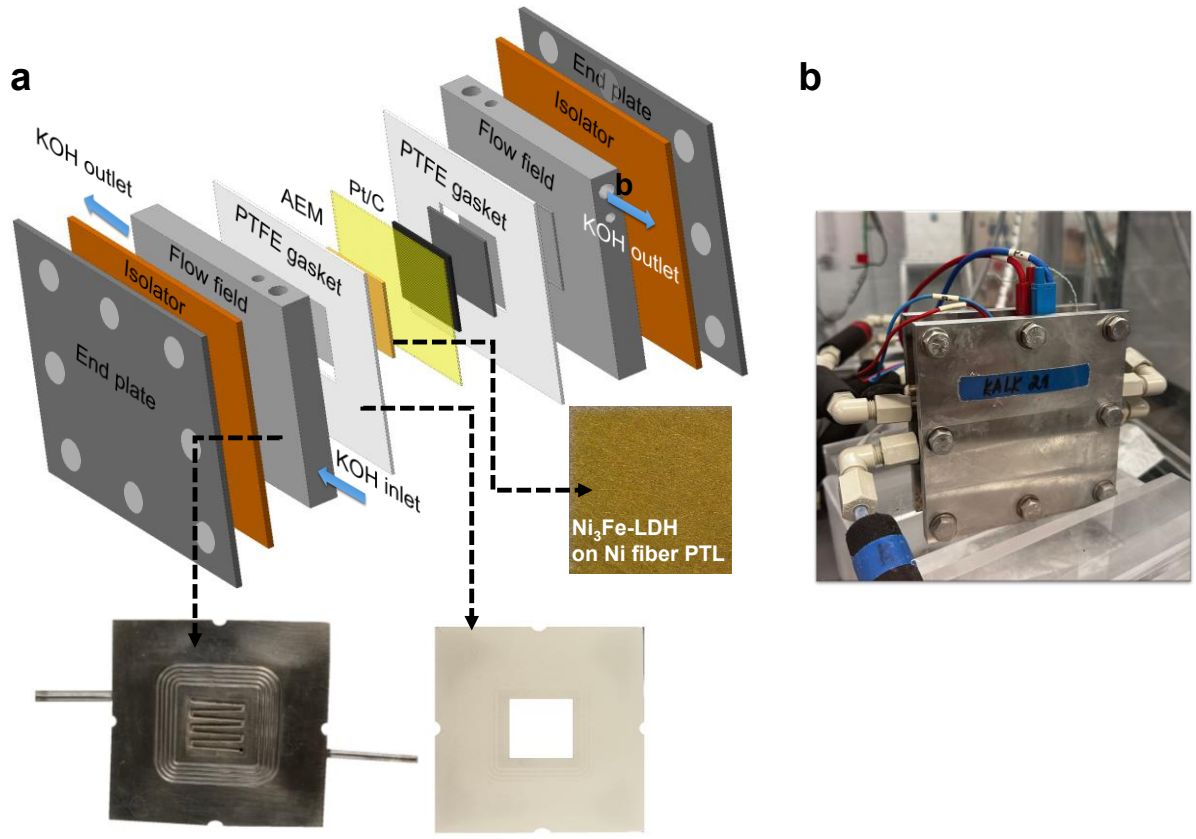

Figure 4.6. (a) Schematic representation of the AEMWE single-cell setup used in this work, including photographs of the electrode, PTFE gasket, and flow field; (b) photographic image of the assembled electrolyzer cell.

The electrochemical characterization was performed in an in-house alkaline test rig (Figure 4.7). This setup allowed simultaneous testing of two single-cells. The setup enabled parallel operation of two single cells. The anolyte and catholyte reservoirs consisted of stainless-steel vessels with polyethylene liners and were connected by a PTFE line to equalize the electrolyte composition as concentration gradients develop during electrolysis. In the cell, anode and cathode compartments were supplied separately with electrolyte of identical, defined concentration at a flow rate of 10 mL min^{-1} cm^{-2}. Unless stated otherwise, measurements were conducted at ambient pressure, 60 °C, and in 1 M KOH electrolyte.

When varying electrolyte concentration (Chapter 5.1.4), a fresh MEA was used for each condition. For temperature-dependent tests, the cell temperature was increased after the previous run and held for 3 h to equilibrate before continuing.

For the in situ electrolyte switching experiments (Chapter 5.4.2), MEA components were pre-soaked in 1 M KOH before assembly. After the initial performance test, the electrolyte was removed while keeping the cell assembled, the system was flushed with 2 L DI H_2O for 1 h, then filled with 1.5 L of 0.1 M KOH and circulated for 1 h. A 50 mL outlet sample was collected to determine electrolyte density and verify concentration. The measured concentration deviated by <0.01 M from the target, corresponding to <1% uncertainty for 1 M KOH and <10% for 0.1 M KOH. Subsequent electrolyte changes followed the same procedure.

Electrolytes were circulated using membrane pumps (KNF Simdos 10). A water supply with a level sensor (TURCK GmbH & Co. KG) maintained electrolyte level and concentration. Before connecting the cells, the station and electrolyte tanks (1.5 L) were degassed by N_2 bubbling (Air Liquide) for at least 2 h. Heating rods attached to the flow fields warmed the cell and electrolyte; temperature was controlled by a thermocouple and thermostat. All measurements were performed using a BioLogic BT-815 battery cycler potentiostat (15 A, up to 10 kHz). Testing protocols are described in Chapter 4.5.

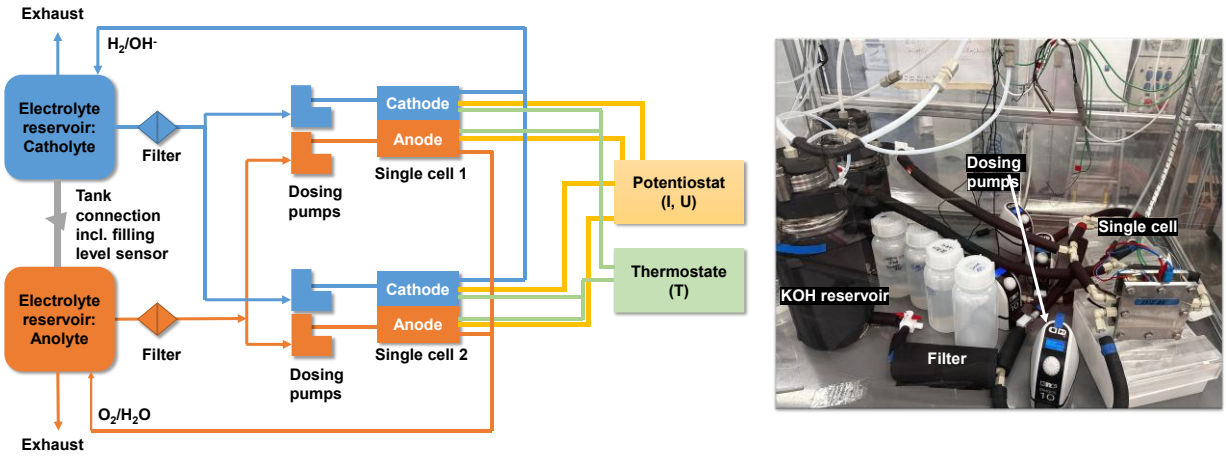

Figure 4.7. (a) Schematic layout of the single-cell test rig; (b) photographic image of the test rig. The electrolyte reservoir includes a built-in gas separator.

4.5 CHARACTERIZATION TECHNIQUES

All characterization techniques used are summarized in the following Figure 4.8 for an overview.

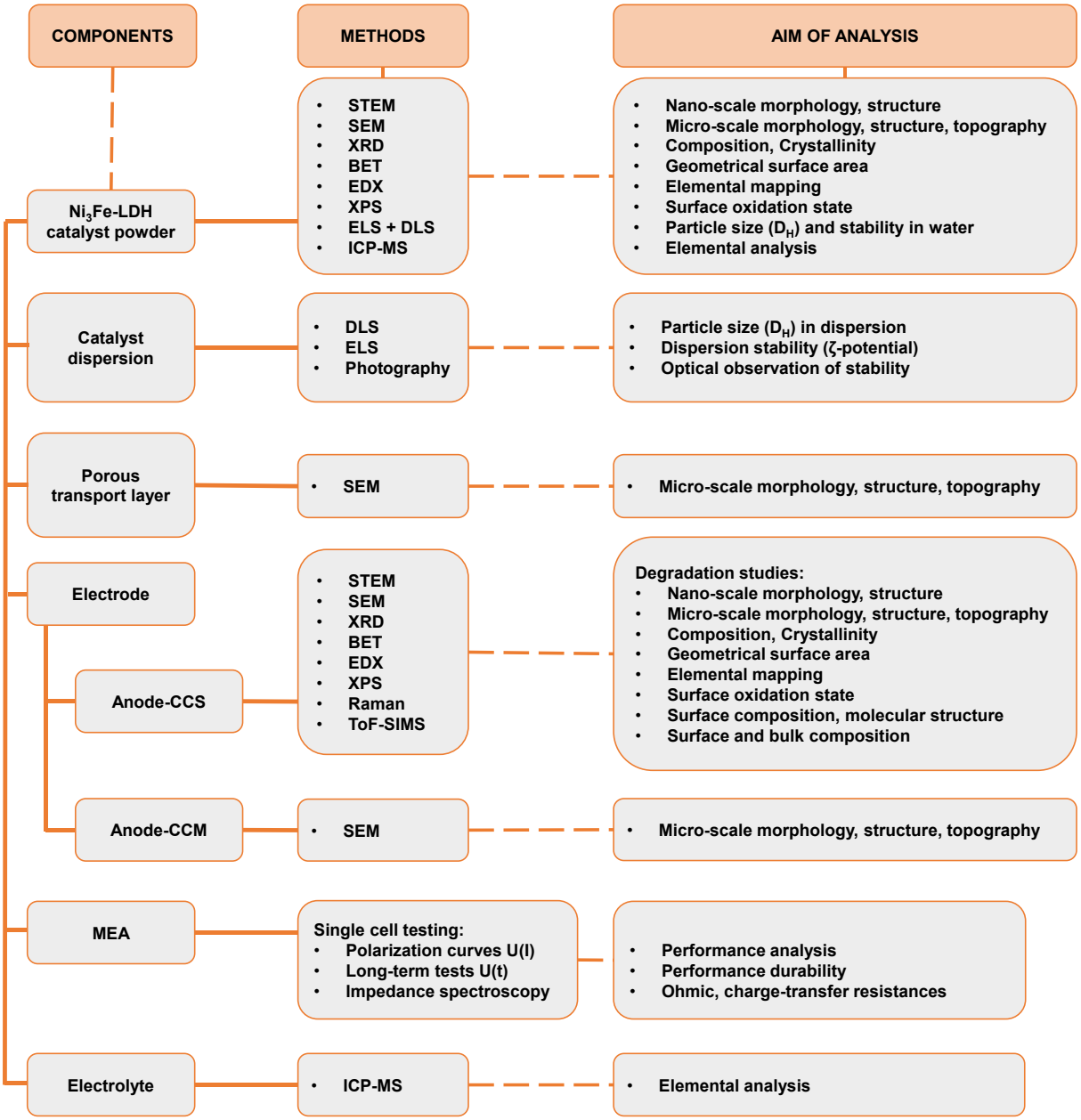

Figure 4.8. Schematic overview of analyzed components and materials, the used techniques and aims of characterization.

Chapter 5.1 provides a comprehensive characterization of the catalyst powder, assessing reproducibility and quality through X-Ray diffraction (XRD), X-Ray photoelectron spectroscopy (XPS), inductively coupled plasma optical emission spectroscopy (ICP-OES), and electrochemical testing. The influence of CL composition and operating conditions was evaluated electrochemically and complemented by scanning electron microscopy (SEM).

Chapter 5.2 focuses on degradation tracking of the Ni_3Fe-LDH anode using in situ electrochemical testing, including polarization curves, electrochemical impedance spectroscopy (EIS), and durability tests (time-voltage). Electrolyte composition was monitored by ICP-MS. Post-mortem electrode characterization included XRD, XPS, Raman spectroscopy, time-of-flight secondary ion mass spectrometry (ToF-SIMS), and detailed microstructural analysis by SEM/EDS, FIB-SEM, HR-TEM, and STEM-EDS on FIB-prepared sections.

Chapter 5.3 investigates the impact of powder milling using SEM and STEM-EDS, Brunauer-Emmett-Teller (BET) surface area analysis, XRD, XPS, Raman spectroscopy, and dispersion characterization by dynamic light scattering (DLS) and electrophoretic light scattering (ELS). Electrode morphology was examined by SEM, and single-cell performance was assessed by polarization curves, EIS, and bulk resistance measurements.

Chapter 5.4 compares CCS and CCM anode configurations primarily through electrochemical testing (polarization curves, EIS, and durability measurements) and correlates performance with MEA microstructure using SEM to resolve catalyst-layer morphology and interfacial features.

In Chapter 5.5, electrochemical testing combined with EIS analysis was conducted to address the challenges of performance reproducibility.

4.5.1 ELECTROCHEMICAL CHARACTERIZATION

The performance of single-cell electrolyzers is usually evaluated through galvanostatic (or potentiostatic) testing, which reveals the performance of such under specific cell conditions. The results typically appear as polarization curves and time-dependent voltage or current changes (stability curves). Impedance spectroscopy, when combined with polarization curve analysis, offers a deeper understanding of electrochemical systems. A short introduction to the fundamentals of impedance spectroscopy is given further.

Basics of impedance spectroscopy

EIS is an electrochemical analysis method to characterize ionic, electronic and mass transport properties of materials, coating or electrochemical systems. EIS probes the frequency (f) dependent response of a water electrolyzer and enables analysis of the main loss contributions that affect cell performance, including ohmic, charge-transfer, and mass transport (diffusion related) losses.[275] In EIS, a small amplitude AC perturbation (voltage or current) is applied around a defined DC operating point under potentiostatic or galvanostatic control over a selected frequency range. The measured response is used to calculate the complex impedance, $Z(\omega)$ (where $\omega = 2\pi f$). The spectra are commonly represented as Nyquist plots (Figure 4.9) and interpreted using equivalent electrical circuit (EEC) models, which provide a phenomenological description of the dominant electrochemical processes in the cell.[275,302]

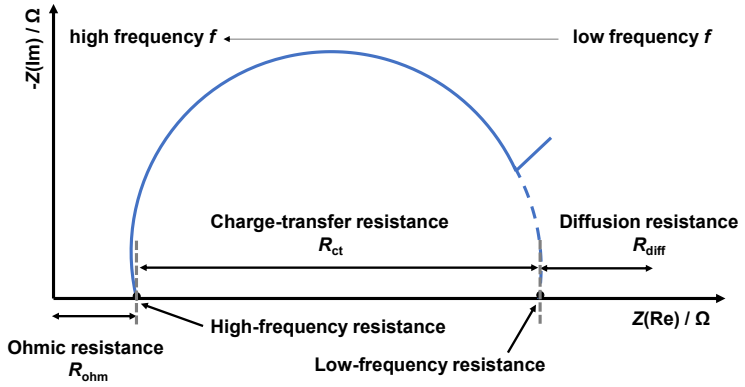

Figure 4.9. Schematic illustration of a Nyquist plot, where the resistance (R) and constant phase element (CPE) are in parallel connection and in series with an electrolyte resistance.

The choice of a suitable EEC must be guided by the characteristic physical processes of the system. In this work, the spectra were fitted using an EEC consisting of two parallel resistance-constant phase elements (*R-CPE)* in series with an additional resistor (*R*), as reported elsewhere[102,303–305] (Figure 4.10). In this case and in other words, the model can be written as $R_{\mathrm{Ohm}} + R_1||\mathrm{CPE}_1 + R_2||\mathrm{CPE}_2$. The series resistance R_{Ohm} corresponds to the high-frequency intercept of the Nyquist plot with the real axis ($Z(Re)$) and represents the total ohmic resistance of the cell, the ionic and electronic resistances, including contributions from the membrane, PTLs, electrodes, bipolar plates, electrolyte, and contact resistances.[306]

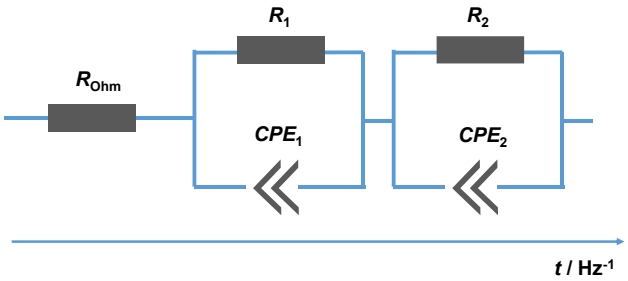

Figure 4.10. Equivalent circuit used to fit the EIS data consisted of two R-CPE parallel combinations in series with an additional resistor.

The use of CPEs instead of ideal capacitors accounts for non-ideal capacitive behavior caused by electrode roughness, surface inhomogeneity, and distributed relaxation times.[307] In full cell measurements, the fitted resistive elements R_1 and R_2 are often assigned to interfacial processes at the cathode and anode, and are frequently discussed in terms of apparent charge transfer resistances of the HER and OER.[308] However, the assignment of individual arcs is not unique in a two-electrode full cell and remains debated in the literature. Some studies assign the high-frequency arc mainly to HER related processes[309,310] and the second arc to OER related processes,[308] whereas others attribute the first arc to charge-transfer and double-layer related effects in conductive regions of the catalyst layer or active layer components, meaning $R_1 = R_{\mathrm{ct}}$.[311–313] In this work, both fitted resistive branches ($R||\mathrm{CPE}$) are interpreted as apparent interfacial contributions from cathodic and anodic processes,

while considering that the slower multistep four electron OER can strongly influence the overall interfacial resistance. In addition, one branch (often denoted apparent R_{ct}) may also include contributions from adsorption and desorption of reaction intermediates. The second branch, especially in the lower frequency range, may further include contributions from bubble formation, bubble coverage, and mass transport limitations at the electrode electrolyte interface.[314] In some spectra, two partially overlapping and depressed semicircles are observed, indicating at least two concurrent processes with similar characteristic time constants that are not fully resolved. The origin of this behavior is not unambiguously established and is discussed controversially in the literature.[315]

Testing protocol for performance analysis

For programming and running the electrochemical characterization techniques, the program BT-lab V 1.55 was used. The fitting of impedance spectroscopy data (Nyquist plots) was conducted with the tool *Zfit*. The chosen measurement protocol based on the European Union's harmonized guidelines for low-temperature water electrolysis[275] and the project-intern protocol "COMMON TEST PROTOCOLS ANIONE-CHANNEL-NEWLY H2020 FCH JU projects" and is presented in Table 4.8. The testing began with a 3 h open circuit voltage step to heat and equalize the electrolyte between the cells and the test station. This was followed by a break-in (or conditioning) step involving a linear voltammetry sweep at a scan rate of 5 mV s^{-1}, ranging from 1.4 to 2.1 V, and then a conditioning phase at a constant current of 1 A cm^{-2} for 4 h. The linear current sweep verified the functionality of the cell and acted as a short-circuit-check, while the controlled constant current step activated the catalysts. Constant current steps of values of 0.016 A cm^{-2} to 3 A cm^{-2} for 1 min of dwell time (pseudo steady state condition) resulted in one recorded polarization curve. Two successive polarization curves were recorded with a 1 h OCP step in between, and both with a voltage limit of 2.1 V. For performance evaluation, the second current-voltage curve was selected, confirming the cell's complete conditioning, as demonstrated by the similarity between the initial and the second polarization curves. Afterwards, galvanostatic EIS (GEIS) measurements were performed at 20 different points, spanning current densities from 40 mA cm^{-2} to 2 A cm^{-2}, with a 10% DC amplitude and a frequency spectrum from 0.1 Hz to 10 kHz. Each specific current density was maintained for 5 min prior to GEIS evaluation. The recorded high-frequency resistances (R_{Ohm}) were then utilized for iR-correction of the polarization curves as described in Chapter 2.1. The named protocol presented a 15 h short-term single-cell performance test, including the break-in phase. For long-term operational analysis, a 1000 h test was conducted by integrating loops into the protocol and maintaining 1 A cm^{-2} for 100 h constant current with a polarization curve and impedance spectroscopy test in between.

Table 4.8. Single-cell testing protocol with details and explanation of techniques.

	Testing technique	Details	Description / aim
	System heating		
1	Open circuit potential	3 h, no applied current or voltage	Equalization of electrolyte flow and temperature

	Break-in (conditioning)		
2	Sweep voltammetry	1.4 to 2.1 V with 5 mV s^{-1} scan rate	Verification of cell functionality and short-circuit check and assessment of the maximum operating current density
3	Constant current	1 A cm^{-2} for 4 h	Favoring membrane hydration, in situ purification and stabilization of the anode and cathode catalysts oxidation states
4	Polarization curve	0.016 A cm^{-2} - 3 A cm^{-2} with 1 min dwell time with cut-off voltage of 2.2 V ♦ 0.016 to 0.12 A cm^{-2}: step of 0.016 A cm^{-2} ♦ 0.12 to 0.2 A cm^{-2}: step of 0.02 A cm^{-2} ♦ 0.2 to 1.4 A cm^{-2}: step of 0.05 A cm^{-2} ♦ 1.4 to 3 A cm^{-2}: step of 0.1 A cm^{-2} Each step held for 1 min	Stepwise steady-state current sweep (applying consecutive current density steps) and recording the resulting cell voltage ♦ Serves as a second more precise LSV curve
5	Open circuit potential	1 h	Recovery of reversible degradation phenomenon
	Performance testing		
6	Polarization curve	See above	Actual polarization curve for performance evaluation. The Begin-of-Test (BoT) polarization curve for long-term tests At the end of testing, End-of-Test (EoT) polarization curve
7	Galvanostatic impedance spectroscopy	40, 80, 100, 120, 160 mA cm^{-2} and 0.2, 0.24, 0.3, 0.4, 0.5, 0.6, 0.8, 1, 1.2, 1.4, 1.5, 1.6, 1.7, 1.8, 2 A cm^{-2}	For iR-correction of polarization curve and impedance spectroscopical analysis
	Stability testing		
8	Stability curve	100 h at 1 A cm^{-2}	Recording the resulting cell voltage in dependence of operation time
Loop to achieve >1000 h stability testing: repetition from technique 6 to 8			

Electrode internal resistance tests

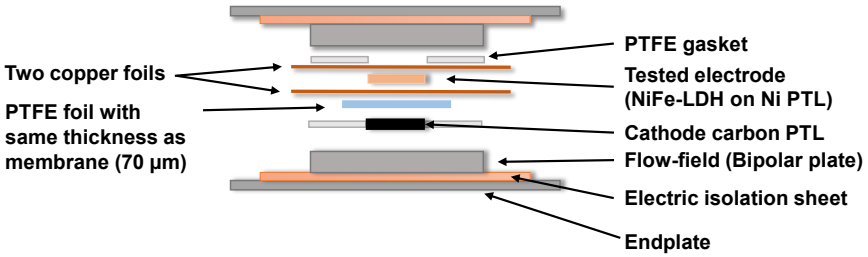

Figure 4.11. Experimental design for measuring contact and bulk resistances of electrodes, illustrating electrode positioning.

The total internal resistance of the electrode, including interfacial contact and bulk resistances, was evaluated in a sandwich-like single-cell setup. In this arrangement, the anode electrode was positioned between two copper plates (as shown in Figure 4.11). A PTFE foil of the same thickness as the used membrane (60 µm) replaced the former, and a nickel foam, matching the thickness of the carbon paper (370 µm), substituted for the cathode-PTE. Four cables, two for voltage and two for current, were connected, with each voltage-current cable pair attached to one of the copper plates. The cell was subjected to 15 A ($I_{applied}$, equivalent to 3 A cm^{-2}), and the total voltage was recorded after a 5 min period of voltage stabilization. The electrode contact resistance was then calculated as follows:

$$\frac{E_{\text{cell}_{\text{measured}}}}{I_{\text{applied}}} = R_{\text{measured}} \qquad \text{Equation 4.1}$$

$$[R_{\text{measured}}\ (\text{m}\Omega) - R_{\text{2x copper plates}}(\text{m}\Omega)] * A_{\text{cell}} = R_{\text{electrode}} \qquad \text{Equation 4.2}$$

$R_{\text{2x copper plates}}$ (internal resistance of the copper plates) was measured by applying current to one copper plate and then multiplied with 2. A_{cell} is the active cell area (5 cm^2), $R_{\text{electrode}}$ is the final electrode internal specific resistance.

It is important to mention that the resistance measured in this manner includes both the contact resistance on each side and the bulk resistance of the electrode substrate.

4.5.2 PHYSICAL CHARACTERIZATION

The analytical characterization techniques mentioned here are commonly used in research and are well-established. For this reason, detailed explanations of their fundamental principles will be omitted. Instead, the focus will be placed on providing testing parameters and equipment information. Given the rare application and documentation of electrophoretic and dynamic light scattering methods in water electrolysis research, these methods will be described in more detail.

Scanning Electron Microscopy Coupled with Energy Dispersive X-ray Spectroscopy

SEM is the most frequently employed technique for visual examination.[144,316] Morphology of PTEs and anode-CCMs was examined using a Zeiss Gemini Ultra Plus SEM operated at 2–20 kV in vacuum (10^{-6} mbar). Images were acquired with the SE2 and InLens secondary-electron detectors (surface-sensitive topography) and the AsB detector (angle-selective backscattered electrons for atomic-

number and compositional contrast). For cross-sectional imaging, samples were embedded in Epofix epoxy, polished, and, when required due to low conductivity, sputter-coated with Pt to reduce charging and improve image contrast.

Electron microscopy was combined with energy-dispersive X-ray spectroscopy (EDX/EDS) to assess the bulk elemental composition of the catalyst powder and of pristine and tested anode PTEs/MEAs, providing insight into degradation processes such as elemental dissolution and segregation.[317] EDS measurements were performed using an Ultim Max 100 detector (Oxford Instruments) at an accelerating voltage of 20 kV and a working distance of 8.5 mm.

A focused ion beam (FIB) SEM system (FEI Helios NanoLab 460F1) was used to prepare lamellae and acquire high-resolution cross-sectional SEM images from individual catalyst-coated fibers of the anode-PTE. In FIB, a finely focused beam of accelerated ions, typically Ga^+, emitted from a liquid metal ion source, is rastered over the sample surface. The ions physically sputter atoms from the surface, enabling site-specific cutting, trenching, and thinning of material to electron-transparent lamellae, often assisted by in situ deposition of protective Pt or C layers. All FIB-SEM procedures were carried out under high vacuum (10^{-7} bar).

TEM analysis enables the detection of particle clustering or deterioration of the support material. To confirm the LDH structure, TEM and HR-TEM images were obtained using a FEI Titan device with a Cs corrector for the objective lens (CEOS GmbH).[318] The microscope was operated at 300 kV.

STEM imaging and EDS mapping were conducted with a Thermo Scientific Titan 80–200 electron microscope equipped with a probe corrector (CEOS) and a high angle annular dark field (HAADF) detector. “Z-contrast” conditions were achieved by using a probe semi-angle of 30 mrad and an inner collection angle of the detector of 75 mrad.[319] For the lattice fraction calculations, the program DigitalMicrograph 3.7.4. by Gatan Inc. was used. The visible patterns were analyzed by the contrast extraction tool and confirmed by the Reduced *FFT tool*.

X-ray Photoelectron Spectroscopy

XPS is a surface-sensitive tool for assessing the surface composition and the oxidation state of a sample.[320,321] Here, XPS was used as a tool to explore catalyst surface composition on the anode-PTEs using Kratos Axis Ultra DLD device with monochromatic Al X-ray source (1.486 keV). The survey spectra were obtained at 187.5 eV pass energy, 0.8 eV per step, 100 ms per step. The detailed core-level spectra were recorded with a pass energy of 23.5 eV and 0.1 eV per step. Charge-correction was conducted by setting the C-C 1s bond peak to 285 eV.

X-ray Diffraction

XRD offers insights into the crystallinity, structural ordering, and the average size of crystallites.[322] Understanding the formation and changes of phases, along with measuring crystallite size, is crucial for tracking alterations in the catalyst during or after the OER. The structural characterization of the catalyst powder and the surface anode-PTEs was confirmed using a D8 Discovery X-ray Diffractometer

with Cu-Kα radiation (0.154 nm) in Bragg-Brentano geometry. The diffractograms were recorded in the 2θ range 5°–70°. The measurement protocol involved a continuous scan mode across a predetermined range, utilizing a step size of 0.02° and a step time of 5 s, all conducted at RT. The X-ray generator settings were fixed at 40 kV and 40 mA, with a detector slit width of 9.5 mm.

Brunauer-Emmett-Teller Analysis

The surface area was quantified by N_2 physisorption using the Brunauer–Emmett–Teller (BET) method. Note that the BET surface area represents the geometric (accessible) surface area and does not necessarily equal the electrochemically active surface area (ECSA). Measurements were performed on a Gemini VII instrument (Micromeritics). Prior to analysis, samples were outgassed at 80 °C under high vacuum for at least 24 h. For BET evaluation, a multilayer adsorption model was assumed, and the BET equation was fitted in the linear region of the adsorption isotherm, at relative pressures p/p_0 where a linear BET plot is obtained (typically in the range 0.05–0.30 for N_2 at 77 K).

Raman Spectroscopy

Raman spectroscopy probes molecular vibrations via inelastic light scattering. Monochromatic laser light interacts with the sample, and the resulting frequency shifts of the scattered photons correspond to vibrational modes, providing a fingerprint of bonding and structure. Ex situ Raman spectroscopy was carried out using the WITec alpha300 R confocal Raman device equipped with a 532 nm laser. The aperture was fixed at 50 x 1000 µm, and spectral resolution was ≈1 cm^{-1}, single spectrum was accumulated at an integration time of 3 s, the obtained signals were averaged over few single scans.

Inductively Coupled Plasma Spectroscopy

ICP-OES detects element-specific optical emission, whereas ICP-MS detects ions by mass-to-charge ratio. Powder compositions were measured by ICP-OES (iCAP 7600, Thermo Scientific). Catalyst powder (30 mg) was dissolved in 3 mL HCl and 1 mL HNO_3 for 30 min in an ultrasonic bath, diluted to 50 mL with DI H_2O, and further diluted 100-fold prior to measurement. Electrolyte samples were analyzed by ICP-MS (Agilent 7900). Aliquots of 20 mL were 100-fold diluted. Each sample was measured in triplicate and averaged, with concentrations reported in µg L^{-1}.

Time-of-Flight Secondary Ion Mass Spectrometry

ToF-SIMS, the depth-profile analysis, was used to analyze the amount of Ni, Fe and C, the latter being linked to the anion-conducting binder. For analysis, the instrument IONTOF ToF-SIMS 5.ncs including the microscope Cameca LEAP 4000 3D-Atomprobe were used. Average sputtering time of 12 000 s was measured what corresponds to a depth of about 10 µm. Cs ions were used for sputtering.

Electrophoretic and Dynamic Light Scattering

ELS and DLS techniques are acknowledged spectroscopic methods for characterizing particle systems, particularly in evaluating particle size and *ζ*-potential, which indicates the dispersion stability. Both techniques rely on analyzing the light scattering patterns produced by moving particles. In this case, the Brownian motion of particles is captured and used for particle size analysis. For spectroscopic

characterization techniques, the transformation of the spectroscopic measurement signal into size-distributed values is possible through numerical methods, which however impose limitations on detail on the resulting values. When comparing results from ELS and DLS with other techniques, it's crucial to recognize that different methods, while potentially accurate on their own, may yield deviating outcomes.

The DLS analysis is an optical method for dispersion characterization, which evaluates the fluctuations of scattered light to quantify the dynamic of processes like mechanic oscillations. The immediate result is represented as the intensity-weighted hydrodynamic equivalent diameter distribution. Medium properties such as density, diffraction index or dielectric permittivity are generally independent of the size, shape and distribution of the particles. The main principle is based on a laser light shining through the sample. As the light interacts with the particles, it scatters in various directions. This scattering is not static but fluctuates over time due to the Brownian motion of the particles. DLS measures these fluctuations in light intensity over time. By analyzing these fluctuations, the technique can determine the speed at which particles are moving, which is then used to calculate their size. The underlying principle is that smaller particles move faster than larger ones, allowing DLS to determine the size distribution of particles in the sample.

Prior to DLS analysis, it's crucial to address certain specifics. Firstly, DLS cannot differentiate between primary particle sizes and agglomerate sizes; agglomerates are detected as single units. If dispersion exhibits signs of fast sedimentation, which should be verified beforehand through ζ-potential analysis, DLS may not be suitable, as it might fail to capture all particles. Additionally, DLS yields size distributions, making the precise separation of specific particle sizes impossible. These considerations were considered before conducting the tests. Moreover, for effective DLS analysis, it is essential to know the refractive index and viscosity of the medium (solvents) and have a qualitative understanding of the particle morphology. To exclude possible effects of multi-light scattering, the dispersion should be strongly diluted (lower than 1 vol%). The dispersion preparation for the DLS analysis was described in Chapter 4.2.

ELS is a technique used for analyzing the ζ-potential of particles in dispersions. ζ-potential potential is a measure of the electrical charge on the surface of particles in a colloidal system. In ELS, a laser light is directed at the particles suspended in fluid. When an electric field is applied, charged particles move toward the electrode of opposite charge. This movement, known as electrophoresis, causes a shift in the frequency of the scattered light. By measuring this shift, ELS determines the velocity of the particles. The velocity, combined with the strength of the applied electric field, allows for the calculation of the ζ-potential. This ζ-potential is crucial for understanding the stability of colloidal dispersions, as it indicates the degree of repulsion or attraction between particles. Similarly, to DLS measurements, it should be considered in the ELS analysis that the ζ-potential is influenced not only by the particles themselves but by the composition of the dispersion medium, along with its physical and chemical characteristics. The particle size range should span from 1 nm to 20 µm.

To avoid the overlapping of double layers of particles in dispersions, it is recommended to establish optimal solid concentration through specific titration experiments. The objective is to achieve a dispersion that is clear, without visible sedimentation. The clarity of the dispersion can be verified by monitoring light transmission, which ideally should be between 20–100%, as determined by the analytical software used. In this study, the evaluation of measurement data consistently involved thorough sample preparation, visual inspection, and analyses of autocorrelation functions and phase plots. However, providing a detailed explanation of these procedures is beyond the scope of this work and its application. For an in-depth understanding of these evaluation methods, specialized literature on the subject offers extensive information.[323–325]

For DLS and ELS analyses the Litesizer 500 by Anton Paar GmbH was used. The solvent parameters used for the measurement were presented in Table 4.7. For the DLS measurements, macro cuvettes (Omega Cuvette, Anton Paar GmbH) were used for the measurements, and a total of 30 measurement runs were carried out. For ELS analysis, a reusable cuvette with Ω capillaries (Omega Cuvette, Anton Paar GmbH) was used. 100 measurement cycles per sample were carried out with a maximum voltage of 200 V. Each sample was measured three times to determine an average value. The measured values were then evaluated using the Smoluchowski approximation. All samples were tempered to 25 °C, the equilibration time was set to 1 min. The evaluation was performed with Kalliope software. All analyses were performed by the author at the GHI, RWTH Aachen university.

5 RESULTS AND DISCUSSION

The first Results and Discussion chapter addresses the integration of Ni_3Fe-LDH into an AEMWE single-cell. This chapter answers research questions Q1 and Q2 (Chapter 3) by assessing (i) the suitability of Ni_3Fe-LDH for AEMWE and (ii) the most critical electrode-design parameters (catalyst loading and ionomer content) and operating conditions (temperature and KOH concentration) for achieving high performance while maintaining stable operation. A performance benchmark is established by comparing Ni_3Fe-LDH- and Ir-based single-cells. Finally, the catalyst-to-binder ratio is optimized and the effects of temperature and electrolyte concentration on single-cell efficiency are evaluated.

In previous work,[131] it has been found that Ni-enriched Ni_3Fe-LDH exhibits electrocatalytic activity, durability and reversible alteration behavior compared to Ni-Fe-LDH catalysts with different Ni-to-Fe ratio, this work selected Ni_3Fe-LDH (Ni:Fe=3:1) as the OER catalyst for implementation into the AEMWE system.

5.1 IMPLEMENTATION OF NI_3FE-LDH ANODES

5.1.1 NI_3FE-LDH SYNTHESIS REPRODUCIBILITY AND QUALITY CONTROL

The Ni_3Fe-LDH catalyst was synthesized in-house and is not commercially available; therefore, routine quality control was required to ensure reproducible OER activity and handling. To maintain consistent catalyst properties, the powder was characterized after every synthesis. In this chapter, three to four batches are prepared, compared, and analyzed at approximately six-months intervals.

The composition and elemental content of the catalysts were verified using ICP-OES analysis. The Ni:Fe ratios for four as-synthesized catalyst batches, targeting a 3:1 ratio as specified by the nomenclature, are displayed in Figure 5.1. The calculated values exhibit minor variations, with an overall mass ratio of 3.86±0.59 and an atomic ratio of 3.36±0.59, closely matching reported values for Ni_3Fe-LDH catalysts.[326,327]

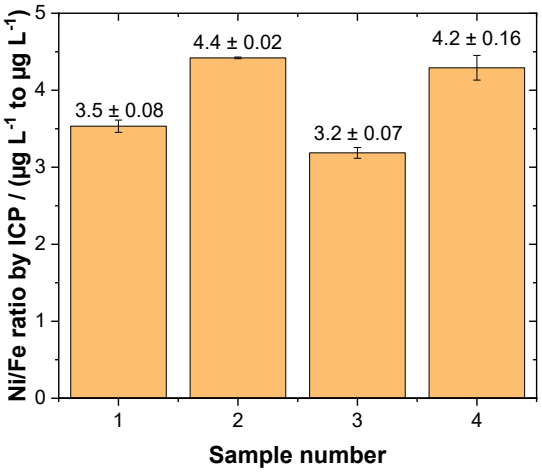

Figure 5.1. ICP-OES results of four as-synthetized Ni_3Fe-LDH powders, calculated Ni/Fe ratio (µg L^{-1} to µg L^{-1}).

To confirm structural integrity, three Ni_3Fe-LDH catalyst batches were analyzed via XRD. The peaks observed at around 11°, 22°, 33°, 35°, 39°, 46°, 60° and 61° (Figure 5.2a) align with the diffraction planes of (003), (006), (009), (012), (015), (018), (110) and (113), respectively, of Ni-Fe-LDH (JCPDS#40-0215).[328,329] The (003) plane is indicative for the LDH layers spacing is present in all batches, though batch 2 exhibits lower intensity, suggesting reduced exfoliation.[131,266] The (006) peak presents the basal plane ordering, while (009), (012), and (015) correspond to in-plane metal hydroxide layer periodicity.

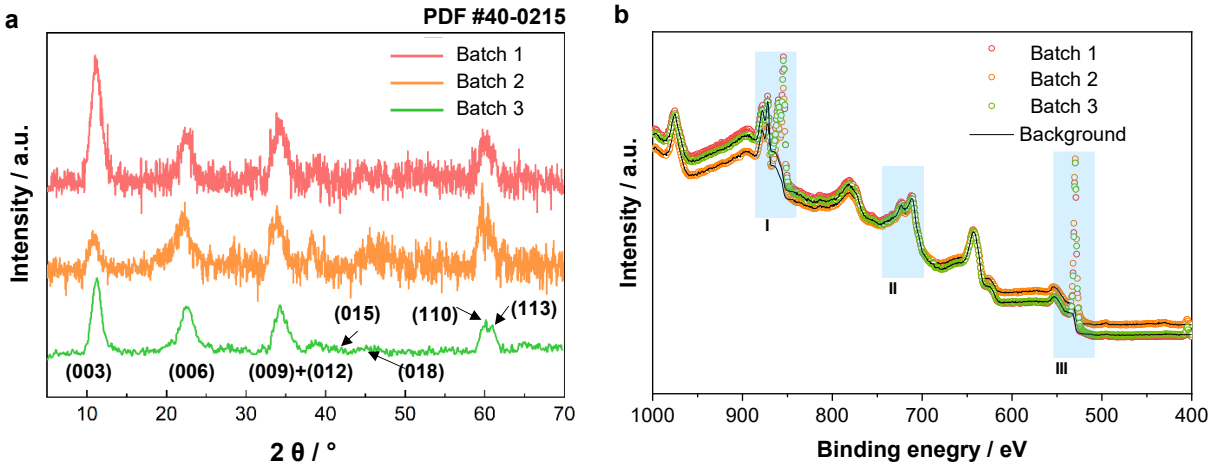

Figure 5.2. Structural characterization of three as-synthetized Ni_3Fe-LDH catalyst batches: (a) XRD patterns, (b) XPS spectra survey profiles with marked areas (light blue) for I-Ni $2p_{3/2}$, II-Fe 2p, III-O 1s.

The composition was investigated through XPS analysis. A fast recorded survey profile enabled the confirmation of elemental composition and the detection of the absence of any contaminative components (Figure 5.2b). The peaks corresponding to Ni 2p (area I), Fe 2p (area II), and O 1s (area III) are overlapping and reproducible, further validating the consistency of the catalyst composition.

The electrocatalytic OER performance of the catalysts was screened using an RDE setup. The preparation of the thin film electrode and testing was performed with support of colleagues, according to methodologies described in the literature.[131,326] Figure 5.3 shows the polarization curves for three batches of the as-synthesized Ni_3Fe-LDH catalyst, with each powder tested on a separate electrode three times.

While RDE provides a fast and simple method to evaluate catalyst activity, preparing thin films on glassy carbon electrodes presents challenges, including precise catalyst loading, uniform distribution, consistent layer thickness, and mass transport limitations due to bubble effects.[330–332] Given these limits, and considering that no optimization steps were performed while the electrodes were prepared through manual drop-casting, the observed performances and variability in resulting current densities are considered as reproducible. The reproducibility of the catalyst, tested in a two-electrode single-cell is confirmed individually in the following chapters.

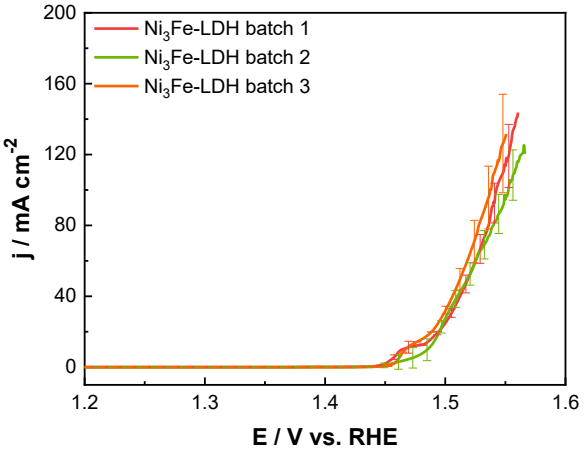

Figure 5.3. Electrochemical OER performance of three batches of the as-synthetized Ni_3Fe-LDH catalyst. Polarization curves were recorded in the RDE setup. Experimental details are presented in literature.[131,326]

5.1.2 BENCHMARKING THE AEMWE SYSTEM

The successful deposition of both catalysts on the Ni PTL was proven by XRD and SEM (Figure-A 1 and Figure-A 2). Both anodic PTEs (aPTEs) were tested for their performance under identical conditions. The polarization curves are presented in Figure 5.4. The Ni_3Fe-LDH single-cell outperformed the Ir-based cell, recording 1.82±0.02 V at 1 A cm^{-2}, compared to 1.91±0.02 V achieved by the Ir-based single-cell. This improvement is attributed to the higher intrinsic OER activity of Ni_3Fe-LDH, consistent with RDE measurements reported by Jiang et al.[131] and with prior reports showing LDH-based, PGM-free anodes can match or exceed Ir/IrO_2 due to high active-site accessibility. In addition, the combination of Ni_3Fe-LDH with the Ni PTL likely provides a synergistic contribution, as both components are electrocatalytically active.[13,18,131,158,166,170,333] This observation is supported by EIS analysis, where the measured charge-transfer resistance (R_{ct}) for the Ni_3Fe-LDH aPTE was 184 mΩ cm^2 compared to 218 mΩ cm^2 for the Ir-based aPTE (Figure 5.4b).

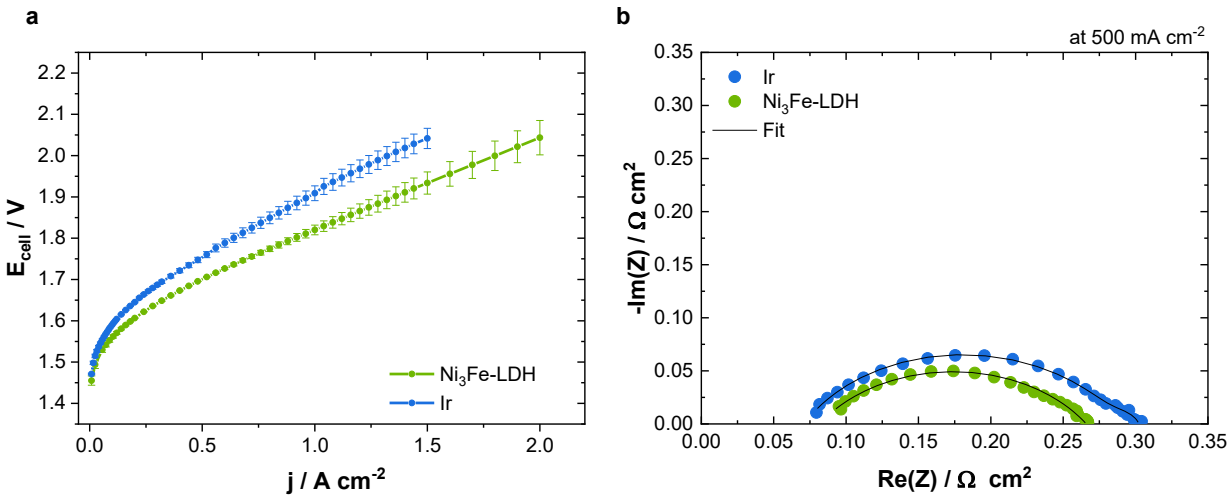

Figure 5.4. Comparison of Ni_3Fe-LDH-based single-cell (green) and Ir-based single-cell (blue): (a) Polarization curves; (b) Nyquist plots obtained by impedance spectroscopy at 500 mA cm^{-2} with simulated fit curves. Anode loading is 1 mg cm^{-2} (20 wt% binder). Cathode: Pt/C 0.6 mg cm^{-2} (25wt % binder). Testing conditions: 1 M KOH and 60 °C.

By demonstrating the good single-cell capabilities of Ni_3Fe-LDH as an OER catalyst, along with its reproducibility in structure and superiority over the benchmark Ir catalyst, further evaluations were focused on implementation factors. These include optimizing the interplay of parameters in CL fabrication and examining the catalyst's behavior under different testing conditions.

5.1.3 EFFECT OF CATALYST LAYER PARAMETERS ON ELECTROLYZER PERFORMANCE

Designing a CL requires optimizing transport pathways for electrons, ions, water, and gases (Chapter 2.3). Electron transport occurs through catalyst particles and metallic PTLs, while ions move through liquid and solid electrolytes, and product gases diffuse through the porous catalyst structure. Effective electrode design goes beyond enhancing catalyst activity as it demands a holistic integration of all components for optimal performance.[334] To optimize the Ni_3Fe-LDH anodic CL, a comprehensive study was conducted, focusing on key electrode parameters: ionomer (binder) content and catalyst loading. Each parameter was systematically analyzed to assess its individual and combined impact on CL performance.

Influence of catalyst loading

While in PEMWE, the decrease in anode catalyst loading is crucial for system sustainability and cost reduction, AEMWE optimization focuses on maximizing electrode activity and stability rather than minimizing catalyst use. Anodes with catalyst loadings of 1, 2, and 5 mg cm^{-2} were fabricated and tested in a single-cell setup.

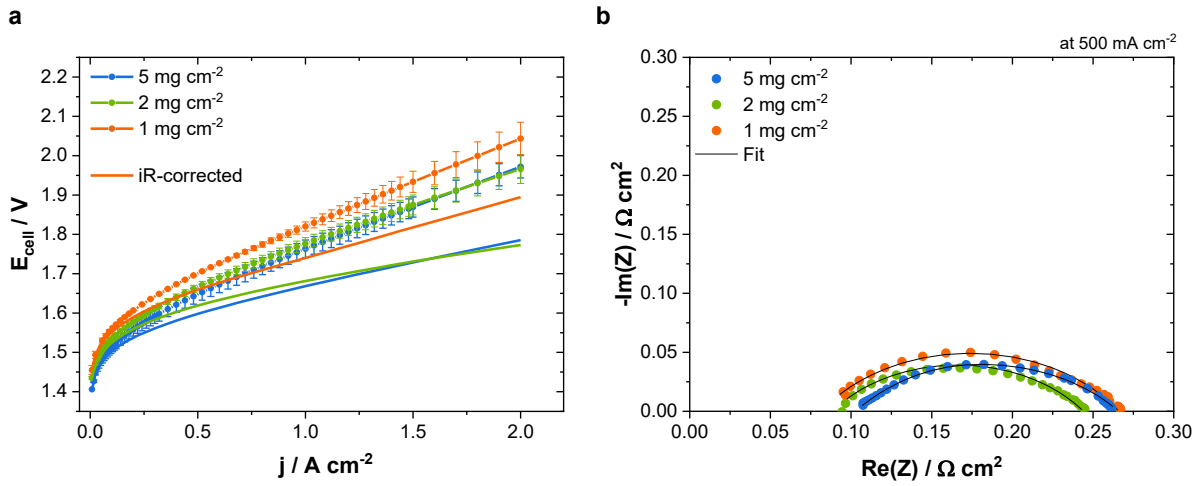

Figure 5.5. Comparison of Ni_3Fe-LDH-based single-cell with different anode catalyst loadings: 1 cm cm^{-2} (orange), 2 cm cm^{-2} (green) and 5 cm cm^{-2} (blue), all with binder content of 25 wt%. (a) Polarization curves, incl. iR-correction, based on the average polarization curve values, (b) Nyquist plots obtained by impedance spectroscopy at 500 mA cm^{-2}. Cathode: Pt/C 0.6 mg cm^{-2} (25wt % binder). Testing conditions: 1 M KOH and 60 °C.

Polarization curves and Nyquist plots, from impedance spectroscopy data obtained at 500 mA cm^{-2}, are presented in Figure 5.5a–b. The R_{Ohm} and R_{ct} values are summarized in Table-A 1.

The performance difference of cells with 2 and 5 mg cm^{-2} revealed insignificant differences. At 2 A cm^{-2}, the 2 mg cm^{-2} cell achieved 1.97±0.03 V, while the cell with 5 mg cm^{-2} required 1.96±0.04 V, with overlapping standard deviations (indicated by error bars in the graph). The 1 mg cm^{-2} cell showed lower performance, requiring 2.04±0.04 V at the same current density. iR-corrected cell voltages obtained from impedance spectroscopy analysis revealed a similar trend with values of 1.89 V, 1.77 V and 1.78 V at 2 A cm^{-2} for 1, 2 and 5 mg cm^{-2} cells, respectively.

R_{ct} decreased with increasing catalyst loading, as expected. The 1 mg cm^{-2} cell exhibited the highest R_{ct} of 184±4 mΩ cm^2, while cells with a higher anode CL loading showed R_{ct} values of 156±9 mΩ cm^2 and 154±6 mΩ cm^2 for 2 and 5 mg cm^{-2}, respectively. Increasing the catalyst loading from 1 to 2 mg cm^{-2} improved the performance without significantly affecting the R_{Ohm} (82±5 mΩ cm^2 to 89±6 mΩ cm^2). However, at 5 mg cm^{-2} the ohmic resistance increased to 103±9 mΩ cm^2.

The morphology of CLs plays a crucial role in performance differences. Figure 5.6a–c display the anode structures for 1, 2, and 5 mg cm^{-2} catalyst loadings from a top-view perspective, while images d–f show cross-sectional views.

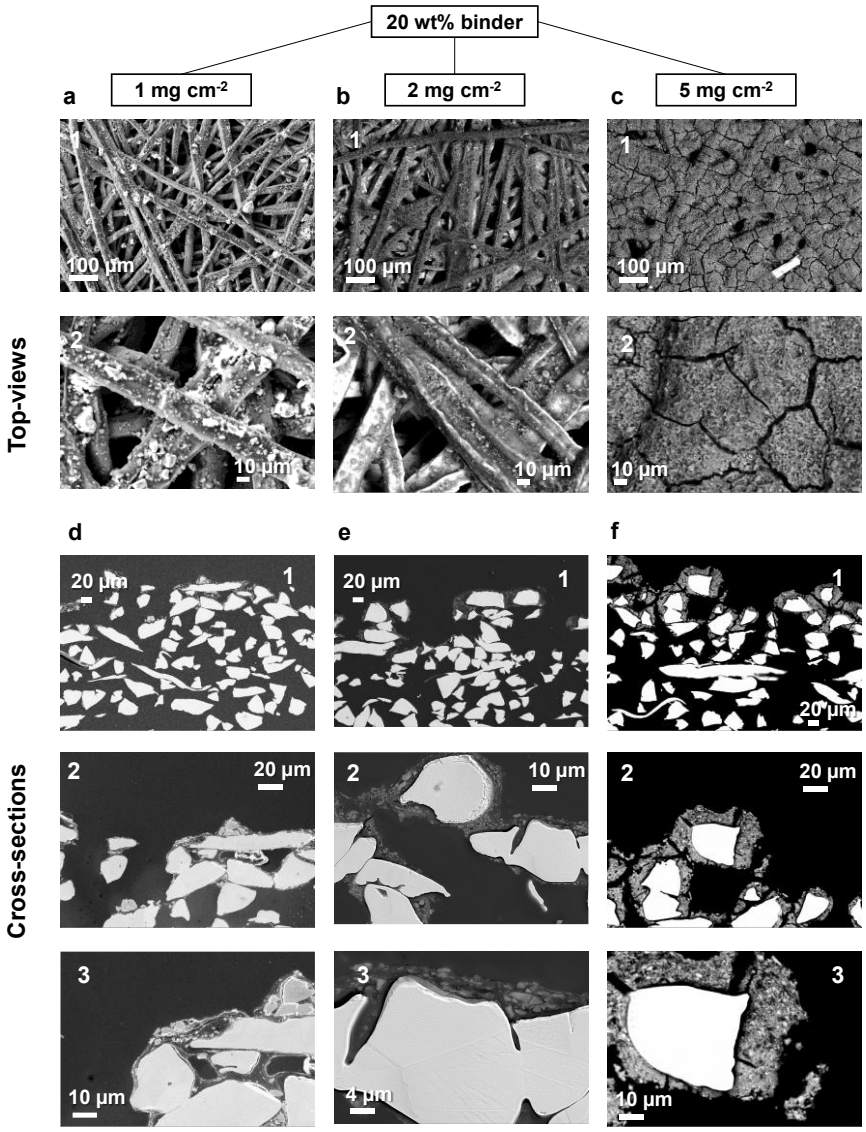

Figure 5.6. SEM images of aPTEs with different catalyst loadings and equal binder content of 20 wt% (in the initial catalyst dispersion): (a) 1 mg cm^{-2}, (b) 2 mg cm^{-2}, (c) 5 mg cm^{-2} from top-view at magnifications x250, x1k from top to bottom, (d) 1 mg cm^{-2}, (e) 2 mg cm^{-2}, (f) 5 mg cm^{-2} from cross-sectional view at magnifications x500, x1k, x2.5k from top to bottom.

The 1 mg cm^{-2} layer was inhomogeneous, with large catalyst agglomerates randomly distributed across the PTL, resulting in areas of high ionomer but insufficient catalyst coverage. In contrast, 2 and 5 mg cm^{-2} loadings provided proper PTL coverage, but with key differences. The 2 mg cm^{-2} CL formed a thin, uniform catalyst film of 5–15 µm that enveloped the Ni fibers, with minor cracking attributed to PTL flexibility. The catalyst penetration depths reached 140 µm, as observed from SEM images of various samples. The term "penetration depth" refers to the distribution of the CL within the PTL-bulk during the fabrication process, as the dispersion penetrates deeper layers of the PTL and dries there. The 5 mg cm^{-2} loading, however, resulted in a thicker film of 25–30 µm that partially filled PTL pores but exhibited more cracks and delamination, likely due to longer drying times;[335] the catalyst penetration depth was similar. The thicker CL of the 5 mg cm^{-2} anode could explain the higher R_{Ohm}, which is not only dependent on the electrolyte resistance, the CL–AEM interface but also the CL–PTL interface and the CL bulk resistance. Thicker layers moreover introduce structural challenges, as

reported in previous studies on CL morphology and durability. Crack formation in fuel cell catalyst layers has been extensively analyzed, demonstrating that thicker layers develop more cracks due to non-uniform drying, mechanical stress, and poor flexibility.[336] An excessively thick CL could hinder reactant and product transport at the MEA interface, reducing electrochemical performance.[337,338]

The similarity in performance of the 2 and 5 mg cm^{-2} cells was further supported by kinetic analysis. The so-called current increase rates, referred to as Tafel slopes in three-electrode setups, confirmed negligible kinetic differences. As R_{Ohm} varies with current densities, the $R_{\mathrm{Ohm}}(j)$ functions were fitted for each cell (Figure-A 3). Based on the R_{Ohm} values derived in this way, the iR-corrected polarization curves were plotted and observed within the specific current density interval of 0.03–0.1 A cm^{-2}. This specific interval was selected to emphasize kinetic phenomena while minimizing the interference from possible mass transport limitations. By using linear fitting to the polarization curves in this selected area, the *dE*/*d*log*j* slopes were obtained (Figure 5.7).

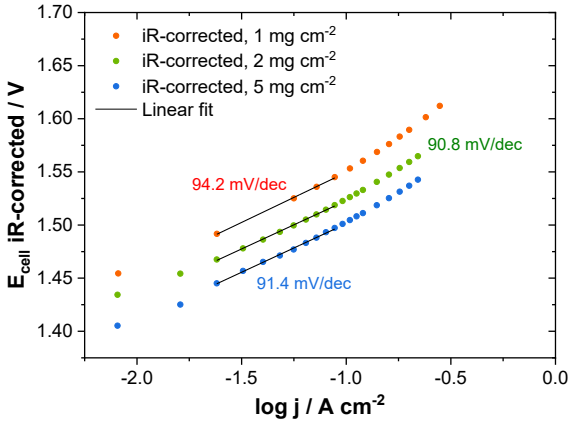

Figure 5.7. Current density increase rates (*E* vs log(*i*)) of the iR-corrected voltage data from Figure 5.5, obtained from a linear fit of values between 0.03–0.1 A cm^{-2}, including the linear fit in the chosen interval, for the MEAs containing Ni_3Fe-LDH aPTEs with varying catalyst loading of 1 mg cm^{-2} (orange), 2 mg cm^{-2} (green) and 5 mg cm^{-2} (blue).

The obtained values of around 94 mV dec^{-1} for the low-loaded single-cell and 91 mV dec^{-1} for the 2 and 5 mg cm^{-2} loaded cells indicate negligible kinetic deviation among all anode configurations.

The low catalyst loading of 1 mg cm^{-2} led to reduced performance, while increasing the loading did not result in proportional performance increase. A 2.5-fold increase from 2 to 5 mg cm^{-2} provided no further improvements, indicating low catalyst utilization. This may be explained by reduced electrochemically active surface area due to crack formation and catalyst detachment or suboptimal utilization, where only upper catalyst layers participate while the bulk remains inactive.

As in literature catalyst loadings between 2 and 10 mg cm^{-2} are employed depending on the catalyst,[83,159,161] and the performance difference between the 2 and 5 mg cm^{-2} cells is insignificant, both studied loadings could be chosen for further studies or explained as optimal for the chosen system. Considering the more pronounced crack formation in the thicker CL, the higher delamination risk, increased catalyst consumption and longer electrode fabrication times, a 2 mg cm^{-2} catalyst

loading on the anode side was selected for further studies. It balances performance, CL integrity and material efficiency without unnecessary structural drawbacks.

Influence of ionomer content

To improve MEA performance, not only the catalyst type and loading are important, but also the effective incorporation of the anion-conducting binder (ionomer) into the CL. The ionomer must provide efficient OH^- transport while avoiding blockage or insulation of catalyst active sites and allowing unhindered product gas release. At the same time, sufficient electronic contact between catalyst particles and the current collector (or PTL) must be maintained.[169,339]

Initial studies on the AEMWE focused on the optimization of ionomer content, often implementing PTFE as binder,[82,146,149,161] explaining the choice by the advantageous electrode stability and higher cell durability due the excellent chemical stability of PTFE-based materials[340] and no improvement in single-cell performance when using anion-conducing binders instead. The optimal binder concentration usually falls within 5–20 wt%, varying based on several factors and requiring thorough experimental determination.[146,147,163,341] These values served as a baseline, with 20 wt% binder set as the standard, while further reductions to 15 wt% and 10 wt% were investigated.

Before electrochemical characterization, the aPTEs with varying binder content were analyzed by SEM to evaluate their morphological and structural impact on single-cell performance. Figure 5.8a–c display the anodic CL with a catalyst loading of 5 mg cm^{-2} and ionomer contents of 10, 15, and 20 wt%, respectively. Although porosity could not be assessed conclusively, differences in CL homogeneity and integrity were evident. Lower binder content produced a more brittle CL and less uniform PTL coverage. For 2 mg cm^{-2} (Figure 5.8d–f), the PTLs 20 wt% appeared sufficiently covered, but the lower binder contents led to increased crack formation and partial mechanical detachment, indicating reduced stability. Such structural weaknesses can negatively impact mass transport, and MEA durability, and increase electrolyzer contamination risk due to detached CL fragments.

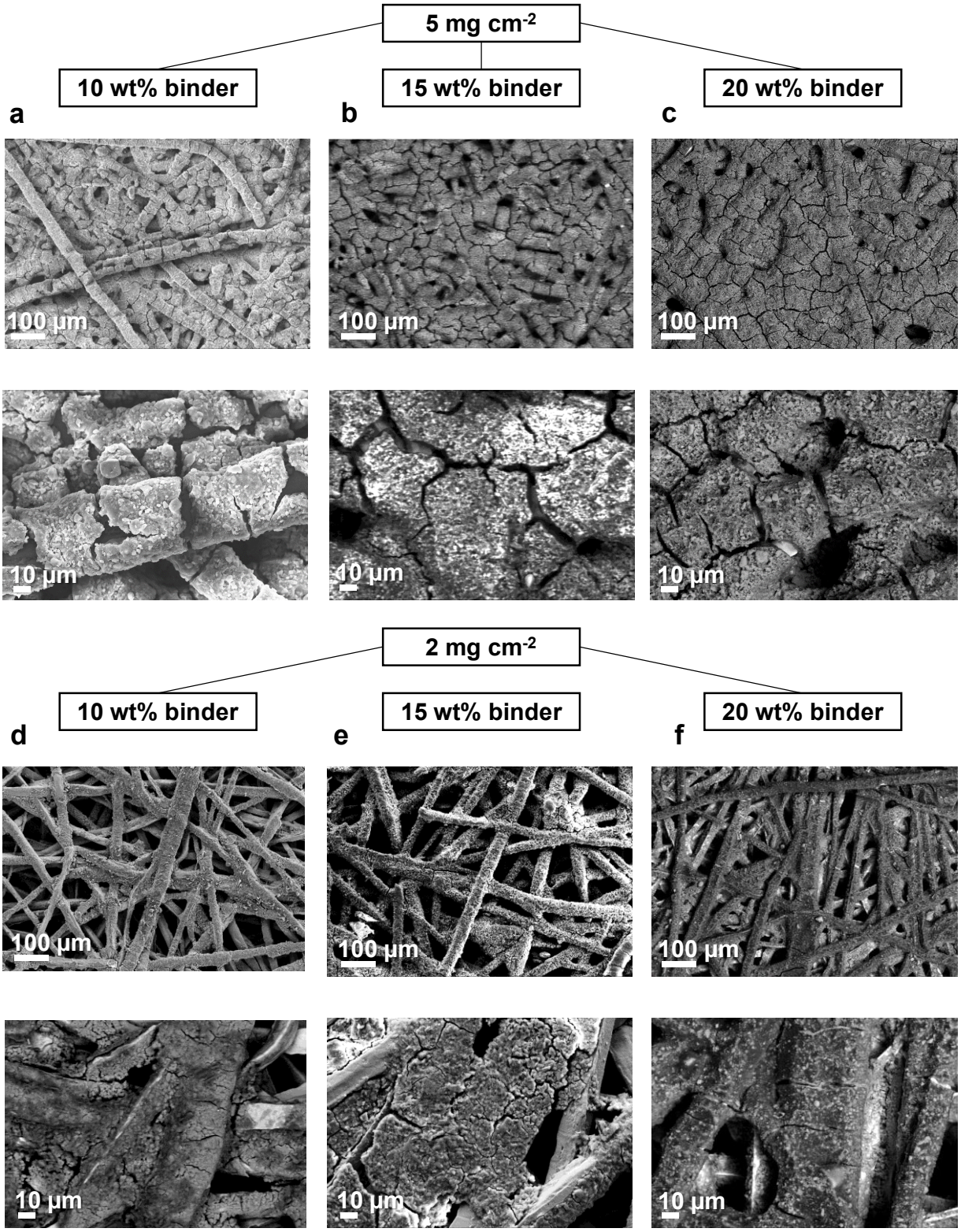

Figure 5.8. SEM images of aPTEs with different binder contents (in initial catalyst dispersions) from top-view: (a) 5 mg cm^{-2} and 10 wt% binder (b) 5 mg cm^{-2} and 15 wt% binder, (c) 5 mg cm^{-2} and 20 wt% binder at magnifications x250 and x1k from top to bottom, (d) 2 mg cm^{-2} and 15 wt% binder, (e) 2 mg cm^{-2} and 20 wt% binder at magnifications x250 and x1k from top to bottom.

To assess electrochemical performance, anodes with a constant 2 mg cm^{-2} catalyst loading and 10, 15, and 20 wt% binder were tested in a single-cell. Figure 5.9a presents the polarization curves, showing

repeatability across at least three cells per binder variation. Nyquist plots (Figure 4.11b) display impedance data at 500 mA cm^{-2}, and iR-corrected polarization curves are provided in Figure-A 4. Performance differences between the cells were insignificant, with overlapping error bars. A minor variation was observed at higher current densities, where the 10 wt% binder cell presented slightly lower cell voltages (1.95±0.02 V at 2 A cm^{-2}) compared to the 1.97±0.02 V recorded for the other two configurations. In iR-corrected polarization curves (Figure-A 4), the 15 wt% binder cell appeared to outperform the others, but all differences were within statistical error. Charge-transfer resistance values also followed this trend, with the 15 wt% cell showing the lowest (109±6 mΩ cm^2), while the 10 and 20 wt% binder cells exhibited similar values with 149±4 and 150±2 mΩ cm^2, respectively (Table-A 2).

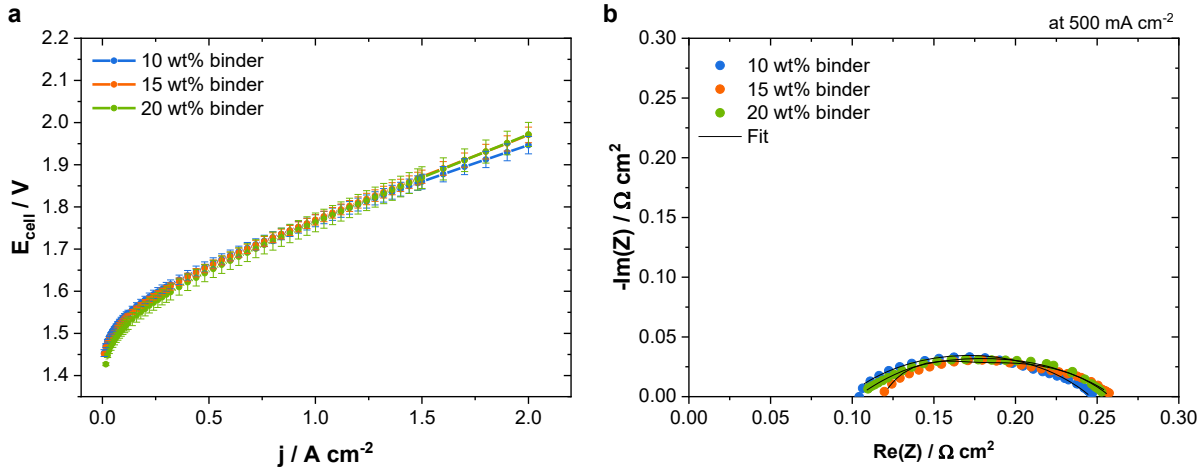

Figure 5.9. Comparison of Ni_3Fe-LDH-based single-cells with different anion-conducting binder contents of 10 wt% (blue), 15 wt% (orange) and 20 wt% (green) with equal catalyst loadings of 2 mg cm^{-2}: (a) Polarization curves; (b) Nyquist plots obtained by impedance spectroscopy at 500 mA cm^{-2}. Cathode: Pt/C 0.6 mg cm^{-2} (25wt % binder). Testing conditions: 1 M KOH and 60 °C.

To investigate durability, 500 h tests at 1 A cm^{-2} were conducted on the 15 and 20 wt% binder cells. Figure 5.10 presented the time-dependent voltage trends, where both cells showed an initial voltage decrease over the first 200 h, followed by a slight increase in voltage, which was reproducibility observed across multiple MEAs and further discussed in Chapter 5.2. Throughout testing, the 15 wt% binder cell exhibited lower voltages of 1.65 to 1.8 V, whereas the 20 wt% binder cell operated at 1.85–1.9 V with a more stable cell voltage trend. 51 µV h^{-1} increase were obtained for the 20 wt% binder cell, while 86 µV h^{-1} were observed for the lower-binder electrode.

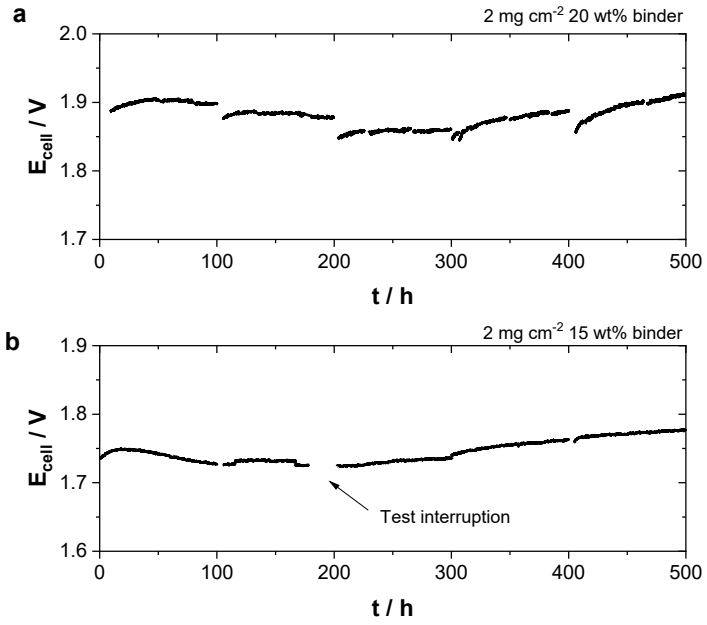

Figure 5.10. Time-resolved cell voltage changes during durability tests of 500 h at a constant 1 A cm^{-2} for Ni_3Fe-LDH-based single-cells with (a) 2 mg cm^{-2} catalyst loading and 20 wt% binder content; (b) 2 mg cm^{-2} catalyst loading and 15 wt% binder content. Cathode: Pt/C 0.6 mg cm^{-2} (25wt % binder). Testing conditions: 1 M KOH and 60 °C. The y-scales are chosen in a different interval to emphasize the curve trend.

The results align with previous studies on binder content optimization in OER electrodes. Park et al. investigated IrO_2-based anodes with FAA-3 ionomer (by Fumatech) and found 20 wt% of binder to be an optimal content. The work revealed, unlike in this study, that lower and higher binder contents of 10 and 30 wt%, respectively, significantly decreased the single-cell performance. This phenomenon, where a mid-range binder content enhances performance, is typically attributed to an optimal balance that facilitates efficient charge-transfer, supports ionic conductivity, and prevents catalyst particle insulation, thereby preserving a high electrochemically active surface area.[342,343]

Cossa et al. observed less dependency on binder content using Ni-Fe-based catalysts, similar to this study, where cracking increased at lower binder contents, but performance remained mostly unaffected between 7, 15, and 25 wt% FAA-3 binder.[344] In contrast, studies using $CuCoO_x$ anodes with Aemion™ ionomer found no significant single-cell performance differences between 10 and 30 wt% binder.[147] Meanwhile, other work on IrO_x anodes in CCM-MEA configurations demonstrated a strong dependency on Aemion™ binder content, significantly affecting performance.[148]

The outcomes of the current study are consistent with observations made by Faid el al.[151], showing insignificant influence of binder content on the single-cell performance. The research group found that in CCS-configurations, NiO anode performance remained unaffected by the anion-conducting binder content within a range of 10–40 wt%. Given the strong interplay between catalyst-binder pairs, single-cell configuration, and component interaction, the results of this study are applicable to the specific materials used and may not be transferable to other catalyst-ionomer systems, as proven by the controversy results of the literature overview.

To sum up, although the 15 wt% binder configurations initially shower slightly lower R_{ct}, SEM analysis revealed increased cracking and delamination in these layers. Additionally, stability issues in catalyst dispersion during electrode fabrication complicated reproducibility. Despite initial expectations, single-cell tests showed no significant performance differences among anodes with different binder contents raising the question of the role of such an anion-conducting binder. Given its greater mechanical stability and reproducibility, the 20 wt% binder MEA was chosen for further studies, although both electrode types are suitable for AEMWE applications.

5.1.4 EFFECT OF OPERATING CONDITIONS ON ELECTROLYZER PERFORMANCE

Temperature

To assess the practical and industry-relevant applicability of Ni_3Fe-LDH-based AEMWE, operational parameters were investigated, focusing on temperature effect.[19,81,288] Since AEMWEs operate as near-ambient temperature electrolyzers, a 30–80 °C range was chosen to evaluate single-cell performance. Each condition was tested on at least three separate cells with fresh MEAs to ensure repeatability.

Figure 5.11 presents the polarization curves and the Nyquist plots, while Figure-A 5a additionally shows the iR-corrected curves, following the performance-temperature dependency.

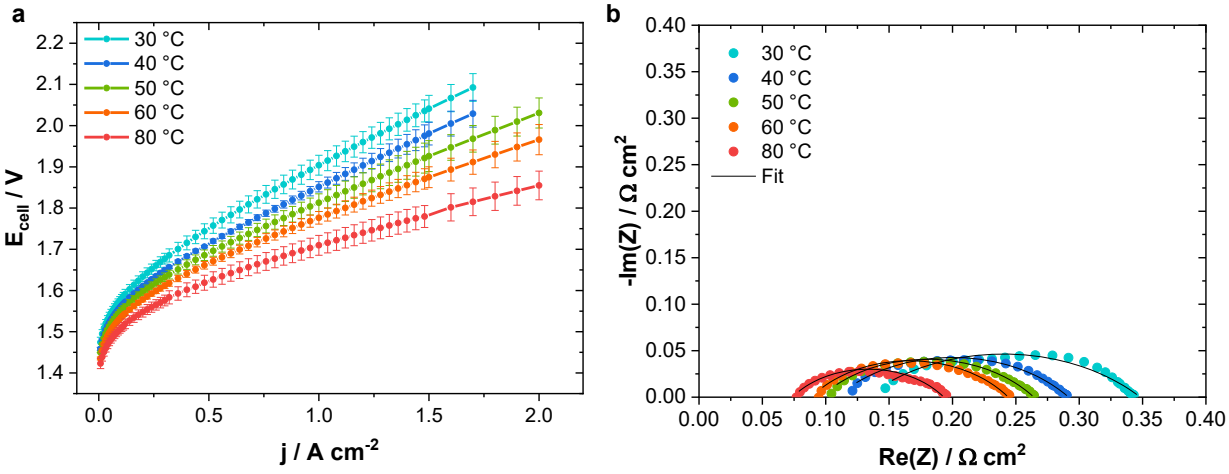

Figure 5.11. Comparison of Ni_3Fe-LDH-based single-cell performance at different operation temperatures: 30 °C (light blue), 40 °C (blue), 50 °C (green), 60 °C (orange) and 80 °C (red). (a) Polarization curves; (b) Nyquist plots obtained by impedance spectroscopy at 500 mA cm^{-2}. Cathode: Pt/C 0.6 mg cm^{-2} (25wt % binder). Testing conditions: 1 M KOH and 60 °C.

A consistent performance improvement was observed with increasing temperature, with the best performance obtained at 80 °C. Specifically, the cell voltage at 1 A cm^{-2} decreased from 1.776±0.015 V at 60 °C to 1.701±0.023 V at 80 °C, yielding a total gain of nearly 200 mV from 30 °C to 80 °C. The specific cell voltages are summarized in Table-A 3.

When considering non-iR-corrected cell potentials, a 40±5 mV reduction per 10 °C increment was observed. Impedance analysis confirmed this trend, showing a continuous decrease in both ohmic and

charge-transfer resistance. R_{Ohm} dropped from 132±4 mΩ cm^2 at 30 °C to 67±9 mΩ cm^2 at 80 °C, while R_{ct}, decreased from 216±6 mΩ cm^2 to 119±14 mΩ cm^2. The resistance values are summarized in Table-A 4. These finding align with expectations, as higher temperature is associated with accelerated electrode kinetics, improved ionic conductivity, and enhanced mass transport.[17,82–84,229,345,346]

Higher temperatures improve electrolyzer performance by accelerating reaction kinetics and reducing kinetic overpotentials, while also increasing KOH and membrane ionic conductivity through higher ion mobility and lower solution viscosity.[75,347–351] In addition, OH^- transport is enhanced by improved hopping conduction (including the Grotthuss mechanism), which further supports charge transport and overall efficiency in this temperature range.[352–354] While improving performance, higher temperatures can accelerate MEA degradation; many AEMs show chemical and functional deterioration near 100 °C and may lose ion exchange capacity during prolonged operation even at 80 °C. Elevated temperatures can also reduce the durability of Fe-containing components due to Fe leaching in alkaline media above 80 °C, which may contaminate the electrolyte and weaken long-term system stability.[69,72,278,346,355–360]

A balance between performance and stability is required. Since 60 °C provided a clear performance gain while remaining industrially relevant, it was selected as the standard temperature for subsequent studies and as a practical benchmark.

Electrolyte concentration

Following the optimization of electrode configuration and operating temperature, the influence of electrolyte concentration on single-cell performance was examined. While AEMWEs typically operate in low-concentration alkaline electrolytes, there is ongoing research into their practicality in near-neutral or pure water conditions. Usually, this aim is explained by safety reasons and the corrosive alkaline environment, which limits the choice of glasses, metals and plastics.[81,361] In this study, KOH concentrations ranging from 1 M to 0.01 M were tested to evaluate their impact on performance.

Figure 5.12a presents the polarization curves and Figure 5.12b shows the Nyquist plots, recorded at 500 mA cm^{-2} for varying KOH concentrations. The iR-corrected polarization curves, illustrating the performance-electrolyte dependency, are provided in the Appendix (Figure-A 6). A steady decline in performance was observed with decreasing electrolyte concentration. At 1 A cm^{-2}, the cell voltage increased from 1.750±0.013 V in 1 M KOH to 1.802±0.010 V in 0.5 M KOH and further to 1.924±0.013 V in 0.1 M KOH. The lowest electrolyte concentration tested, 0.01 M, could not sustain performance up to 1 A cm^{-2}, achieving a maximum of 2.051±0.044 V at 0.88 A cm^{-2}. This resulted in an overall voltage increase of ≈360 mV (at 0.88 A cm^{-2}) over the chosen electrolyte concentration range.

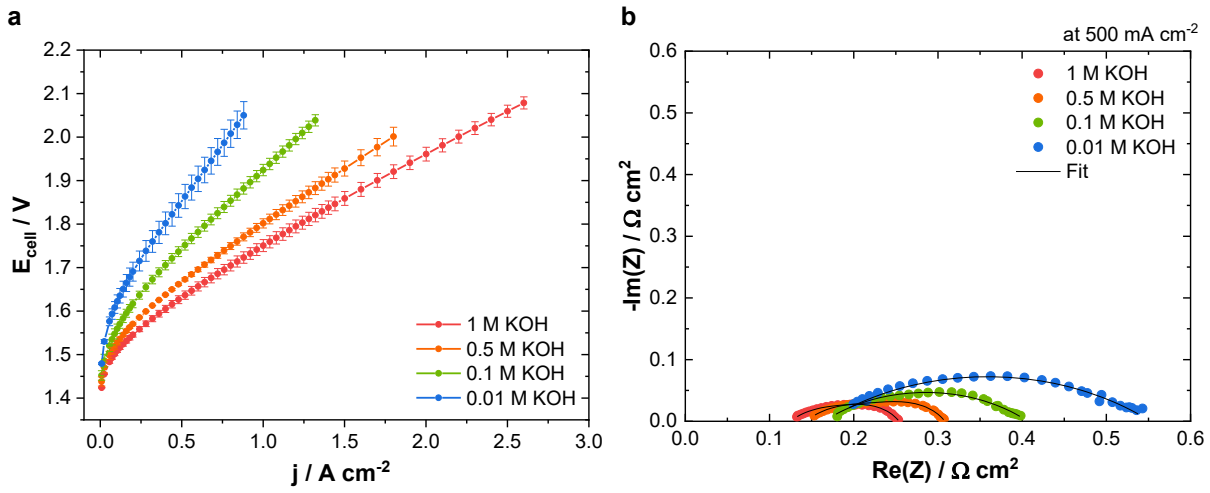

Figure 5.12. Comparison of Ni_3Fe-LDH-based single-cell performance at different electrolyte concentrations: 1 M KOH (red), 0.5 M KOH (orange), 0.1 M KOH (green), 0.01 M KOH (blue). (a) Polarization curves; (b) Nyquist plots obtained by impedance spectroscopy at 500 mA cm^{-2}. Cathode: Pt/C 0.6 mg cm^{-2} (25wt % binder). Testing conditions: varying electrolyte concentration and 60 °C.

Impedance analysis revealed significant changes in R_{Ohm} and R_{ct} with varying electrolyte concentrations; the fitted values are summarized in Table-A 5. The most notable change in R_{Ohm} was observed between 1 and 0.1 M, rising from 118±7 mΩ cm^2 to 167±15 mΩ cm^2. A more pronounced effect was observed in R_{ct}, which increased drastically from 129±6 mΩ cm^2 in 1 M KOH to 382±20 mΩ cm^2 in 0.01 M KOH. These trends indicate that lower electrolyte concentrations hinder mass transport and reaction kinetics, primarily due to reduced OH^- availability at the catalyst surface.[81,85,91,102]

The performance decline at lower electrolyte concentration is well-documented and consistent with previous studies.[17,81,85,91,102,147,148,152,163,247,251] This effect is commonly attributed to the dual role of KOH, which supplies OH^- for the OER and enhances membrane and electrolyte ionic conductivity, thereby improving charge transport and reaction kinetics.[147] Accordingly, increasing electrolyte conductivity lowers electrode polarization resistance.[362] In more concentrated alkaline media, ionic conduction is not limited to the membrane interface but extends into the liquid phase, enabling more efficient electrode processes. At lower KOH concentration or in pure water, catalytic efficiency decreases because OER and HER are largely confined to the membrane–catalyst–water interface. In addition, AEM swelling and transport properties depend on both water uptake and interactions with KOH ions within the polymer network. The feasibility of pure water operation is further limited by the pH dependent stability of Ni- and Ni-Fe-based catalysts, which may dissolve or restructure at pH<9.

Higher electrolyte concentrations, as higher operating temperatures, improved cell performance. This study assessed whether KOH concentration could be reduced with limited performance loss and identified both 0.5 M and 1 M KOH as feasible. However, 1 M KOH was selected as the standard reducing the risk of performance loss and material degradation at near neutral conditions.

5.1.5 SUMMARY

To investigate Q1–Q2 (Q&A Chapter 3, Approach 1), Ni_3Fe-LDH was implemented as OER catalyst into an AEMWE single-cell and systematically tested under industrially relevant conditions. The observed trends are transferable to related Ni-Fe-based catalysts. The results can be summarized as follows:

- The catalyst's synthesis quality control by ICP-OES, XRD, and XPS analyses ensured consistent composition and structural integrity. The OER performance of Ni_3Fe-LDH was reproducibly assessed using an RDE, proving its consistent efficiency and reliability across multiple tests and batches.
- Benchmarking Ni_3Fe-LDH against Ir OER catalyst, a reproducibly higher performance and lower charge-transfer resistance were observed. This indicated the potential of Ni_3Fe-LDH as a highly effective non-PGM catalyst for AEMWE.
- By varying catalyst loading and binder content, single-cell performance could be tuned. Increasing the catalyst loading from 1 to 5 mg cm^{-2} did not lead to a proportional performance gain, indicating reduced catalyst utilization and possible transport limitations at higher loadings. A loading of 2 mg cm^{-2} was selected as optimal, providing a balance between sufficient PTL coverage, efficient catalyst utilization, and mechanical stability. Varying the ionomer content from 10 to 20 wt% had only a minor effect on performance, but 20 wt% binder was chosen for subsequent experiments to improve CL integrity and stability on the PTL.
- Operation temperature and electrolyte concentration were varied further optimize Ni_3Fe-LDH-based single-cell performance. Increasing the temperature from 30 °C to 80 °C led to notable improvements in cell performance, attributed to enhanced kinetics and ionic conductivity. Specifically, the highest performance was achieved at 80 °C, demonstrating a reduction in cell voltage. Reducing the electrolyte concentration from 1 M to 0.01 M resulted in a significant decline in performance. The operation parameters must be balanced with considerations for material stability and operational costs. Based on the outcomes of this study, 60 °C and 1 M KOH were selected as the best conditions for further studies due to their alignment with industrial standards and balanced performance-stability profile.

5.2 Durability Assessment and Degradation Mechanisms in Ni_3Fe-LDH Anodes

Considering the great electrochemical performance of the Ni_3Fe-LDH-based cell described in the previous chapter, it was essential to evaluate the durability of the electrolyzer to demonstrate its suitability for practical applications.

The literature on long-term single-cell tests for AEMWE systems is limited, presenting operation duration of a few hundred hours or even less,[84,102–106] with the only notable mentions of 500 h,[107] 1000 h,[108] and 2000 h[66,109] operations. Often, the selected conditions for testing are too mild, such as low current densities and operating temperatures.[92,158,267,339,363] Additionally, the chosen PTLs are frequently carbon-based, which initially makes them prone to oxidation and degradation.[364–367] Furthermore, high catalyst loadings[365,367,368] are sometimes employed, which may impact the overall performance and longevity of the system. Despite their great importance, comprehensive post-mortem studies of electrodes or MEAs, including physico-chemical and electrochemical properties, are usually missing.[69,106] Stability insights from RDE setups do not always reflect the electrode behavior in the MEA,[16] and detailed post-operational reports, particularly for Ni-Fe-LDH electrodes, are limited.

This study presents a general approach of single-cell durability tracking during long-term steady-state operation. In situ electrochemical characterization is coupled with ex situ physicochemical methods to observe the internal chemical and morphological changes that occur on the anode–electrode. By this, a protocol of investigating and tracking the catalyst layer degradation in applied AEMWEs is demonstrated.

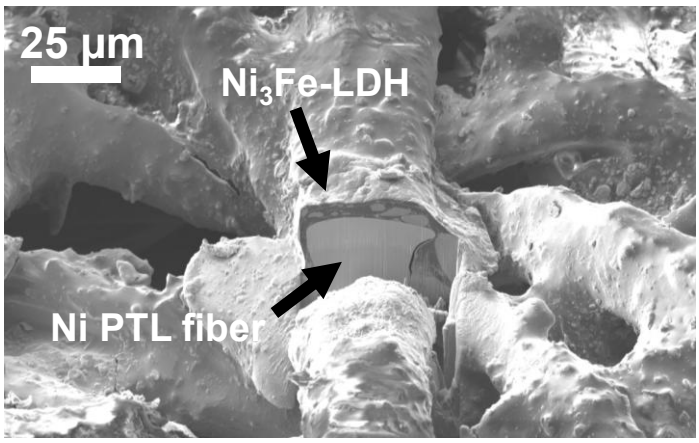

Figure 5.13. SEM image of a Ni_3Fe-LDH coated Ni fiber, FIB-cut and shown from a 45° angle.

The core element of the analyzed single-cell is the aPTE with a Ni_3Fe-LDH loading of 2 mg cm^{-2} and a binder content of 20 wt%, which is presented in Figure 5.13. The FIB-cut cross-section of an individual Ni fiber confirms that the PTL fiber is uniformly enclosed by the catalyst coating. The cross-sectional SEM image (Figure-A 7) shows the catalyst-binder distribution, with catalyst agglomerates up to 2 µm and a CL thickness of 10–15 µm, varying by region. Minor vertical cracks were observed. EDS mapping confirms a homogeneous element distribution throughout the CL.

5.2.1 ELECTROCHEMICAL EVALUATION OF SINGLE-CELL DURABILITY

The Ni_3Fe-LDH single-cell performance with a catalyst loading of 2 mg cm^{-2} on the aPTE is presented in Figure 5.14a, reaching 1 A cm^{-2} at 1.77±0.02 V or 2 A cm^{-2} at 1.97±0.04 V. Following iR-correction, only 1.69 V were required to achieve 1 A cm^{-2}.

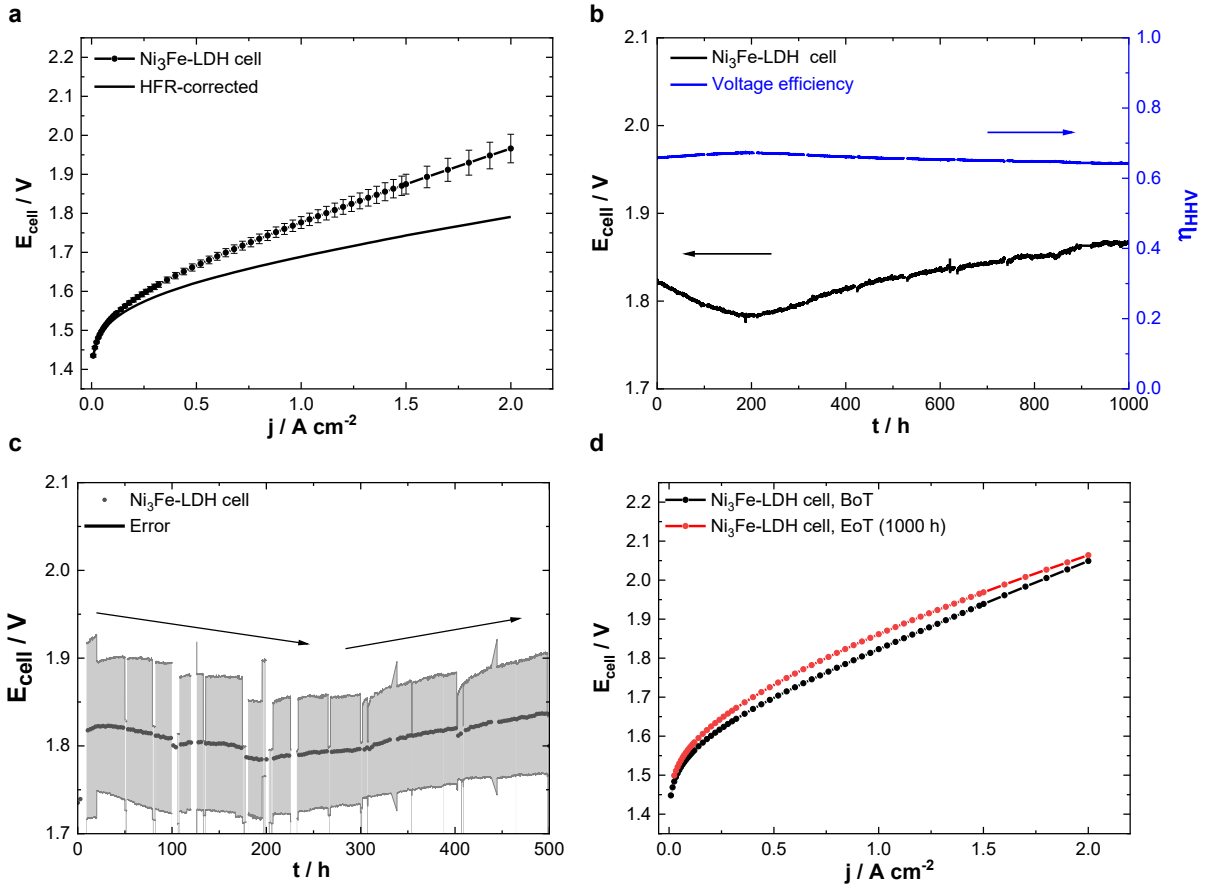

Figure 5.14. (a) Polarization curve of the Ni_3Fe-LDH (2 mg cm^{-2}, 20 wt% binder) cell system, incl. iR-corrected polarization curve; (b) cell voltage and voltage efficiency during long-term 1000 h single-cell operation at a constant current density of 1 A cm^{-2} in 1 M KOH and 60 °C; (c) durability tests presented as a time-resolved cell voltage change curve incl. reproducibility measurements; (d) polarization curves at beginning of test (BoT) and end of test (EoT, after 1000 h). Cathode: Pt/C 0.6 mg cm^{-2} (25wt % binder). Testing conditions: 1 M KOH and 60 °C.

To track steady-state long-term stability of the Ni_3Fe-LDH-based single-cell, it was subjected to a constant current density of 1 A cm^{-2} for 1000 h, with performance and EIS measurements every 100 h. Figure 5.14b shows the resulting potential across the entire durability test, as well as the calculated cell voltage efficiency (Equation 2.12).[158] During the first 200 h, a decrease in cell potential by ≈39 mV was observed. This most likely corresponds to a break-in of the cell where the optimal interface between the catalyst and electrolyte is formed.[80] This behavior differs from the one reported in the literature for Ni-Fe-LDH-based electrolyzers,[158,159,267,327] where a recently reported break-in procedure lasts for ≈80 h.[107] Still, decreasing voltage behavior is not uncommon and often presented in literature;[77,107,108] it is to be expected that ion exchange and soaking of the membrane still proceeds to some degree. Moreover, the catalyst oxidizes to active species layer by layer, as the Ni_3Fe-LDH catalyst used here is a multi-layered catalyst. In addition, the catalyst agglomerate size inhomogeneity,

i.e., in the range of 1–100 µm, which is an important parameter of the catalyst layer and that is supposed to be the main factor in the long conditioning procedure. Furthermore, following the observed conditioning of 200 h, where the oxidation of Ni_3Fe-LDH to the active γ-NiOOH occurs, additional Fe might be absorbed from the electrolyte. Together with the initially present Fe content, this additional incorporation leads to an Fe concentration high enough to significantly improve the catalytic activity.[93]

The determination of the moment at which the system is considered to obviously start degrading is a topic for deeper discussion, as the system break-in (conditioning) time should be carefully investigated and defined for each AEMWE system. Different cell voltage behavior has been observed during long-term tests, as described in literature.[80] As different processes inside a cell can occur simultaneously and overlap, the reported rate of cell degradation may not provide a true representation of the cell's actual degradation process. The terms degradation, durability, and stability are used in literature for the description of different voltage trends.[77,102,107,108,307,369] Those include the decrease, increase or even a mixed behavior in which one type follows the other. In this study, we differentiate between the overall voltage increase (EoT minus BoT values) and degradation, in which the voltage values are considered from the lowest value (200 h) to the highest and final voltage at EoT. Following this terminology, the cell presents a low overall voltage increase of 45 µV h^{-1} (2.49%) and a considered cell degradation from 200 h of 84 µV h^{-1} or 4.68%. This is significantly lower than previously reported for Ni-Fe-LDH catalysts.[159,274] Interestingly, the cell voltage efficiency is only marginally affected by the potential change. Over the course of the entire experiment, it is in the range of 64–65%, which is comparable to previously reported values.[158]

After long-term operation, a color change in the aPTE was observed (Figure 5.15). The transformation from yellow–orange to brown–black indicates an oxidation of the catalyst layer. The membrane, however, did not show a color change and was not visibly damaged after long-term test. Residues of the applied pressure inside the cell, as well as minor catalyst leftovers from both sides, are also visible.

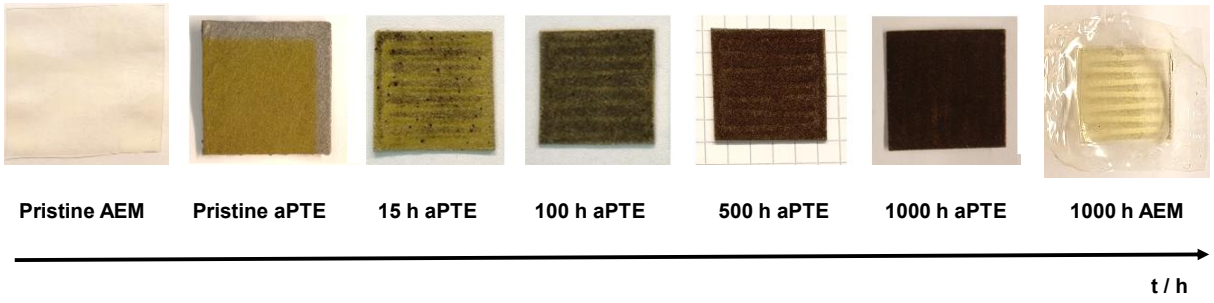

Figure 5.15. Photographic images of Ni_3Fe-LDH aPTE and AEM, showing color changes from pristine state to post-operation after 1000 h.

In literature, far too little attention is paid to the reproducibility of long-term tests due to the time required for single-cell measurements and the uncertainty of system behavior. Most literature in the PEM and AEM research fields focuses on the degradation behavior presented by only one time-resolved curve[63,80,370–372] or rounds of voltammetry cycling operation.[373] To fill this gap for the

presented Ni_3Fe-LDH-based system, long-term stability was further repeated three times with a shorter operational duration of 500 h (Figure 5.14c) to investigate the reproducibility of the degradation trends. A scattering in performance of nearly 200 mV at 1 A cm^{-2} was obtained due to the use of different material batches, whereas the trend of an ≈200 h break-in time is reproducible.

To identify possible sources of the performance loss during steady single-cell operation, the intermittent polarization curves and EIS data were analyzed. Figure 5.14d presents the polarization curves at BoT and EoT. At 2 A cm^{-2} the potential increases by ca. 15 mV, which is only a minor increase in cell voltage. Figure-A 8 furthermore shows the significant performance gain during the first 200 h of operation, with a maximum performance of 1.96 V at 2 A cm^{-2} and a decrease of R_{ct} down to 0.169±0.001 Ω cm^2 (Table-A 6).

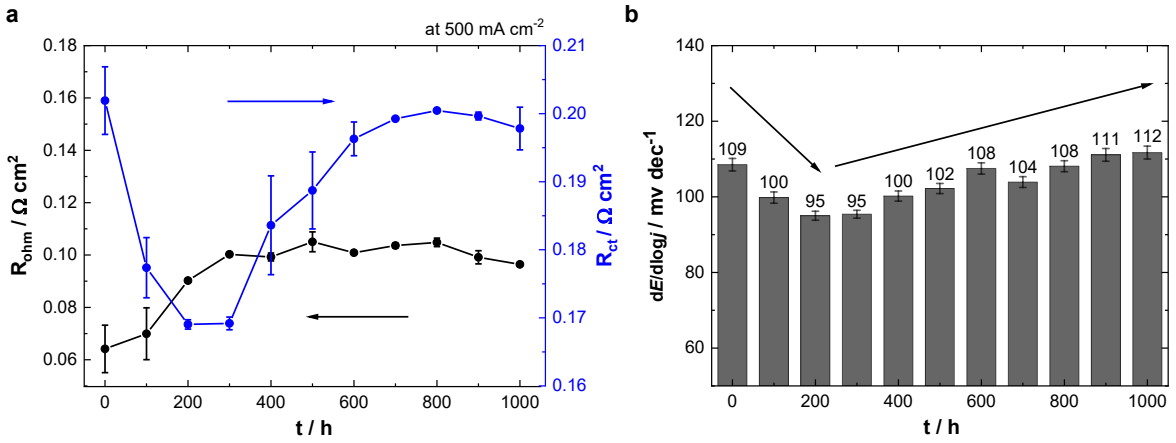

Figure 5.16. Electrochemical analysis of the Ni_3Fe-LDH–Pt/C single-cell: (a) Operation time-dependent change in R_{ct} and R_{Ohm} of the system obtained from in situ impedance spectroscopy analysis; (b) operation time-dependent change of the dE/dlog$j$ slopes.

Figure 5.16a shows the time-resolved trends of R_{Ohm} und R_{ct}. As the Nyquist plots do not intersect the x-axis (Figure-A 8b) and the plot fit is extrapolated, there is a variation in the simulated high-frequency resistance values (R_{Ohm}). To ensure the reproducibility of the obtained resistance values, the fitting procedure was repeated three times (Table-A 6). During the stability test, R_{Ohm} increased from the BoT to EoT by 32±1 mΩ cm^2 (Figure 5.16a, black curve). A significant part, i.e., 26±1 mΩ cm^2, was observed during the first 200 h of operation. This increase can indicate a minor initial change in the membrane or anion-conducting binder in the catalyst layer, or a change in the membrane–electrode interface, which stands, at first glance, in contrast to the overall performance increase observed during the break-in time. Furthermore, no major change in R_{Ohm} was detected for the rest of the test. The R_{ct} values, reflecting charge-transfer resistances of both OER and HER, $R_{\mathrm{ct,a}}$ and $R_{\mathrm{ct,c}}$, respectively, exhibit a more complex trend (Figure 5.16a, blue curve). First, up to 200 h, a decrease is noticeable, indicating improved charge-transfer kinetics. This is in line with the increase in OER performance during this period and could have a stronger influence than the increase in R_{Ohm}. Furthermore, the observed increase in the R_{ct} after 300 h correlates well with the degradation of the cell as observed in the potential trend (Figure 5.14b und c). The increase in R_{ct} could be related to a

partial loss in electrocatalytic activity and a decrease in the electrochemical surface area by losing or deactivating catalyst and/or binder material; precise deconvolution of the effects is not trivial without extended studies of the anion-conducting binder compound.

The change in catalyst kinetics is further confirmed by changes in the observed current increase rate (Figure 5.16b). The *dE*/*d*log*j* slopes were extracted from a linear fit of the polarization curves on a logarithmic current scale, following iR-correction, in the current density range of 0.03–0.1 A cm^{-2} (Figure-A 9). This narrow region was chosen to account for primarily kinetic effects, avoiding the possible effects of the saturation of surface coverage of adsorbates and mass transport limitations. Starting with 109±2 mV dec^{-1}, the *dE*/*d*log*j* slope slightly decreased for the first 300 h of operation to 95±1 mV dec^{-1} and subsequently increased to 112±2 mV dec^{-1}. These observations correlate well with the trend of charge-transfer resistances (Figure 5.16a) and the overall durability trend (Figure 5.14b), fitting the correlation between those parameters. Contributions from changes in cathode performance and partial cover effects may be non-negligible, as the current–voltage trend contains both electrodes. A separation of the overlapping contributions is, however, not trivial.[374] As the OER is slower and considered the more energy-demanding reaction,[77,81] it is expected that the contribution of the anode, the Ni_3Fe-LDH aPTE in this case, will be more pronounced.

After 1000 h of operation, the single-cell was disassembled and the original electrodes were re-assembled with a fresh membrane. Interestingly, performance regeneration was observed that it almost reached the performance obtained after 200 h, i.e. shortly after the break-in time (Figure-A 8a). This also corresponded to a reset of R_{ct} as well as a decrease in R_{Ohm} (Figure-A 8b and Table-A 6). During the AEM exchange procedure, in addition to refreshment of the membrane, the reassembly could lead to improved contact between the electrodes and membrane. Furthermore, the reassembly of the cell could induce further effects like bubble removable. Whether the different effects of the replacement of the membrane or restart have a greater influence, and to what extent, remains unclear from this study and should be further investigated in the future.

5.2.2 MORPHOLOGICAL AND ELEMENTAL DEGRADATION OF THE ANODE

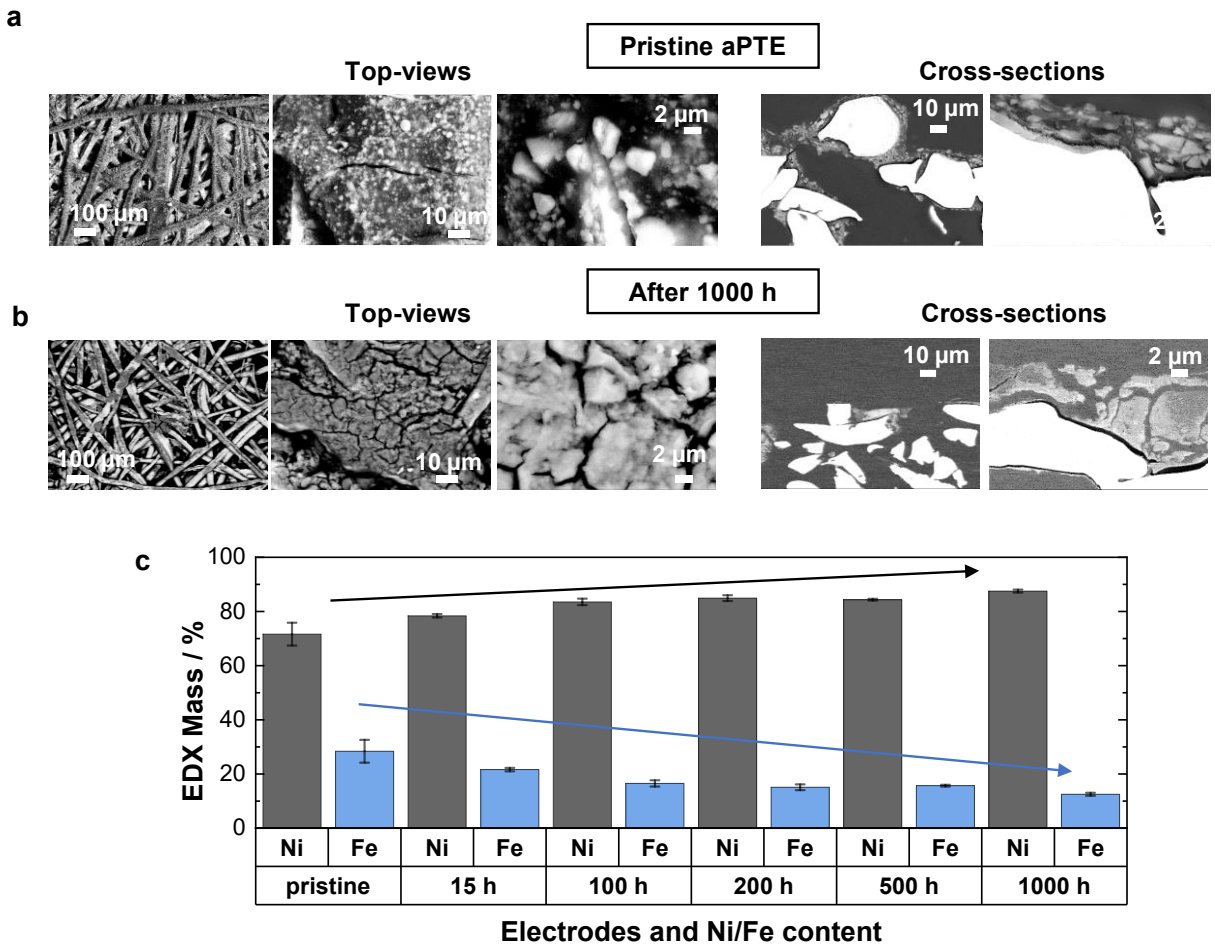

Figure 5.17. Top-view and cross-section SEM images at different magnifications of (a) pristine Ni_3Fe-LDH aPTE; (b) aPTE after 1000 h of operation; (c) EDS analysis results of the aPTEs, showing elemental Ni and Fe mass content (%) from pristine samples to those after 1000 h of operation. Cross-sections of catalyst layer bulks were analyzed.

Figure 5.17a presents the top-view and cross-sectional SEM images of the Ni_3Fe-LDH aPTE directly after fabrication, whereas the same electrode after 1000 h of operation is shown in Figure 5.17b. The intermediate conditions of the aPTE after 15 h, 100 h, 200 h, and 500 h are presented in Figure-A 10. It should be noted that due to the necessity of disassembling the cell, each figure set corresponds to a new electrode and experiment. The same is valid for all following characterization analyses performed ex situ. Pristine aPTE exhibits proper coverage of the Ni PTL fibers. Due to the relatively low catalyst loading of 2 mg cm^{-2}, the resulting catalyst layer is distributed over the individual fibers rather than forming a closed layer. The initial catalyst layer demonstrates minor fractures, likely induced by the drying process and flexibility of the PTLs.

When discussing the changes in the catalyst layer, the damage that occurred when the MEA was disassembled from the cell hardware should be considered (Figure-A 11). Some parts of the catalyst layer remained attached to the membrane. The use of an aPTE with higher loading (for example, 5 mg cm^{-2}, as presented in Figure-A 12a and b) would lead to negligible changes, revealing the actual stable catalyst layer and thus electrode structure.

Comparing the top-view images of the pristine aPTE and the one after 1000 h (Figure 5.17a and b), a roughening of the catalyst layer surface can be observed. Moreover, the crack formation becomes more pronounced. The cracks do not necessarily lead to a loss of activity, if the attached catalyst does not drastically diminish and the different parts remain in electrical contact, as well as being in contact with the membrane. It was already proven that a cracked surface might even be preferred, as it helps with faster bubble removal and might even decrease catalyst dissolution during OER.[165] The apparent roughness of the catalyst layer can also be explained by the ablation of the catalyst layer or the relative reduction in the binder compound content[148,361,375,376] that appeared during the single-cell test, as was also shown by ToF-SIMS analysis below. This could also explain the increase in R_{Ohm} over the course of the experiment, as the contact between the catalyst and binder, and respectively the membrane, is decreased. Nevertheless, even after 1000 h, neither significant thinning of the CL, nor full delamination from the PTL substrate can be recognized.

Interestingly, the cross-sectional images reveal a significant structural change in the catalyst particles after 1000 h. A slight re-dispersion within the catalyst layer can already be seen after 500 h. A more detailed examination of the changes within the catalyst layer bulk is outlined in the next section. The reconstruction of the catalyst layer is often considered one of the main causes of degradation. Another critical degradation factor is the leaching of chemical elements, i.e., Fe in Ni-Fe-based catalysts.[106] Therefore, the metal contents of the extracted aPTEs were analyzed by means of EDS. Figure 5.17c presents the mass percentage of Ni and Fe contained in the catalyst layer bulk of the aPTE after different stages of the durability test (0, 15, 100, 200, 500, and 1000 h). Based on the initial aPTE with a mass ratio of (3±0.4):1 Ni:Fe, the Fe content is continuously decreasing and reaches a final ratio of (7±0.3):1 after 1000 h, confirming the leaching of Fe. This is additionally confirmed by the analysis of the electrolyte after 1000 h of operation by ICP–MS (Table 5.1). Although the pristine electrolyte already contains Fe (50–90 µg L^{-1}), Ni (10–70 µg L^{-1}) and other trace elements (<1 µg L^{-1}), the Fe content increased at EoT to 200–400 µg L^{-1}, whereas the Ni content decreased (<3 µg L^{-1}). Fe leaching is extensively discussed in literature, but the mechanisms are not yet fully understood. For instance, under electrochemical conditions, anodic polarization leads to oxidation of the metal sites within the Ni_3Fe-LDH. It is expected that this can lead to structural or composition changes.[377] Thus, we also assume a restructuring of the catalyst due to Fe loss. Although Fe has been discussed in the literature as the active site for OER,[244,253,257,258] e.g., due to the short Fe–O bond;[244,253] in this work, the single-cell performance remains at a high level, even after long-term operation and in spite of the significant Fe leaching. Furthermore, in the literature it has been reported that the actual content and means of preparation or incorporation of the Fe^{3+} compound does not play a significant role.[253] Thus, even the low amount of Fe remaining in the catalyst structure could be sufficient for promoting the high activities recorded.

Table 5.1. ICP-MS results of the 1 M KOH electrolyte analysis before and after 1000 h of single-cell operation.

KOH	Fe / µg L^{-1}	Ni / µg L^{-1}	Fe to Ni
Pristine	93±7	73±5	1.3±0.1
Pristine	55±3	13±1	4.2±0.5
1000 h	186±5	2.2±0.6	84±23
1000 h	220±12	3.1±0.6	71±14
1000 h	420±60	2.6±0.4	161±33

The catalyst layer composition was further examined by high resolution SEM and STEM on a 250 µm FIB lamella prepared from a catalyst-coated Ni fiber (Figure 5.18a). The initial CL contains bright and dark regions: the bright regions are assigned to catalyst particles with a homogeneous Ni and Fe distribution, while the dark regions are attributed to anion-conducting binder mixed with smaller catalyst particles. Irregular catalyst particle sizes and agglomerates up to 1 µm were observed, consistent with EDS mapping, which confirmed Ni and Fe in an approximate 3:1 ratio. After 1000 h (Figure 5.18b), a sponge-like structure of the catalyst layer is recognized, which is reported for structures converting to oxyhydroxides.[106,378] Various non-PGM catalysts, especially Ni–Fe-based ones, are known for structural evolution under electrochemical conditions.[244,379] The Ni_3Fe-LDH morphological changes can be related to the influence of the surface tension of oxygen evolution bubbles that can squeeze ultrathin and flexible LDH nanosheets and significantly alter the Ni_3Fe-LDH surface morphology.[266,363] Likewise, CoO, which is electrochemically-oxidized in alkaline media, is known to undergo a considerable morphology change by breaking bigger material particles into many interconnected smaller grains under in situ electrochemical oxidation. This phenomenon fosters a well-distributed layer of small catalyst particles, creating numerous nanopores.[380] In the present case, Ni and Fe are well-distributed amongst the homogenized catalyst layer and no other agglomerates are visible. A significant film rupture was, moreover, not observed.

Ex situ HR-TEM analysis was carried out on the initial sample (Figure 5.18c 1–3), as well as after 1000 h of operation (Figure 5.18d 4–6) to further investigate the morphological evolution of the Ni_3Fe-LDH electrodes.

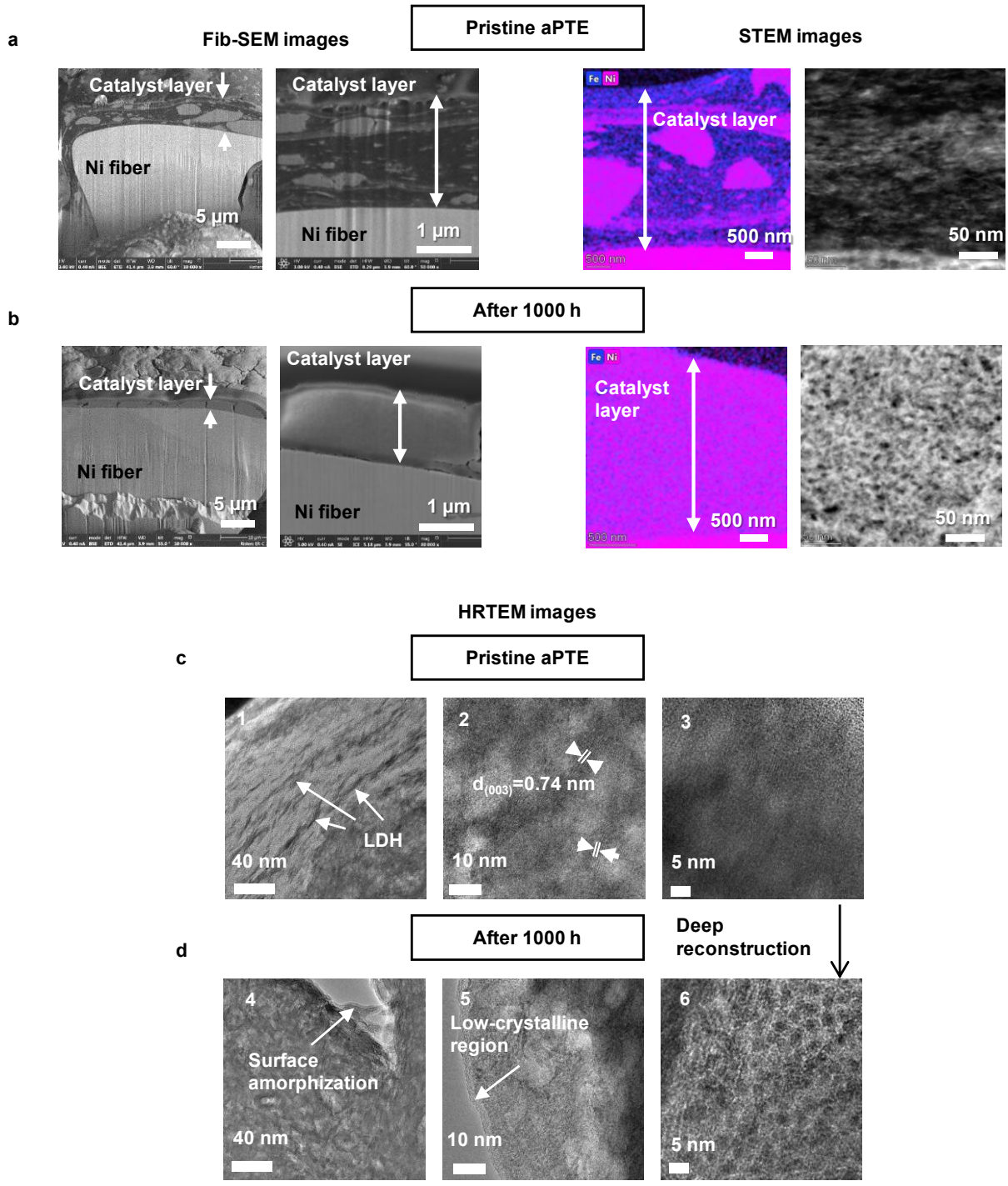

Figure 5.18. SEM images of fib-cut Ni PTL fibers coated with catalyst layers and STEM images of the catalyst layer, incl. EDS-mapping for Ni and Fe: (a) for initial (pristine) aPTE; and (b) after 1000 h; HR-TEM images of (c) initial (pristine) catalyst layer of aPTE (1-3); (d) catalyst layer after 1000 h of operation (4-6) with different magnifications.

To confirm the initial Ni_3Fe-LDH's existence and its structure on the pristine aPTE, the lattice fractions of several areas were analyzed. The darker areas of image 1 can be attributed to the stacked LDH

nano-sheets, which were previously presented in the literature.[131,327,381,382] Images 2 and 3 show the higher magnified HR–TEM images, in which the basal spacing along the c-axis of 0.74 nm and the distance of 0.19 nm are measured, corresponding to the (003) and (018) planes (Figure-A 13).[242,270,271] The calculation of lattice fractions for the sample after 1000 h is not meaningful, as those of Ni_3Fe-LDH, NiOOH and FeOOH can be recognized, whereas the values of the measured distances are too close to be clearly identified. The LDH nano-sheets are still partially visible after 1000 h (image 4), as the Ni-Fe-LDH formation is reversible. Long-term operation does not irreversibly harm the nano-sheets. The HR–TEM images (image 6) exhibit a mosaic texture with domains up to 5 nm with a large concentration of micro-strains, even more than in the initial sample. This appearance was previously reported for β-NiOOH.[383] Although the structure of the formed oxides and oxyhydroxides was claimed to be amorphous, it can be assumed that the 1000 h of aPTE presents a mixed structure of Ni_3Fe-LDH and unbound Ni- and Fe-hydroxides. Local crystallite spots are visible, whereas the outer parts of the catalyst layer after 1000 h exhibit amorphization (images 4 and 5).

5.2.3 ATOMIC AND ELECTRONIC STRUCTURE CHANGES

To understand the chemical and physical changes during 1000 h of single-cell operation, XRD, Raman, XPS and ToF-SIMS were conducted ex situ on the aPTEs. The initial aPTE has a catalyst particle size and local catalyst–binder inhomogeneity, which was further investigated with XPS and XRD.

XRD analysis

Figure 5.19 displays the XRD patterns of the Ni_3Fe-LDH aPTE directly following the fabrication process (pristine) and after 100, 200, 500 and 1000 h of single-cell operation. The initial XRD spectra provides all expected peaks for the Ni-Fe-LDH (JCPDS#40-02 15 Ni-Fe-LDH).[138,265,328] The XRD patterns of all samples display peaks at 2Θ values of ≈12°, 23°, 35°, and 60°, corresponding to (003), (006), (012), and (110) of Ni_3Fe-LDH; in addition, Ni peaks for (111) and (200) at 2Θ values of ≈44°, 50° were observed originating from the Ni PTL. No other contaminative crystalline phases were detected, indicating the high purity of the product. Minor contributions of Ni- and Fe- oxides and oxyhydroxides can however not fully be excluded due to the overlapping of the possible peaks. After 1000 h of operation, all peaks for the Ni-Fe-LDH remained. The two peaks at 11° and 23° became more intense, which originated from the overlapping of the NiFe–LDH and NiOOH peaks, because of the NiOOH species formed under electrochemical conditions. The flat shoulder-like peak at ≈25°, which is visible starting from 500 h, also indicates the presence of NiOOH species. The full distinction between individual phases that have formed in between, such as NiOOH, FeOOH, or Fe oxides, is not precisely possible, as the individual peaks overlap and therefore cannot be kept apart, as indicated by the reference pattern (Figure 5.19, bottom). The formation of mixed structures is expected as the catalyst layer structure is inhomogeneous and so gradually occurring oxidation steps are presumed. To underline this observation, Raman spectroscopy was further used.

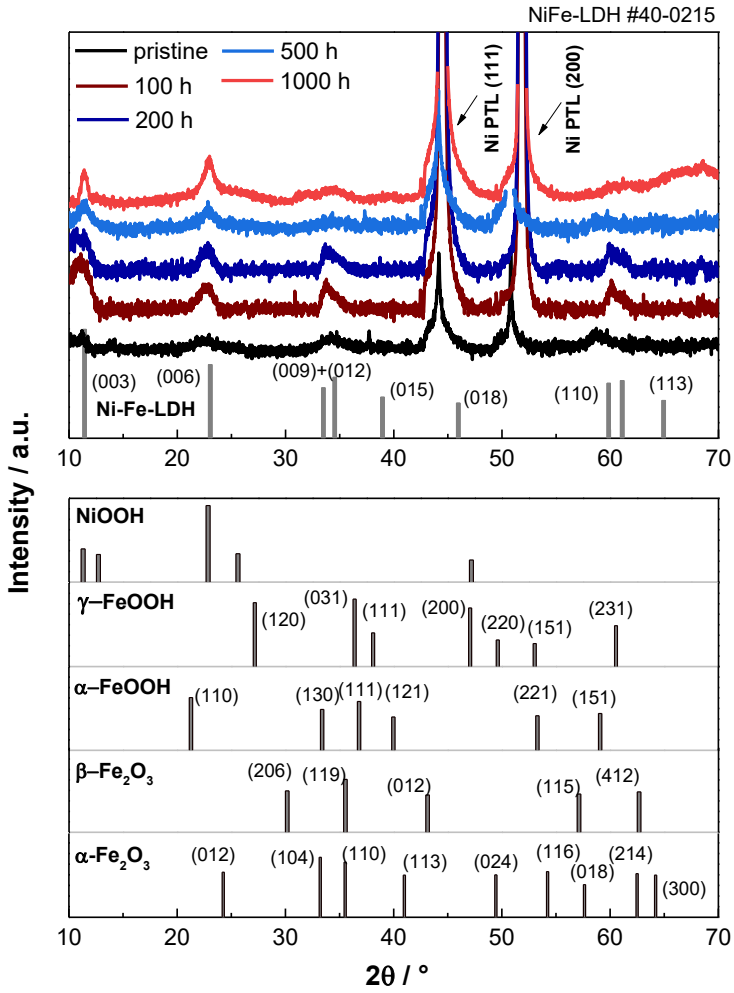

Figure 5.19. XRD patterns of the Ni_3Fe-LDH aPTE samples before and after 100, 200, 500 and 1000 h of single-cell operation, including the peaks for possibly formed Ni- and Fe-species (bottom). The analysis on all five samples was performed ex situ.

Raman spectroscopy analysis

Raman spectra of the pristine aPTEs, after 100 h, 200 h, 500 h, and 1000 h of operation, are presented in Figure 5.20. The pristine electrode shows several peaks distributed across the entire measured interval. Two overlapping bands at 420 and 460 cm^{-1}, a triple peak system at ≈510, 540, and 560 cm^{-1}, and bands around 600 up to 650 cm^{-1}, are weakly-resolved and most probably highly disturbed by possible anion-conducting binder peaks, as the binder coverage at the catalyst surface is highest for the pristine aPTE. The bands around 510, 600 cm^{-1} correspond to β-$Ni(OH)_2$, whereas the weak band around 460 cm^{-1} may come from α-$Ni(OH)_2$.[384] Broad hill-like bands around 460 and 550 cm^{-1} are attributed to the lattice vibrations of the LDH structure.[249] After 100 and 200 h of single-cell operation, the surface undergoes a major change. The formation of Ni-Fe-LDH species becomes apparent as the binder content at the surface decreases, accompanied by the emergence of characteristic bands around 460 and 530 cm^{-1}, which are characteristic for the Fe^{3+}/Ni^{2+}–O–Ni^{2+} and Fe^{3+}–O–Fe^{3+} bonds.[137,385] Usually, the peak for the intercalating CO_3^{2-} anion is observed at 670–700 cm^{-1},[327,384,386] here, a peak at 660 cm^{-1} is observed. The shift to lower wavenumbers is an indication of reduced symmetry from D_{3h} to possibly C_{2v} or C_3, as described elsewhere.[386] Minor bands at 295 and 710 cm^{-1},

which are attributed to the brucite structure, so M–O vibrations of M-OH, are also visible. After 500 h of single-cell operation, two clear peaks emerged at 480 and 560 cm^{-1}, indicating oxidation of $Ni(OH)_2$ to γ-NiOOH.[249,387] The band at 480 cm^{-1} is attributed to the polarized stretching mode A_{1g} and the 560 cm^{-1} band to the depolarized bending mode E_g of γ-NiOOH.[257] This correlates well with the R_{ct} behavior during long-term operation time, which stabilizes after 300 h, also indicating a formation of highly active species like γ-NiOOH. After 1000 h, two broad bands are observed at higher Raman shifts of 560 and 680 cm^{-1}. Here, the bands for γ-FeOOH and γ-NiOOH seem to overlap, containing signals for both species, 526 and 690 cm^{-1}[388–390] for surface γ-FeOOH and the bonds at 480 and 560 cm^{-1}, corresponding to the Ni-O bending and stretching vibrations of NiOOH. The shoulder at 700–900 cm^{-1}, corresponding to $Ni(OH)_2$ disappears. Raman analysis confirms the structural transition from NiFe-LDH to Ni(Fe)OOH. In the initial sample, the NiFe-LDH signals are partially obscured by binder coverage, whereas after 1000 h, characteristic Ni(Fe)OOH features become dominant. These results correlate well with those obtained by means of XRD.

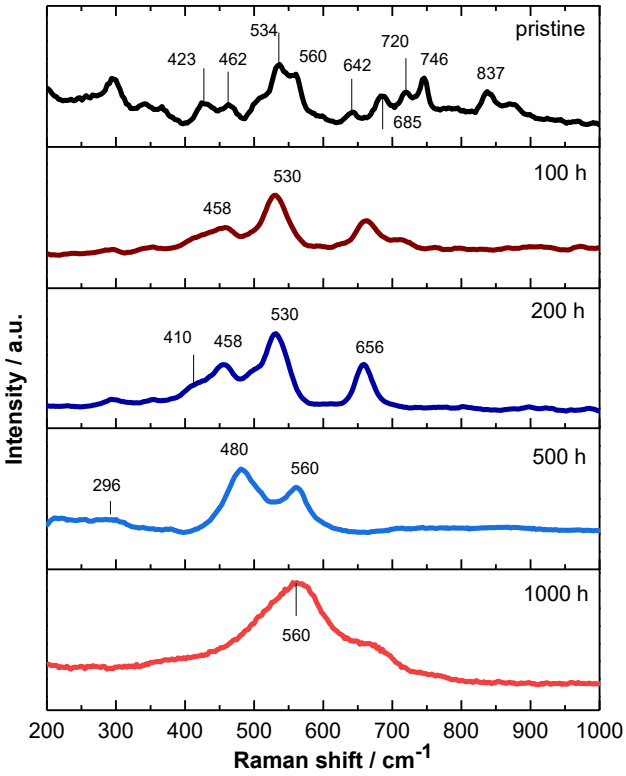

Figure 5.20. Raman spectroscopy spectra of the Ni_3Fe-LDH aPTE samples before and after 100, 200, 500 and 1000 h of single-cell operation. The analysis on all five samples was performed ex situ.

XPS analysis

XPS measurements were carried out not only to prove the elemental composition but also to analyze the surface electronic states. The XPS high-resolution spectra of Ni 2p, Fe 2p and O 1s are shown in Figure 5.21**.** For Ni 2p pristine, a spectrum of higher loaded aPTE was used, as the binder film on the aPTE surface weakened the XPS signal (Figure-A 14). The fitted peak parameters, including the

positions (binding energy) and expected formed species, are summarized in Table-A 7. Ni (Figure 5.21a) has two spin–orbit coupling doublets of Ni 2p1/2 and Ni 2p3/2. For the pristine aPTE, the fitted peaks at 854.71, 855.73, and 857.38 eV correspond to Ni^{2+} 2p3/2 and $Ni^{2+/3+}$ 2p3/2 orbitals, whereas the peaks at 860.64 eV, 861.51 eV, and 866.22 eV can be attributed to the Ni^{2+} 2p3/2 and Ni^{3+} 2p3/2 satellite peaks.

Interestingly, as can be seen in Table-A 7, the pristine sample has NiO and $Ni(OH)_2$ compounds and the catalyst layer after electrolysis operation of 1000 h shows $Ni(OH)_2$ and NiOOH species, indicating the altering of electronic configurations during electrolysis and the change in the electron density of the Ni species. The precise distinguishment between β-and γ-NiOOH is not trivial due to the subtle differences in XPS spectra.

The Fe2p spectra (Figure 5.21b) display a peak at 706.14 eV, which corresponds to the Ni auger one. The Fe 2p spectra also shows two obvious peaks located at 724.62 and 712.53 eV, which can be assigned to the Fe 2p1/2 and Fe 2p3/2 of Fe^{3+} in Ni_3Fe-LDH. The other peak at 718.64 eV can be attributed to the satellite peak. Notably, the binding energy of Fe 2p has a negative shift of 0.3 eV, suggesting that electrolysis operation can modulate the electron density and the oxidation state of Fe^{3+}, indicating that Fe exists at high valence states in LDH. The changes in O 1s spectra presented in Figure 5.21c correspond to the oxygen species of both the catalyst and anion-conducting binder. The pristine sample spectrum displays peaks at 531.55 eV and 533.45 eV corresponding to metal-OH (M-OH) and C-O-H bond peaks, mostly confirming the binder compound. After 15 h of operation, a minor additional peak at 529.95 eV related to metal-oxygen (M-O) bond is formed, matching to some detected Ni oxides, in addition to M-OH and C-O-H peaks. Up to 500 h of operation, two peaks of M-OH and M-O are presented, whereas the C-O-H peak disappears. This change could be explained by the relative reduction in the anion-conducting binder compound content, which was further supported by the ToF-SIMS analysis (see below). The 1000 h aPTE spectrum only shows one peak of the M-OH bond, which stands in good agreement with the Raman data, proving the final completed formation of metal oxyhydroxides.

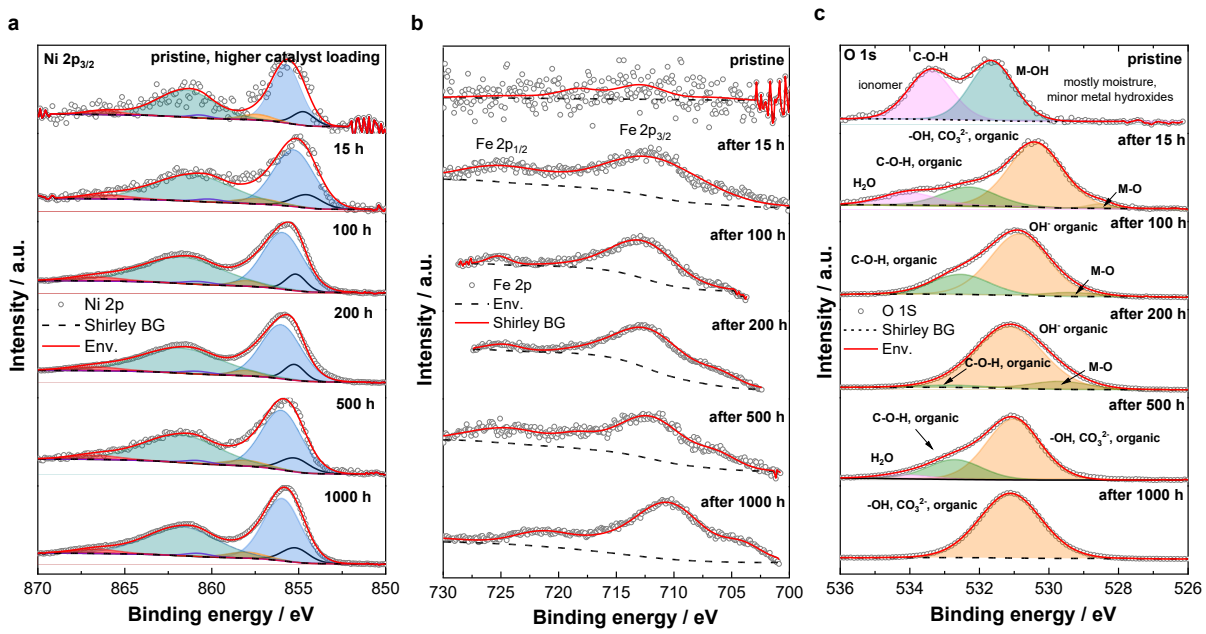

Figure 5.21. XPS high resolution spectra of (a) Ni 2p, (b) Fe 2p and (c) O 1s for the Ni_3Fe-LDH aPTE samples: pristine and after 15, 100, 200, 500, 1000 h operation. The analysis on all samples was performed ex situ.

ToF-SIMS analysis

To complement the previous data and further investigate the changes within the catalyst layer, a depth-dependent ToF-SIMS analysis was performed to prove the observation of Fe leaching and characterize changes in the anion-conducting binder distribution within the CL during 1000 h of operation. Figure 5.22 shows the results for the initial and the samples after 15, 100, 200, 500 and 1000 h of cell operation. Thereby, the catalyst layer was continuously sputtered, and the released ions were detected. The counts corresponding to Fe- or Ni-containing ions were those of the catalyst (Fe^{x+}, Ni^{x+}), whereas the C-containing ones were assigned to the anion-conducting binder. The counts are plotted against the sputtering time, where 1-3 µm of catalyst layer are removed within ~3600 s, and so up to ~10 µm of the layer are visible. For all aPTEs, Ni (orange) was observed to be nearly evenly distributed across the depth of the catalyst layer. The overall amount, indicated by the intensity, decreased insignificantly with operation time, which stands in good agreement with the morphological results described previously. Fe (blue) was found to drastically decrease from pristine aPTE to the 1000 h sample, which correlates with the EDS and ICP data presented above und underlines the partial Fe leaching out of the anode catalyst layer. Interestingly, the distribution of Fe decreases from the surface to the bulk of the layer. Fe may be supplied to the outer catalyst layer by redepositing Fe from the electrolyte, whereas only a permanent loss of Fe is possible in the inner layer. The limit of Fe leaching, as well as the recomposing mechanism in relation to catalyst structure and morphology, as well as electrolyte impurities, could be interesting topics of study in the future, but are beyond the scope of this work. The intensity for the carbon signal (C, black) was notably reduced already after 500 h of steady state operation, indicating a relative reduction in the binder compound content. Either the partial dissolution due to the given electrode structure in terms of inhomogeneous catalyst-binder

distribution or the partial delamination of surficial layers upon disassembly of the MEA can be considered as possible effects but need further investigations in the future.

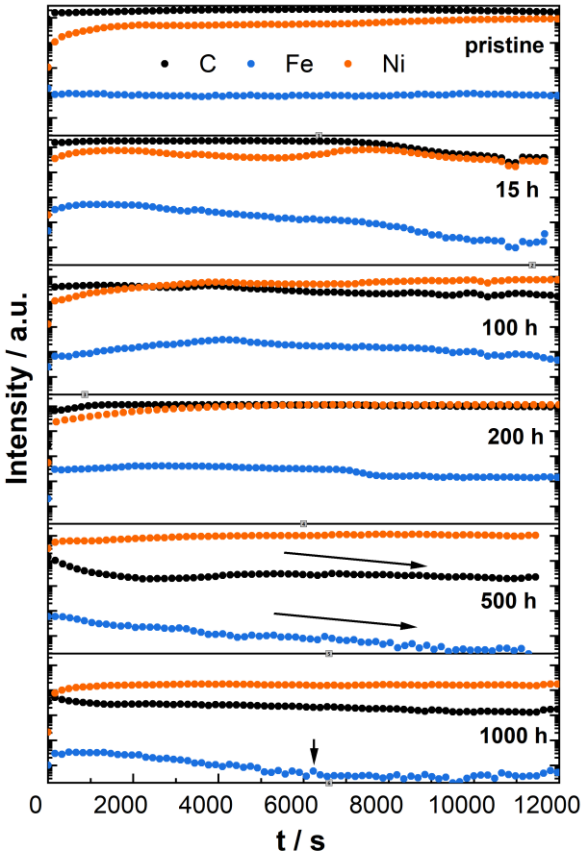

Figure 5.22. ToF-SIMS analysis results performed on the Ni_3Fe-LDH aPTE samples: pristine and after 15, 100, 200, 500, 1000 h operation. The analysis on all samples was performed ex situ.

5.2.4 SUMMARY

This study addressed Q3 (Q&A Chapter 3, Approach 2) by assessing the durability of a Ni_3Fe-LDH-based single-cell and investigating anode degradation under industrial-like conditions:

- Electrochemical characterization confirmed stable operation over 1000 h, with a minor degradation rate of 84 µV h^{-1}, significantly outperforming previously reported values. Repeated 500 h tests verified a reproducible voltage trend, including an initial 200 h break-in (or conditioning) phase.
- Deeper insights into the anode changes were obtained by a variety of analytical methods. In situ impedance spectroscopy, correlated with single-cell voltage trends, showed an initial increase in electrocatalytic activity over 200 h, followed by a slight decline. Raman spectroscopy revealed a sequential transformation of the Ni_3Fe-LDH, from Ni-Fe-LDH to γ-NiOOH, and finally to Ni(Fe)OOH, which is probably a mixture of γ-NiOOH and amorphous FeOOH.

- To disprove the possible Ni-Fe-LDH structural and elemental collapse during durability tests, EDS and STEM on the aPTE cross-sections and ICP-MS analysis of the electrolyte were performed. While elemental leaching occurred, LDH destruction was not confirmed, and a significant catalyst layer reconstruction took place without compromising significantly performance. Fe leaching, reaching 43% after 1000 h, was confirmed. XPS analysis proved Ni valence state alterations during electrolysis, while ToF-SIMS revealed continuous anion-conducting binder release and indicated surface Fe enrichment alongside bulk leaching. Typically, these findings were made at the laboratory scale in a three-electrode cell setup, which is usually insufficient to be compared with a real-world single-cell.[106] Nonetheless, the leaching behavior presented in this work was consistent with the one reported in literature.
- The study linked morphological and chemical changes in the Ni_3Fe-LDH anode to the electrochemical behavior of the single-cell, correlating oxidation state evolution with internal resistance variations (R_{Ohm} and R_{ct}).
- Post-mortem HR-TEM analysis confirmed that while the catalyst retained recognizable LDH nanosheets, a mixed crystalline-amorphous structure emerged. SEM analysis between 500 h and 1000 h further revealed extensive catalyst layer reorganization, attributed to oxyhydroxide formation and the development of crystalline mixed phases. Despite partial crack formation, no significant catalyst layer detachment was observed after long-term operation.

The potential influences of the cathode side, as well as changes in the PTL supports and AEM, could ideally be considered, but this would be beyond this work's scope. The leaching of Fe, reduction of the anion-conducting binder compound, and the morphological reconstruction of the catalyst layer were observed to occur during the 1000 h operation under industrial conditions.[19,288] Taking all of these factors into account, the Ni_3Fe-LDH-based aPTE exhibited highly promising results.

5.3 Enhanced AEMWE Performance through Catalyst Milling and Layer Design

Single-cell performance depends not only on the catalyst activity and stability, but also on the availability of active sites within the electrode. CL design is therefore critical: reaction kinetics and ion transport are strongly governed by CL morphology, which is set during powder processing and CL fabrication. Optimizing Ni-Fe-LDH inks through controlled dispersion and improved electrode fabrication increases catalyst utilization by promoting uniform catalyst–binder distribution and enlarging triple-phase boundaries, where the electrochemical reaction occurs[18,143] Properly dispersed catalysts limit agglomeration, improve ionic pathways and mass transport, and can reduce charge-transfer resistances while enhancing durability.[391–394]

Having established long-term stability of the Ni_3Fe-LDH in a single-cell and thoroughly investigated anode degradation (Chapter 5.2), the next step is to improve performance and reproducibility. This chapter investigates scalable processing routes, such as tumbler ball milling, roller bench milling, and dispersion control, to tune particle size distribution and surface accessibility, thereby improving Ni_3Fe-LDH-based single-cell performance and process reliability.

5.3.1 Catalyst Quality Control and Reproducibility: Structural and Particle Size Analysis

This chapter examines the impact of catalyst milling on the Ni_3Fe-LDH powder by analyzing structural and morphological changes at different scales. TEM is used to investigate nanoscale modifications, while SEM assesses particle clustering at the microscale. Additionally, BET analysis determines the geometrical surface area, and the hydrodynamic diameter (D_H) of such clusters is analyzed by DLS. The study compares three catalyst types: the as-synthesized initial catalyst (i-NiFe-LDH)[5], the catalyst treated by tumbler ball milling for 15 h (mTM-NiFe-LDH) and the one milled on a roller bench for 48 h (mRB-NiFe-LDH).

[5] The catalyst, which was used in the previous studies and chapters, is referred to here as i-NiFe-LDH.

TEM imaging

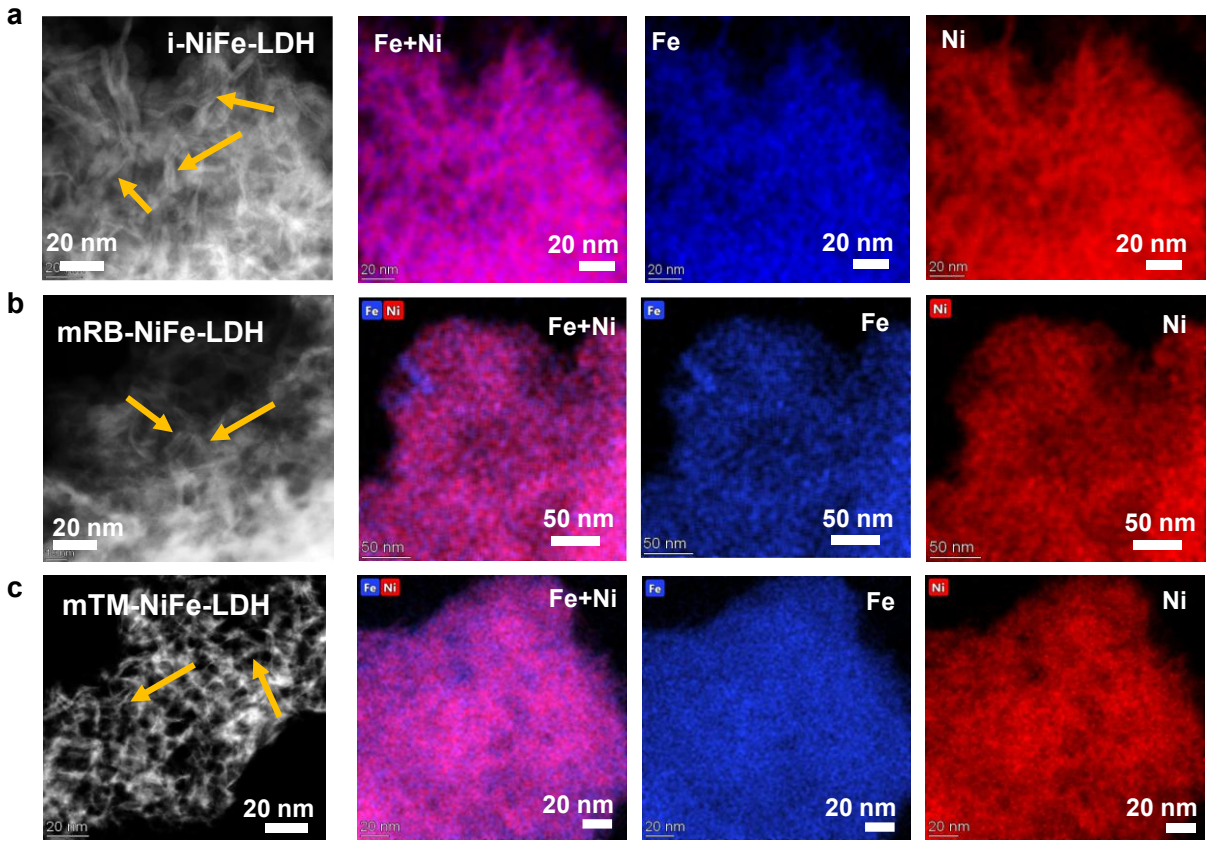

Figure 5.23. Changes on catalyst particle level upon milling. STEM images, including EDS mapping of (a) initial (i-NiFe-LDH) and the two milled catalyst powders (b) mRB-NiFe-LDH and (c) mTM-NiFe-LDH. For the EDS mapping, the Ni+Fe mix is shown in pink, Fe in blue, and Ni in red.

To confirm the preservation of the LDH structure of the milled catalysts, TEM analysis was performed. Figure 5.23a shows the structures of the i-NiFe-LDH powder with the corresponding EDS mappings for Ni (blue), Fe (red) and mixed Ni:Fe (pink) and those of the milled catalysts mRB-NiFe-LDH (Figure 5.23b) and mTM-NiFe-LDH (Figure 5.23c). All three TEM images confirm the presence of the LDH nanosheets, revealing the characteristic stacked nanosheets known from literature.[131,269,395] EDS mappings of the catalyst powders do not reveal any differences either in the Ni to Fe distribution or in the elemental atomic ratio. For i-NiFe-LDH powder, 74 at% Ni and 26 at% Fe were analyzed, while 75 at% Ni and 25 at% Fe were found for mRB-NiFe-LDH and 76 at% Ni and 24 at% Fe were detected for mTM-NiFe-LDH. These findings confirm that the milling process did not alter the LDH sheet structure or disrupt the elemental homogeneity of the catalyst.

SEM imaging

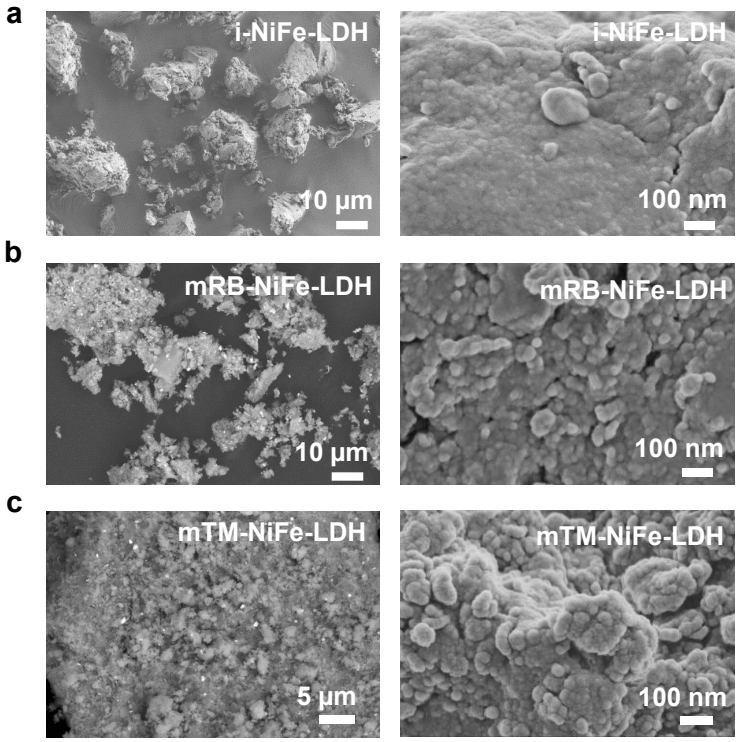

Figure 5.24. SEM images of the catalyst powders at x1k (left images) and x100k (right images) magnification for (a) i-NiFe-LDH; (b) mRB-NiFe-LDH and (c) mTM-NiFe-LDH.

Figure 5.24a presents the SEM images of the i-NiFe-LDH catalyst agglomerates, Figure 5.24b and c show the finer catalyst powders resulted after milling for mRB-NiFe-LDH and mTM-NiFe-LDH, respectively. Directly after synthesis, the catalyst agglomerate size is non-uniform and exhibits a broad distribution. Starting from nanometer-scale agglomerates, the particles grow to sizes of 1 µm and even 100 µm as presented in Figure-A 15. Based on previous observations made in this study, larger particles of the initial catalyst are not fragmented or broken down during the catalyst ink dispersion process alone (Chapter 5.2–5.1). After milling, the fine powders obtained for both mRB-NiFe-LDH and mTM-NiFe-LDH are predominantly disaggregated and non-compacted (Figure 5.24b and c, left images), and the resulting clusters show a size of 100-300 nm with minor units of down to 30 nm (Figure 5.24b and c, right images).

BET analysis

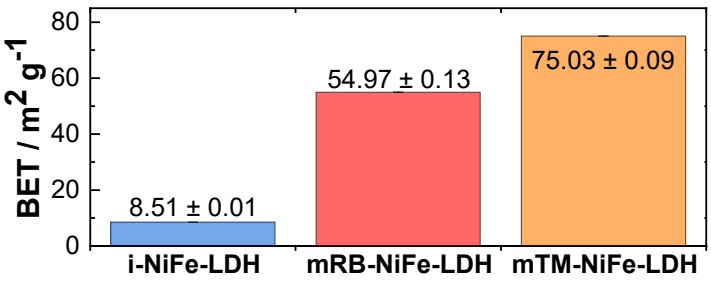

Figure 5.25. BET analysis results, presenting the surface area of the initial i-NiFe-LDH (blue) and milled catalysts mRB-NiFe-LDH (red) and mTM-NiFe-LDH (orange).

To evaluate the geometrical surface area of the three different catalyst powders, BET analysis was conducted. To guarantee the accuracy and reproducibility of the measurements, three separate batches of each powder type were analyzed. As shown in Figure 5.25, the catalyst milling, regardless of the method used, significantly increased the geometrical surface area of Ni_3Fe-LDH. The surface area increased from 8.51±0.01 m^2g^{-1} for the unmilled powder to 54.97±0.13 m^2g^{-1} for the mRB-NiFe-LDH, and further to 75.03±0.09 m^2g^{-1} for the mTM-NiFe-LDH. This significant enhancement from a 6.5 to 8.8-fold increase aligns with the expected outcome of the milling process, which reduces the size of the agglomerates, thereby exposing more surface area. This enlargement in the surface area suggests an increase in the quantity of active sites that are accessible for catalytic reactions, a crucial aspect for enhancing the catalyst's overall efficiency.

DLS analysis

To determine the hydrodynamic diameter (D_H) of the powders, DLS measurements were performed. Reproducibility of the particle-size distributions was verified by repeating the measurements on three independent catalyst batches for each powder type. The resulting agglomerate/cluster sizes, reported as D_H with corresponding size distributions and error bars, are shown in Figure 5.26.

The i-NiFe-LDH powder demonstrated a bimodal particle size distribution (Figure 5.26a), with peaks occurring approximately at D_H of 400 nm and 6000 nm. 48 h of catalyst milling on a roller bench resulted in a reduction of the D_H and transformed the initially bimodal size distribution to a nearly unimodal pattern, though with some outliers at both higher and lower D_H values (Figure 5.26b). For the mTB-NiFe-LDH catalyst milled in a tumbler mixer (Figure 5.26c), a unimodal D_H size distribution was achieved. Thus, the milling process not only shifted the D_H to lower values, but it moreover narrowed and changed the size distribution curve from a bimodal distribution to a unimodal one.

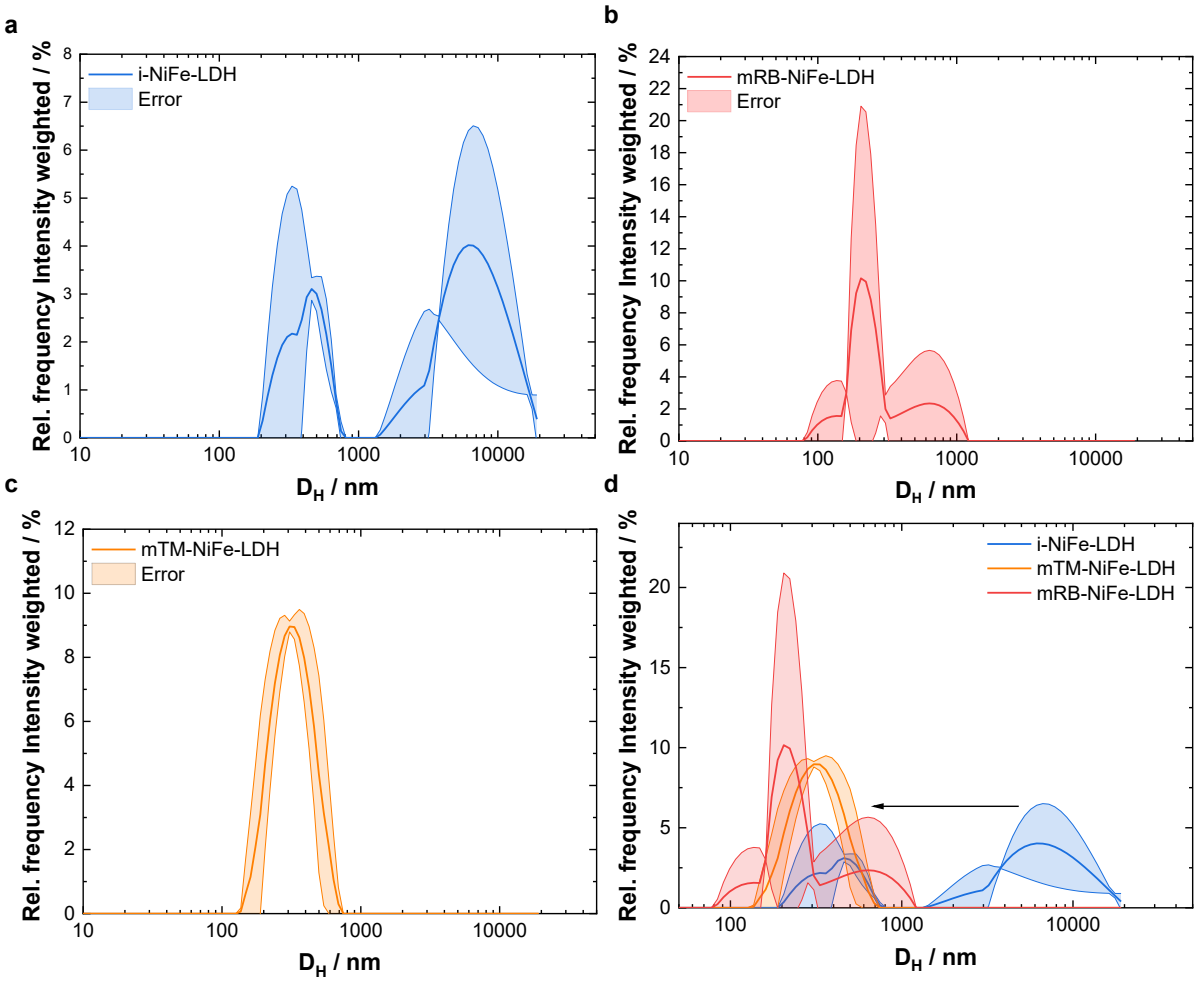

Figure 5.26. DLS results of (a) the initial i-NiFe-LDH (blue); (b) milled mRB-NiFe-LDH (red); (c) milled mTM-NiFe-LDH catalyst powders in DI H_2O without additional dispersion treatment, presenting the distribution of the clusters' hydrodynamic diameter (D_H), incl. the corresponding error areas; (d) comparison of the diameter distributions: milling narrowed and shifted the size distribution towards unimodal single peak distribution.

Considering the peak positions of all distributions, the averaged D_H are presented in Figure 5.27. The as-synthetized i-NiFe-LDH powder shows a D_H of 2564±779 nm. After milling, the D_H decreases to 355±21 nm for mRB-NiFe-LDH and to 341±52 nm for mTM-NiFe-LDH, corresponding to a 7.5-fold reduction for mTM-NiFe-LDH relative to the as-synthesized powder. In addition, milling improved size reproducibility, as reflected by the smaller error bars (shaded areas).

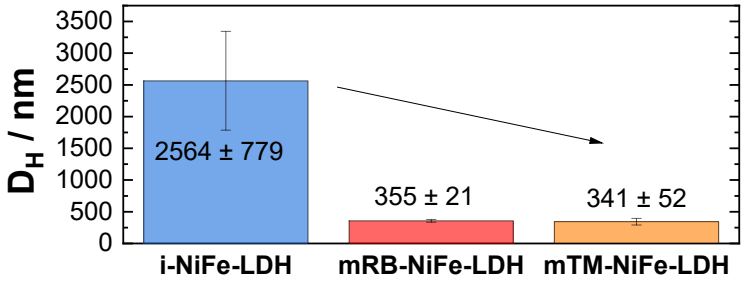

Figure 5.27. Hydrodynamic diameter (D_H) values of of the initial i-NiFe-LDH (blue) and milled catalysts mRB-NiFe-LDH (red) and mTM-NiFe-LDH (orange) obtained on catalyst dispersed in DI H_2O.

These experiments provide a reference for future DLS analysis of catalyst inks containing solvents and binders. The comparison of cluster sizes and distributions highlights the TM method as the most effective. This process significantly reduced D_H values and resulted in a more refined and uniform particle size distribution, making it the preferred milling approach.

5.3.2 CHEMICAL CHARACTERIZATION OF THE MILLED CATALYSTS

Next, the effect of catalyst milling and whether milling affects the catalyst's surface composition, crystalline structure, chemical environment, phases and presence of impurities or defects were investigated.

XRD analysis

Heat generation and accumulation during milling, caused by friction between the catalyst powder and grinding balls as well as within the powder, can induce structural changes in the LDH structure, potentially leading to partial or complete collapse.[396,397] To test this, the structural characteristics of i-NiFe-LDH, mRB-NiFe-LDH, and mTM-NiFe-LDH were investigated by XRD analysis (Figure 5.28).

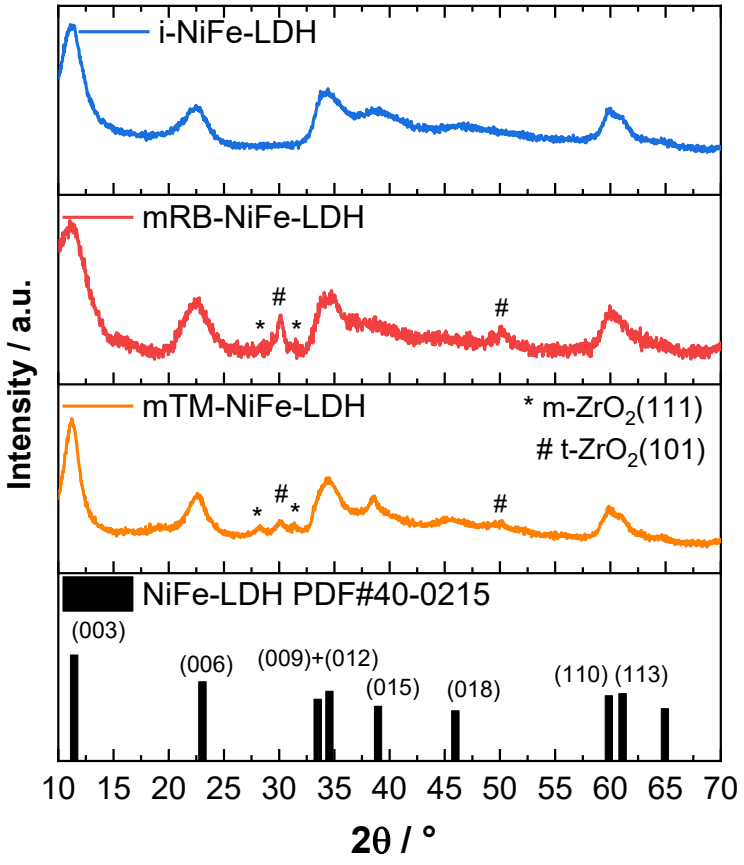

Figure 5.28. XRD profiles of the initial i-NiFe-LDH (blue) and milled catalysts mRB-NiFe-LDH (red) and mTM-NiFe-LDH (orange), incl. the characteristic XRD diffraction spectra for Ni-Fe-LDH. Peak markers (*, #) highlight contributions from ZrO_2, assigned to the monoclinic (*) and tetragonal (#) phases.

The main characteristic peaks for Ni-Fe-LDH at 2Θ values of ≈12°, 23°, 35°, 60° corresponding to (003), (006), (012), and (110) lattice planes (JCPDS#40-02 15 Ni-Fe-LDH), respectively, are observed for all catalyst powders.[138,265,328] For both milled catalysts, a minor amount of abrasion leftovers of ZrO_2 was detected at 27° and 33° for monoclinic m-(111) and at around 50° for the tetragonal t-(101) ZrO_2.[398] The decreased intensity of ZrO_2 peaks in the mTM-NiFe-LDH sample suggest that tumbler ball milling, in contrast to using a roller bench, is a more effective milling method, especially when combined with a shorter milling duration. As ZrO_2 is not OER active, its minor contamination in the milled samples is unlikely to impact their catalytical performance. However, further refinement of the grinding process is needed to avoid such grinding ball abrasion in future. Importantly, no changes in catalysts' structure, phase, crystallinity, or purity were detected. Considering these results and the observations obtained from TEM images, it can be concluded that the LDH structure did not experience significant changes following the milling treatment.

Raman spectroscopy analysis

Raman spectroscopy was performed to complement the results of XRD (Figure 5.29).

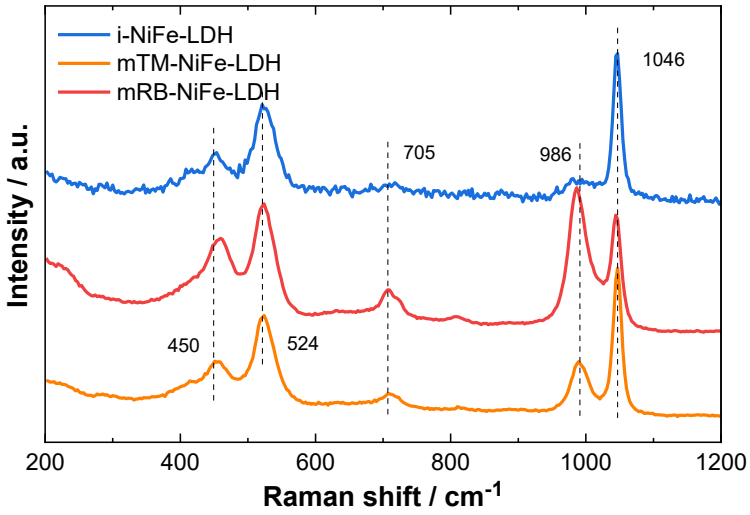

Figure 5.29. Raman spectra of the initial i-NiFe-LDH (blue) and milled catalysts mRB-NiFe-LDH (red) and mTM-NiFe-LDH (orange).

Raman spectra of i-NiFe-LDH showed the characteristic bands at ≈450 and ≈524 cm^{-1} (Fe^{3+}/Ni^{2+}-O-Ni^{2+} and Fe^{3+}-O-Fe^{3+})[137,385], consistent with the assignments discussed in the previous Chapter 5.2. Minor bands at ≈705 cm^{-1} (Ni^{II}-O-H[399]) and ≈986 cm^{-1}, and ≈1046 cm^{-1} (residual NO_3^- and interlayer CO_3^{-2}/NO_3^-) were also observed. [270,387] For all samples, the peak intensity ratio ≈450 cm^{-1}/≈524 cm^{-1} is unchanged,[104,400] indicating that milling did not affect the bond lengths.

After milling, the intensity ratio of the ≈986 and ≈1046 cm^{-1} bands (interlayer anions) shifts, with the ≈986 cm^{-1} band becoming more pronounced. Because Raman intensities depend on factors such as polarizability and concentration of active groups, this suggests a milling-induced change in the NO_3^- response rather than a compositional change. Consistent with the unchanged XRD patterns, the data indicates that milling affects interlayer-related spectral signatures without fundamentally altering the catalyst's bulk structure.

XPS analysis

XPS analysis was performed to investigate the chemical composition, and possible changes in the oxidation states and electronic structures of all three catalysts. Previous studies have indicated that ball-milling enhances the binding strength of the oxygenated intermediates of Ni-Fe-LDH and to shift the electron-equilibrium states towards more electron-rich structures.[138]

In contrast to the XRD data, which represents the bulk sample, the XPS data, reflecting a local spot within the catalysts' batch only, indicates a negligible presence of ZrO_2 abrasion, as shown in the survey spectra in Figure 5.30a.

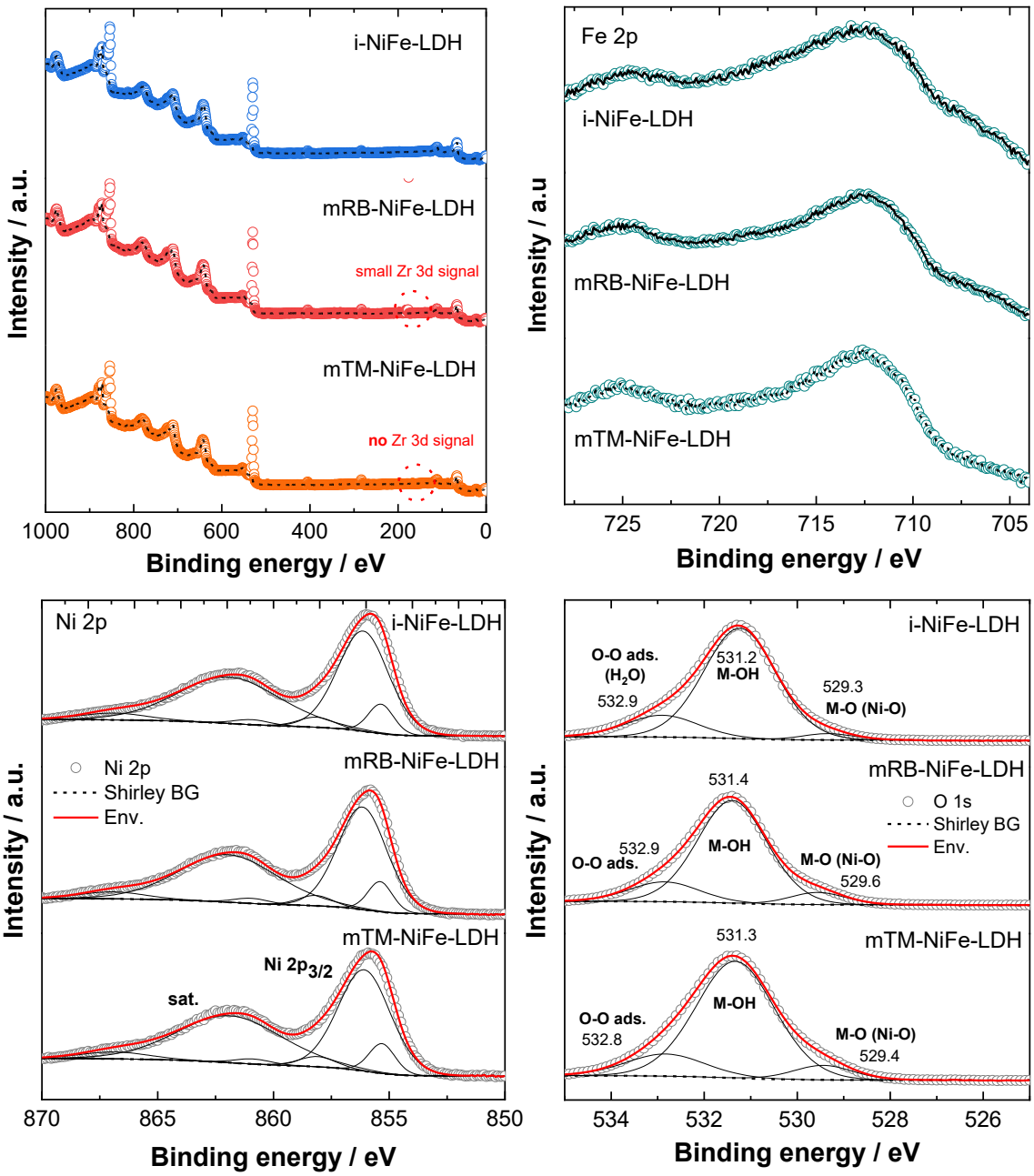

Figure 5.30. (a) XPS survey; (b) high-resolution XPS spectra of Fe 2p; (c) of Ni 2p and (d) of O 1s for the i-NiFe-LDH, mRB-NiFe-LDH and mTM-NiFe-LDH.

The high-resolution spectra of Fe 2p (Figure 5.30b) shows the characteristic peaks for Fe^{3+} in Ni_3Fe-LDH at ≈724.8 eV and ≈712.4 eV, corresponding to Fe 2p1/2 and Fe 2p3/2, respectively. In all three powder samples, Ni exhibits the two spin-orbit coupling doublets of Ni 2p1/2 and Ni 2p3/2 (Figure 5.30c). The O 1s spectra (Figure 5.30d) displays a minor presence of an M-O oxide at 529.3 eV, a hydroxide M-OH (Ni^{2+}-, Fe^{3+}-hydroxide) at 531.3 eV and the adsorbed water at 532.8 eV. No significant differences were found in the high-resolution spectra between the pristine and the milled catalyst samples, indicating no impact on oxidation states or electronic structure.

5.3.3 CATALYST DISPERSION CONTROL

This chapter presents the characterization of catalyst dispersions prepared from the initial powder and the two milled powders in various dispersion media (DM). The aim is to identify ink formulations with improved stability and homogeneity relative to the standard EtOH:H_2O (1:1) mixture ("baseline ink"). First, ELS measurements (*ζ*-potential) establish a reference by assessing the surface charge and colloidal stability of the catalyst and polymeric binder in DI H_2O. The study then examines catalyst–DM interactions via stability lifetime tests and evaluates the impact of binder addition. Ink properties are quantified by ELS and DLS (D_H). Finally, cluster-size distributions and reproducibility are compared between the baseline ink and the optimized formulations.

Dispersion stability by ELS analysis

A comprehensive characterization of dispersions, especially those with complex structures like LDHs and added anion-conducting binder, typically involves analyzing solid material concentrations, pH values, size, shape, and spatial arrangement of components,[14,291] as well as agglomeration and ζ-potential. However, this study does not cover such extensive analysis due to the incomplete knowledge of the binder's preliminary structure and properties. The morphological behavior of the polymer, such as clustering and micelle formation in various solvent concentrations (like water volume fraction in dispersion), similar to what is observed with Nafion,[401–403] is not explored here.

Instead, the focus is on a thorough investigation of the polymer's ζ-potential, considering the electrophoretic mobility of the polymer chains, while keeping the dispersions' pH values at 6.7±0.2. The dispersion control effort in this section is an additional means to enhance and facilitate ink stability and CL fabrication.

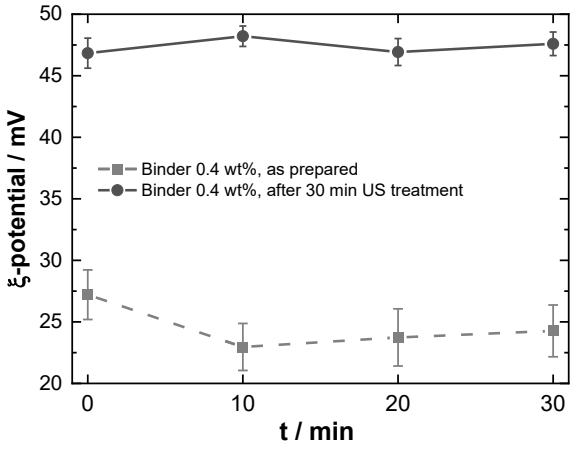

Figure 5.31. ζ-potential values of the as-prepared anion-conducting binder and after additional 30 min of ultrasonic dispersion treatment, within 30 min dwell time.

Figure 5.31 shows the ζ-potentials of the diluted anion-conducting binder (0.4 wt%), in the initial as-dissolved state and after 30 min of ultrasonic horn treatment. The anion-conducting binder presented a positive *ζ*-potential of 27±2 mV after being dispersed, which decreased to 24±2 mV after 30 min. Following the ultrasonic treatment of 30 min, an elevated stability of the binder dispersion was

achieved as indicated by the increased ζ-potential of 47±1 mV. The latter parameter holds greater significance, as it reflects the factual condition of the binder in the resulting electrocatalyst dispersion. The positive ζ-potential values of the anion-conducting binder meet the expectations, as the binder used contains positively charged cationic moieties. Values of 23 to 27 mV and even of 47 mV highlight a relatively high local charge density along the polymer chains,[401] especially for a low-concentrated binder dispersion of 0.4 wt%. For comparison, Nafion dispersions usually show ζ-potential values close to 30 mV (absolute value) at concentrations not lower than 8 wt% solids.[401] In general, ζ-potential values above 30 mV are considered to prove strong repulsive forces of the dispersed particles, enough to prevent agglomerate formation, which is essential for a stable dispersion.[404,405] The higher the ζ-potential value, the more stable is the dispersion.

To set a baseline for the i-NiFe-LDH and the selected mTM-NiFe-LDH, the ELS analysis was conducted on the plain powders, dispersed for 30 min in DI H_2O and within 30 min dwell time (Figure-A 16). The ζ-potentials of 35±1 mV for the i-NiFe-LDH and 43±1 mV for the mTM-NiFe-LDH indicate the positive charge of the catalyst clusters. Notably, while the mTM-NiFe-LDH exhibited enhanced stability in DI H_2O, both catalysts maintained their stability for a duration of at least 30 min.

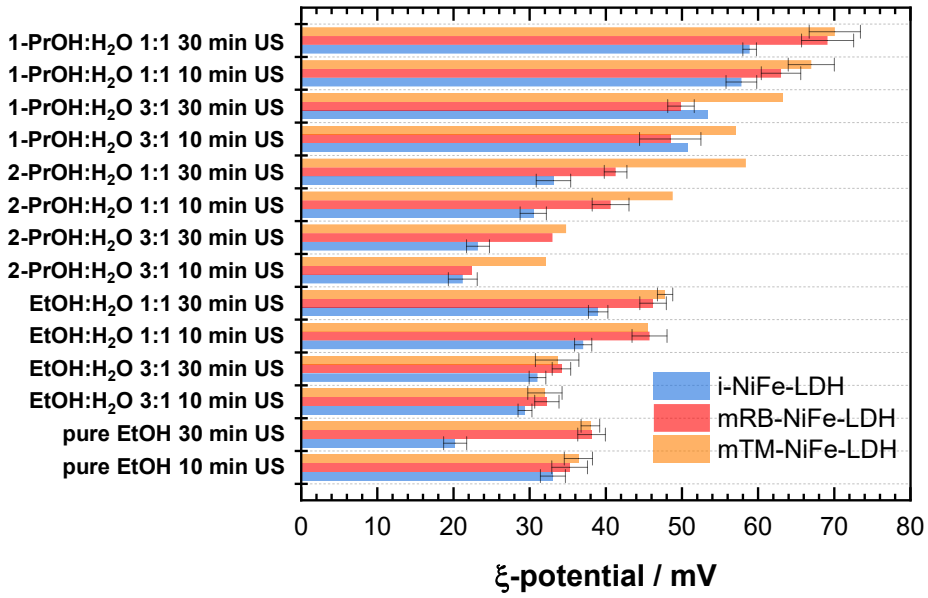

Figure 5.32. ζ-potential values of all catalyst dispersions with i-NiFe-LDH, mRB-NiFe-LDH and mTM-NiFe-LDH, and varied dispersion media (DM) and ultrasonic dispersing times of 10 or 30 min; no binder was added to dispersions.

Further, the stability of the as-prepared catalyst dispersions without binder, determined by varied DMs and ultrasonic dispersing times of 10 or 30 min, was assessed (Figure 5.32). The varying lengths of the bars show that all factors, as catalyst type, DM, and dispersing time, impact ink stability. The inks based on the milled catalysts show consistently a higher ζ-potential value. In general, the longer dispersing time of 30 min leads to higher ink stability than after 10 min, although the enhancement is smaller in comparison to a changed DM. The highest stability was observed for both mRB-NiFe-LDH and mTM-NiFe-LDH in 1-PrOH:H_2O 1:1 after 30 min of dispersing, reaching a ζ-potential value of 70±3 mV.

In contrast, the baseline DM composition (EtOH:H_2O 1:1, 30 min dispersing) delivered a value of 48±1 mV for the mTM-NiFe-LDH dispersion, and 46±2 mV for mRB-NiFe-LDH. The standard dispersion based on the i-NiFe-LDH showed a ζ-potential of 39±1 mV. For further comparisons and discussions, the focus shifted therefore to the most stable dispersions (mRB-NiFe-LDH and mTM-NiFe-LDH dispersed in 1-PrOH:H_2O 1:1 for 30 min and including the binder), while the baseline ink (EtOH:H_2O 1:1, 30 min dispersing) was used as a comparative standard. The ζ-potential values for all other inks are summarized in Table-A 8.

Since both milled catalysts exhibited similar ζ-potential values, with mTM-NiFe LDH showing better ink stability for some DM, together with the previously identified better size distribution, further experiments focus on comparing inks based on i-NiFe LDH and mTM-NiFe LDH.

To investigate the influence of the binder on the stability of the selected catalyst dispersions, further ζ-potential measurements on selected inks were performed (Figure 5.33).

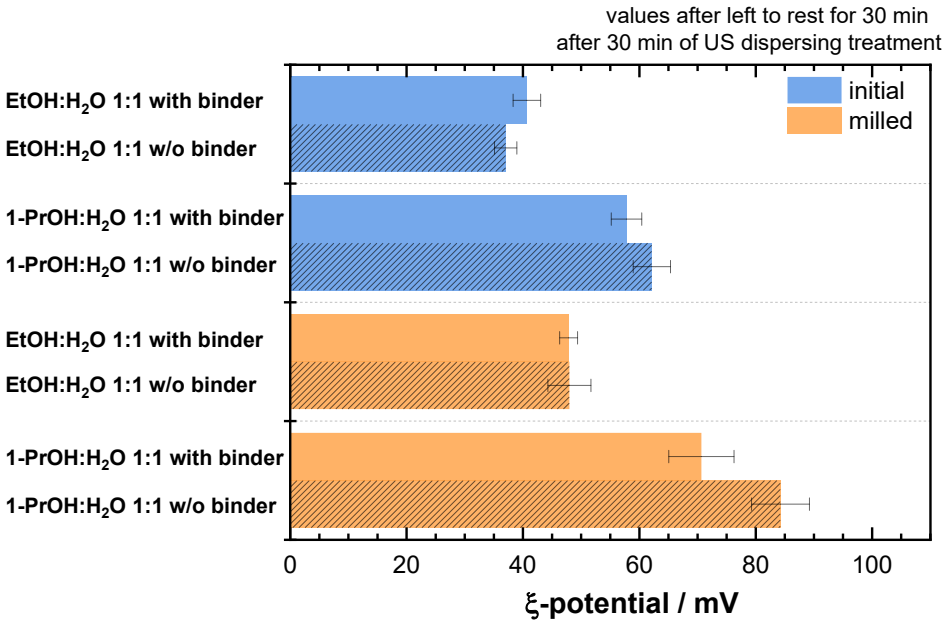

Figure 5.33. ζ-potential values of different catalyst inks with and without added binders, left to rest for 30 min after a 30 min ultrasonic dispersing treatment.

The ζ-potential values (Figure 5.33) are recorded 30 min after dispersion to compare the stability of the eight ink formulations; full time-resolved data are provided in the Appendix. Figure-A 17a tracks binder-free dispersions over the first 30 min, while Figure-A 17b shows that ζ-potential remains essentially constant for binder-containing inks over 120 min, indicating sufficient stability for electrode fabrication. Notably, 1-PrOH:H_2O 1:1 dispersions are more stable than EtOH:H_2O 1:1, possibly because 1-PrOH promotes a more effective interfacial solvation environment and thus a more extended electrical double layer around the particles. With the binder addition, the ζ-potential decreases (Figure 5.33 colored vs. dashed bars). Typically, the addition of a binder to the ink is expected to increase the stability of the dispersion by providing an additional repulsive force amongst the particles in the shape

of steric hindrance. In general, the decrease of the ζ-potential (in absolute values) reveals weaker electrostatic interactions.[406] Such an effect is often associated with the absence of complete polymeric binder adsorption among the catalyst particles.[401,407,408] Another possible reason for this could be the formation of polymer bridges between the chains, which were indeed adsorbed by the particles.[409] Overall, the results highlight the non-trivial interplay between binder, particles, and dispersion medium. To complement these results, the four binder-containing inks were assessed by visual stability inspection (Figure-A 18). The mTM-NiFe-LDH-based inks show no sedimentation after 12 h, whereas both i-NiFe-LDH-based inks exhibit pronounced agglomeration and sediment formation.

Cluster size analysis by DLS analysis

DLS was performed to evaluate the reproducibility of the formed particle cluster sizes and their distribution within the chosen dispersions. For the tests, each of the studied inks was diluted 50-fold, achieving a solid content of 0.04 wt%. This dilution follows established DLS methodology, as particle-size determination is more reliable at sufficiently low concentrations.[292]

Earlier, DLS analysis was conducted on the bare catalyst particles to establish a reference for the expected cluster sizes and size distributions. For the anion-conducting binder, preliminary experiments have shown that pure binder dispersion cannot be reliably detected using DLS, even at varying solid concentrations. This may be due to changes in the polymer state, such as dynamic molecular movements. Consequently, it is expected that the measured D_H values for the ink samples only reflect the catalyst particles.

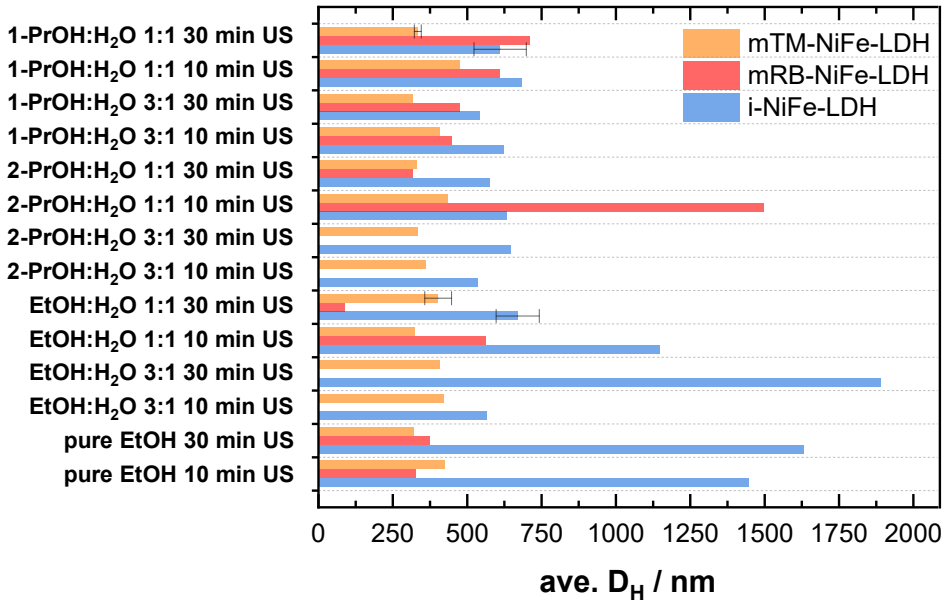

Figure 5.34. Average hydrodynamic diameter (D_H) values for the i-NiFe-LDH, mRB-NiFe-LDH and mTM-NiFe-LDH catalyst powders obtained in 50-fold diluted catalyst inks (including the binder and varied DM, and dispersing times).

D_H was measured for all chosen catalyst dispersions, revealing consistently lower values for milled catalyst-based inks compared to the initial catalyst-based inks (Figure 5.34). As the D_H (and the

double-layer size) of the particles are affected by the DM used, differences in the values obtained here (Figure 5.34) to those measured in DI H_2O (Figure 5.26, Figure 5.27) are reasonable. The D_H values for inks based on i-NiFe-LDH exhibit significant variability, especially in EtOH-based DMs. There is some correlation with the ζ-potential values, where larger particles, causing sedimentation and agglomeration within the dispersion, result in low stability for pure EtOH and EtOH:H_2O 3:1 inks.

To focus on the reproducibility of catalyst cluster sizes and size distribution, three DLS measurements for each catalyst type (i-, mRB-, and mTM-NiFe-LDH) were performed on the chosen inks based on 1-PrOH:H_2O 1:1 and the baseline inks based on EtOH:H_2O 1:1 (Figure 5.35). For dispersions based on the initial catalyst (Figure 5.35a and b), a partial bimodal distribution with additional peaks at higher sizes, indicating agglomeration, was observed. Conversely, both milled catalyst-based inks (Figure 5.35c-f) demonstrated a nearly unimodal distribution with notable size distribution reproducibility, especially for the 1-PrOH:H_2O 1:1 ink. Cluster sizes for the i-NiFe-LDH catalyst of ≈670 nm in the EtOH:H_2O 1:1 ink and 610 nm in the 1-PrOH:H_2O 1:1 DM, were reduced to 328 nm and 334 nm for the mRB-NiFe-LDH and 402 nm and 332 nm for the mTM-NiFe-LDH, respectively, in the corresponding solutions.

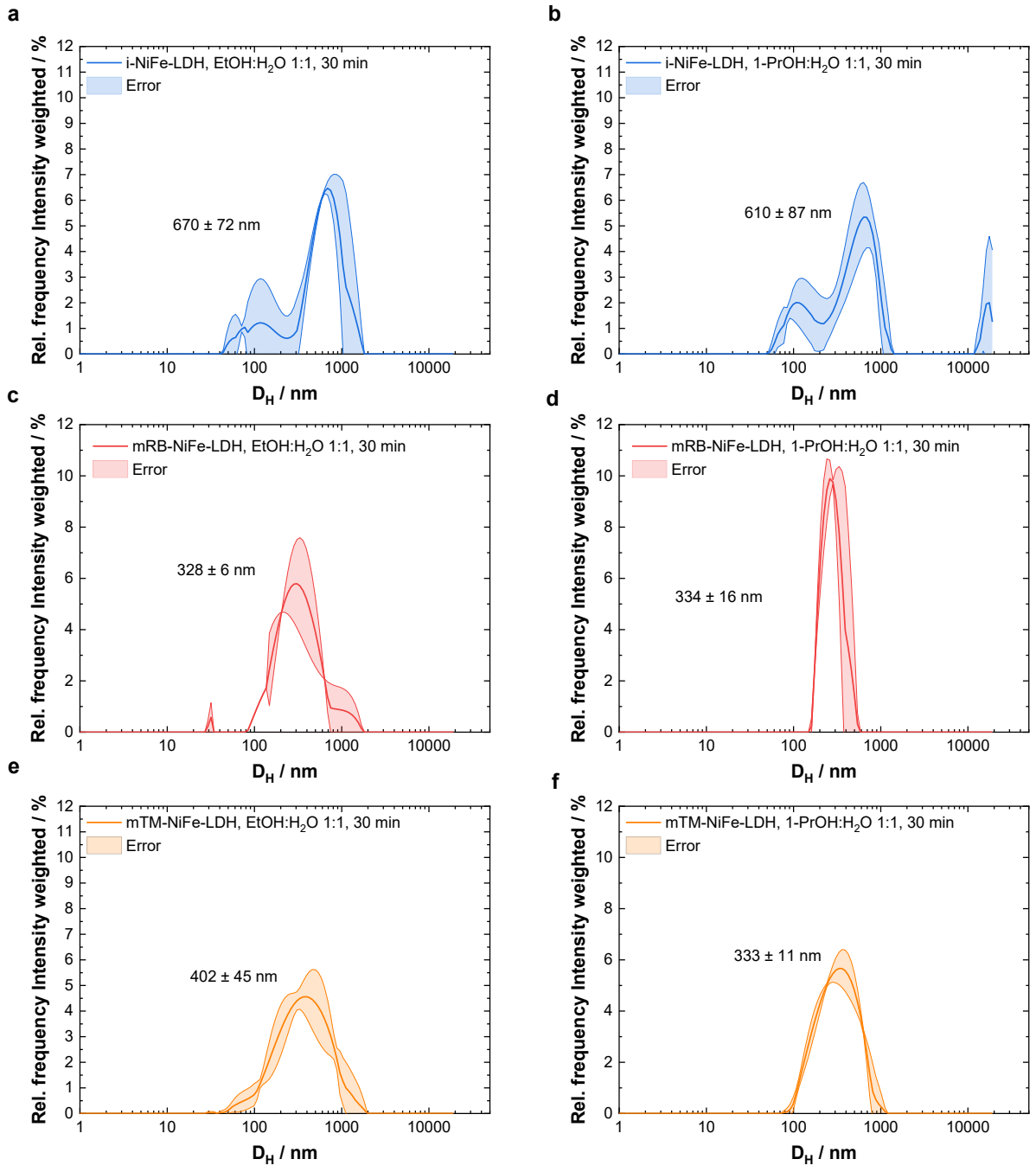

Figure 5.35. Catalyst cluster size distribution for inks including the anion-conducting binder and after 30 min of ultrasonic dispersion treatment: (a) i-NiFe-LDH in EtOH:H_2O 1:1, (b) i-NiFe-LDH in 1-PrOH:H_2O 1:1, (c) mRB-NiFe-LDH in EtOH:H_2O 1:1, (d) mRB-NiFe-LDH in 1-PrOH:H_2O 1:1, (e) mTM-NiFe-LDH in EtOH:H_2O 1:1, (f) mTM-NiFe-LDH in 1-PrOH:H_2O 1:1.

Based on these results, mTM-NiFe-LDH dispersed in 1-PrOH:H_2O 1:1 using an ultrasonic horn for 30 min is selected for electrode fabrication due to its increased ink stability and reproducibility. Electrodes prepared from the baseline ink (i-NiFe-LDH in EtOH:H_2O 1:1, 30 min) are subsequently compared with those fabricated from the optimized ink (mTM-NiFe-LDH in 1-PrOH:H_2O 1:1, 30 min) to quantify improvements in electrode quality and performance.

5.3.4 MORPHOLOGICAL CL OPTIMIZATION

Tailoring electrode morphology is key to maximizing accessible active sites and catalyst utilization. It governs mass transport and, in turn, overall MEA performance through its impact on activity and stability. Even without altering the intrinsic Ni_3Fe-LDH structure, reducing particle size is expected to improve catalyst utilization by increasing surface accessibility.

To investigate the effect of catalyst milling and enhanced dispersion, three electrodes with a catalyst loading of 5 mg cm^{-2} were prepared by means of ultrasonic spay deposition. This increased loading allows for a more detailed examination of the CL's characteristics, as a thicker layer is formed. The electrodes were prepared from the i-NiFe-LDH in EtOH-H_2O (1:1, 30 min), the mRB-NiFe-LDH and the mTM-NiFe-LDH both in 1-PrOH:H_2O (1:1, 30 min). These are further referred to as the i-electrode (or i-cell) and mRB-electrode (or mRB-cell) and mTM-electrode (or mTM-cell).

Top-view and cross-sectional SEM images of these electrodes are presented Figure 5.36. The CLS appear broadly similar across all three samples (Figure 5.36a1, b5 and c9). In each case, the substrate fibers are uniformly covered, although surface cracks are present. The optimized dispersions, however, produce less pronounced cracking on the PTL fibers. Pronounced cracks can reduce single-cell performance through catalyst loss and partial delamination.[289,336,410] although they may also promote oxygen bubble detachment compared with a fully closed surface.[165] For the Ni_3Fe-LDH anode, cracks on the nanometer scale have previously[131] shown no detrimental impact on performance and durability, consistent with the results discussed earlier (Chapter 5.2.1) and later in this work (Chapter 5.3.5).

The zoomed-in SEM images (Figure 5.36a-c, images 2, 6, 10) reveal clear differences in CL surface structure. Compared with the i-electrode, the mRB- and mTM-electrodes show smaller catalyst clusters and a correspondingly rougher surface. The cross-sectional images (Figure 5.36a-c, images 3-4 vs. 7-8 vs. 11-12) reveal the strongest differences in the CL structures. Using 1-PrOH instead of EtOH together with milled mRB- and mTM-NiFe-LDH improves CL adhesion to the Ni PTL. Local CL delamination is observed for the i-electrode (white arrows), whereas the milled-electrode CLs remain fully bonded. Crack formation is comparable across all samples, with similar vertical tears extending from the CL surface to the PTL fibers. Magnified cross-sections (Figure 5.36a-c, image 4 vs. 8 vs. 12) confirm a more homogenous particle distribution in the milled-electrodes. The mRB-electrode in more uniform compared to the i-electrode, some large catalyst clusters are still visible. In contrast, the mTM-electrode shows most homogeneity and catalyst-binder distribution (Figure 5.36c, image 12).

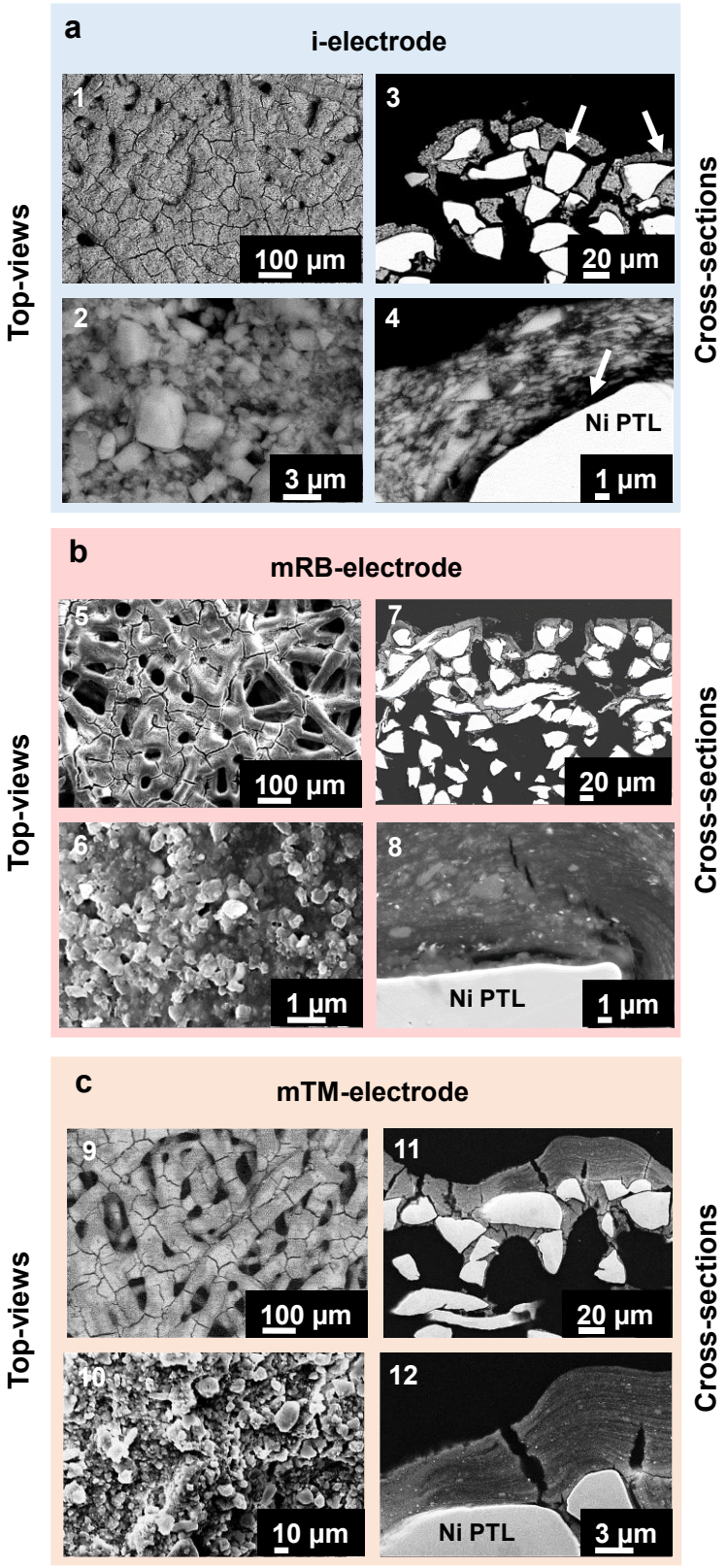

Figure 5.36. SEM images at different magnifications of the electrodes with (a) i-NiFe-LDH and the dispersion based on EtOH:H_2O 1:1, 30 min dispersing, (b) mRB-NiFe-LDH and the dispersion based on 1-PrOH:H_2O 1:1, 30 min dispersing, (c) mTM-NiFe-LDH and the dispersion based on 1-PrOH:H_2O 1:1, 30 min dispersing. The catalyst loading of each electrode is 5 mg cm^{-2}; the images are made of the electrodes' top-view and from cross-sections. Arrows indicate delamination of the catalyst layer from the PTL.

EDS mappings comparing the i-electrode and the mTM-electrode show stronger elemental inhomogeneity and pronounced layering in the i-electrode (Figure-A 19a, image 1), likely caused by particle sedimentation during fabrication. The smaller cluster size, rougher surface, and improved catalyst-binder distribution of the mTM-electrode are expected to increase accessible surface area and active-site density; this link to performance is examined in the following Discussion section.

5.3.5 IMPROVED SINGLE-CELL PERFORMANCE

Electrode activity in single-cell

MEAs based on i-, mRB-, and mTM-electrodes were prepared with identical parameters. All three MEAs were tested with an anode catalyst loading of 5 mg cm^{-2}, their polarization curves and corresponding Nyquist plots are shown in Figure 5.37.

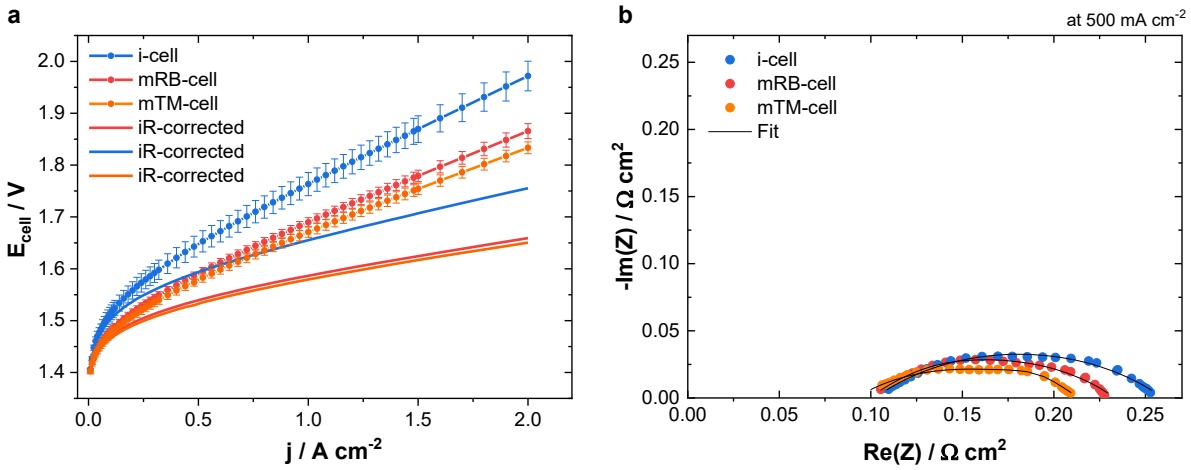

Figure 5.37. Comparison of single-cell performance of the initial and the two milled catalysts: (a) Polarization curves of identical MEAs, containing varied anodes based on the i-NiFe-LDH and the EtOH:H_2O 1:1 DM (blue), mRB-NiFe-LDH (red) and mTM-NiFe-LDH (orange) with 1-PrOH:H_2O 1:1, including the iR-corrected polarization curves; anode catalyst loading was 5 mg cm^{-2}. The iR-correction was completed according to the fit Figure-A 20. (b) Corresponding Nyquist plots recorded at a current density of 500 mA cm^{-2} including the simulated fit. Cathode: Pt/C 0.6 mg cm^{-2} (25 wt% binder). Testing conditions: 1 M KOH, 60 °C.

Both milled-cells outperform the i-cell with mRB-cell reaching 1.69±0.01 V at 1 A cm^{-2} (or 1.89±0.01 V at 2 A cm^{-2}), and the mTM-cell 1.67±0.01 V at 1 A cm^{-2} (or 1.83±0.01 V at 2 A cm^{-2}). This corresponds to ≈140 mV lower cell voltages than the i-cell (1.76±0.03 V at 1 A cm^{-2} or 1.97±0.03 V at 2 A cm^{-2}). Additionally, milling improved performance reproducibility, as reflected by smaller error bars in the polarization curve data.

To investigate the origin of the enhanced single-cell performance, galvanostatic EIS measurements were carried out over 0 to 2 A cm^{-2}. The cell resistances (R_{Ohm}, R_{ct}) were derived using the modelled electric circuit (refer to Figure 4.10). As the Nyquist plots frequently do not intersect the real axis, R_{Ohm} carries some uncertainty. Therefore, R_{Ohm} functions ($R_{\mathrm{Ohm}}(j)$) are fitted (exponential for i-cell and mRB-cells, linear for mTM-cell, Figure-A 20) and used for iR-compensation of the polarization curves. The fits are chosen according to the data trends. The iR-corrected curves (Figure 5.37a) exhibit

significant differences, indicating that the performance gap is not primarily driven by ohmic losses. Since the remaining single-cell components are unchanged, the improvement is attributed mainly to enhanced anode performance. The smaller catalyst clusters and more homogeneous catalyst-binder distribution observed by SEM (Figure 5.36) likely increase active-site accessibility and utilization,[19,138] while reduced particle size may also promote more uniform gas evolution.[80]

Consistent with this interpretation, the Nyquist plots (Figure 5.37b) show similar R_{Ohm} values of 102 mΩ cm^2, 99 mΩ cm^2 and 92 mΩ cm^2 for the i-cell, mRB-cell and mTM-cell, respectively (Table-A 9). Comparable R_{Ohm} is expected given identical AEMs and 1 M KOH, with the remaining ~10 mΩ cm^2 possibly arising from the CL thickness variations or contact resistances at the electrode-AEM interface.[87,345,411,412] In contrast, the semicircle diameter (R_{ct}) decreases from i-cell to mRB-cell to mTM-cell, corresponding to 157 mΩ cm^2, 129 mΩ cm^2, and 113 mΩ cm^2, respectively. Typically, lower R_{ct} indicate faster kinetics and improved catalyst utilization,[303,413] aligning with the polarization curve trends (Figure 5.37a). The depressed semicircles show a slight mixed character that may hint at an additional arc, potentially linked to processes in different pore networks and/or minor mass-transport effects.[310,414] A dedicated analysis of this feature is beyond the scope of this study.

Figure 5.38 shows the cell potential on a logarithmic current scale from the iR-compensated polarization curves. In this study, linear fits derived over the region of low overpotentials (η=0.2–0.45 V) at current densities of 0.03 to 0.1 A cm^{-2} (Figure-A 20) yield the potential increase rates *dE*/*d*log*j*. The linear *dE*/*d*log*j* fits with R-squares of 0.99 for all tested cells (Figure-A 21).

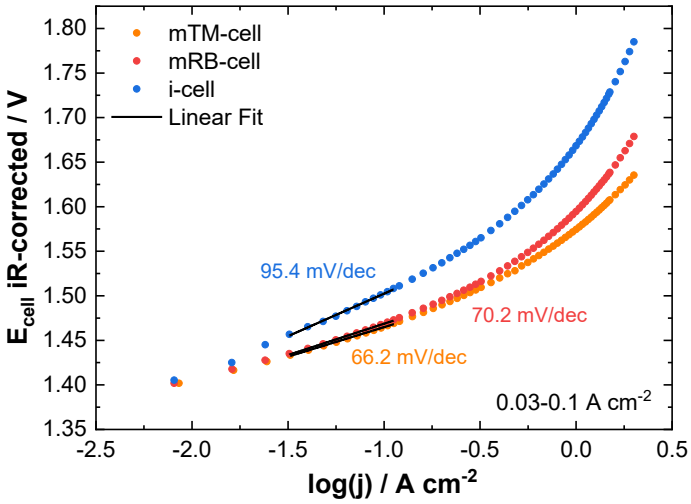

Figure 5.38. Current density increase rates (*E* vs log(*i*)) of the iR-corrected voltage data from Figure 5.37a, obtained from a linear fit of values between 0.03-0.1 A cm^{-2}, including the linear fit in the chosen interval, for the MEAs containing varied anodes based on the i-NiFe-LDH and the EtOH:H_2O 1:1 DM (blue), mRB-NiFe-LDH (red) and mTM-NiFe-LDH (orange) with 1-PrOH:H_2O 1:1, including the iR-corrected polarization curves, and a catalyst loading of 5 mg cm^{-2}.

For the single-cell based on the i-electrode, a *dE*/*d*log*j* slope of 95.4±1.7 mV dec^{-1} was determined, while for the mRB-cell 70.2±1.0 mV dec^{-1} and for the mTM-cell 66.2±0.9 mV dec^{-1} were achieved. This lower *dE*/*d*log*j* slope for the milled-electrodes not only confirms improved single-cell performance but may also suggest kinetic enhancements. A smaller *dE*/*d*log*j* slope typically indicates faster

charge transfer at the electrocatalytic interface, suggesting increased intrinsic catalytic activity for the milled catalysts. However, as demonstrated in previous sections, no intrinsic catalyst alterations in bond lengths, oxidation state shifts, or crystallinity modifications were observed. The primary change following catalyst milling and dispersion control is the modified anode CL structure. Consequently, the kinetic improvements can be attributed to enhanced catalyst utilization due to improved catalyst and binder distribution. This in turn indicates enhanced triple-phase boundaries within the CL, as evidenced by the reduced R_{ct}.[415] The contribution from the cathode side cannot fully be neglected, however the separation of the electrode contribution is complex. Nevertheless, the anode is considered to contribute more significantly due to the slower kinetic and higher energy requirements of the OER.[77,81]

Internal electrode resistance

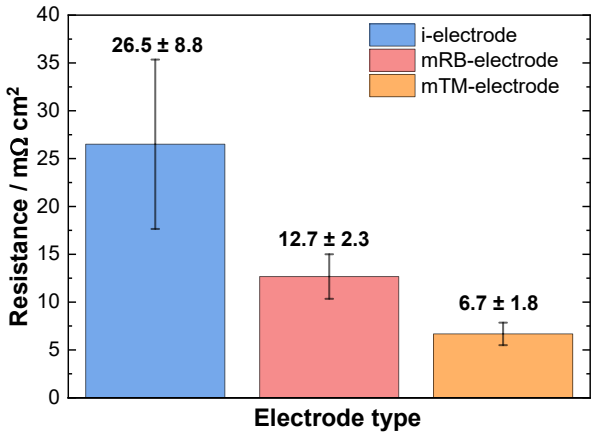

Figure 5.39. Internal resistances (interfacial contact+bulk) of the varied anodes based on the i-NiFe-LDH and the EtOH:H_2O 1:1 DM (blue), mRB-NiFe-LDH (red) and mTM-NiFe-LDH (orange) with 1-PrOH:H_2O 1:1, including the iR-corrected polarization curves, and a catalyst loading of 5 mg cm^{-2}.

To evaluate the impact of electrode structural modifications on electrical and interfacial contact properties, the internal (interfacial contact and bulk) electrode resistance $R_{\mathrm{electrode}}$ was measured in a sandwich-like setup. The arrangement is detailed in Chapter 4.5.[416–418] Published research, especially in the field of PEMWE, highlights the importance of minimizing interfacial resistance to enhance performance and durability. The internal resistance[345,419] measured in this work include both the contact resistance and the bulk resistance of the electrodes. Latter can be subtracted from the full value. As the obtained resistance values are compared just among each other, this calculation step is not required. It is important to note that the R_{Ohm} values obtained earlier are not directly comparable to the resistance values derived from the internal electrode resistance method. The latter specifically tests a single electrode, maintaining direct contact with the copper plates on both coated and uncoated sides of the electrode. On the contrary, the R_{Ohm} measurement includes not only the resistance of the electrode but also that of the membrane and the electrolyte. Indeed, low interfacial contact resistance can yield decreased R_{Ohm} in a single-cell.[122,420]

Figure 5.39 presents the internal electronic resistances for the i-electrode, the mRB-electrode, and the mTM-electrode. The i-electrode showed a resistance of 26.5±8.8 mΩ cm^2, while the milled-electrodes

exhibited significantly lower resistances of 12±2.3 mΩ cm^2 and 6.7±1.8 mΩ cm^2, for the mRB- and the mTM-electrode, respectively. This represents a 2-fold and 4-fold decrease in internal resistance. Notably, the smaller error bars for the optimized electrode suggest improved reproducibility and reliability. This reduction in resistance directly reflects an increase in internal electronic conductivity, which is likely due to finer ionomer-catalyst distribution and overall smaller size of the catalyst particles in the CL, as well as better CL adhesion to the Ni PTL. An optimally distributed catalyst particle network is expected to enhance conductivity through more effective three-phase boundaries, thereby reducing both internal and interfacial resistances and ultimately boosting the overall performance of the single-cell.

Electrode durability in single-cell

Long-term stability of single-cells is a key factor in the commercial use of AEMWEs, ensuring that the optimized electrodes can perform under industrial conditions.[19,161,288] For the durability tests, only the i-cell and mTM-cell were compared, and a catalyst loading of 2 mg cm^{-2} on the anode side was chosen to complement and compare the results to the data presented in a previous study (see Chapter 5.2[154]).

To validate loading effects (Chapter 5.1.3), single-cell tests comparing the i-cell and mTM-cell at Ni_3Fe-LDH loadings of 2 and 5 mg cm^{-2} were performed (Figure-A 22) and showed similar performance, indicating that the durability results at 2 mg cm^{-2} are comparable to the performance study conducted at 5 mg cm^{-2}.

Figure 5.40a presents the steady-state durability of the single-cells over 1000 h at 1 A cm^{-2}. Polarization curves were recorded at 100 h intervals of operation, providing insights into the time-dependent cell voltage trend (Figure-A 23); the intermittent polarization curves for the i-cell were presented in Chapter 5.2.1.

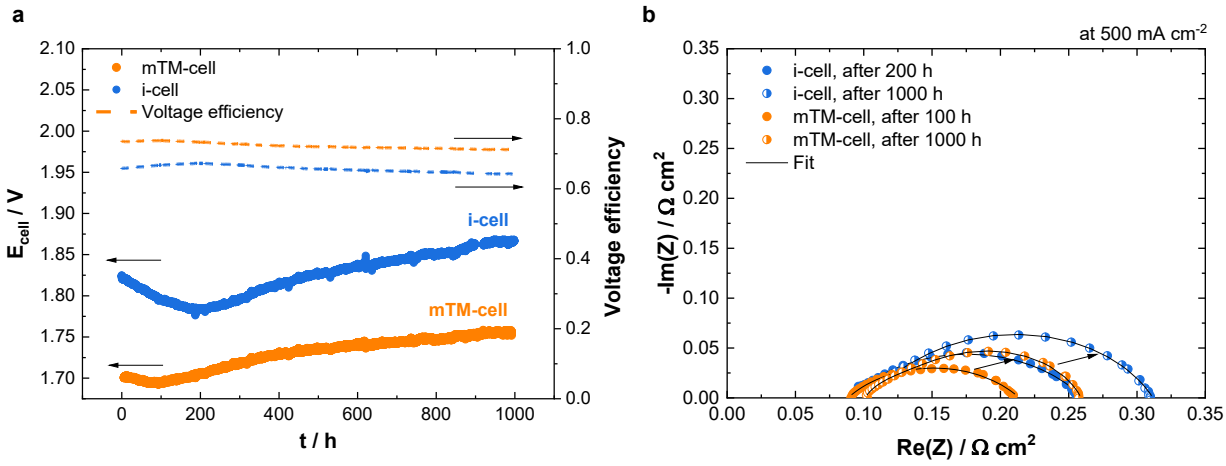

Figure 5.40. Performance stability of the i-cell (blue) and the mTM-cell (orange), with initial and TM-milled Ni_3Fe-LDH catalysts, respectively; catalyst loading on anode is 2 mg cm^{-2}: (a) Cell voltage and voltage efficiency during long-term 1000 h single-cell operation at constant 1 A cm^{-2} in 1 M KOH and at 60 °C, (b) corresponding Nyquist plots for the mTM-cell after the break-in time (200 h of operation) and at the end of the test (EoT, 1000 h), impedance data collected at 500 mA cm^{-2}. Cathode: Pt/C 0.6 mg cm^{-2} (25 % binder), 1 M KOH, 60 °C.

As observed in Figure 5.40a, for the i-cell, the best performance was noted after 200 h. The period up to this point is considered as conditioning time (Chapter 5.2).[154,421] In contrast, the mTM-cell reached its highest performance faster, just after 96 h of operation, as further proven by the polarization curves and Nyquist plots (Figure-A 23 and Figure-A 24). As the catalyst cluster size for the i-electrode is inhomogeneous, it is supposed to be the primary factor contributing to the extended conditioning process. Both cells exhibited relatively stable performance throughout the operation period. The mTM-cell consistently outperformed the i-cell, maintaining a voltage range of 1.7–1.75 V, while the i-cell operated at a higher voltages of 1.78–1.87 V. This improvement aligns with previous findings and highlights the advantages of the mTM-electrode's structure.

A key challenge in water electrolysis is defining the onset of degradation. Voltage evolution trends are informative: a small decrease that quickly stabilizes typically reflects break-in (conditioning) rather than degradation.[80] To accurately measure degradation, it should be assessed from the lowest stabilized voltage. For the mTM-cell, degradation begins at 96 h, while for the i-cell, it starts at 200 h. Over the remaining 904 h (mTM-cell) and 790 h (i-cell), the degradation rates were 62 µV h^{-1} (or 3.66 %) and 84 µV h^{-1} (or 4.68 %), respectively, a lower rate for the i-cell. Over 1000 h, the i-cell shows a total voltage increase of 45 mV, compared with 54 mV for the mTM-cell. While improved catalyst accessibility enhances performance, smaller particles and more exposed active sites can also accelerate degradation processes during OER, potentially compromising long-term stability.[197]

The voltage efficiencies shown in Figure 5.40a underline the performance improvement for the mTM-cell, as evidenced by a calculated efficiency of ≈73%, compared to the i-cell, which yielded an efficiency of ≈65% at 1 A cm^{-2}.

To further assess the single-cell durability, EIS data was evaluated. Figure 5.40b shows Nyquist plots recorded after completion of the conditioning phase and after 1000 h of operation (EoT) for both cells.

The resistance values are not directly comparable to Figure 5.37b because the long-term tests use a lower anode loading (2 mg cm^{-2} Ni_3Fe-LDH instead of former 5 mg cm^{-2}). Nevertheless, the mTM-cell consistently exhibits smaller semicircles than the i-cell. At 100 h and at 500 mA cm^{-2}, R_{Ohm} is similar for both cells (88 vs. 90 mΩ cm^2), whereas R_{ct} is markedly lower for the mTM-cell (126 vs. 168 mΩ cm^2). At EoT, both semicircles increase, corresponding to a ΔR_{ct} of +27 mΩ cm^2 for the mTM-cell and +29 mΩ cm^2 for the i-cell, while R_{Ohm} changes only insignificantly, indicating largely stable anion-conducting components and interfacial/contact resistances.

Electrode stability observed by SEM

To finalize the stability investigation of the chosen electrodes, SEM characterization was conducted.

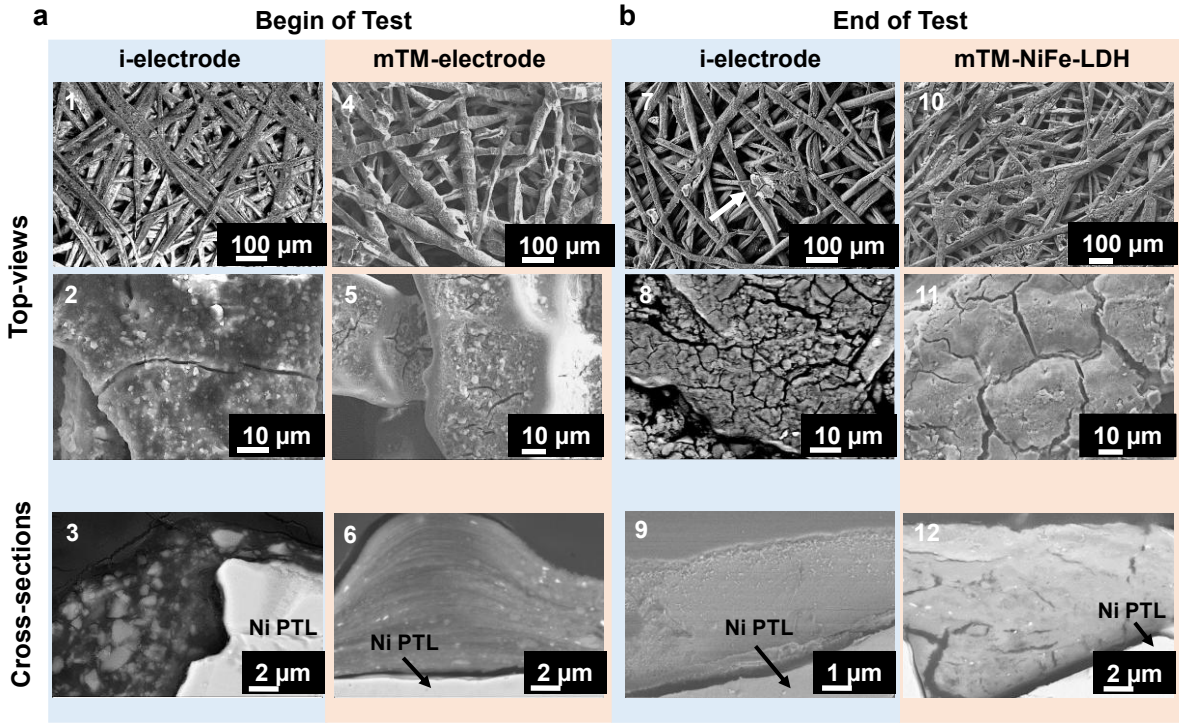

Figure 5.41. SEM images at magnifications x250, x2.5k, x10k (from top to down) of the i-electrode and mTM-electrode with a catalyst of 2 mg cm^{-2} from top-view (1, 2, 4, 5, 7, 8, 10, 11) and from cross-section view (3, 6, 8, 12): (a) at BoT and (b) end of test, after 1000 h (EoT).

Figure 5.41 presents top-view and cross-sectional SEM images of the i-electrode and the mTM-electrode at BoT (a) and EoT (b). At BoT, both electrodes (Figure 5.41a 1-6) show morphologies similar to the higher catalyst-loaded anodes (Figure 5.36). At EoT, notable differences occur: the mTM-electrode retains more catalyst at the surface (Figure 5.41b 10) and exhibits less pronounced crack formation. Its CL surface evolved into an island-like structure, whereas the i-electrode developed larger primary cracks along with smaller secondary cracks. Cross-sections (Figure 5.41a 3, 6 and Figure 5.41b 9, 12) indicate partial CL delamination from the PTL in both cases, with more severe cracking and detachment for the i-electrode. Overall, both electrodes undergo a marked structural evolution from a finely structured CL to a sponge-like morphology, consistent with previous results (Chapter 5.2).[154]

5.3.6 SUMMARY

This study investigated Q4 (Q&A Chapter 3, Approach 3) whether catalyst milling and dispersion control enhance the technical relevance of Ni_3Fe-LDH anodes in terms of manufacturability, reproducibility, and long-term stability under realistic AEMWE conditions. Approach 3 couples powder processing with ink and CL optimization and validates the impact via morphology and single-cell performance and durability tests. The main outcomes are:

- The wet tumbler ball milling process yielded an 8.8-fold increase in the geometrical surface area of the catalyst clusters and optimized the particle size distribution from bimodal to unimodal, significantly reducing the average hydrodynamic diameter. SEM analysis confirmed changes in the agglomerate density and dimensions of the catalyst clusters, while STEM verified that the LDH structure remained intact after milling. Comprehensive analyses using XRD, Raman spectroscopy, and XPS have demonstrated that the milling of catalyst powder does not induce notable intrinsic alterations in the LDH structure, elemental oxidation states, composition, phase, or crystallinity. The milling process positively influenced the size of catalyst clusters, noticeably reducing them, and enhanced the accessible geometrical surface area, which is integral to the catalyst's efficiency.
- By fine-tuning various factors in catalyst ink preparation, like solvent types and dispersing durations, an optimal composition was identified for the milled (mTM-NiFe-LDH) Ni_3Fe-LDH catalyst with a 1:1 H_2O:1-PrOH DM, treated with ultrasonic horn for 30 min. These adjustments resulted not only in a more stable catalyst ink, easing the electrode fabrication process, but also in a more uniform microstructure of the CL. This uniformity reduced internal electrode resistance and charge-transfer resistance, indicating improved catalyst accessibility. The chosen optimization steps significantly enhanced single-cell performance and reproducibility, demonstrating a durability of up to 1000 h. To be more precise, compared to the baseline Ni_3Fe-LDH-based single-cell, the new electrode yielded higher single-cell activities, a faster conditioning of the system and a lower degradation rate.

The results show that AEMWE performance is strongly governed by electrode structure and catalyst-binder distribution within the CL. Optimized ink formulations that maximize catalyst accessibility are therefore essential for reproducible, high-performance AEMWEs. The workflow presented provides a scalable route to reproducible ink preparation and highlights the importance of processing from catalyst synthesis to electrolyzer integration for real-world performance.

5.4 STRUCTURAL AND ELECTROCHEMICAL INSIGHTS INTO ANODE CONFIGURATIONS

In previous chapters, MEAs were assembled from a cathode-CCS and an anode-CCS, with the membrane sandwiched in between. Catalyst deposition directly onto the substrate was preferred due to its simplicity and suitability for small-scale fabrication, consistent with common AEMWE practices.[78,81] The opposite method is applying the catalyst directly on the membrane, forming a CCM-MEA. More details of both MEA configurations, their characteristics and fabrication methods are described in Chapter 2.3.2.

In the first part of this chapter, two types of membranes are used: an anion-conducting membrane DURAION® (Evonik) and the imidazolium-hydrocarbon-based polymer membranes Aemion+™ (Ionomr Innovations Inc.), each with their corresponding anion-conducting binders. The membranes have comparable thicknesses, allowing for a meaningful single-cell performance comparison. A key difference is in the polyolefin reinforcement network in the Aemion+™ membrane, which was selected to limit swelling during CCM fabrication and to benefit from improved mechanical stability. Aemion+™ materials were included to broaden the scope beyond pre-commercial materials and to enable reproducibility by third parties, as DURAION® materials were not commercially accessible at the time of these studies; related reproducibility challenges are discussed in the next chapter.

The shift from CCS to CCM was studied on the anode side, which is the focus of this work. Therefore, the following chapter compares Ni_3Fe-LDH-based anode-CCSs and anode-CCMs. From this chapter onward, the milled Ni_3Fe-LDH catalyst (mTM-NiFe-LDH) and the optimized DM (1-PrOH:DI H_2O, Chapter 5.3) are used. The Pt/C cathode remained consistent and was fabricated as CCS throughout all studies.

5.4.1 EFFECT OF IONOMER CONTENT ON CCM-MEA PERFORMANCE

Optimization based on the DURAION® AEM

In this section, CCM optimization is performed using the DURAION® AEM and CCS-derived electrode parameters are transferred as the initial baseline.

Direct transfer of electrode parameters

To enable the direct performance comparison between anode-CCS and anode-CCM MEAs, the fabrication parameters previously optimized for the anode-CCS (Chapter 5.1 and 5.3), were transferred to the anode-CCM, namely a catalyst loading of 2 mg cm^{-2} and an ionomer content of 20 wt%.

The two resulting electrode types exhibit different characteristics. In the CCS configuration, the CL is deposited onto the porous PTL, yielding a more “open” architecture that can enhance mass transport by improving water (or KOH electrolyte) access and enabling rapid removal of gas bubbles through the pore network.[75,134] The PTL further supports capillary-driven water management, helping to mitigate local flooding or dry-out, benefits that become particularly relevant at high current density.

In contrast, CCM architectures form a compact, continuous ("closed") CL on the AEM surface. While the intimate CL-AEM contact benefits ionic conduction, the reduced porosity can hinder reactant delivery and product gas removal at high current densities, including limited water penetration from the membrane side and restricted access of additional water/or OH^- from the liquid electrolyte, as well as slower gas evacuation through the dense CL.[67]

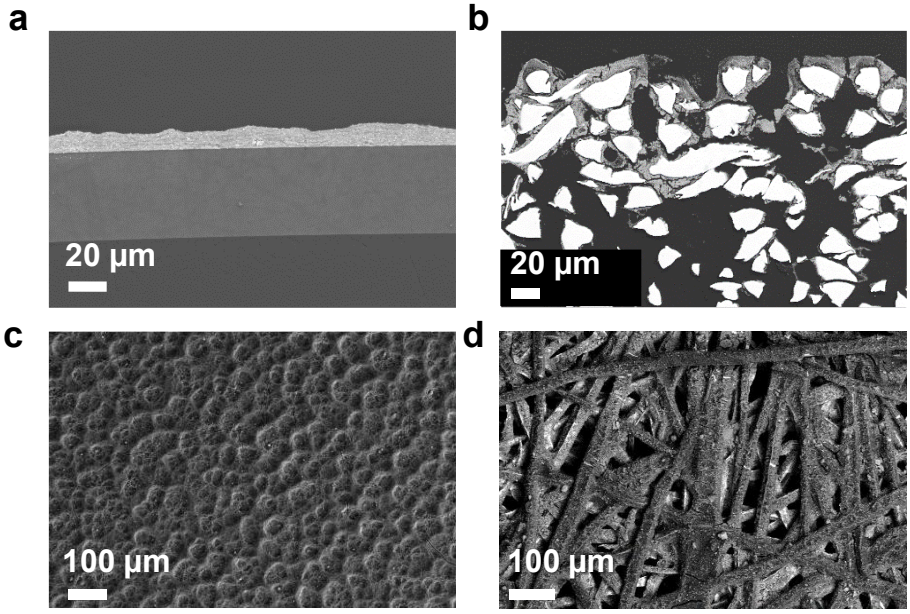

Figure 5.42. SEM images of the anode-CCM from (a) cross-section and (c) top-view and of the anode-CCS from (b) cross-section and (d) top-view. The catalyst loading and ionomer content are the same in the presented CLs.

These structural differences are directly reflected in Figure 5.42. The anode-CCM presents a uniform CL of 15-20 µm thickness evenly distributed on the membrane (Figure 5.42a, c). In contrast, the anode-CCS exhibits pronounced catalyst penetration into the PTL, reaching depths up to 140 µm as the catalyst dispersion permeates surface and internal fibers during fabrication (Figure 5.42b, d), which is expected to increase the electrochemically accessible area. The CCM surface displays a bubble-like topography (Figure 5.42c), likely arising from solvent evaporation and membrane swelling and deswelling; this feature appears less pronounced in cross-section (Figure 5.42a). For the CCS, the CL is well distributed and effectively encases the upper fiber layers (Figure 5.42b), consistent with the open PTL structure (Figure 5.42d).

To investigate the performance difference of the two anode configurations, single-cell tests were performed. Figure 5.43a shows the polarization curves of anode-CCS cells and anode-CCM cells operated in 1 M KOH at 60 °C. The anode-CCS cell required 1.67±0.01 V at 1 A cm^{-2}, while the anode-CCM cell achieved 1.77±0.01 V at the same current density, showing a performance decrease of around 100 mV for the CCM cell type. EIS spectra (Figure 5.43b) provide further insights. Compared with the anode-CCS cell, the anode-CCM cell shows a slightly higher R_{Ohm} and a more pronounced increase in R_{ct}. Specifically, R_{Ohm} increases 79 mΩ cm^2 to 92 mΩ cm^2, which is unexpected given the uniform, well-adhered CL of the anode-CCM (Figure 5.42a).

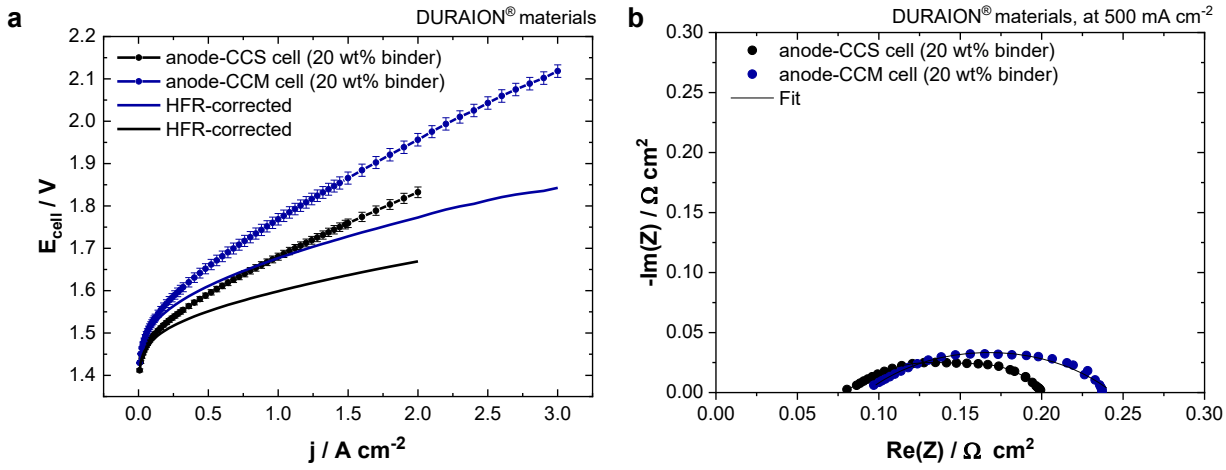

Figure 5.43. Electrochemical performance comparison of an anode-CCS-based single-cell and an anode-CCM one. The CL layer parameters as well as the testing conditions remain consistent. (a) Polarization curves incl. iR-corrected curves, (b) corresponding Nyquist plots recorded at 500 mA cm^{-2} incl. simulated fits. Cathode: Pt/C 0.6 mg cm^{-2} (25 wt% binder), 1 M KOH, 60 °C.

A plausible explanation is the thicker CL of 15–20 µm, which increases effective ionic pathway length. In contrast, the CCS exhibits thin local films on individual Ni fibers with deep penetration of ≈140 µm (Figure 5.42b), potentially shortening average ion-transport distances and improving local connectivity.

The iR-corrected polarization curves (Figure 5.43a) confirm that the performance gap is not attributable to R_{Ohm} alone. Notably, R_{Ohm} includes both ionic and electronic resistances, so the dominant origin cannot be isolated here. If ionic transport is assumed to dominate R_{Ohm}, as expected with using highly conductive metallic PTLs, the lower R_{Ohm} of the CCS suggests more effective ion pathways. Alternatively, if electronic conductivity within the CL is limiting, reactions preferentially occur near electronically connected PTL fibers; the CCS would then benefit from the large electronically percolated fiber area, while the CCM could suffer from poorer electronic access through its denser, ionomer-rich layer. Both effects may contribute.

The observed difference in R_{ct} (124 mΩ cm^2 for the CCS and 145 mΩ cm^2 for the CCM) is consistent with higher accessible surface area and better catalyst utilization in the CCS, where catalyst is distributed along the conductive Ni fiber network. In the CCM, the denser CL (with 20 wt% ionomer) and weaker electronic coupling to the PTL can reduce the number of electrochemically active sites, so R_{ct} reflects both kinetics and effective active-site density.

Overall, these results imply that CCM optimization requires rebalancing internal morphology, e.g., lowering ionomer content and/or improving electronic connectivity (conductive additives), to increase utilization and close the CCS-CCM performance gap. Similar trends have been reported previously, where CCS architectures outperform CCMs due to larger effective catalytic area,[134] and where the preferred MEA configuration depends on whether electrolyte flows through one or both electrodes.[128] Matching ion and electron transport pathways and maximizing effective reaction area

are therefore critical for achieving comparable CCM performance, as discussed in the following chapters.[148,422]

Adjustment of binder content in anode

Directly transferring the CL parameters from the anode-CCS to the anode-CCM proved suboptimal. Therefore, anode-CCMs were fabricated with varying anion-conducting binder contents (5–20 wt%) and were subjected to electrochemical characterization.

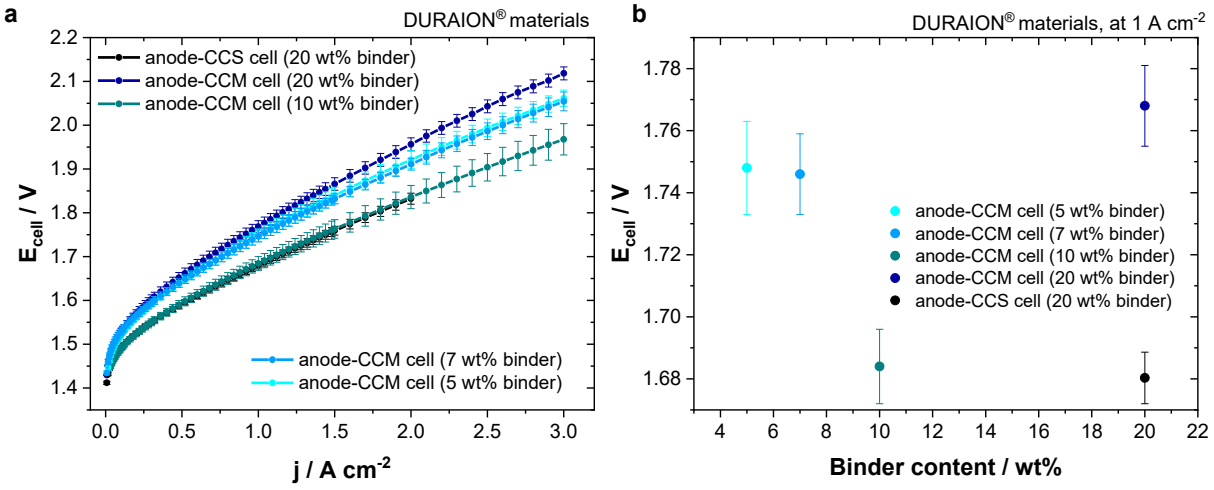

Figure 5.44. Comparison of anode-CCM cells with different binder contents (5, 7, 10, 20 wt%) in the catalyst dispersion with the anode-CCS cell and among each other: (a) Polarization curves, (b) Cell voltages obtained at 1 A cm^{-2}. The MEAs were fabricated based on DURAION® materials. All components, except the MEAs are identical. Cathode: Pt/C 0.6 mg cm^{-2} (25 % binder); 1 M KOH, 60 °C. The polarization curve of the anode-CCS is hidden under the anode-CCM (10 wt%) curve, as they mostly overlap.

Figure 5.44a shows the polarization curves of the anode-CCS cell together with four anode-CCM cells. Figure 5.44b illustrates how the measured voltages at 1 A cm^{-2} vary across the different cells, offering a clear indication of the most effective binder content in the anode. Notably, the anode-CCM cell with a reduced ionomer content of 10 wt% demonstrated the best performance among the CCM cells, achieving 1.68±0.01 V at 1 A cm^{-2}, and maintaining a voltage below 2 V even at 3 A cm^{-2}. Decreasing the ionomer further to 7 and 5 wt% did not lead to additional performance improvements. While still better than the 20 wt% CCM cell, the MEAs with 5 and 7 wt% binder in the anode, achieved similar voltages of 1.75±0.02 V and 1.75±0.01 V at 1 A cm^{-2}, respectively. iR-corrected polarization curves confirmed these trends, demonstrating that the MEA with 10 wt% binder achieved a performance nearly equivalent to the CCS reference (Figure-A 25).

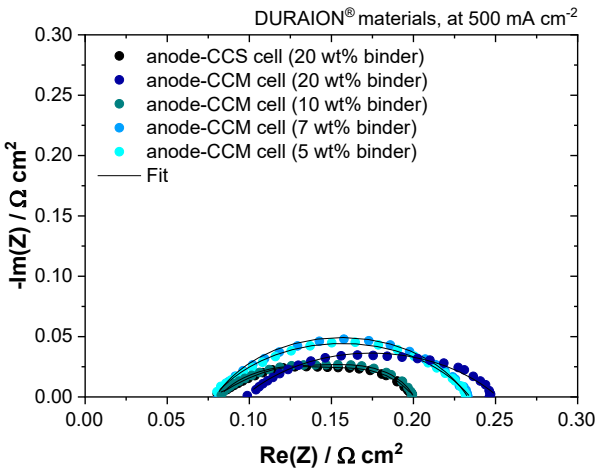

Figure 5.45. Comparison of anode-CCM cells with different binder contents (5, 7, 10, 20 wt%) in the catalyst dispersion to the anode-CCS cell (20 wt% binder) and among each other: Nyquist plots obtained from impedance spectroscopy at 500 mA cm^{-2} incl. simulated fits. The MEAs were fabricated based on DURAION® materials. All components, except the MEAs are identical. Cathode: Pt/C 0.6 mg cm^{-2} (25 % binder). Testing conditions: 1 M KOH, 60 °C.

The Nyquist plots of all cells are shown in Figure 5.45, and resistance values are provided in Table-A 10. Among all the cells evaluated, the anode-CCM cell with 20 wt% binder exhibited the highest R_{Ohm} with 95 mΩ cm^2, while the remaining cells showed R_{Ohm} values in a narrow range (77–86 mΩ cm^2). Literature[145] suggests that once the ionomer content exceeds the free volume between catalyst particles, excess binder may form a continuous, electronically insulating phase, particularly at the CL-PTL interface of within the CL. This effect is likely most pronounced for the 20 wt% anode-CCM, where the dense CL promotes binder accumulation, whereas the more porous CCS architecture disperses excess ionomer along the PTL fibers and mitigates insulating film formation.

Unlike the best performing 10 wt% anode-CCM cell, all other cells exhibited high R_{ct} values. For the 20 wt% anode-CCM cell, the poor charge transport could originate from an insufficient availability of electrochemically active sites due to binder blockage. However, the opposite extreme can be present in the 5 and 7 wt% anode-CCMs. These cells showed higher charge-transfer resistance compared to the 10 wt% anode-CCM cell, despite having less insulating binder. This indicates that insufficient binder compromises ionic conductivity, as the continuous OH^- conduction pathways within the CL become discontinuous or poorly connected. Moreover, inadequate binder content may weaken adhesion between the CL and the AEM, leading to interfacial delamination, which further blocks ionic and electronic transfer processes. Previous studies have demonstrated a similar non-trivial trend, indicating the importance of an optimal intermediate ionomer content for each specific CCM-electrode.[145,148,423,424]

Stability tests

To ensure that the selected anode-CCM cells exhibit a stable and reproducible performance behavior, short-term stability tests of 16 h at a constant load of 1 A cm^{-2} were conducted (Figure 5.46). These tests confirm that the polarization curves reflect not only initial single-cell performance but also a

stable operating level over time. The 16 h voltage-hold measurements are repeated three times (Figure 5.46) and show good reproducibility, with an overall uncertainty of ≈10 mV.

The voltage stability curves were recorded after conditioning, the initial polarization curve, and EIS, and therefore reflect stabilized steady-state behavior rather than the initial transient response. This is confirmed by repeated polarization-curve comparisons. Accordingly, the 0 h point corresponds to 15 h of operation. Long-term operation data discussed later (Figure 5.47) are acquired using the same protocol.

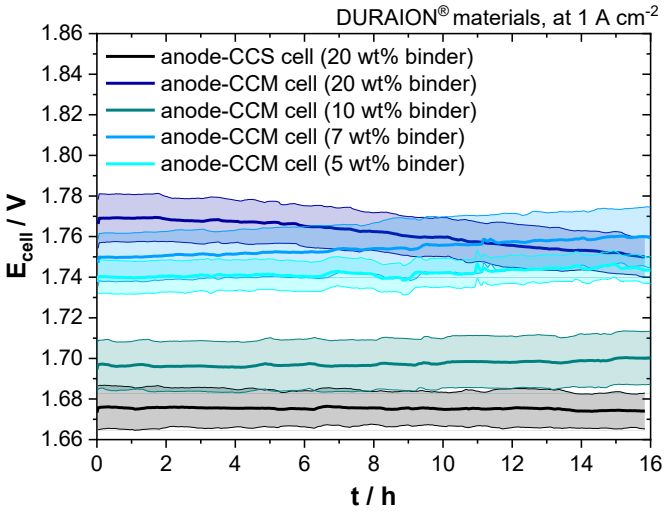

Figure 5.46. Cell voltage changes during 16 h single-cell operation at constant 1 A cm^{-2} for the anode-CCMs with varying binder content (5, 7, 10, 20 wt%) and the anode-CCS (20 wt% binder). The tests were conducted three times each; the light-colored area on the graph represents the standard deviation (error bars). The MEAs are fabricated using pre-commercial DURAION® materials. Cathode: Pt/C 0.6 mg cm^{-2} (25 wt% binder). Testing conditions: 1 M KOH, 60 °C.

The anode-CCS cell shows the lowest voltages, closely followed by the anode-CCM cell with 10 wt% binder, while the anode-CCM cell with 20 wt% binder performs worst. All stability curves exhibit similar trends, except the 20 wt% anode-CCM, which shows a slight improvement during the test. Although the slope change appears pronounced at this scale, it corresponds to only 16 mV overall (≈1 mV h^{-1}). This activation-like behavior, similar to Chapter 5.2, may be influenced by the higher content of anion-conducting binder and the denser CL structure, as discussed further (Figure 5.49). Supporting this observation, polarization and EIS data (Figure-A 26) recorded before and after the stability test reflect a similar trend, with the Nyquist plots indicating reduced R_{ct} for the anode-CCM cell with 20 wt% binder but highest R_{Ohm} (Figure-A 26b, c).

As discussed in Chapter 5.2, short-term tests over a few to several tens of hours primarily capture the system's break-in (or conditioning) phase. While such tests can confirm initial operational stability, i.e., that no early failures occur, they are insufficient for identifying meaningful performance trends, such as long-term voltage degradation or improvement. Accurate assessment of these trends requires extended operation over longer durations. This limitation is also demonstrated in Figure 5.47.

A longer durability test of 550 h (Figure 5.47) was performed one year later using a varying batch of materials (challenges related to this are described in Chapter 5.5).

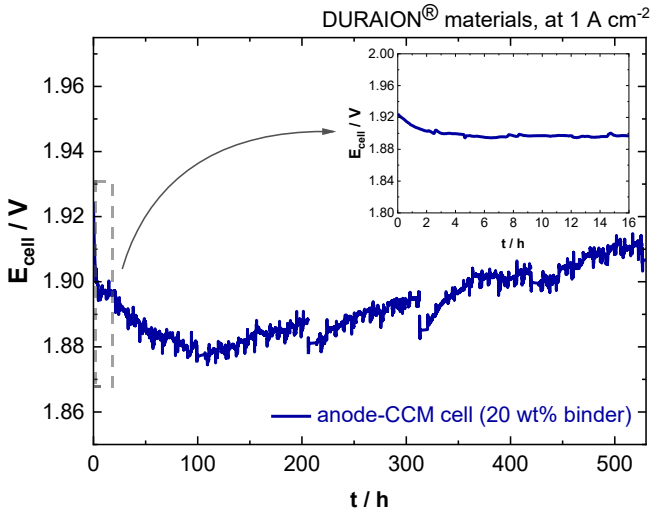

Figure 5.47. Cell voltage changes during 550 h single-cell operation at constant 1 A cm^{-2} for anode-CCM with 20 wt% binder. The test was conducted one year later using differing material batches; the zoomed-in graph presents the first 16 h of the test. The apparent interruptions occurring every 100 h of operation are due to polarization curves recorded in between. Cathode: Pt/C 0.6 mg cm^{-2} (25 wt% binder). Testing conditions: 1 M KOH, 60 °C.

The durability curve of the anode-CCM cell (20 wt% binder) exhibited a conditioning trend similar to those observed in Chapter 5.2.1 (Figure 5.16) and Chapter 5.3.5 (Figure 5.40), with a gradual voltage decrease over the first ≈100 h of steady-state operation. On a shorter timescale (cutout in Figure 5.47), its behavior closely matches that of a comparable cell tested a year earlier, despite differences in catalyst, binder, and membrane batches. This consistency explains the observed performance gap of ≈120 mV at 1 A cm^{-2}, compared to those in Figure 5.46. Excluding the initial 100 h break-in (Figure 5.47), the following 450 h show a voltage loss of 33 mV, corresponding to a degradation rate of 74 µV h^{-1}, comparable to the full-CCS cell with identical electrode parameters. However, the data indicate that either MEA architecture can be suitable, depending on system requirements, operating environment, and fabrication constraints. Overall, these results reinforce the need for long-term testing to quantify degradation reliably and avoid overinterpreting short-duration trends.

Morphology of the catalyst layers

To further assess the effect of binder content in the anode-CCMs, the morphology was examined by SEM.

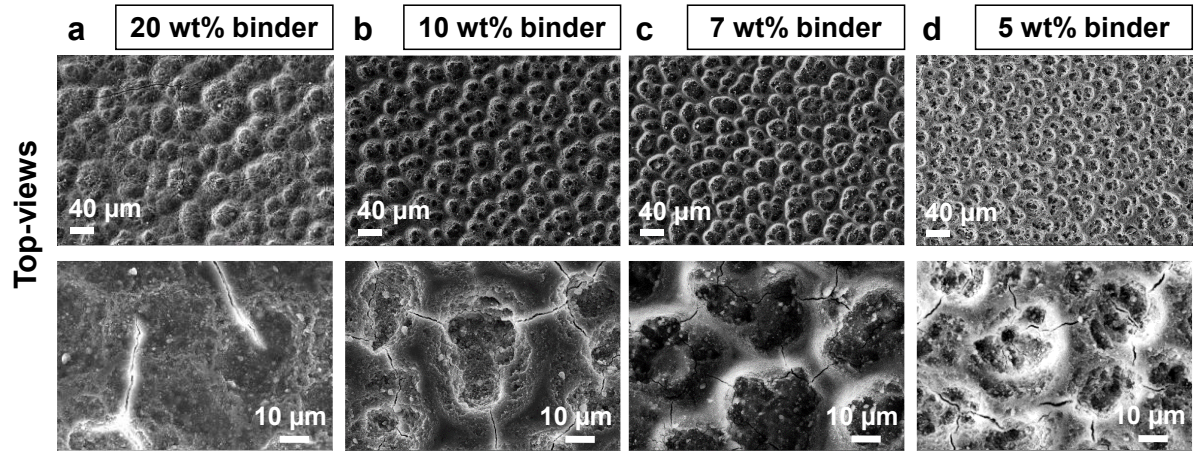

Figure 5.48. SEM images of the anode-CCMs from top-view at magnifications x500 (top), x5000 (bottom): (a) aCCM-anode with 20 wt% ionomer, (b) anode-CCM with 10 wt% ionomer, (c) anode-CCM with 7 wt% ionomer, (d) anode-CCM with 5 wt% ionomer. The catalyst loadings are 2 mg cm^{-2} for all the presented CLs. The AEM and binder are pre-commercial DURAION® materials.

Figure 5.48 shows the top-view SEM images of the four DURAION® material-based anode-CCMs with varied ionomer content (20, 10, 7, 5 wt% binder). All CCMs exhibit the bubble-like surface texture already observed in Figure 5.42, likely caused by rapid solvent evaporation during coating. Decreasing the ionomer content progressively increases surface roughness and promotes crack formation, consistent with the trends shown in the cross-sectional images (Figure 5.49). Figure 5.49 further reveals pronounced thickness non-uniformity (up to ≈10 µm). The 20 wt% binder anode-CCM reaches a maximum thickness of 15 µm, whereas the 10–7 wt% anode-CCMs are typically about 20 µm, and the 5 wt% anode-CCM is even thicker and most heterogeneous. Overall, lower ionomer content correlates with higher apparent porosity and more cracking.

The anode-CCMs with 5 and 7 wt% binder did not show improved single-cell performance, which is plausibly linked to insufficient CL-AEM adhesion. As indicated in Figure 5.49e and the photographs in Figure-A 27, a slight separation between CL and AEM is visible, and physically, the CL can be easily detached or scratched of from the AEM (Figure-A 27, left). Adhesion issues also become evident after cell testing as parts of the CCM-deposited CL transferred onto the Ni PTL (Figure-A 27, right).

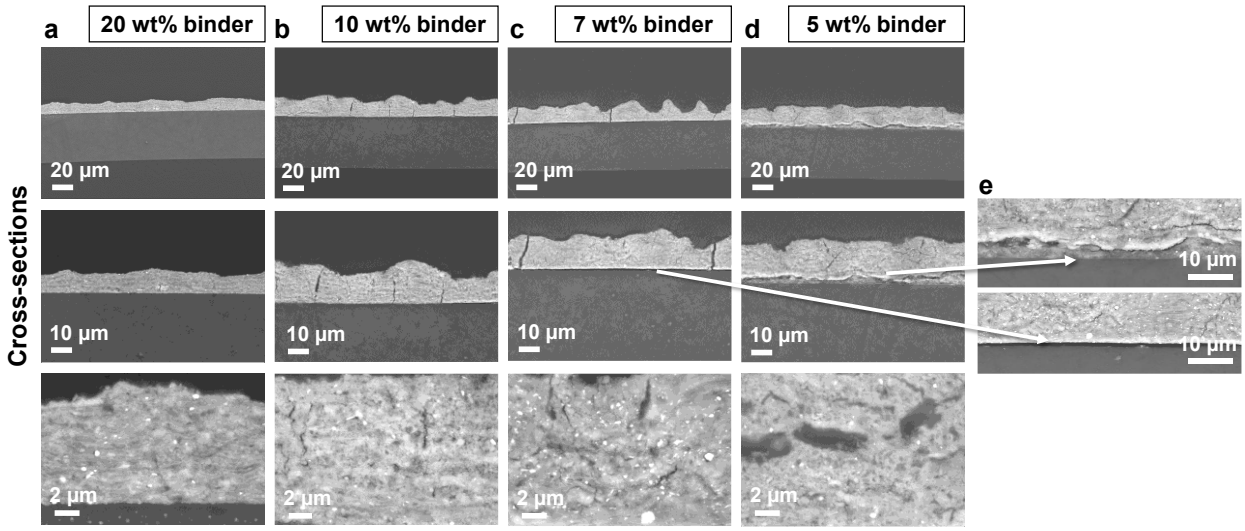

Figure 5.49. SEM images of the anode-CCMs from cross-section view at magnifications x500, x1000, x5000 (from top to bottom): (a) anode-CCM with 20 wt% ionomer, (b) anode-CCM with 10 wt% ionomer, (c) anode-CCM with 7 wt% ionomer, (d) anode-CCM with 5 wt% ionomer, (e) zoom-in views of the interface AEM-CL for the 5 w% (top image) and 7 wt% (bottom image) ionomer anode-CCM. The catalyst loadings are 2 mg cm^{-2} for all the presented CLs. The AEM and binder are pre-commercial DURAION® materials.

SEM images of the PTL after operation (Figure-A 28) show extensive transfer of the 20 wt% binder CL as a cracked, partially connected sheet with residues on individual fibers, indicating partial CL relocation while a few fractions remain on the membrane. Similar observations have been sporadically reported.[128] The transfer could occur during the dismantling of the cell given that the cell components are tightly compressed at the active surface area (up to 2 N mm^{-2}). In-operation detachment cannot be excluded but would likely remain confined to micro-scale events and is not directly evidenced here. The detachment might be further supported be the shear forces originating from the circulating electrolyte, or chemical binder degradation. Interestingly, the use of a PTFE binder proved to provide adequate adhesion, preventing the catalyst particles from transferring to the PTL.[128] Delamination has also been attributed to mismatched thermal expansion and water uptake between ionomer and membrane.[163]

Optimization based on the Aemion+™ AEM

To compare the results obtained with pre-commercial DURAION® with the commercially available Aemion+™ materials, the same experiments were performed. It proved that some results are very comparable and are hence discussed only shortly with respective Figures given in the Appendix.

Direct transfer of electrode parameters

A comparative study was conducted to optimize the CL parameters for anode-CCM based single-cells using commercially available Aemion+™ materials. The Aemion+™-based electodes (anode-CCSs) were initially used without systematically adjusting the binder content but using the same composition as for the DURAION® materials.

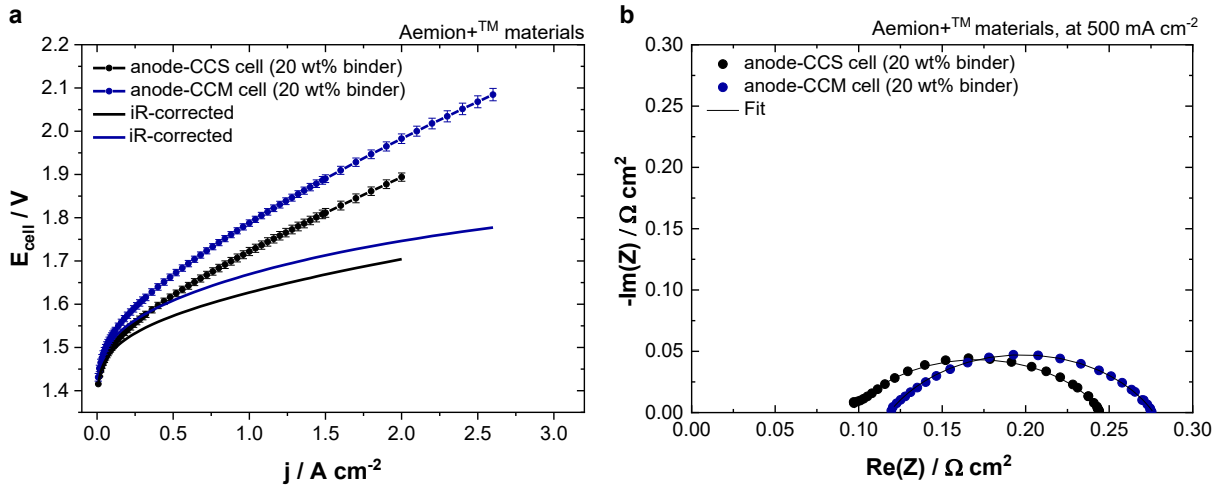

Figure 5.50. Electrochemical performance comparison of an anode-CCS-based single-cell and an anode-CCM one, the MEA is based on Aemion+™ materials. The CL layer parameters as well as the testing conditions remain consistent among the two tests. (a) Polarization curves incl. iR-corrected curves, (b) corresponding Nyquist plots recorded at 500 mA cm^{-2} incl. simulated fits. Cathode: Pt/C 0.6 mg cm^{-2} (25 wt% binder). Testing conditions: 1 M KOH, 60 °C.

Despite no optimization of catalyst loading, dispersion composition, or binder content, the CCS-based single-cell achieved 1.72±0.01 V at 1 A cm^{-2} (Figure 5.50a). Consistent with earlier findings using DURAION® materials, the anode-CCM cells with 20 wt% binder performed poorer than the anode-CCS cells, requiring 1.79±0.01 V at 1 A cm^{-2}. The polarization curves, adjusted for R_{Ohm}, validate these findings and demonstrate that the performance differences are not related to R_{Ohm} only.

The obtained performance surpassed those published in 2022,[164] where a similar cell achieved 68 mA cm^{-2} at 1.8 V with 25 wt% binder content on the anode side, and 136 mA cm^{-2} at 1.8 V with 15 wt%. Unlike previous studies, no issues with ink stability or homogeneity were faced in this work, likely due to the use of an ultrasonic probe for dispersion preparation, different to moderate stirring or an ultrasonic bath proposed by literature[148,164] and documentation (Ionomr Documentation: FM-7005-E).

The Nyquist plots (Figure 5.50b) show differing R_{Ohm}, unlike in the case of DURAION® materials. The anode-CCM exhibits a higher R_{Ohm} of 118 mΩ cm^2 compared with 95 mΩ cm^2 for the anode-CCS, while R_{ct} is similar for both configurations (155 vs. 152 mΩ cm^2). The elevated R_{Ohm} suggests lower conductivity of the ion-conducting components and/or increased interfacial resistance. Although SEM images indicate good CL-AEM adhesion (Figure-A 31), this mismatch implies that physical contact alone does not ensure efficient ionic transport, potentially due to local non-uniformities (Figure-A 32) or poor ionomer distribution inside the CL.

Adjustment of binder content in anode

While Cossar et al. proved 7 wt% of Aemion™ binder to be optimal for a $Ni_{0.1}Fe_{0.9}$ anode-CCS configuration with Pt/C at the cathode side,[164] in this work, 20 wt% were used as the baseline content for the Ni_3Fe-LDH anode. To investigate the impact of ionomer content on the anode-CCM cell performance, the dispersion formulation was adjusted to include 3, 5, 7 or 10 wt% binder, relative to

solid content. Figure 5.51a displays the polarization curves for all ionomer contents, iR-corrected polarization curves are shown in the Appendix (Figure-A 33). Figure 5.51b presents the voltages achieved at 1 A cm^{-2} for each cell allowing for a straightforward comparison and clearly identifying the optimum binder content.

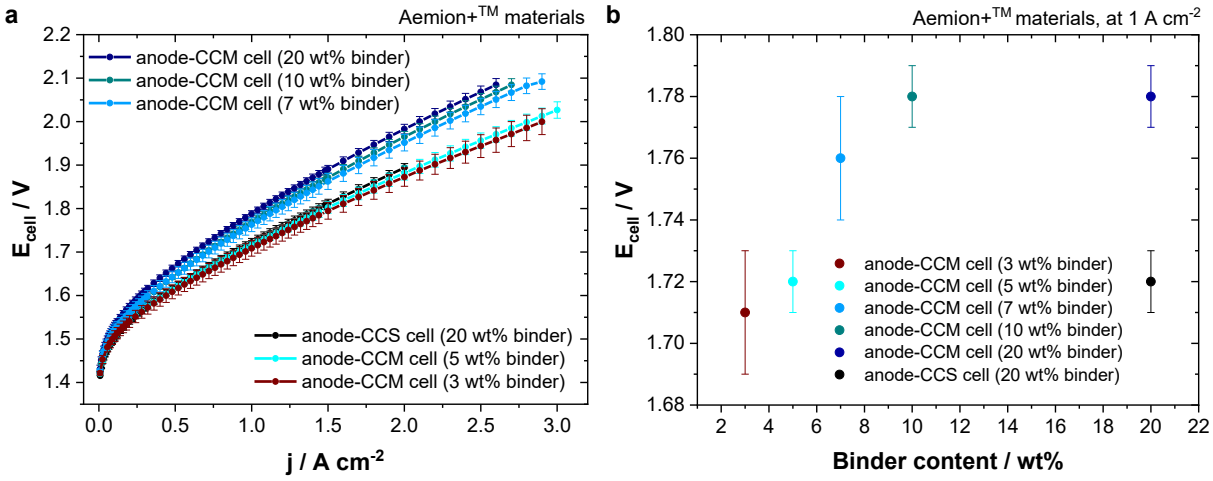

Figure 5.51. Comparison of anode-CCM cells with different binder contents (5, 7, 10, 20 wt%) in the catalyst dispersion to the anode-CCS cell (20 wt% binder) and among each other: (a) Polarization curves, (b) Cell voltages obtained at 1 A cm^{-2}. The MEAs were fabricated based on Aemion+™ materials. All components, except the MEAs are identical. Cathode: Pt/C 0.6 mg cm^{-2} (25 wt% binder). Testing conditions: 1 M KOH, 60 °C.

Halving the binder content to 10 wt%, only a minor performance improvement from 1.79±0.01 V (20 wt% binder) to 1.78±0.01 V at 1 A cm^{-2} was obtained. An even lower binder content of 7 wt% in the anode-CCM increased the cell performance further to 1.76±0.02 V. The lowest binder contents finally resulted in highest single-cell performance reaching 1.72±0.01 V and 1.71±0.02 V at 1 A cm^{-2} for the 5 wt% and the 3 wt% anode-CCM cells, respectively. Notably, the iR-corrected curves show an even clearer benefit: the 3 and 5 wt% anode-CCMs outperform the anode-CCS, with 5 wt% appearing optimal in the iR-corrected comparison.

This general trend aligns with findings by Huang et al. made in 2020, where a different set of materials was used and the examined ionomer contents ranged from 15 to 45 wt%. Similar to the results discussed here, the researchers observed that the lowest ionomer content led to improved performance.[150] In 2021, a similar trend was presented, when the lowest analyzed 4 and 7 wt% binder contents were proposed to be optimal for a full-CCM single-cell configuration, based on the catalysts IrO_2 and Pt/C and Aemion+™ materials.[148] This was explained by the possibly higher porosity and higher accessibility of catalytically active sites within the CL when reduced binder contents were used. These insights support the idea that cell performance can be binder-limited, and minimizing binder, while still ensuring ionic percolation, is key to high-performance electrolyzer operation.

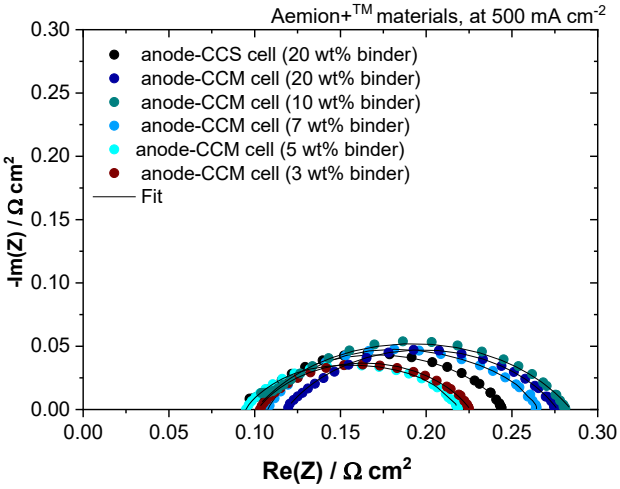

Figure 5.52. Comparison of anode-CCM cells with different binder contents (5, 7, 10, 20 wt%) in the catalyst dispersion to the anode-CCS cell (20 wt% binder) and among each other: Nyquist plots obtained from impedance spectroscopy at 500 mA cm^{-2} incl. simulated fits. Cathode: Pt/C 0.6 mg cm^{-2} (25 wt% binder). Testing conditions: 1 M KOH, 60 °C.

Figure 5.52 presents the Nyquist plots recorded at 500 mA cm^{-2} for all cells; R_{ct} and R_{Ohm} values are summarized in Table-A 11. The anode-CCS (20 wt% binder) and the anode-CCM with 5 wt% binder exhibit identical R_{Ohm} values of 95 mΩ cm^2. The anode-CCM cells with 3, 7 and 10 wt% binder show progressively higher R_{Ohm}, culminating in the value of 118 mΩ cm^2 observed for the 20 wt% binder anode-CCM. These R_{Ohm} variations reflect combined contributions from the electrical resistance of the CL, PTLs, as well as the ionic resistance of the AEM or binder. Aside from the structural difference between CCM and CCS configurations, all parameters were kept constant, indicating that the observed R_{Ohm} trends predominantly arise from changes in the CL's ionic resistance. Notably, the 3 and 5 wt% binder anode-CCM cells exhibited smallest R_{ct} values, both around 124 mΩ cm^2, indicating improved catalyst accessibility and interfacial charge transfer.

Stability tests

Short-term 16 h galvanostatic hold tests were conducted to access the operational stability of the anode-CCM and the anode-CCS cells (Figure 5.53). To accelerate potential degradation, the cells were operated at 1 A cm^{-2}, comparable to test on DURAION®-based cells, but twice the current density previously reported for Aemion+™ systems.[17] Although these tests are not repeated, the voltage evolution follows the trend of the initial polarization curves (Figure 5.51), indicating consistent short-term behavior with pristine performance.

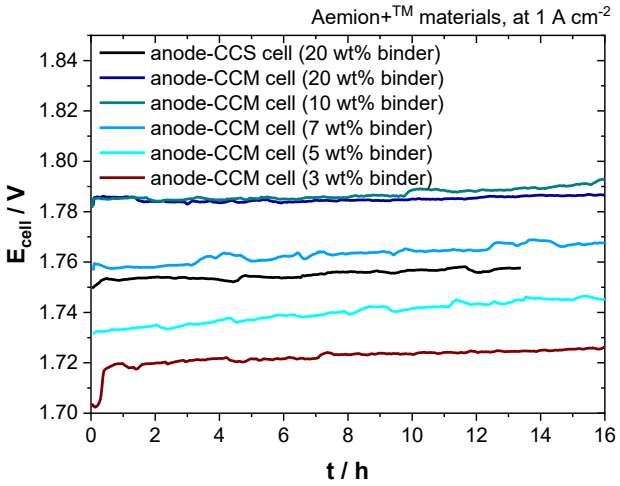

Figure 5.53. Cell voltage changes during 16 h (or 13 h for the anode-CCS cell) single-cell operation at constant 1 A cm^{-2} of anode-CCMs with varying binder content (3, 5, 7, 10, 20 wt%). The MEAs are fabricated using commercial Aemion+™ materials. Cathode: Pt/C 0.6 mg cm^{-2} (25 wt% binder). Testing conditions: 1 M KOH, 60 °C.

All single-cells withstood the durability test of 13 or 16 h, exhibiting negligible degradation. Considering the corresponding operation times, the degradation rates can be sorted in increasing order as follows: anode-CCM (20 wt% binder)—0.01 mV h^{-1}, anode-CCM (10 wt% binder)—0.37 mV h^{-1}, anode-CCM (3 wt% binder)—0.51 mV h^{-1}, anode-CCS (20 wt% binder)—0.59 mV h^{-1}, anode-CCM (7 wt% binder)—0.69 mV h^{-1}, anode-CCM (5 wt% binder)—0.83 mV h^{-1}. These results reveal a much smaller degradation rate than previously reported for similar CCS-based single-cells.[164] Considering both activity and short-term stability, all tested anode-CCM cells demonstrated good performance. Among them, an anode ionomer content of 3 and 5 wt% offered the most favorable balance between initial efficiency and resistance to performance loss at 1 A cm^{-2}. Longer term measurements would be required for more detailed analysis, which was not possible due to time constraints.

Morphology of the catalyst layers

The lower R_{ct} observed for the anode-CCMs with reduced binder content likely reflects higher accessibility of catalytically active sites, consistent with the more pronounced porosity and structural heterogeneity of the CL seen in cross-sectional SEM images (Figure 5.54).

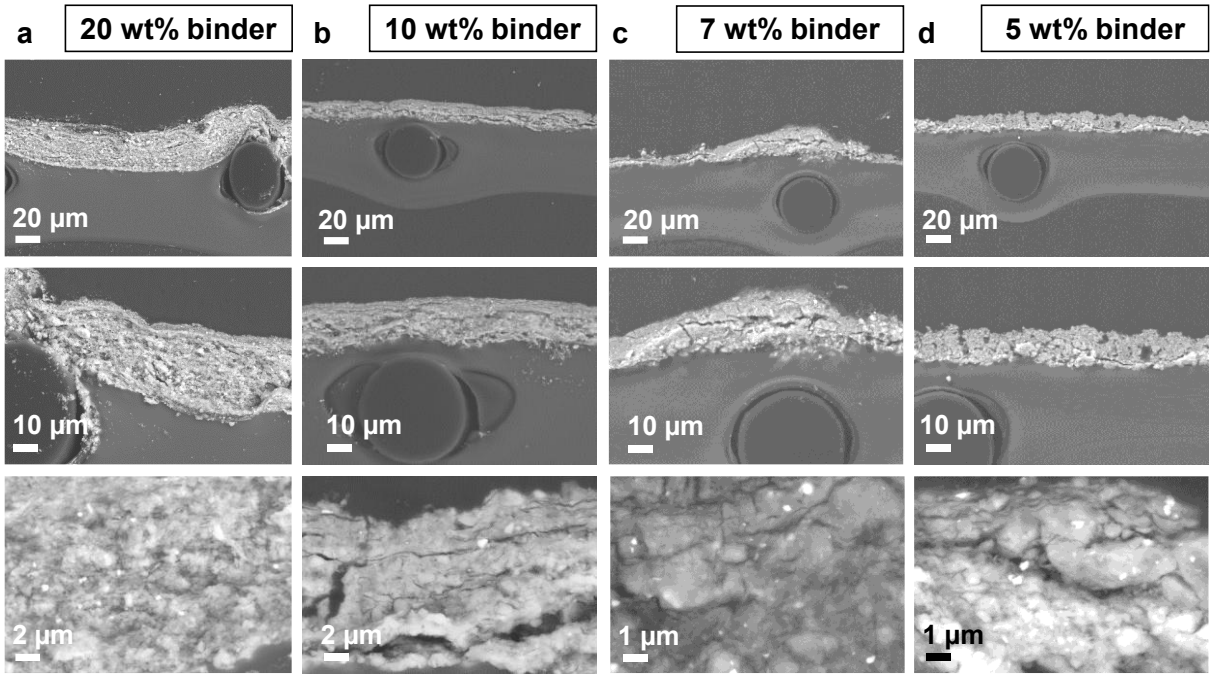

Figure 5.54. SEM images of the anode-CCMs from cross-section view at magnifications x500, x1000, x5000 (from top to bottom): (a) anode-CCM with 20 wt% ionomer, (b) anode-CCM with 10 wt% ionomer, (c) anode-CCM with 7 wt% ionomer, (d) anode-CCM with 5 wt% ionomer, The catalyst loadings are 2 mg cm^{-2} for all the presented CLs. The AEM and binder are commercial Aemion+™ materials. Here, the anode-CCM (3 wt% binder) is missing; presumably the structure would be similar to the one with 5 wt%. The dark-grey circles are the cut PEEK reinforcement mesh parts in the AEM.

All CL show sufficient initial adhesion to the membrane, as no delamination could be found; however, their bulk morphologies differ. The more porous CL structures likely increase active-site exposure and can therefore enhance catalytic activity. As discussed above, robust CL-AEM adhesion is important not only after fabrication but also after single-cell operation, which can promote partial CL transfer to the PTL. For Aemion+™-based anode-CCMs, the level or amount of CL transfer from AEM to PTL depended on the ionomer content in the CL (Figure-A 29). Although a higher binder content did not result in high single-cell performance, it reduced the CL transfer from the AEM to the PTL. In contrast to the DURAION®-based anode-CCMs, all Aemion+™ CCMs (3–20 wt% binder) adhere well initially (Figure 5.54), and noticeable imprinting/transfer is only observed after operation. CL transfer phenomena have been reported previously for Aemion+™ membranes (type AF1-HNN5 and AF1-HNN8),[17] although the explanation was not given further than by partial catalyst (Ir, Pt/C) dissolution. In this work, insufficient interfacial robustness is attributed primarily to fabrication- and ink-related factors that may not yet be optimized for the Aemion+™ materials. Future improvements may include ink reformulation tailored to the membrane chemistry and targeted AEM surface pre-treatment to strengthen interfacial adhesion.

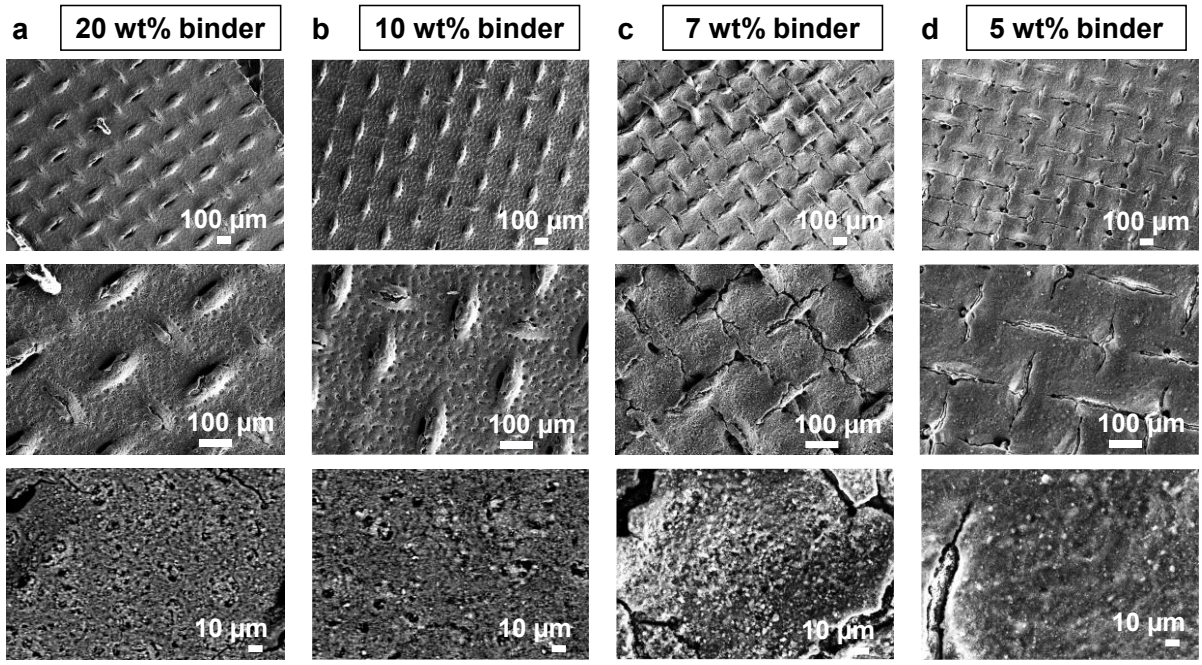

Figure 5.55. SEM images of the anode-CCMs from top-view at magnifications x100, x250, x1000 (from top to bottom): (a) anode-CCM with 20 wt% ionomer, (b) anode-CCM with 10 wt% ionomer, (c) anode-CCM with 7 wt% ionomer, (d) anode-CCM with 5 wt% ionomer. The catalyst loadings are 2 mg cm^{-2} for all the presented CLs. The AEM and binder are commercial Aemion+™ materials by Ionomr. The repeated pattern are marks from the reinforcement net.

The surface topographies of the anode-CCMs are shown in Figure 5.55, while the anode-CCS (20 wt% binder) is presented in Figure-A 34. The anode-CCS reveals a non-uniform coverage of the Ni PTL, with some spots showing only individual fiber coatings and others displaying larger CL-covered areas. In contrast, the anode-CCMs form largely well-integrative continuous CL films. The dominant visible features arise from the reinforcement network. At the 10 µm scale, the 20 and 10 wt% binder anode-CCMs appear particularly uniform, with some porosity observed, but no visible cracks.

For the layers with 5 and 7 wt% binder, significant crack formation is observed likely due to mechanical tension in the CL between and on the fibers or a brittleness of the layer. With a decreased binder amount in the anode-CCMs, these cracks become more pronounced. Partly, the cracks are likely due to the structure of the AEM itself, as the reinforcement network peek out from the surface. The observations are in contrast with those made by Koch[148] and Cossar[164], who attributed crack formation to increased dispersion instability with higher binder content.

Thicker catalyst layers are generally more prone to crack formation, a phenomenon primarily attributed to capillary forces arising during the drying process. As the solvent evaporates, capillary pressure develops within the porous structure of the wet catalyst ink. In thicker layers, these forces become more pronounced due to longer diffusion paths and a greater volume of solvent retained within the microstructure. The resulting stress gradients can exceed the mechanical cohesion of the catalyst film, leading to tensile stress accumulation and subsequent crack propagation.

In this work, no catalyst dispersion instability was observed, and a higher amount of binder maintained the integrity of the CL better than the layer with less binder.

The optimal binder content is a key factor in electrode design. Increasing the ionomer amount in the CL usually enhances anionic conductivity, yet it may also fill porous spaces, negatively affecting mass transport and interrupting electrical connections between catalyst particles by electrically isolating them. On the contrary, a reduced amount of anionic conductive binder could undesirably influence performance too: it may lead to better formation of the TPB with reduced isolation of electrically conductive catalyst particles but may not provide enough ionic conductivity. Therefore, it is critical to find the right content of ionomer in the CL to ensure both adequate ionic and electronic conductivity. For DURAION®-based anode-CCMs, an optimal ionomer content of 10 wt% was found, while for Aemion+™-based CLs, a content of 3 to 5 wt% seem to be suitable. This discussion underscores the important role of ionomer content in electrode design and the importance of careful parameter optimization when shifting between electrode configurations, such as from CCS to CCM electrodes.

5.4.2 PERFORMANCE RESPONSE TO IN SITU ELECTROLYTE CONCENTRATION SWITCHING

In this work as well as in many previous studies,[87,91,148,152,178] electrochemical cells are often tested under different operating conditions to investigate the influence of various parameters. Among the most examined factors are temperature, electrolyte composition, and concentration. Many of these aspects have already been discussed in detail in Chapter 5.1.4. In earlier experiments of this work, a new MEA was assembled for each test involving a change in electrolyte. In contrast, this present chapter focuses on the investigation of residual KOH electrolyte during single-cell operation, possibly retained in hardware, components or materials, and their impact on the electrochemical performance of the single-cells. During these electrolyte switching tests, the MEAs were not replaced, allowing for the observation of performance changes resulting only from variations in electrolyte concentrations.

The presence of KOH electrolyte residues is a crucial factor to consider when switching to pure water or less concentrated electrolytes during cell testing. A frequently used method for operating AEM single-cells in pure water (or low-concentrated alkaline) environment involves first conditioning the cell and the components in an alkaline electrolyte, possibly then purging it with pure water, and finally assessing its performance.[82,89,90,92] Moreover, the AEM ex situ conditioning is usually performed in higher concentrated electrolyte than used during electrochemical testing. The transition from the activation conditions to the single-cell testing environment often lacks detailed specifications, such as the duration of MEA or AEM soaking, system flushing protocols, and the exact amount of electrolyte used.[89,92,175,425,426] These details are often overlooked, which can significantly impact the reproducibility and comparability of results across different studies. While these aspects may be neglected, the shift in electrolyte concentration can positively or negatively influence the following measurements, thereby affecting the reliability of experimental results. Studies involving changes in KOH electrolyte concentration should thus be carefully adjusted in terms of electrolyte choice for pre-soaking the AEM, and possibly electrodes, and ensuring the purity of the testing set-up.

In 2022, Hassan et al. demonstrated that, after switching from alkaline operation to DI H_2O feed, the system requires several hours to reach its intrinsic performance level under pure-water conditions.[85] A PtNi-coated carbon felt cathode and IrO_x-coated Ni felt anode were operated in a

CCS-configuration, while the electrolyte feed was switched from 0.3 M KOH to DI H_2O. Building on this, the present study adopted a back-and-forth testing protocol in which the electrolyte concentration was changed between 1 M and 0.1 M KOH in a sequence of five stages (four switches), while continuously tracking single-cell performance. Both MEA configurations, the CCS- and CCM-MEAs, were evaluated using the pre-commercial DURAION® AEM and the corresponding anion-conducting binder. Because pure-water operation was unstable in this setup, only 0.1 M KOH was selected as the lowest concentration. This choice also avoids a key pitfall reported in earlier work: conditioning with alkaline electrolyte can leave residual KOH that artificially boosts apparent "pure-water" performance unless the system is extensively purged.[90,425] More generally, conditioning ex situ or in situ in the electrolyte used for testing is required to obtain representative results, as implemented previously in this work (Chapter 5.1.4).

Here, MEA components were ex situ conditioned in 1 M KOH and then assembled for testing, where 1.5 L 1 M KOH was used as the circulating electrolyte for each initial test. Between electrolyte changes, the system was flushed with 2 L of DI H_2O for 1 h for. Then, the next electrolyte was filled into the system. More details are described in the Experimental part (Chapter 4.4).

Figure 5.56 shows the performance behavior of a full-CCS single-cell tested in alternating electrolyte concentrations. At the start and end of each 20 h stability test (Figure 5.56a), polarization curves (Figure 5.56c–d) and EIS data (Figure 5.56b) were recorded; Nyquist plot obtained after 20 h operation are shown in Figure-A 35a. Due to an error, a constant current was applied during the first test, while for the subsequent four tests, a constant voltage of 1.8 V was hold throughout the 20 h.

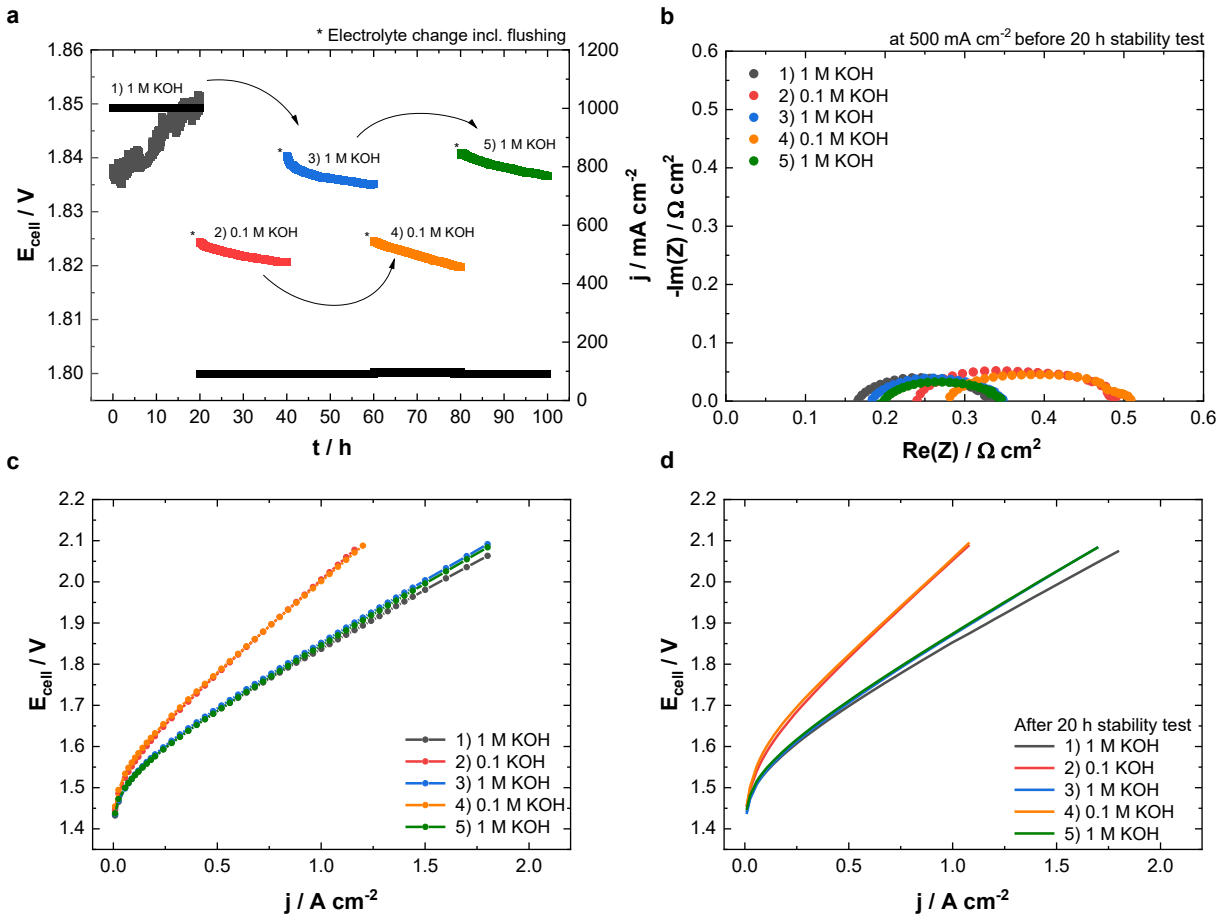

Figure 5.56. The performance behavior of a full-CCS single-cell evaluated in varying electrolytes in the following testing order: 1) 1 M KOH, 2) 0.1 M KOH, 3) 1 M KOH, 4) 0.1 M KOH, 5) 1 M KOH. (a) Test 1 was conducted for 20 h at a constant current of 1 A cm^{-2}, tests 2-5 were performed at a constant voltage of 1.8 V, with the corresponding voltage or current response recorded. The timeline presents only the testing time, except the electrolyte exchange pauses, (b) Nyquist plots obtained from impedance spectroscopy measurements recorded at a current density of 500 mA cm^{-2}; polarization curves tested (c) before and (d) after the 20 h stability test. Anode: Ni_3Fe-LDH 2 mg cm^{-2}, 20 wt% binder. Cathode: Pt/C 0.6 mg cm^{-2} (25 wt% binder), DURAION® materials, tested at 60 °C.

The comparison between the tests 1-3-5 and 2-4 allows an evaluation of the overall performance alteration trend, the reproducibility after changing the electrolyte back and forth, and the immediate performance behavior following an electrolyte switch within a 20 h period.

For test 1, conducted at 1 A cm^{-2}, a slight increase in cell voltage from 1.84 to 1.85 V was observed, indicating a decrease in cell performance. Despite this, the overall performance remained comparable to the results reported earlier for the anode-CCS configuration.

Switching to a lower concentrated electrolyte led to a decrease in cell performance, as expected.[87] Both tests conducted in 0.1 M KOH (tests 2 and 4) and at 1.8 V showed a slight decrease in current density over the tests duration from ≈550 to 460 mA cm^{-2}. For the tests 3 and 5 in 1 M KOH, also reproducible current density decreases of 850 to 750 mA cm^{-2} were observed. Despite the intervals for flushing and repeated electrolyte exchanges, which can affect the MEA components, likely the anion-conducting compound, the performance level and trend were reproducible. The tests 2–4 and 3–5

show a good reproducibility, therefore, a noteworthy degradation of the MEA components due to the electrolyte switching can be excluded[427,428] at least during the presented testing times. The current-time curves during the 20 h tests clearly showed a decline, with no initial performance improvement in the early hours of the test, unlike what has been observed in similar studies.[85,425] This trend shows neither a residual positive effects from higher-concentration electrolytes after flushing, nor a negative effect after the low concentrated electrolytes. This suggests that the short flushing of 1 h was sufficient and effective in removing residual electrolytes, ensuring that following tests were solely influenced by the newly introduced concentration. At first glance, the performance decrease observed within each 20 h test seems to contradict the overall conditioning and durability trends discussed over 1000 h of operation in Chapters 5.2.1 and 5.3.5 (Figure 5.16, Figure 5.40). However, this short-term trend aligns with the performance decline noted in the initial testing hours of CCM-based MEAs, as Figure 5.46 and Figure 5.47. As discussed in Chapter 5.5, such variations in the break-in period are expected and do not necessarily indicate different intrinsic changes in the materials.

The Nyquist plots recorded before and after the 20 h tests (Figure 5.56b and Figure-A 35a) support this observation. Notably, they show a slight increase in R_{Ohm}, while the observed semicircle progressively shrinks with each subsequent test, indicating decreasing interfacial/charge-transfer losses. This trend mirrors the behavior observed during the first 100–200 h of operation for the full-CCS single-cell discussed earlier (Chapters 5.2.1 and 5.3.5).

The experiment was repeated with an anode-CCM containing 20 wt% binder. Given the differences between the MEA configurations, particularly in CL structure, distribution, and contact with the AEM, it was anticipated that both the CL and AEM are less accessible to electrolyte penetration in the CCM setup. Consequently, a different behavior in this experiment could be expected.

Figure 5.57 shows the cell current density changes within each constant voltage test of 20 h (at 1.8 V). As in previous experiments, although the timeline is presented as a continuous test, electrolyte exchange was carried out between each 20 h test, following the procedure described earlier. Additionally, polarization curves were recorded at both the beginning and end of each 20 h stability test to monitor performance changes over time (Figure 5.57c–d). Nyquist plots recorded before the stability test are presented in Figure 5.57b, those after the 20 h test are shown in Figure-A 35b.

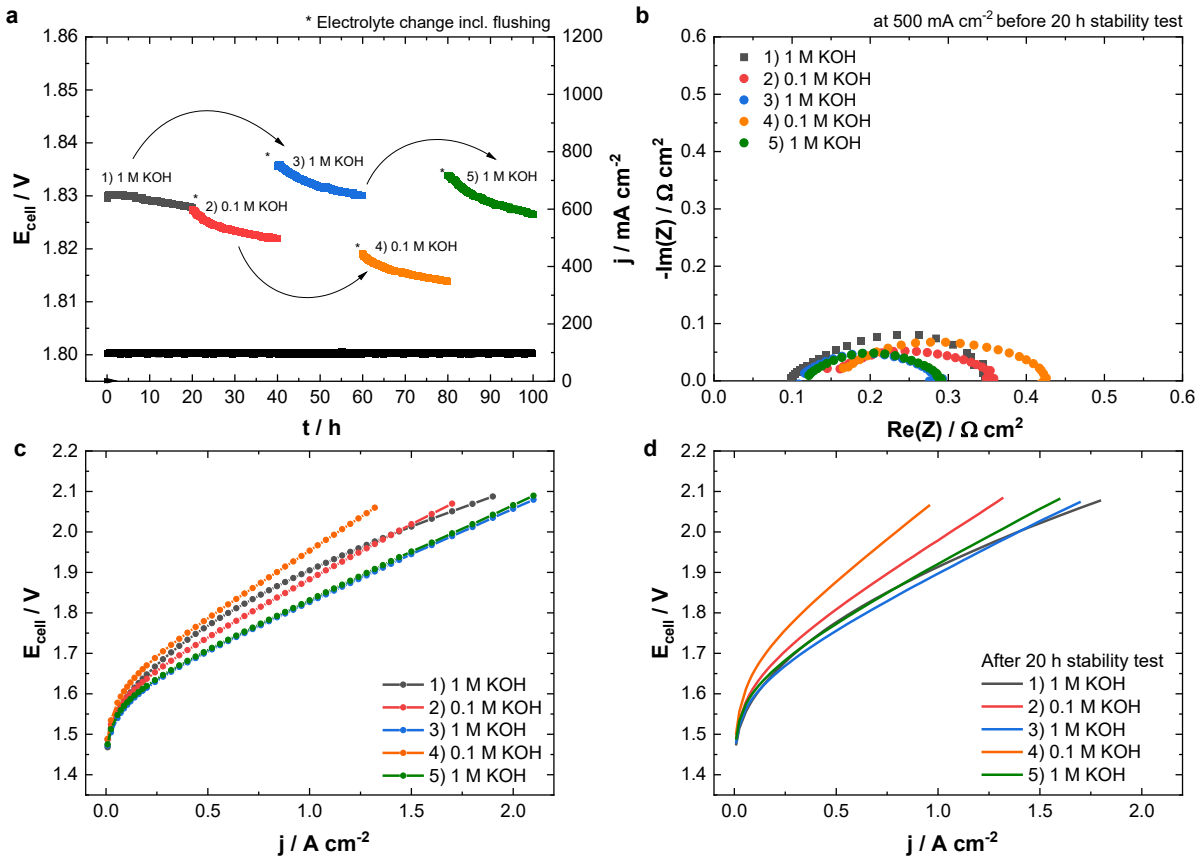

Figure 5.57. The performance behavior of an anode-CCM single-cell evaluated in varying electrolytes in the following testing order: 1) 1 M KOH, 2) 0.1 M KOH, 3) 1 M KOH, 4) 0.1 M KOH, 5) 1 M KOH. (a) 20 h stability tests were performed at a constant voltage of 1.8 V, with the corresponding voltage or current response recorded. The timeline presents only the testing time, except the electrolyte exchange pauses, (b) Nyquist plots obtained from impedance spectroscopy measurements recorded at a current density of 500 mA cm^{-2}; polarization curves tested (c) before and (d) after the 20 h stability test. Anode: Ni_3Fe-LDH 2 mg cm^{-2}, 20 wt% binder. Cathode: Pt/C 0.6 mg cm^{-2} (25 wt% binder), DURAION® materials, tested 60 °C.

Interestingly, unlike the full-CCS single-cell, the anode-CCM cell tested in 1 M KOH (tests 1, 3, and 5) demonstrate an initial improvement in cell performance (from test 1 to 3), followed by a stabilization (test 3 vs. 5). The trend as shown in Figure 5.57a, aligns with the 500 h durability test behavior of a similar anode-CCM single-cell, where performance improved over the first 100 h of operation (Figure 5.47) and was considered as part of the single-cell break-in time.

This improvement is most evident in the polarization curves and Nyquist plots (Figure 5.57b–d; black vs. blue). The decrease in R_{ct} suggests that the performance increase mainly originates from changes within the CL or/and at the CL-AEM interface rather than from the membrane itself.

The first switch to the lower electrolyte concentration (between tests 1 and 2) did not markedly change the performance behavior (Figure 5.57c, black vs. red), although the 20 h voltage-hold shows a faster decay in 0.1 M KOH (5.3 mA h^{-1}) than in 1 M KOH (2.2 mA h^{-1}). A minor influence of residual 1 M KOH cannot be fully excluded, but the subsequent tests (2–3, 3–4, and 4–5) show clear concentration-dependent differences, arguing against residual electrolyte as the dominant driver.

Repeated operation in 1 M KOH (tests 3 and 5) yielded nearly identical results, with no significant deviations observed either between the tests or over the 20 h period (Figure 5.57a blue vs. green). In contrast, operation in 0.1 M KOH (tests 2 and 4) showed decreased reproducibility, and a clear performance loss. Initially, the cell reached 715 mA cm^{-2} at 1.8 V, while after switching back from 1 M KOH, only 555 mA cm^{-2} were achieved. Nyquist plots (Figure 5.57b, red vs. orange) confirm this trend: R_{Ohm} changes slightly, whereas the semicircle enlarges in test 4, indicating increased R_{ct} and suggesting degradation within the CL or/and the CL-AEM interface. Consistent with this, post-test inspection reveals extensive CL delamination from the AEM and transfer to the Ni PTL, making the CCM interface a key topic for the following subchapter.

Across all 20 h tests, the current-time curves consistently decline, confirming that no unexpected improvements in performance appear and supporting that the electrolyte exchange protocol effectively avoids concentration carryover within the 0.1–1 M KOH window.

In the case of a standard full-CCS single-cell, the observed performance trend is consistent. However, the CCM-based cell requires further research to understand the intrinsic changes and the factors influencing the uneven trend observed during the initial hours of operation, or the first two tests when switching electrolyte concentrations back and forth. Another critical question raised by this study is why the CCM-based cell appears to degrade faster in 0.1 M KOH compared to operation in 1 M KOH.

The electrolyte exchange procedure, draining first 1 M KOH without allowing the cells to run dry, followed by flushing with 2 L DI H_2O for 1 h, is sufficient to avoid residual electrolyte carryover when switching between 1 and 0.1 M KOH. For intended DI H_2O operation, larger flushing volumes and/or repeated flush cycles will likely be required to remove residual alkaline species. DI H_2O testing is beyond the scope of this study due to AEM batch limitations, but the results provide guidance for adjusting protocols across electrolyte concentrations.

Unlike Chapter 5.1.4, where a new MEA was assembled after each electrolyte change, the present data indicate that in situ concentration switching can be adequate if MEA integrity is maintained, reducing variability from repeated assembly (while noting that gradual MEA changes during prolonged operation must be considered). Overall, the work highlights the need for strict control and documentation of test conditions to ensure reproducibility and correct attribution of observed trends.

5.4.3 ION TRANSPORT DIFFERENCES BETWEEN CCS AND CCM-BASED CELLS

In the previous electrolyte-residue study comparing anode configurations, all electrode parameters (2 mg cm^{-2} Ni_3Fe-LDH, 20 wt% binder) and testing conditions were kept constant. Under these conditions, the anode-CCM single-cell showed a less predictable performance trend: during the first ≈50 h, only minor performance variations were observed in both 1 M and 0.1 M KOH, whereas the anode-CCS cell responded more clearly to electrolyte concentration changes. The origin of these phenomena remained unclear.

SEM (Chapter 5.4.1), the two electrode architectures differ significantly. The anode-CCM forms a continuous, dense CL that ensures strong AEM contact but interacts with the PTL only via the upper fiber layers. In contrast, the anode-CCS exhibits a porous, fiber-distributed CL, providing increased surface area and improved electrolyte accessibility.[83] As CCS performance is strongly electrolyte-dependent,[123] it should benefit from concentrated KOH, whereas the CCM could become advantageous at low KOH or water feed where CL-AEM contact dominates transport.[423]

A concentration-dependent study is therefore performed using the same anode configurations as in Chapter 5.4.2, but with a new batch of MEAs. Testing followed the protocols outlined in the Experimental section and the electrolyte-switching procedure presented in Chapter 5.4.2.

Both anode-CCM and anode-CCS cells were tested at 1 A cm^{-2} while KOH was varied from 1 M to 0.01 M and back, in three rounds (13 tests, 312 h of operation). The resulting cell voltages are shown in Figure 5.58a. R_{Ohm} and R_{ct} derived from Nyquist plots at 500 mA cm^{-2} are presented in Figure 5.58b.

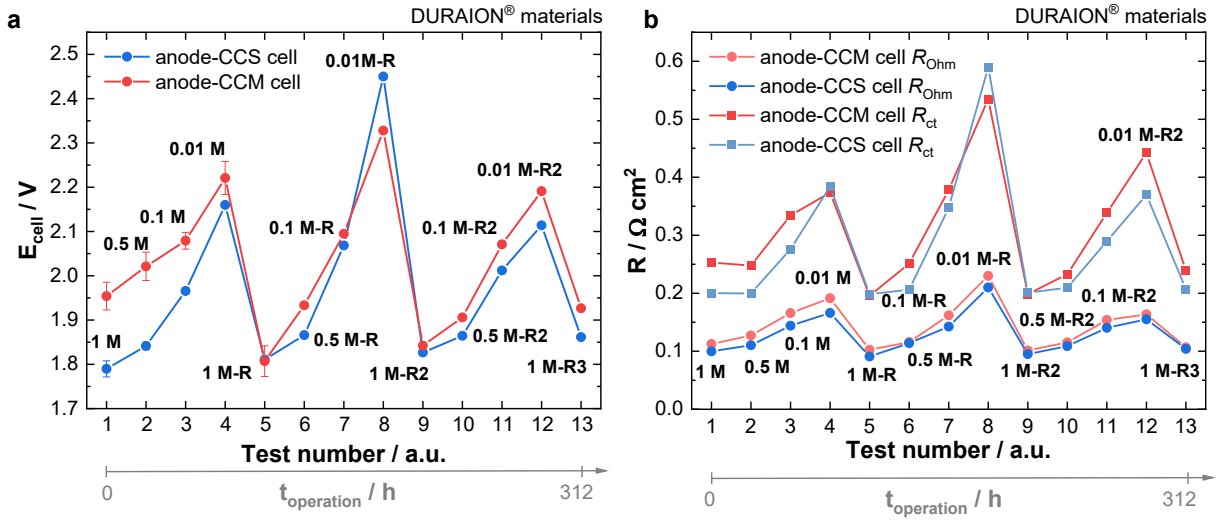

Figure 5.58. Performance comparison of anode-CCS and anode-CCM single-cells obtained in varying electrolytes in the displayed testing order: (a) Cell voltages at 1 A cm^{-2}, (b) R_{Ohm} and R_{ct} obtained from Nyquist plots recorded at 500 mA cm^{-2}. Anode: Ni_3Fe-LDH 2 mg cm^{-2}, 20 wt% binder. Cathode: Pt/C 0.6 mg cm^{-2}, 25 wt% binder, DURAION® materials, tested at 60 °C. "R" stands for repeat and is used when the cell has already been tested in the specified electrolyte.

In the first electrolyte concentration reduction run (test 1–4), the anode-CCS outperforms the anode-CCM cell, consistent with previous results (Chapter 5.4.1); but the performance gap narrow as concentration decreases. At 0.01 M KOH (test 4), cell voltages are close within uncertainty: 2.16±0.01 V for the anode-CCS and 2.22±0.04 V for the anode-CCM cell. No clear cross-over point in performance is observed.

In later rounds of electrolyte-switching tests (tests 5–9 and 9–13), both cells behave more similarly across concentrations, aside from a likely outlier (test 8), anode-CCM remains slightly worse and the strong initial difference largely vanishes by the return to 1 M KOH (test 5). This raises whether CCS/CCM comparisons should emphasize early operation (break-in active) or only stabilized behavior, consistent with earlier long-term observations.

EIS data (Figure 5.58b) mirrors these voltage trends (resistance values summarized in Table-A 12). The anode-CCM shows slightly higher R_{Ohm} than the anode-CCS across all tests, largely independent of concentration (as already seen in Chapter 5.4.1). A lower CCM binder content (as the previously optimized 10 wt%) would likely reduce R_{Ohm}. R_{ct} reflects the performance trend, with the anode-CCS showing lower R_{ct} during early tests (1–3); averaging of values makes the R_{ct} contrast appear smaller than the voltage separation. This suggests that the direct relationship between performance and electrolyte concentration should be explained by R_{Ohm}. An overall higher R_{ct} in the anode-CCM cell, regardless of electrolyte pH, suggests less efficient charge transfer.

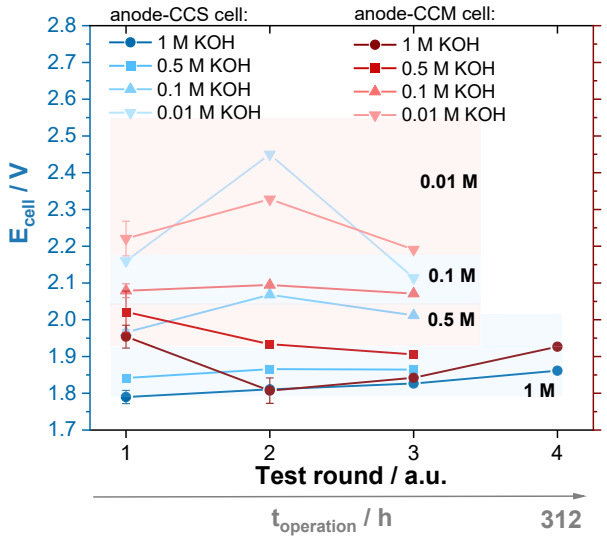

Figure 5.59. Voltages at 1 A cm^{-2} of anode-CCS (blue) and anode-CCM (red) single-cells obtained in varying electrolytes displayed in testing rounds derived from Figure 5.58. Anode: Ni_3Fe-LDH 2 mg cm^{-2}, 20 wt% binder. Cathode: Pt/C 0.6 mg cm^{-2}, 25 wt% binder, DURAION® materials, tested at 60 °C.

The degradation or alteration within specific electrolyte concentration could reveal insight into the specific cell behavior at a specific pH environment. Figure 5.59 complements Figure 5.58 by reorganizing the dataset by electrolyte and testing round, highlighting time trends within an electrolyte. An early voltage decrease is visible not only in 1 M but also in 0.5 M (first ≈160 h; pH decrease from 14 to ≈13.7), whereas at lower pH no consistent improvement trend emerges and scatter increases (especially at very dilute 0.01 M KOH). Importantly, no turning point is observed at 0.1 M where CCM clearly outperforms CCS.

These trends are unexpected, and their origin cannot be established without further investigation. Nevertheless, the small performance gap between CCS and CCM suggests three likely contributing factors: (i) material-effects, (ii) role of binder, and (iii) delamination issues.

(i) Catalyst activity, degradation and AEM transport are pH-dependent, low KOH approaches water-like limits for OH^- transport in both AEM and binder-containing CLs.[85,287,337]

(ii) The binder is the most likely driver of electrolyte-dependent CCS/CCM differences. It must provide OH^- pathways without blocking pores or electronically isolating catalyst. In concentrated KOH, intrinsic

ionomer conductivity is less critical; at low KOH or water feed it becomes the dominant OH^- conductor. Thus, a strong CCM drop with decreasing KOH suggests insufficient intrinsic binder conductivity, an effect proposed for Aemion™.[147]

(iii) CL connectivity to the AEM in CCMs and to the PTL in CCS can dominate the observed trends. CL transfer from AEM to Ni PTL was documented earlier (Figure-A 11 and Figure-A 27—Figure-A 30, Chapters 5.4.1—5.4.2). Here it becomes nearly complete after concentration switching, leaving only minor CL fragments on the AEM. Swelling and deswelling during concentration changes likely alter component dimensions, adhesion, and water-uptake matching between membrane and binder. The timing (during operation or disassembly) cannot be resolved; macroscopic in situ delamination is unlikely under constant compression, but micro-scale interfacial changes could explain why early CCS/CCM differences diminish later if the CCM architecture is no longer intact. Although binder and AEM chemical similarity should reduce interfacial resistance and swelling mismatch,[11] delamination persists, making CL-AEM connectivity a key target for scalable CCMs.

A limitation is that the anode-CCS included the optimal CL (20 wt% binder), whereas the anode-CCM likely performs better at 10 wt% binder. Parameters are kept constant to isolate architecture effects, but the next step is to repeat the concentration-dependent study using optimized electrodes for both architectures. Binder content and catalyst loading can shift architecture sensitivity, similar to reports in PEMFCs.[432]

5.4.4 SUMMARY

This chapter follows Approach 4 (Chapter 3, Q&A) to answer Q5: how CCS and CCM architectures influence performance and whether a tailored MEA can operate efficiently at reduced electrolyte concentration while remaining robust to residual KOH and interface degradation. The approach integrates (i) ionomer-content screening in CCMs, (ii) direct CCS–CCM comparisons using two AEM/binder pairs, and (iii) validated in situ electrolyte switching for controlled concentration-dependent testing. The main outcomes are:

- Increasing anion-conducting binder in the CL improves anion transport, but excess ionomer can fill pore space, hinder mass transport, and electronically isolate catalyst particles by forming an insulating phase. Conversely, lower ionomer contents can promote TPB formation and reduce catalyst isolation, but may not provide sufficient ionic pathways. Overall, CCM performance requires balancing ionic and electronic conductivity. In this study, the optimum is 10 wt% for DURAION®-based anode-CCMs, whereas 3–5 wt% provides the best compromise between performance and mechanical integrity for Aemion+™ anode-CCMs.
- Comparing CCS and CCM operation across electrolyte concentrations shows that the electrolyte exchange procedure, draining 1 M KOH without drying the cell and flushing with DI H_2O, effectively removes residues when switching between 1 M and 0.1 M KOH. This supports in situ concentration switching without rebuilding the MEA, reducing variability from repeated assembly. For intended pure-water operation, larger flushing volumes and/or

multiple flushing cycles would likely be required, and strict documentation remains essential for reproducibility.

- Performance trends across electrolyte concentration (varying pH) are non-trivial. At higher concentrations (0.1–0.5 M) the anode-CCS initially outperforms the anode-CCM, but voltages converge as concentration decreases to 0.01 M, and no clear advantage remains. This convergence may arise from strong electrolyte-dependent effects of the catalyst environment, limited anion conduction within the ionomer network in the catalyst layer of the CCM, or CCM-specific interface instability. Delamination of the CL and transfer to the PTL were observed after in situ testing. This can weaken the intended CL-AEM contact and make the CCM behave more CCS-like.

5.5 REPRODUCIBILITY CHALLENGES AND THEIR IMPACT ON RESEARCH OUTCOMES

The development of AEMWE technology remains in the research and development phase, particularly regarding membranes and catalysts. Many components are still pre-commercial or continuously evolving, leading to material variability that affects result reproducibility and raises concerns about data validity, especially in fundamental studies.

Over the three and a half years of this research, various catalyst batches and anion-exchange materials were used. Conducted within the CHANNEL project, this research provided anion-conducting materials as received or following recommended procedures, without additional quality control or benchmarking. However, in-house synthesized materials, components, and hardware were thoroughly tested for reliable quality and functionality.

It is essential to distinguish between reproducibility and repeatability. Each chapter represents a separate work package, with materials carefully selected and benchmarked to ensure repeatability within each study, typically spanning six months to a year. However, variations in catalyst, AEM, or binder batches between work packages influenced overall reproducibility across chapters.

To maintain focus on scientific outcomes, specific material batches were not emphasized throughout the work, as they were not critical to the core findings. This chapter highlights key material batches and their usage to address this gap. Despite variations in performance reproducibility between chapters, the presented findings remain valid, and this section serves to acknowledge possible limitations.

5.5.1 MATERIAL BATCHES, PERFORMANCE VARIABILITY, AND QUALITY CONTROL

This chapter discusses discrepancies in reproducibility of single-cell performance and voltage stability trends observed during the work on Chapters 5.2 and 5.4. Although identical hardware and test stations were used, absolute performance decreased over time, indicating batch-dependent variability in pre-commercial materials. While all tests are internally consistent within each experimental block (one parameter varied at a time), absolute values can differ across chapters; this introduces some scatter but does not change the overall trends and parameter dependencies.

A second reproducibility issue concerns DI H_2O cell operation: early batches showed reproducible single-cell operation (Figure-A 36), whereas later batches (Figure 5.12) failed within a few hours under identical conditions. Since pure-water stability is not guaranteed by the supplier datasheets, these outcomes are not pursued further.

To identify potential causes of performance variations, each component and parameter were examined individually. Differences in results and reproducibility could stem from multiple factors, including not only material batches, but also ion-exchange duration, storage time of raw materials and prepared components (electrodes and MEAs), and storage conditions.

Potential performance reductions may come from lower catalytic activity, changes in binder chemistry affecting ionic conductivity or functional group stability, batch-to-batch membrane variations, or modifications in test station setup and single-cell hardware. However, due to agreements with project partners, no direct testing or analysis of the AEM and binder was conducted. Proposed differences were solely based on observations, assumptions, and the exclusion of changes or degradation in the remaining components. Investigations focused on catalysts, electrodes, testing hardware, and storage and handling conditions.

Table 5.2 summarizes all material batches, test conditions, and performance results used in this thesis, with material changes highlighted in **bold**; the corresponding polarization curves and Nyquist plots are provided in Figure-A 37, while Figure 5.60 shows the time evolution of cell voltage and resistances (R_{Ohm}, R_{ct}). To address reproducibility, additional electrochemical tests are performed on selected batches, including older stored electrodes and new batches not used in earlier chapters (test 3 and 5), to identify potential causes of the observed discrepancies. For all tests, the optimized electrodes based on mTM-NiFe-LDH catalyst (Chapter 5.3) were used.

Table 5.2. Description of performance tests and trends presented in Figure 5.60 and Figure-A 37, incl. comments on test conditions and test results, and material batches. The changed components in each following test are marked bold. The observation begins with Chapter 5.3 as only the milled catalyst (mTM-NiFe-LDH) is considered.

Test number	Test / material description and Chapter[6]	Ni_3Fe-LDH batch (milled)	Membrane batch	Ionomer batch	Comment on test results
1	Baseline tests with high performance; Chapter 5.3	NiFe-1 (2020)	AEM-1 (12.2020)	Binder-1 (2020)	Reproducible baseline performance
2	First repeat with different catalyst batch, same binder and AEM batch; Chapter 5.4.1	**NiFe-2 (2021)**	AEM-1 (12.2020)	Binder-1 (2020)	UI and EIS results comparable → catalysts perform comparable

[6] Tests 3 and 5 are not linked to any earlier chapter and are performed additionally to support the observed performance evolution and reproducibility trends.

3	Electrode prepared simultaneously with those from test 1, different AEM batch used	NiFe-1 (2020)	**AEM-2 (2021)**	Binder-1 (2020)	R_{Ohm} higher, R_{ct} comparable→ Poorer performance due to different AEM or other contributors to Ohmic resistance
4	Repeat with different electrode, same membrane batch; Chapter 5.4.2, 5.4.3	**NiFe-3 (2021)**	AEM-2 (2021)	**Binder-2 (2021)**	R_{Ohm} and R_{ct} higher→lower performance due to electrode contribution and AEM storage
5	Repeat of test 4 with identical electrode, 3 months stored	NiFe-3 (2021)	AEM-2 (2021)	Binder-2 (2021)	Similar R_{Ohm}, R_{ct} higher→lower performance due to electrode contribution (storage effect)
6	Test with a new MEA, containing a new batch of catalyst, binder and AEM; Chapter 5.5.2	**NiFe-4 (2022)**	**AEM-3 (2022)**	**Binder-3 (2021-b)**	Lower R_{ct}→Performance higher than for previous repetition but lower compared to initial benchmark; comparable to test **4**
7	Test with newer binder; Chapter 5.5.2	NiFe-4 (2022)	AEM-3 (2022)	**Binder-4 (2022)**	Similar R_{ct}, slightly higher R_{Ohm}→Performance similar to previous repetitions but lower compared to initial benchmark, comparable to test 4 and 6

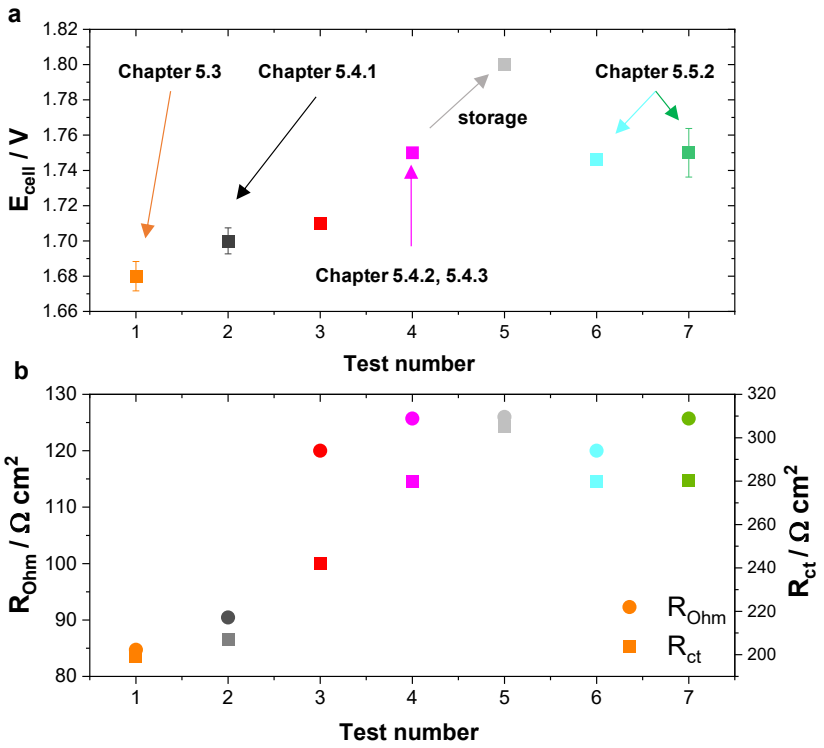

Figure 5.60.(a) Cell voltages obtained at 1 A cm^{-2} and (b) R_{Ohm} and R_{ct} values for the MEAs of each performance test, presented in and Table 5.2 and Figure-A 37. Tests 3 and 5 are not linked to any earlier chapter and are performed additionally to support the observed performance evolution and reproducibility trends.

Test 1 (orange) employed the first batch of milled Ni_3Fe-LDH, while test 2 (black) introduced a second catalyst batch keeping the anion-conducting materials unchanged. Performance remained within the error margins, with only a minor decrease, and comparable semicircle sizes were obtained in the Nyquist plots. This second catalyst batch was used in Chapter 5.4.1 and showed no significant differences relative to the first batch used in Chapter 5.3.

Next, a different AEM batch was introduced in test 3 (red), performed approximately one year after the first test. As the anode, an electrode fabricated at the same time as those used in test 1 (using the same binder and catalyst) was utilized. This test showed further performance drop. Both R_{Ohm} and R_{ct} increased, with the changes in R_{Ohm} being particularly pronounced. This behavior may originate from the AEM batch (as differences in thickness, swelling behavior, or chemistry) or degradation of electrodes during storage times. Although the electrodes are carefully stored sealed in PE plastic bags and protected from UV light, environmental factors such as temperature and humidity fluctuations are not monitored and may have affected polymer-containing components rather than the catalyst, which remains catalytically active even after years of storage. This MEA is not used elsewhere in the work.

In test 4 (pink-purple), a newly fabricated electrode was used with the same AEM as in test 3 but with different batches of catalyst and binder. This test showed a more significant performance decrease, primarily driven by an increase in R_{ct} (Figure 5.60b). The decline may reflect preparation and testing influences rather than intrinsic catalyst activity. The binder may have also played a role,[433] as visual

inspection reveals color variations from light yellow to orange, suggesting possible chemical changes during storage.

Test 5 (grey) showed the lowest performance observed in this study. Unlike the earlier tests that involved one or two batch changes, test 5 reused the same AEM and electrodes as test 4 after three months of storage. While R_{Ohm} remains similar, R_{ct} further increases, indicating that storage time again affects cell performance, consistent with the trend observed for test 3.

To complete the testing, two additional binders provided for the final durability experiments (Chapter 5.5.2), were introduced. Test 6 (light blue) replaced all components, including the catalyst, binder, and AEM, resulting in performance comparable to test 4, which was promising for further studies. Similarly, test 7 (green), likely a newly synthesized binder, produced similar results, confirming reproducibility for the final tests. Given the limited opportunity for additional screening, these components are selected despite the overall decline in absolute performance compared to earlier studies.

To exclude potential effects of the hardware (single-cell setup including periphery) and the test station, such as possible oxidation of the Ni flow-fields and bipolar plates, system contamination despite careful cleaning and maintenance, or degradation of any components that could impact final single-cell performance, a MEA with commercial Aemion+™ materials (Ni_3Fe-LDH on the anode and Pt/C on the cathode) was repeatedly tested. These tests were conducted with intervals of around one and a half years between them. The two tested MEAs were identically prepared, differing only in the Ni_3Fe-LDH catalyst batch. The membrane and binder remained the same as in previous tests, with the only variation being their age due to storage.

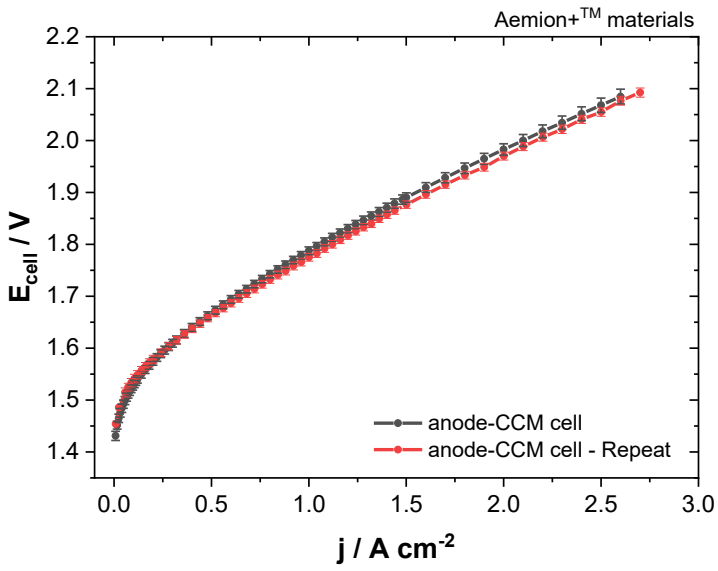

Figure 5.61. Electrochemical performance comparison of single-cells tested two years apart, emphasizing reproducibility of single-cell hardware and test station. The components as well as the testing conditions remain consistent. Anode: milled (mTM-NiFe-LDH) Ni_3Fe-LDH 2 mg cm^{-2} (20 wt% binder), Cathode: Pt/C 0.6 mg cm^{-2} (25 wt% binder). Testing conditions: 1 M KOH, 60 °C.

Figure 5.61 presents the polarization curves with error bars from three repetitions. The significant overlap of the curves confirms the reproducibility of electrochemical performance tests conducted under identical conditions though shifted in time. This finding excludes the possibility of hardware-related factors negatively contributing to the performance variations discussed earlier, thereby confirming the stability and reliability of the testing setup.

5.5.2 DECOUPLING CELL DURABILITY TRENDS FROM INTRINSIC ELECTRODE CHANGES

As shown, batch-to-batch variation in the anion-conducting materials led to measurable differences in single-cell performance, raising the question of how robust and transferable the conclusions from the preceding chapters are. In addition, the observed scatter in short-term performance implied that durability metrics may also be influenced by material variability and must therefore be interpreted with appropriate caution and batch context.

Durability tests with the unmilled catalyst (i-NiFe-LDH) were repeated after an interval of 1.5 years, following the protocol used in Chapter 5.2. Figure 5.62 shows the time-resolved cell voltage evolution for four MEAs. The blue curve corresponds to the test conducted in 2020 (Chapter 5.2). A 550 h test performed in 2022 (red curve) was conducted using an identical anode, but after a two-year storage, along with a cathode and AEM from different batches. Despite a higher absolute cell voltage, the stability trend is similar and includes a conditioning phase of ≈160 h; importantly, the estimated degradation rate remains comparable.

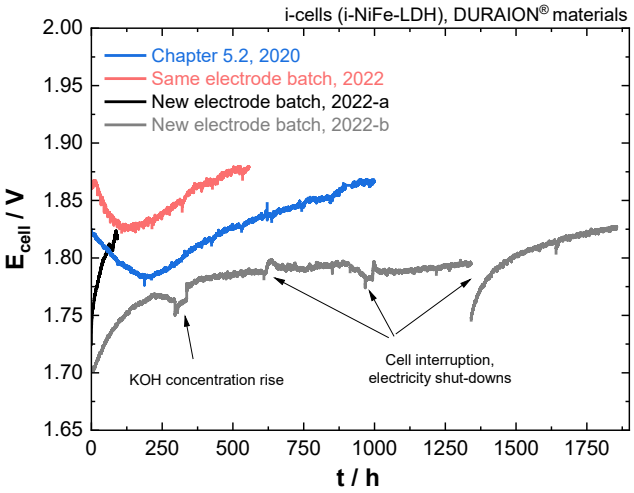

Figure 5.62. Single-cell durability tests presented as a time-resolved cell voltage change curve incl. reproducibility measurements, at a constant current density of 1 A cm^{-2}. Anode: Ni_3Fe-LDH 2 mg cm^{-2} (20 wt% binder); Cathode: Pt/C 0.6 mg cm^{-2} (25 wt% binder), DURAION® materials, CCS-MEA configuration. Testing conditions: 1 M KOH, 60 °C.

In contrast, newly fabricated anodes tested in 2022 (black and grey curves) show a different conditioning behavior. Instead of the performance improvement previously observed during the first 160-200 h, the cell voltage increases from the start, indicating immediate performance loss. The earlier conditioning behavior was attributed to processes such as NiFe anode activation (oxidation), Fe leaching and re-deposition toward an optimal surface composition, CL morphological evolution, and ionomer ion-exchange or swelling effects (Chapter 5.2). The altered 2022 response suggests that additional changes, potentially related to material batch variability, component aging, or fabrication-induced differences, overlap with or suppress these conditioning mechanisms.

To further investigate the observed trends, durability testing was repeated using anodes with the milled catalyst (mTM-electrodes, Chapter 5.3). Figure 5.63a compares the durability curve presented earlier (orange, Chapter 5.3.5), with two additional tests performed about one year of electrode storage (grey and green). In contrast to the i-cells (Figure 5.62), where time-shifted tests retained similar conditioning behavior, when using identical electrodes, even after some storage time, the mTM-cells showed a clear change in the initial voltage evolution. In the initial test (orange), the cell voltage decreased during the first 100 h, indicating a break-in period. In the later tests (green and grey), the voltage increased immediately. Despite this difference, both electrodes, one tested immediately in 2021 and the others after storage, showed comparable single-cell performance (Figure 5.65b). The slight performance loss could be attributed to electrode aging, leading to increased charge-transfer resistance (Figure-A 38). Importantly, although the presence or absence of an initial conditioning phase differs, the degradation rates beyond 100 h are comparable across the tests.

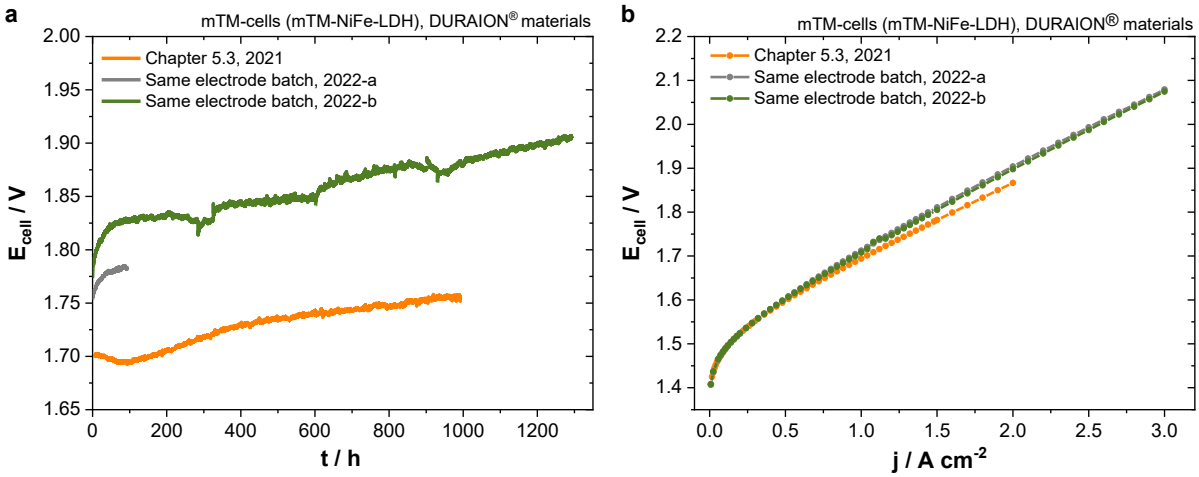

Figure 5.63. (a) Single-cell durability tests presented as a time-resolved cell voltage change curve incl. reproducibility measurements, at a constant current density of 1 A cm^{-2} (b) polarization curves of the same single-cells, recorded before the durability tests. Anode: mTM-NiFe-LDH 2 mg cm^{-2} (20 wt% binder), cathode: Pt/C 0.6 mg cm^{-2} (25 wt% binder), DURAION® materials, CCS MEA configuration. Testing conditions: 1 M KOH, 60 °C.

Comparing dynamic (polarization) and static (galvanostatic durability) measurements reveals noticeable differences (Figure 5.65 a vs. b). Across this work, the voltages at 1 A cm^{-2} derived from polarization curves often deviate from those measured under steady-state operation at the same current density; here, the newer MEAs even show a slightly lower initial voltage at the start of the durability test than in the polarization measurement. A plausible explanation is differing gas-bubble dynamics and evolving electrode surface coverage: during rapid polarization sweeps, the short dwell time at each current density promotes continuous transient surface conditions, whereas under static operation a more stable bubble population and wetted area establish over time, which can shift the apparent performance.

The origin of the differing conditioning-phase trends during the first hours of long-term testing remains unclear, and even the few studies that repeat durability experiments rarely provide a definitive explanation.[434] The observed variability likely reflects shifts in the relative contribution of conditioning-related processes, including differences in the initial oxidation state of freshly prepared versus aged electrodes, binder aging, and other time- and environment-dependent effects. Similar early-stage variability has also been reported in inter-laboratory PEMWE durability tests using identical MEAs and cells, where constant-voltage current traces differed for up to 16 h before converging due to conditioning; cells were considered comparable as long as post-conditioning degradation trends matched.[434]

Figure 5.64 schematically illustrates this variable conditioning behavior, distinguishing a short break-in time (t_0 to t_1), a conditioning time (t_1 to t_2), in which performance can change markedly, and a subsequent degradation regime (t_2 to t_∞), characterized by a given degradation rate.

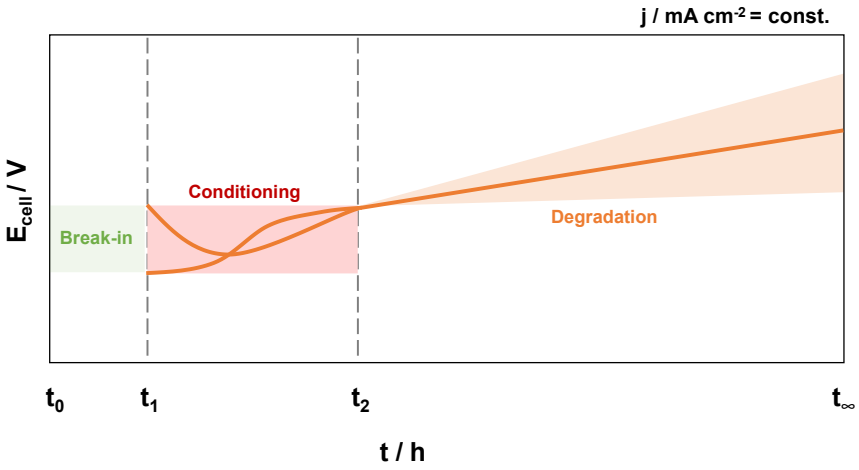

Figure 5.64. Observed durability trends after initial break-in (t_0 to t_1), described in the Experimental part, with a varying conditioning curve (t_1 to t_2) observed afterwards and a final degradation curve (t_2 to $t\infty$).

Impact of conditioning behavior on structural observations

The radically different degradation behavior observed raised questions about whether the intrinsic changes in the anode, as discovered and intensively described in Chapter 5.2, are indeed fundamental and occur in the electrode independent of the observed conditioning trends. To investigate this, Raman spectroscopy analysis was conducted on the "2022-a" (black curve in Figure 5.62) and "2022-b" (grey curve in Figure 5.62) aPTEs. Spectra were collected before the durability test (BoT, Figure 5.65a) and after 1800 h for the 2022-b sample (Figure 5.65c), and after 100 h for the 2022-a anode (Figure 5.65b). The newly obtained spectra were then compared to those previously discussed in Chapter 5.2.3 (blue curves).

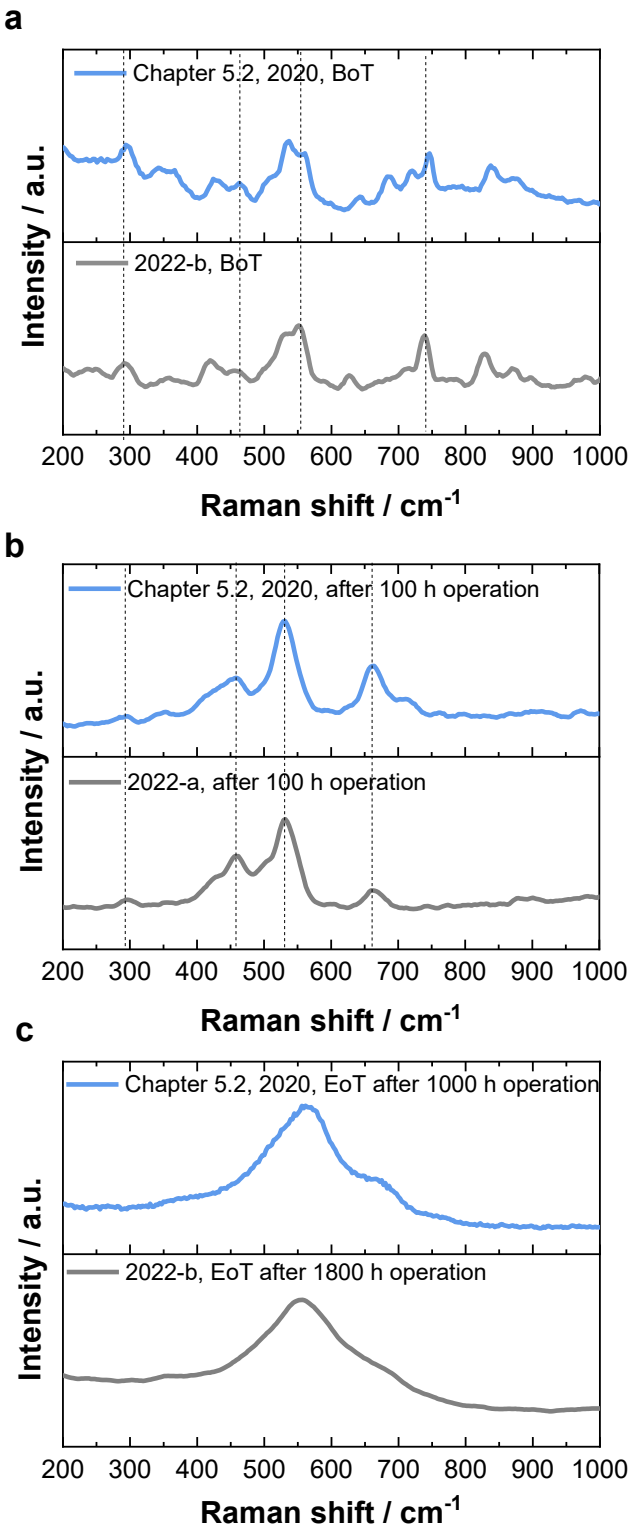

Figure 5.65. Raman spectra (a) at BoT, for the 2022-b aPTE, (b) after 100 h of operation, for the 2022-a aPTE, (c) at EoT, for the 2022-b aPTE (after 1800 h), compared to the Ni_3Fe-LDH aPTEs used in Chapter 5.2 (2020, blue curve) at specified time points (BoT, 100 h, 1000 h).

The key outcome is that all spectra are consistent with those reported previously. The electrodes show comparable BoT spectra (expect some peaks around 650-700 cm^{-1} due to signals disturbed by the surficial binder film), with overlapping contributions from binder and catalyst. After 100 h of operation,

distinct Ni_3Fe-LDH features appear for both electrodes, independent of the conditioning trend, likely because removal of the top binder layer during disassembly or peeling increases catalyst signal intensity. Finally, the mixed NiOOH/FeOOH signatures observed after 1000 h are also present after extended operation to 1800 h, confirming the formation and persistence of these species over time.

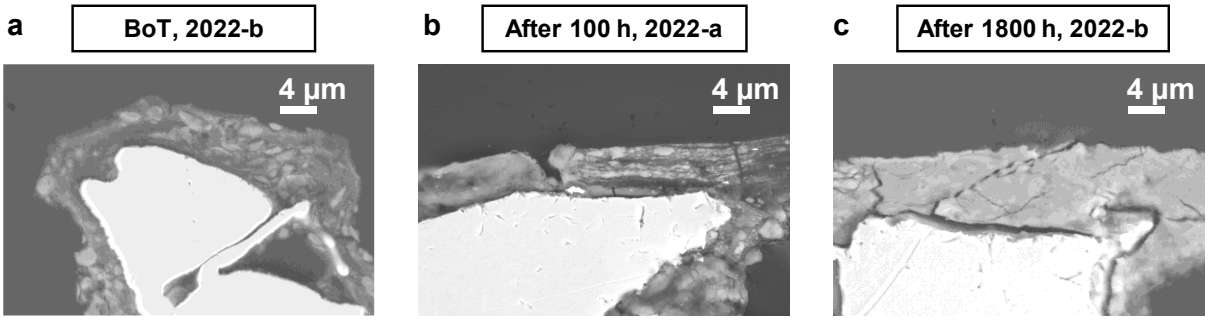

Figure 5.66. Cross-sectional SEM images of the i-NiFe-LDH-based aPTE direct after fabrication (BoT), after 100 and 1800 h of operation at x2500 magnification (2 mg cm^{-2}, 20 wt% binder, DURAION® materials), used in the repeated durability test.

Additionally, cross-sectional SEM analysis of the aPTEs is performed to assess key morphological changes (Figure 5.66). The observed structural evolution is consistent with the trends discussed in Chapter 5.2.2, supporting the reliability of these results despite differences in the initial conditioning behavior.

5.5.3 SUMMARY

In response to Q6 (Q&A Chapter 3, Approach 5), this chapter evaluates how batch-to-batch variability in pre-commercial AEM and binder materials affects reproducibility across work packages and how data validity is ensured despite evolving materials. The main outcomes are:

- Drifts in absolute performance and voltage-stability trends across chapters are mainly linked to batch variability of AEM and binder, occasionally catalyst, as well as ion-exchange treatment and storage time and conditions, while repeatability within each experimental block remains valid.
- To validate the core findings, durability tests were repeated for Ni_3Fe-LDH-based MEAs using both unmilled (i-NiFe-LDH) and milled (mTM-NiFe-LDH) anodes, confirming repeatability of the degradation trends reported in Chapter 5.2 and Chapter 5.3. Although absolute performance varies with material batch and electrode age, degradation rates stabilize after an initial period, supporting the robustness of the conclusions.
- Repeated Raman spectroscopy and SEM analyses of the newly introduced aPTEs reproduced the intrinsic evolution observed previously, including comparable anode surface oxidation behavior and similar morphological changes.
- Physical characterization indicates that independent of the conditioning phase behavior (as shown in Figure 5.64, t_1 to t_2) and even if the subsequent degradation rate varies (t_2 to t_∞), the time-dependent changes within the Ni_3Fe-LDH aPTE remain consistent and reliable.

6 CONCLUSION

This thesis investigated the feasibility of the promising Ni_3Fe-LDH OER catalyst to be integrated into AEMWE systems, with the overarching focus of developing and validating Ni_3Fe-LDH-based MEAs that are suitable for scalable use and future stack integration. This aim was successfully achieved by demonstrating integration of the developed MEA concept in Enapter's 16-cell stack (active area 64 cm^2) within the European CHANNEL project, as documented in the publicly available project reports.

The study was structured around six research questions (Q1–Q6, Chapter 3) and was addressed experimentally in Chapters 5. Feasibility of catalyst integration and optimal electrode parameter identification were established in Chapter 5.1, long-term durability and anode degradation behavior were resolved in Chapter 5.2, directed catalyst dispersion and electrode engineering were referred to in Chapter 5.3, MEA configuration and electrolyte-concentration effects were analyzed in Chapter 5.4, and reproducibility under evolving anion-conducting materials was assessed in Chapter 5.5.

A central outcome of the work is the successful transfer of Ni_3Fe-LDH from catalyst development into realistic AEMWE single-cell operation, answering Q1 (Chapter 5.1). Reproducible catalyst synthesis and powder-level quality control ensured consistent starting materials, while benchmarking against an Ir-based reference confirmed the suitability of Ni_3Fe-LDH as a competitive non-noble OER catalyst in the AEMWE environment. Beyond feasibility, systematic variation of CL together with operating conditions strongly determines achievable performance. Tested across loadings of 1–5 mg cm^{-2}, binder contents of 10–20 wt%, and conditions of 30–80 °C and 0.01–1 M KOH, catalyst loading of 2 mg cm^{-2} was found to offer a good balance between single-cell performance and material utilization, while 20 wt% anion-conducting binder ensured mechanical integrity without compromising electrochemical performance. Answering Q2, in this work, operation at 60 °C with 1 M KOH yielded optimal performance while maintaining catalyst and membrane stability. Provided that the thermal stability of the anion-conducting materials can be ensured at elevated temperatures, operation at 80 °C would be a viable alternative, offering enhanced single-cell performance.

For Q3 (Chapter 5.2), long-term operation was investigated through extended electrochemical testing combined with time-resolved electrode analysis. The data show stable Ni_3Fe-LDH-based single-cell operation over 1000 h under industrial-like conditions (1 M KOH, 60 °C, 1 A cm^{-2}), with degradation rates in the stabilized region remaining low and competitive for an emerging AEMWE anode concept. A key novelty of this work lies not only in the fact that, at the time the data were generated, a Ni_3Fe-LDH-based anode had not yet been investigated in an electrode configuration, but also in the durability methodology itself. Instead of repeatedly interrupting the operation of a single cell, multiple identical single-cells fabricated from the same anode batch were operated under identical conditions and stopped after defined runtimes. This enabled time-resolved post-mortem analysis while avoiding the risk of mixing true operating-time effects with artifacts caused by repeated cell disassembly. Thus, the results interpretation is reliable, and the observed degradation trends can be attributed more

confidently to reproducible time-dependent changes rather than to the behavior of a single-cell outlier.

The results confirm that sufficiently long test durations are essential when reporting durability because a pronounced conditioning phase can extend over hundreds of hours and would otherwise be misinterpreted as degradation. Consistent with this, degradation is quantified from the lowest stabilized voltage. For the baseline (unmilled) i-cell (Chapter 5.2), stable operation over 1000 h is achieved with a minor degradation rate of 84 µV h^{-1} and an overall voltage rise of 45 mV, while the later optimized mTM-based cell (Chapter 5.3) shows a degradation rate of 62 µV h^{-1} with an overall voltage rise of 54 mV. The onset of measurable degradation (after stabilization) begins at 200 h for the i-cell and earlier at 96 h for the mTM-cell, indicating that improved catalyst accessibility can accelerate the onset of degradation while enabling low degradation rates once the stabilized regime is reached. Electrochemical impedance spectroscopy trends support that long-term voltage evolution is governed primarily by evolving interfacial and charge-transfer contributions rather than by large changes in ohmic losses: R_{Ohm} changes only insignificant over long-term operation, whereas R_{ct} increases with time, consistent with gradual losses in effective active-site utilization and/or changes at the CL-ionomer-AEM interface.

Time-resolved anode characterization showed catalyst reconstruction towards Ni(Fe)OOH active states, consistent with the dynamic structural evolution known for Ni-Fe-based OER materials. Over extended operation, microstructural recombination of the CL occurs, including crack formation and morphological restructuring, yet large-scale CL detachment is not observed, supporting mechanical robustness of the electrode. While binder release and Fe dissolution were detectable and represent relevant degradation processes, the cell did not show an immediate performance collapse within the investigated operation window, indicating that the MEA tolerates these changes without pronounced voltage increases under the applied conditions.

Answering Q4 (Chapter5.3), the work demonstrates that directed electrode engineering, including catalyst post-treatment and ink dispersion control, significantly increases manufacturability, reproducibility, and performance. Wet tumbler ball milling increased the geometrical surface area of catalyst clusters by x8.8 and shifted the cluster-size distribution from bimodal to unimodal while preserving the LDH structure and chemistry. Quantitatively, a 7.5-fold reduction in hydrodynamic diameter was achieved by milling, while SEM/STEM confirmed the formation of smaller clusters without collapse of the LDH structure.

Systematic dispersion control by screening of dispersion media and durations identified a 1:1 1-PrOH:H_2O mixture with ultrasonic horn dispersion for 30 min as more suitable than the previously used EtOH:H_2O mixture, yielding increased ink stability and improved homogeneity of catalyst-binder distribution. These implementation steps translate directly into single-cell improvements: compared to the baseline i-cell (1.76±0.03 V at 1 A cm^{-2}), the milled-catalyst MEAs reached substantially lower voltages, with the mTM-cell achieving 1.67±0.01 V at 1 A cm^{-2}. EIS supported that the improvement is driven by better utilization rather than reduced ohmic loss. Importantly, durability of the optimized

electrode is reassessed, directly linking microstructural improvements to long-term behavior and confirming stability under industrial-close electrolyzer conditions.

For Q5 (Chapter 5.4), this thesis demonstrates that MEA architecture is a key performance determinant and must be optimized specifically for CCS and CCM designs. CCS-based anodes provide a more open, deeply penetrated catalyst structure with improved electrolyte accessibility, whereas anode-CCMs form a thinner and denser CL on the membrane. Accordingly, CCS-derived parameters cannot be directly transferred to CCM.

The main outcome of this work is the systematic ionomer-content study for anode-CCMs across different anion-conducting material systems. The results show that the optimum binder content strongly depends on the specific AEM-binder combination. While DURAION®-based anode-CCMs required 10 wt% binder to match the anode-CCS benchmark, Aemion+™-based anode-CCMs performed best at only 3 wt%, showing that high ionomer contents are not inherently beneficial in dense CCM layers.

A novelty is the validated in situ electrolyte-exchange procedure for concentration-dependent testing, which avoids repeated MEA reassembly and minimizes electrolyte carryover. Using this method, CCS showed higher performance at high electrolyte concentration, whereas the gap to CCM decreased at lower concentration. Overall, the results identify CL-AEM interface integrity, including delamination effects, as a decisive limitation that can override the expected transport advantages of the MEA architecture.

Finally, Q6 (Chapter 5.5) is answered by treating material variability as an inherent methodological constraint in AEMWE development and by showing that the main scientific conclusions remain valid despite evolving pre-commercial components. Different binder and AEM batches caused shifts in absolute performance, even when identical hardware and test stations were used. The thesis therefore distinguishes repeatability within individual experimental series from reproducibility across the full study and focuses on robust trends rather than absolute voltage values. Importantly, repeated durability tests, supported by Raman spectroscopy and SEM, consistently reproduced the key time-dependent anode evolution.

In summary, the novelty of this thesis lies in delivering a complete, experimentally validated pathway from Ni_3Fe-LDH catalyst to realistic AEMWE operation (not only in single-cell but stack) while establishing (i) a time-resolved durability methodology that separates conditioning from degradation and enables reproducible degradation phenomena interpretation, (ii) a directed electrode-engineering strategy (milling with dispersion control) that improves manufacturability, reproducibility, and performance without altering catalyst chemistry, (iii) a CCM optimization that reveals strong ionomer sensitivity and interface limitations across a pre-commercial and commercially available AEM-binder combinations, and (iv) a reproducibility framework that preserves data validity under evolving materials through repeated testing and post-mortem confirmation. Overall, these outcomes demonstrate the potential of Ni_3Fe-LDH as a high-performance, durable, and scalable OER catalyst for

AEMWE and provide practically pathways for MEA design, testing strategy, and future stack-relevant implementation.

7 OUTLOOK

Based on the evaluation of the results and the numerous research questions and potential pathways that developed, several possibilities for further research have been identified. These can be summarized within the sub-topics covered by this thesis.

In Chapter 5.1, the ionomer content of the pre-commercial anion-conducting binder did not show a significant impact within the 10-20 wt% range in the CL, rising a few follow-up questions:

- Would a different (e.g., commercially available) anion-exchange binder have a stronger influence on AEMWE performance and the longevity of the system, especially after showing the degradation mechanisms are associated with binder alteration and dissolution (in Chapter 5.2)?

Similarly, as catalyst loadings of 2 and 5 mg cm^{-2} yielded comparable results:

- How much of the deposited catalyst is electrochemically active, and what fraction contributes to actual OER under operational conditions?
- Which catalyst loading can be considered economically and technically optimal, balancing material costs, performance, and durability?

Chapter 5.2 examined the degradation behavior of the Ni_3Fe-LDH anode over 1000 h, but several aspects could be considered in future:

- To what extent do cathode materials, PTLs, and AEM type contribute to the systems durability or degradation, and how do their degradation mechanisms interact with those of the anode?
- How might post-treatment handling and storage conditions after electrochemical testing affect the accuracy of ex situ characterization results?

The catalyst powder milling and dispersion control, presented in Chapter5.3, led to improved electrode fabrication, resulting in enhanced single-cell performance with greater reproducibility and reliability.

- Would the electrode fabrication improvements demonstrated through milling and dispersion adjustments be transferable to other anion-conducting binders?
- What is the role of milling parameters, such as milling ball material and size, in optimizing particle morphology and ink stability?
- Could reduced milling times or alternative processing techniques provide comparable or improved electrode performance while enhancing scalability?

Chapter 5.4 raised important questions, mainly regarding the performance similarities between the anode-CCS and anode-CCM MEA configurations.

- Why did the anode-CCS and anode-CCM configurations show similar performance across varying electrolyte concentrations, despite structural and functional differences?
- Could the binder's ionic conductivity or its interaction with the catalyst play a larger role in low-conductivity environments than previously assumed?
- Is this performance convergence of the two systems consistently across different commercial membranes and ionomers, or is it material-specific?
- To what extent does catalyst layer delamination influence the measured performance in anode-CCM configurations, and does this detachment occur during operation or as a post-mortem phenomenon during cell disassembly?
- If delamination occurs in operando, at what stage does it happen, and how might it impact ion transport and CL-AEM interface stability?
- Are there microscopic changes at the CL-AEM interface caused by mechanical compression during operation, and could these be linked to electrolyte concentration-dependent cell performance?
- What fabrication strategies could be employed to enhance CL adhesion to the membrane in CCM assemblies, and how might this affect long-term stability?

Chapter 5.5 addressed reproducibility challenges and emphasized the importance of using materials that can be reliably benchmarked, reproduced, and analyzed in future research.

- How can reproducibility be improved in AEMWE research, particularly regarding materials, fabrication protocols, and testing procedures?
- What standardized approaches can be developed to ensure that observed performance differences come from material properties rather than procedural variability?
- Would adopting more unified benchmarking protocols enable more reliable cross-comparisons between studies and accelerate progress in AEMWE development?

This outlook summarizes the study's findings and suggests numerous paths for future research. It concludes the current work while pointing to opportunities for further exploration and optimization. For a broader perspective on these future directions, many of the published reviews can be referred to.[11,19,63,70,73–75,79,80,229,286,360,426,435]

Considerable progress has been achieved in this thesis, ranging from the validation of Ni_3Fe-LDH in realistic AEMWE single-cell operation to successful stack-level implementation within the project. At the same time, the results raise a set of well-defined follow-up questions, particularly regarding CL microstructure, ionomer functionality, interface stability, and operation at reduced electrolyte concentration. Overall, AEMWE demonstrates strong potential for continued scientific and technological development, and the insights and methodologies established here provide a solid fundament for further optimization toward robust and scalable systems.

8 REFERENCES

[1] D. Apostolou, P. Enevoldsen, G. Xydis, *Int. J. Hydrogen Energy* **2019**, *44*, 9675.

[2] "Hydrogen Applications. Hydrogen Europe. 2020.," can be found under https://hydrogeneurope.eu/hydrogen-applications, **n.d.**

[3] M. G. Schultz, T. Diehl, G. P. Brasseur, W. Zittel, *Science (80-.).* **2003**, *302*, 624.

[4] S. Venkata Mohan, A. Pandey, in *Biohydrogen*, Elsevier, **2019**, pp. 1–23.

[5] S. van Renssen, *Nat. Clim. Chang.* **2020**, *10*, 799.

[6] IPCC 2018, *Glob. Warm. 1.5°C. An IPCC Spec. Rep. impacts Glob. Warm. 1.5°C above pre-industrial levels Relat. Glob. Greenh. gas Emiss. pathways, Context Strength. Glob. response to Threat Clim. Chang.* **2018**, 132.

[7] S. Shiva Kumar, V. Himabindu, *Mater. Sci. Energy Technol.* **2019**, *2*, 442.

[8] J. Brauns, T. Turek, *Processes* **2020**, *8*, 248.

[9] D. F. C. Matthes, C. Heinemann, D. T. Hesse, P. Kasten, D. R. Mendelevitch, D. Seebach, C. Timpe, V. Cook, *Oeko* **2020**, 145.

[10] D. Bessarabov, H. Wang, H. Li, N. Zhao, Eds., *PEM Electrolysis for Hydrogen Production: Principles and Applications*, CRC Press LLC, Boca Raton, **2016**.

[11] D. Henkensmeier, M. Najibah, C. Harms, J. Žitka, J. Hnát, K. Bouzek, *J. Electrochem. Energy Convers. Storage* **2021**, *18*, 024001.

[12] Clean Hydrogen Partnership, *Annex to GB Decision No. Clean Hydrogen-GB-2022-02: Strategic Research and Innovation Agenda 2021 – 2027*, **2022**.

[13] M. Gong, H. Dai, *Nano Res.* **2014**, *8*, 23.

[14] A. Y. Faid, A. O. Barnett, F. Seland, S. Sunde, *J. Electrochem. Soc.* **2019**, *166*, F519.

[15] J. Mohammed-Ibrahim, *J. Power Sources* **2020**, *448*, 227375.

[16] P. M. Bodhankar, P. B. Sarawade, G. Singh, A. Vinu, D. S. Dhawale, *J. Mater. Chem. A* **2021**, *9*, 3180.

[17] P. Fortin, T. Khoza, X. Cao, S. Y. Martinsen, A. Oyarce Barnett, S. Holdcroft, *J. Power Sources* **2020**, *451*, 227814.

[18] E. Cossar, F. Murphy, E. A. Baranova, *J. Chem. Technol. Biotechnol.* **2022**, *97*, 1611.

[19] N. Du, C. Roy, R. Peach, M. Turnbull, S. Thiele, C. Bock, *Chem. Rev.* **2022**, *122*, 11830.

[20] H. Wendt, G. Kreysa, *Electrochemical Engineering: Science and Technology in Chemical and Other Industries*, Springer Science & Business Media, **1999**.

[21] C. A. Meyer, *Am. Soc. Mech. Eng.* **1993**.

[22] O. Ulleberg, *Int. J. Hydrogen Energy* **2003**, *28*, 21.

[23] J. T. Stock, M. V. Orna, *Electrochemistry, Past and Present*, American Chemical Society, Washington, DC, **1989**.

[24] D. Wahl, *Galvanotechnik* **2005**, *96*, 1600.

[25] S. G. Bratsch, *J. Phys. Chem. Ref. Data* **1989**, *18*, 1.

[26] B. Han, S. M. Steen, J. Mo, F.-Y. Zhang, *Int. J. Hydrogen Energy* **2015**, *40*, 7006.

[27] M. Bernt, A. Siebel, H. A. Gasteiger, *J. Electrochem. Soc.* **2018**, *165*, F305.

[28] M. Suermann, T. J. Schmidt, F. N. Büchi, *Electrochim. Acta* **2016**, *211*, 989.

[29] C. H. Hamann, A. Hamnett, W. Vielstich, *Electrochemistry*, Wiley-VCH Verlag GmbH, Weinheim, **1999**.

[30] A. J. Bard, L. R. Faulkner, *Electrochemical Methods: Fundamentals and Applications*, Wiley, New York, New York, **2001**.

[31] A. J. Bard, J. A. A. Ketelaar, *J. Electrochem. Soc.* **1974**, *121*, 212C.

[32] H. Gerischer, C. W. Tobias, Eds., *Advances in Electrochemical Science and Engineering*, Wiley, **1991**.

[33] H. Vielstich, W, Lamm, A, and Gasteiger, in *United Kingdom*, **2003**.

[34] A. M. Couper, D. Pletcher, F. C. Walsh, *Chem. Rev.* **1990**, *90*, 837.

[35] K. Kinoshita, *Electrochemical Oxygen Technology*, John Wiley & Sons, **1992**.

[36] M. Suermann, Pressurized Polymer Electrolyte Water Electrolysis: Electrochemical Characterization and Energetic Evaluation, ETH Zurich, **2017**.

[37] A. Godula-jopek, *Hydrogen Production by Electrolysis*, **n.d.**

[38] A. Godula-Jopek, W. Jehle, J. Wellnitz, *Hydrogen Storage Technologies. New Materials, Transport and Infrastructure*, Wiley VCH Verlag & Co. KGaA, Weinheim, **2012**.

[39] S. Hocevar, W. Summers, *Hydrogen Technology. Mobile and Portable Applications*, Springer-Verlag, Berlin, Heilderberg, **2008**.

[40] P. Millet, N. Mbemba, S. A. Grigoriev, V. N. Fateev, A. Aukauloo, C. Etiévant, *Int. J. Hydrogen Energy* **2011**, *36*, 4134.

[41] M. Schalenbach, G. Tjarks, M. Carmo, W. Lueke, M. Mueller, D. Stolten, *J. Electrochem. Soc.* **2016**, *163*, F3197.

[42] M. Carmo, D. L. Fritz, J. Mergel, D. Stolten, *Int. J. Hydrogen Energy* **2013**, *38*, 4901.

[43] K. Ayers, N. Danilovic, R. Ouimet, M. Carmo, B. Pivovar, M. Bornstein, *Annu. Rev. Chem. Biomol. Eng.* **2019**, *10*, 219.

[44] U. Babic, M. Tarik, T. J. Schmidt, L. Gubler, *J. Power Sources* **2020**, *451*, 227778.

[45] C. Klose, T. Saatkamp, A. Münchinger, L. Bohn, G. Titvinidze, M. Breitwieser, K. Kreuer, S. Vierrath, *Adv. Energy Mater.* **2020**, *10*, DOI 10.1002/aenm.201903995.

[46] H. Nguyen, C. Klose, L. Metzler, S. Vierrath, M. Breitwieser, *Adv. Energy Mater.* **2022**, *12*, DOI 10.1002/aenm.202103559.

[47] Chemical agency (ECHA), “Five European States Call for Evidence on Broad PFAS Restriction,” can be found under https://echa.europa.eu/de/-/five-european-states-call-for-evidence-on-broad-pfas-restriction, **2022**.

[48] M. Klingenhof, Precious Metal-Free Bifunctional Catalysts for Application in URFCs and AEMWE, from Three-Electrode Setup to Single Cell Measurements, Technische Universität Berlin, **2022**.

[49] C. BOWEN, H. DAVIS, B. HENSHAW, R. LACHANCE, R. LEROY, R. RENAUD, *Int. J. Hydrogen Energy* **1984**, *9*, 59.

[50] D. E. Hall, *J. Electrochem. Soc.* **1981**, *128*, 740.

[51] J. Brauns, J. Schönebeck, M. R. Kraglund, D. Aili, J. Hnát, J. Žitka, W. Mues, J. O. Jensen, K. Bouzek, T. Turek, *J. Electrochem. Soc.* **2021**, *168*, 014510.

[52] D. Henkensmeier, W. C. Cho, P. Jannasch, J. Stojadinovic, Q. Li, D. Aili, J. O. Jensen, *Chem. Rev.* **2023**, DOI 10.1021/acs.chemrev.3c00694.

[53] P. Haug, M. Koj, T. Turek, *Int. J. Hydrogen Energy* **2017**, *42*, 9406.

[54] J. Schillings, O. Doche, J. Deseure, *Int. J. Heat Mass Transf.* **2015**, *85*, 292.

[55] S. Anantharaj, S. R. Ede, K. Karthick, S. Sam Sankar, K. Sangeetha, P. E. Karthik, S. Kundu, *Energy Environ. Sci.* **2018**, *11*, 744.

[56] J. Kieninger, *Electrochemical Methods for the Micro- and Nanoscale: Theoretical Essentials, Instrumentation and Methods for Applications in MEMS and Nanotechnology*, De Gruyter Oldenbourg, **2022**.

[57] L. R. Faulkner, J. A. Bard, H. S. White, *Electrochemical Methods: Fundamentals and Applications*, Wiley, **2022**.

[58] T. Smolinka, J. Garche, *Electrochemical Power Sources: Fundamentals, Systems, and Applications*, Elsevier, Amsterdam Oxford Cambridge, **2022**.

[59] IRENA, *Green Hydrogen Cost Reduction: Scaling up Electro- Lysers to Meet the 1.5°C Climate Goal*, International Renewable Energy Agency, Abu Dhabi, **2020**.

[60] IEA, "Global Hydrogen Review," can be found under https://www.hydrogen.energy.gov/annual_review19_h2fuel.html#electrolysis, **2021**.

[61] "Clean Hydrogen Joint Undertaking," can be found under https://www.fch.europa.eu/, **n.d.**

[62] "Enapter," can be found under https://www.enapter.com/aem-electrolysers/aem-nexus/, **n.d.**

[63] B. Motealleh, Z. Liu, R. I. Masel, J. P. Sculley, Z. Richard Ni, L. Meroueh, *Int. J. Hydrogen Energy* **2021**, *46*, 3379.

[64] J. Hnát, R. Kodým, K. Denk, M. Paidar, J. Žitka, K. Bouzek, *Chemie-Ingenieur-Technik* **2019**, *91*, 821.

[65] Y. S. Park, J. Jeong, Y. Noh, M. J. Jang, J. Lee, K. H. Lee, D. C. Lim, M. H. Seo, W. B. Kim, J. Yang, S. M. Choi, *Appl. Catal. B Environ.* **2021**, *292*, 120170.

[66] M. J. Jang, S. H. Yang, M. G. Park, J. Jeong, M. S. Cha, S. Shin, K. H. Lee, Z. Bai, Z. Chen, J. Y. Lee, S. M. Choi, *ACS Energy Lett.* **2022**, *7*, 2576.

[67] Q. Xu, L. Zhang, J. Zhang, J. Wang, Y. Hu, H. Jiang, C. Li, *EnergyChem* **2022**, *4*, 100087.

[68] M. K. Cho, A. Lim, S. Y. Lee, H. J. Kim, S. J. Yoo, Y. E. Sung, H. S. Park, J. H. Jang, *J. Electrochem. Sci. Technol.* **2017**, *8*, 183.

[69] I. Vincent, D. Bessarabov, *Renew. Sustain. Energy Rev.* **2018**, *81*, 1690.

[70] A. Lim, M. K. Cho, S. Y. Lee, H. J. Kim, S. J. Yoo, Y. E. Sung, J. H. Jang, H. S. Park, *J. Electrochem. Sci. Technol.* **2017**, *8*, 265.

[71] Y. Yang, C. R. Peltier, R. Zeng, R. Schimmenti, Q. Li, X. Huang, Z. Yan, G. Potsi, R. Selhorst, X. Lu, W. Xu, M. Tader, A. V. Soudackov, H. Zhang, M. Krumov, E. Murray, P. Xu, J. Hitt, L. Xu, H. Y. Ko, B. G. Ernst, C. Bundschu, A. Luo, D. Markovich, M. Hu, C. He, H. Wang, J. Fang, R. A. Distasio, L. F. Kourkoutis, A. Singer, K. J. T. Noonan, L. Xiao, L. Zhuang, B. S. Pivovar, P. Zelenay, E. Herrero, J. M. Feliu, J. Suntivich, E. P. Giannelis, S. Hammes-Schiffer, T. Arias, M. Mavrikakis, T. E. Mallouk, J. D. Brock, D. A. Muller, F. J. Disalvo, G. W. Coates, H. D. Abruña, *Chem. Rev.* **2022**, *122*, 6117.

[72] K. F. L. Hagesteijn, S. Jiang, B. P. Ladewig, *J. Mater. Sci.* **2018**, *53*, 11131.

[73] S. A. Grigoriev, V. N. Fateev, D. G. Bessarabov, P. Millet, *Int. J. Hydrogen Energy* **2020**, *45*, 26036.

[74] D. S. Falcão, *Energies* **2023**, *16*, 1.

[75] M. Chatenet, B. G. Pollet, D. R. Dekel, F. Dionigi, J. Deseure, P. Millet, R. D. Braatz, M. Z. Bazant, M. Eikerling, I. Staffell, P. Balcombe, Y. Shao-Horn, H. Schäfer, *Chem. Soc. Rev.* **2022**, *51*, 4583.

[76] H. A. Miller, *Curr. Opin. Electrochem.* **2022**, *36*, 101122.

[77] R. R. Raja Sulaiman, W. Y. Wong, K. S. Loh, *Int. J. Energy Res.* **2022**, *46*, 2241.

[78] P. Shirvanian, A. Loh, S. Sluijter, X. Li, *Electrochem. commun.* **2021**, *132*, 107140.

[79] C. Santoro, A. Lavacchi, P. Mustarelli, V. Di Noto, L. Elbaz, D. Dekel, F. Jaouen, *ChemSusChem* **2022**, DOI 10.1002/cssc.202200027.

[80] D. Li, A. R. Motz, C. Bae, C. Fujimoto, G. Yang, F. Y. Zhang, K. E. Ayers, Y. S. Kim, *Energy Environ. Sci.* **2021**, *14*, 3393.

[81] H. A. Miller, K. Bouzek, J. Hnat, S. Loos, C. I. Bernäcker, T. Weißgärber, L. Röntzsch, J. Meier-Haack, *Sustain. Energy Fuels* **2020**, *4*, 2114.

[82] A. Lim, H. juhn Kim, D. Henkensmeier, S. Jong Yoo, J. Young Kim, S. Young Lee, Y. E. Sung, J. H. Jang, H. S. Park, *J. Ind. Eng. Chem.* **2019**, *76*, 410.

[83] J. E. Park, S. Y. Kang, S. H. Oh, J. K. Kim, M. S. Lim, C. Y. Ahn, Y. H. Cho, Y. E. Sung, *Electrochim. Acta* **2019**, *295*, 99.

[84] I. Vincent, A. Kruger, D. Bessarabov, *Int. J. Electrochem. Sci.* **2018**, *13*, 11347.

[85] N. U. Hassan, Y. Zheng, P. A. Kohl, W. E. Mustain, *J. Electrochem. Soc.* **2022**, *169*, 044526.

[86] K. Ayers, C. Capuano, P. Atanassov, S. Mukerjee, M. Hickner, *High Performance Platinum Group Metal Free Membrane Electrode Assemblies through Control of Interfacial Processes*, Golden, CO (United States), **2017**.

[87] J. Liu, Z. Kang, D. Li, M. Pak, S. M. Alia, C. Fujimoto, G. Bender, Y. S. Kim, A. Z. Weber, *J. Electrochem. Soc.* **2021**, *168*, 054522.

[88] H. Ito, N. Kawaguchi, S. Someya, T. Munakata, N. Miyazaki, M. Ishida, A. Nakano, *Int. J. Hydrogen Energy* **2018**, *43*, 17030.

[89] R. Soni, S. Miyanishi, H. Kuroki, T. Yamaguchi, *ACS Appl. Energy Mater.* **2021**, *4*, 1053.

[90] D. Li, E. J. Park, W. Zhu, Q. Shi, Y. Zhou, H. Tian, Y. Lin, A. Serov, B. Zulevi, E. D. Baca, C. Fujimoto, H. T. Chung, Y. S. Kim, *Nat. Energy* **2020**, *5*, 378.

[91] A. Y. Faid, A. O. Barnett, F. Seland, S. Sunde, *Catalysts* **2018**, *8*, 1.

[92] J. Xiao, A. M. Oliveira, L. Wang, Y. Zhao, T. Wang, J. Wang, B. P. Setzler, Y. Yan, *ACS Catal.* **2021**, *11*, 264.

[93] L. Trotochaud, S. L. Young, J. K. Ranney, S. W. Boettcher, *J. Am. Chem. Soc.* **2014**, *136*, 6744.

[94] M. T. de Groot, *Curr. Opin. Chem. Eng.* **2023**, *42*, 100981.

[95] S. Yin, W. Tu, Y. Sheng, Y. Du, M. Kraft, A. Borgna, R. Xu, *Adv. Mater.* **2018**, *30*, 1705106.

[96] E. Cossar, A. O. Barnett, F. Seland, E. A. Baranova, *Catalysts* **2019**, *9*, DOI 10.3390/catal9100814.

[97] J. HUOT, L. BROSSARD, *Int. J. Hydrogen Energy* **1987**, *12*, 821.

[98] M. A. Riley, P. J. Moran, *J. Electrochem. Soc.* **1986**, *133*, 760.

[99] H. E. G. Rommal, P. J. Morgan, *J. Electrochem. Soc.* **1988**, *135*, 343.

[100] D. M. Soares, O. Teschke, I. Torriani, *J. Electrochem. Soc.* **1992**, *139*, 98.

[101] D. A. Corrigan, R. M. Bendert, *J. Electrochem. Soc.* **1989**, *136*, 723.

[102] A. Y. Faid, A. O. Barnett, F. Seland, S. Sunde, *ACS Appl. Energy Mater.* **2021**, *4*, 3327.

[103] M. J. Jang, J. Yang, J. Lee, Y. S. Park, J. Jeong, S. M. Park, J. Y. Jeong, Y. Yin, M. H. Seo, S. M. Choi, K. H. Lee, *J. Mater. Chem. A* **2020**, *8*, 4290.

[104] P. Thangavel, M. Ha, S. Kumaraguru, A. Meena, A. N. Singh, A. M. Harzandi, K. S. Kim, *Energy Environ. Sci.* **2020**, *13*, 3447.

[105] J. Lee, H. Jung, Y. S. Park, S. Woo, J. Yang, M. J. Jang, J. Jeong, N. Kwon, B. Lim, J. W. Han, S. M. Choi, *Small* **2021**, *2100639*, 1.

[106] A. Mavrič, C. Cui, *ACS Appl. Energy Mater.* **2021**, *4*, 12032.

[107] L. Wang, V. A. Saveleva, M. J. Eslamibidgoli, D. Antipin, C. Bouillet, I. Biswas, A. S. Gago, S. S. Hosseiny, P. Gazdzicki, M. H. Eikerling, E. R. Savinova, K. A. Friedrich, *ACS Appl. Energy Mater.* **2022**, *5*, 2221.

[108] A. K. Niaz, A. Akhtar, J. Y. Park, H. T. Lim, *J. Power Sources* **2021**, *481*, 229093.

[109] L. A. King, M. K. A. Hubert, C. Capuano, J. Manco, N. Danilovic, E. Valle, T. R. Hellstern, K. Ayers, T. F. Jaramillo, *Nat. Nanotechnol.* **2019**, *14*, 1071.

[110] M. Felgenhauer, T. Hamacher, *Int. J. Hydrogen Energy* **2015**, *40*, 2084.

[111] P. Millet, S. Grigoriev, in *Renew. Hydrog. Technol.*, Elsevier, **2013**, pp. 19–41.

[112] A. Y. Faid, S. Sunde, *Energy Technol.* **2022**, DOI 10.1002/ente.202200506.

[113] X. Wu, K. Scott, *J. Mater. Chem.* **2011**, *21*, 12344.

[114] K. E. Ayers, E. B. Anderson, C. B. Capuano, M. Niedzwiecki, M. A. Hickner, C.-Y. Wang, Y. Leng, W. Zhao, *ECS Trans.* **2013**, *45*, 121.

[115] J. Parrondo, C. G. Arges, M. Niedzwiecki, E. B. Anderson, K. E. Ayers, V. Ramani, *RSC Adv.* **2014**, *4*, 9875.

[116] J. Parrondo, M. George, C. Capuano, K. E. Ayers, V. Ramani, *J. Mater. Chem. A* **2015**, *3*, 10819.

[117] M. S. Cha, J. E. Park, S. Kim, S.-H. Han, S.-H. Shin, S. H. Yang, T.-H. Kim, D. M. Yu, S. So, Y. T. Hong,

S. J. Yoon, S.-G. Oh, S. Y. Kang, O.-H. Kim, H. S. Park, B. Bae, Y.-E. Sung, Y.-H. Cho, J. Y. Lee, *Energy Environ. Sci.* **2020**, *13*, 3633.

[118] S. H. Ahn, B.-S. S. Lee, I. Choi, S. J. Yoo, H.-J. J. Kim, E. A. Cho, D. Henkensmeier, S. W. Nam, S.-K. K. Kim, J. H. Jang, *Appl. Catal. B Environ.* **2014**, *154–155*, 197.

[119] F. P. Lohmann-Richters, S. Renz, W. Lehnert, M. Müller, M. Carmo, *J. Electrochem. Soc.* **2021**, *168*, 114501.

[120] V. M. Truong, J. R. Tolchard, J. Svendby, M. Manikandan, H. A. Miller, S. Sunde, H. Yang, D. R. Dekel, A. O. Barnett, *Energies* **2020**, *13*, 1.

[121] Y. K. Choe, C. Fujimoto, K. S. Lee, L. T. Dalton, K. Ayers, N. J. Henson, Y. S. Kim, *Chem. Mater.* **2014**, *26*, 5675.

[122] P. Lettenmeier, S. Kolb, N. Sata, A. Fallisch, L. Zielke, S. Thiele, A. S. Gago, K. A. Friedrich, *Energy Environ. Sci.* **2017**, *10*, 2521.

[123] R. Vinodh, T. Palanivel, S. S. Kalanur, B. G. Pollet, *Energy Adv.* **2024**, *3*, 1144.

[124] H. Tang, S. Wang, S. P. Jiang, M. Pan, *J. Power Sources* **2007**, *170*, 140.

[125] S. Song, H. Zhang, X. Ma, Z. Shao, R. T. Baker, B. Yi, *Int. J. Hydrogen Energy* **2008**, *33*, 4955.

[126] J. Hnát, M. Plevova, R. A. Tufa, J. Zitka, M. Paidar, K. Bouzek, *Int. J. Hydrogen Energy* **2019**, *44*, 17493.

[127] H. Vielstich, W, Lamm, A, and Gasteiger, in *Handb. Fuel Cells*, Wiley, Chichester, **2003**, pp. 538–565.

[128] H. Ito, N. Miyazaki, S. Sugiyama, M. Ishida, Y. Nakamura, S. Iwasaki, Y. Hasegawa, A. Nakano, *J. Appl. Electrochem.* **2018**, *48*, 305.

[129] B. H. Lim, E. H. Majlan, A. Tajuddin, T. Husaini, W. R. Wan Daud, N. A. Mohd Radzuan, M. A. Haque, *Chinese J. Chem. Eng.* **2021**, *33*, 1.

[130] R. Wang, K. Inoguchi, M. Ohashi, S. Someya, T. Munakata, M. Ishida, H. Ito, *Int. J. Hydrogen Energy* **2021**, *46*, 37757.

[131] W. Jiang, A. Y. Faid, B. F. Gomes, I. Galkina, L. Xia, C. M. S. Lobo, M. Desmau, P. Borowski, H. Hartmann, A. Maljusch, A. Besmehn, C. Roth, S. Sunde, W. Lehnert, M. Shviro, *Adv. Funct. Mater.* **2022**, *32*, 2203520.

[132] N. Chen, S. Y. Paek, J. Y. Lee, J. H. Park, S. Y. Lee, Y. M. Lee, S. Y. Baek, J. Y. Lee, J. H. Park, S. Y. Lee, Y. M. Lee, *Energy Environ. Sci.* **2021**, *14*, 6338.

[133] S. Koch, L. Metzler, S. K. Kilian, P. A. Heizmann, F. Lombeck, M. Breitwieser, S. Vierrath, *Adv. Sustain. Syst.* **2022**, *2200332*, DOI 10.1002/adsu.202200332.

[134] J. E. Park, H. E. Bae, M. Karuppannan, K. M. Oh, O. J. Kwon, Y.-H. Cho, Y.-E. Sung, *J. Ind. Eng. Chem.* **2022**, *109*, 453.

[135] Z. Lu, W. Xu, W. Zhu, Q. Yang, X. Lei, J. Liu, Y. Li, X. Sun, X. Duan, *Chem. Commun.* **2014**, *50*, 6479.

[136] L. Yu, J. F. Yang, B. Y. Guan, Y. Lu, X. W. D. Lou, *Angew. Chemie - Int. Ed.* **2018**, *57*, 172.

[137] L. Peng, N. Yang, Y. Yang, Q. Wang, X. Xie, D. Sun-Waterhouse, L. Shang, T. Zhang, G. I. N. Waterhouse, *Angew. Chemie - Int. Ed.* **2021**, *60*, 24612.

[138] D. Zhou, S. Wang, Y. Jia, X. Xiong, H. Yang, S. Liu, J. Tang, J. Zhang, D. Liu, L. Zheng, Y. Kuang, X.

Sun, B. Liu, *Angew. Chemie - Int. Ed.* **2019**, *58*, 736.

[139] X. Lu, C. Zhao, *Nat. Commun.* **2015**, *6*, DOI 10.1038/ncomms7616.

[140] C. Yang, N. Han, Y. Wang, X. Z. Yuan, J. Xu, H. Huang, J. Fan, H. Li, H. Wang, *ACS Sustain. Chem. Eng.* **2020**, *8*, 9803.

[141] G. Rinaldi, A. Nakajo, P. Burdet, M. Cantoni, W. K. S. Chiu, J. Van herle, *Acta Mater.* **2019**, *178*, 194.

[142] E. K. Volk, M. E. Kreider, S. Kwon, S. M. Alia, *EES Catal.* **2024**, *2*, 109.

[143] S. Q. Liu, E. Shahini, M. R. Gao, L. Gong, P. F. Sui, T. Tang, H. Zeng, J. L. Luo, *ACS Nano* **2021**, *15*, 17757.

[144] H. Su, V. Linkov, B. J. Bladergroen, *Int. J. Hydrogen Energy* **2013**, *38*, 9601.

[145] M. Bernt, H. A. Gasteiger, *J. Electrochem. Soc.* **2016**, *163*, F3179.

[146] M. K. Cho, H. Y. Park, S. Choe, S. J. Yoo, J. Y. Kim, H. J. Kim, D. Henkensmeier, S. Y. Lee, Y. E. Sung, H. S. Park, J. H. Jang, *J. Power Sources* **2017**, *347*, 283.

[147] B. Mayerhöfer, F. D. Speck, M. Hegelheimer, M. Bierling, D. Abbas, D. McLaughlin, S. Cherevko, S. Thiele, R. Peach, *Int. J. Hydrogen Energy* **2022**, *47*, 4304.

[148] S. Koch, P. A. Heizmann, S. K. Kilian, B. Britton, S. Holdcroft, S. Vierrath, M. Breitwieser, S. Vierrath, *J. Mater. Chem. A* **2021**, *9*, 15744.

[149] M. K. Cho, H. S. H. Y. Park, H. J. Lee, H. J. Kim, A. Lim, D. Henkensmeier, S. J. Yoo, J. Y. Kim, S. Y. Lee, H. S. H. Y. Park, J. H. Jang, *J. Power Sources* **2018**, *382*, 22.

[150] G. Huang, M. Mandal, N. U. Hassan, K. Groenhout, A. Dobbs, W. E. Mustain, P. A. Kohl, *J. Electrochem. Soc.* **2020**, *167*, 164514.

[151] A. Y. Faid, L. Xie, A. Oyarce, F. Seland, D. Kirk, S. Sunde, *Int. J. Hydrogen Energy* **2020**, 1.

[152] I. Vincent, A. Kruger, D. Bessarabov, *Int. J. Hydrogen Energy* **2017**, *42*, 10752.

[153] L. Wan, Z. Xu, Q. Xu, P. Wang, B. Wang, *Energy Environ. Sci.* **2022**, *15*, 1882.

[154] I. Galkina, A. Y. Faid, W. Jiang, F. Scheepers, P. Borowski, S. Sunde, M. Shviro, W. Lehnert, A. K. Mechler, *Small* **2024**, *2311047*, 1.

[155] L. Titheridge, S. K. Sharma, A. Soisson, C. Roth, A. T. Marshall, *Curr. Opin. Electrochem.* **2025**, *49*, 101607.

[156] D. S. Hwang, C. H. Park, S. C. Yi, Y. M. Lee, *Int. J. Hydrogen Energy* **2011**, *36*, 9876.

[157] Y.-H. Huang, Y.-H. Hsu, Y.-T. Pan, *ACS Appl. Energy Mater.* **2022**, *5*, 2890.

[158] H. Koshikawa, H. Murase, T. Hayashi, K. Nakajima, H. Mashiko, S. Shiraishi, Y. Tsuji, *ACS Catal.* **2020**, *10*, 1886.

[159] S. S. Jeon, J. Lim, P. W. Kang, J. W. Lee, G. Kang, H. Lee, *ACS Appl. Mater. Interfaces* **2021**, *13*, 37179.

[160] S. Dresp, T. Ngo Thanh, M. Klingenhof, S. Brückner, P. Hauke, P. Strasser, *Energy Environ. Sci.* **2020**, *13*, 1725.

[161] C. C. Pavel, F. Cecconi, C. Emiliani, S. Santiccioli, A. Scaffidi, S. Catanorchi, M. Comotti, S. CataPavenorchi, M. Comotti, *Angew. Chemie Int. Ed.* **2014**, *53*, 1378.

[162] L. Xiao, S. Zhang, J. Pan, C. Yang, M. He, L. Zhuang, J. Lu, *Energy Environ. Sci.* **2012**, *5*, 7869.

[163] I. V. Pushkareva, A. S. Pushkarev, S. A. Grigoriev, P. Modisha, D. G. Bessarabov, *Int. J. Hydrogen Energy* **2020**, *45*, 26070.

[164] E. Cossar, F. Murphy, J. Walia, A. Weck, E. A. Baranova, *ACS Appl. Energy Mater.* **2022**, *5*, 9938.

[165] A. R. Zeradjanin, A. A. Topalov, Q. Van Overmeere, S. Cherevko, X. Chen, E. Ventosa, W. Schuhmann, K. J. J. Mayrhofer, *RSC Adv.* **2014**, *4*, 9579.

[166] J. E. Park, H. J. Choi, S. Y. Kang, G. Y. Jang, O. H. Kim, M. Karuppannan, Y. E. Sung, O. J. Kwon, Y. H. Cho, *Int. J. Energy Res.* **2022**, *46*, 16670.

[167] Y. S. Park, J. Lee, M. J. Jang, J. Yang, J. Jeong, J. Park, Y. Kim, M. H. Seo, Z. Chen, S. M. Choi, *J. Mater. Chem. A* **2021**, *9*, 9586.

[168] A. Weiß, A. Siebel, M. Bernt, T.-H. Shen, V. Tileli, H. A. Gasteiger, *J. Electrochem. Soc.* **2019**, *166*, F487.

[169] P. Chen, X. Hu, *Adv. Energy Mater.* **2020**, *10*, 1.

[170] N. U. Hassan, E. Motyka, J. Kweder, P. Ganesan, B. Brechin, B. Zulevi, H. R. Colón-Mercado, P. A. Kohl, W. E. Mustain, *J. Power Sources* **2023**, *555*, 1.

[171] Q. Xu, S. Z. Oener, G. Lindquist, H. Jiang, C. Li, S. W. Boettcher, *ACS Energy Lett.* **2021**, *6*, 305.

[172] B. Chen, A. L. G. Biancolli, C. L. Radford, S. Holdcroft, *ACS Energy Lett.* **2023**, 2661.

[173] M. R. Kraglund, Alkaline Membrane Water Electrolysis with Non-Noble Catalysts, Technical University of Denmark, **2017**.

[174] X. Wu, K. Scott, F. Xie, N. Alford, *J. Power Sources* **2014**, *246*, 225.

[175] Y. Leng, G. Chen, A. J. Mendoza, T. B. Tighe, M. A. Hickner, C. Y. Wang, *J. Am. Chem. Soc.* **2012**, *134*, 9054.

[176] W. E. Mustain, M. Chatenet, M. Page, Y. S. Kim, *Energy Environ. Sci.* **2020**, *13*, 2805.

[177] G. A. Lindquist, Q. Xu, S. Z. Oener, S. W. Boettcher, *Joule* **2020**, *4*, 2549.

[178] F. Razmjooei, A. Farooqui, R. Reissner, A. S. Gago, S. A. Ansar, K. A. Friedrich, *ChemElectroChem* **2020**, *7*, 3951.

[179] T. Huang, G. He, J. Xue, O. Otoo, X. He, H. Jiang, J. Zhang, Y. Yin, Z. Jiang, J. C. Douglin, D. R. Dekel, M. D. Guiver, *J. Memb. Sci.* **2020**, *597*, 117769.

[180] M. Kumari, J. C. Douglin, D. R. Dekel, *J. Memb. Sci.* **2021**, *626*, 119167.

[181] J. Xue, X. Liu, J. Zhang, Y. Yin, M. D. Guiver, *J. Memb. Sci.* **2020**, *595*, 117507.

[182] J. Fan, S. Willdorf-Cohen, E. M. Schibli, Z. Paula, W. Li, T. J. G. Skalski, A. T. Sergeenko, A. Hohenadel, B. J. Frisken, E. Magliocca, W. E. Mustain, C. E. Diesendruck, D. R. Dekel, S. Holdcroft, *Nat. Commun.* **2019**, *10*, 2306.

[183] T. P. Pandey, A. M. Maes, H. N. Sarode, B. D. Peters, S. Lavina, K. Vezzù, Y. Yang, S. D. Poynton, J. R. Varcoe, S. Seifert, M. W. Liberatore, V. Di Noto, A. M. Herring, *Phys. Chem. Chem. Phys.* **2015**, *17*, 4367.

[184] F. Bekkar, F. Bettahar, I. Moreno, R. Meghabar, M. Hamadouche, E. Hernáez, J. L. Vilas-Vilela, L. Ruiz-Rubio, *Polymers (Basel).* **2020**, *12*, 2227.

[185] D. S. Kim, A. Labouriau, M. D. Guiver, Y. S. Kim, *Chem. Mater.* **2011**, *23*, 3795.

[186] B. Zhang, S. Gu, J. Wang, Y. L. B, A. M. Herring, Y. Yan, *Rsc Adv.* **2012**, *2*, 12683.

[187] Z. Tao, C. Wang, X. Zhao, J. Li, M. D. Guiver, *Adv. Mater. Technol.* **2021**, *6*, DOI 10.1002/admt.202001220.

[188] J. Wang, Y. Zhao, B. P. Setzler, S. Rojas-Carbonell, C. Ben Yehuda, A. Amel, M. Page, L. Wang, K. Hu, L. Shi, S. Gottesfeld, B. Xu, Y. Yan, *Nat. Energy* **2019**, *4*, 392.

[189] B. Kim, X. Cheng, D. F. Abbott, E. Fabbri, F. Bozza, T. Graule, I. E. Castelli, L. Wiles, N. Danilovic, K. E. Ayers, N. Marzari, T. J. Schmidt, *Adv. Funct. Mater.* **2018**, *28*, DOI 10.1002/adfm.201804355.

[190] E. López-Fernández, C. G. Sacedón, J. Gil-Rostra, F. Yubero, A. R. González-Elipe, A. de Lucas-Consuegra, *Molecules* **2021**, *26*, 6326.

[191] S. Y. Kang, J. E. Park, G. Y. Jang, O. H. Kim, O. J. Kwon, Y. H. Cho, Y. E. Sung, *Int. J. Hydrogen Energy* **2022**, *47*, 9115.

[192] R. A. Krivina, Y. Ou, Q. Xu, L. P. Twight, T. N. Stovall, S. W. Boettcher, *Accounts Mater. Res.* **2021**, *2*, 548.

[193] J. R. Varcoe, P. Atanassov, D. R. Dekel, A. M. Herring, M. A. Hickner, P. A. Kohl, A. R. Kucernak, W. E. Mustain, K. Nijmeijer, K. Scott, T. Xu, L. Zhuang, *Energy Environ. Sci.* **2014**, *7*, 3135.

[194] D. Strmcnik, P. P. Lopes, B. Genorio, V. R. Stamenkovic, N. M. Markovic, *Nano Energy* **2016**, *29*, 29.

[195] N. Dubouis, A. Grimaud, *Chem. Sci.* **2019**, *10*, 9165.

[196] X. Li, X. Hao, A. Abudula, G. Guan, *J. Mater. Chem. A* **2016**, *4*, 11973.

[197] S. Siracusano, N. Hodnik, P. Jovanovic, F. Ruiz-Zepeda, M. Šala, V. Baglio, A. S. Aricò, *Nano Energy* **2017**, *40*, 618.

[198] N. Mahmood, Y. Yao, J. Zhang, L. Pan, X. Zhang, J. Zou, *Adv. Sci.* **2018**, *5*, DOI 10.1002/advs.201700464.

[199] M. Gong, D. Y. Wang, C. C. Chen, B. J. Hwang, H. Dai, *Nano Res.* **2016**, *9*, 28.

[200] R. Subbaraman, D. Tripkovic, D. Strmcnik, K.-C. Chang, M. Uchimura, A. P. Paulikas, V. Stamenkovic, N. M. Markovic, *Science (80-.).* **2011**, *334*, 1256.

[201] P. Wang, K. Jiang, G. Wang, J. Yao, X. Huang, *Angew. Chemie* **2016**, *128*, 13051.

[202] Z.-J. Chen, G.-X. Cao, L.-Y. Gan, H. Dai, N. Xu, M.-J. Zang, H.-B. Dai, H. Wu, P. Wang, *ACS Catal.* **2018**, *8*, 8866.

[203] H. Yin, S. Zhao, K. Zhao, A. Muqsit, H. Tang, L. Chang, H. Zhao, Y. Gao, Z. Tang, *Nat. Commun.* **2015**, *6*, 6430.

[204] B. Ruqia, S. Choi, *ChemSusChem* **2018**, *11*, 2643.

[205] D. Strmcnik, M. Uchimura, C. Wang, R. Subbaraman, N. Danilovic, D. van der Vliet, A. P. Paulikas, V. R. Stamenkovic, N. M. Markovic, *Nat. Chem.* **2013**, *5*, 300.

[206] Y. Xie, J. Cai, Y. Wu, Y. Zang, X. Zheng, J. Ye, P. Cui, S. Niu, Y. Liu, J. Zhu, X. Liu, G. Wang, Y. Qian, *Adv. Mater.* **2019**, *31*, DOI 10.1002/adma.201807780.

[207] M. Müller, I. Galkina, F. Scheepers, F. Lohmann-Richters, in *Encycl. Electrochem. Power Sources*, Elsevier, **2025**, pp. 33–41.

[208] X. Qin, L. Zhang, G.-L. Xu, S. Zhu, Q. Wang, M. Gu, X. Zhang, C. Sun, P. B. Balbuena, K. Amine, M. Shao, *ACS Catal.* **2019**, *9*, 9614.

[209] Y. Jia, T.-H. Huang, S. Lin, L. Guo, Y.-M. Yu, J.-H. Wang, K.-W. Wang, S. Dai, *Nano Lett.* **2022**, *22*, 1391.

[210] E. J. Popczun, J. R. McKone, C. G. Read, A. J. Biacchi, A. M. Wiltrout, N. S. Lewis, R. E. Schaak, *J. Am. Chem. Soc.* **2013**, *135*, 9267.

[211] J. Kibsgaard, T. F. Jaramillo, F. Besenbacher, *Nat. Chem.* **2014**, *6*, 248.

[212] B. Hinnemann, P. G. Moses, J. Bonde, K. P. Jørgensen, J. H. Nielsen, S. Horch, I. Chorkendorff, J. K. Nørskov, *J. Am. Chem. Soc.* **2005**, *127*, 5308.

[213] T. Wang, M. Wang, H. Yang, M. Xu, C. Zuo, K. Feng, M. Xie, J. Deng, J. Zhong, W. Zhou, T. Cheng, Y. Li, *Energy Environ. Sci.* **2019**, *12*, 3522.

[214] Z. Weng, W. Liu, L.-C. Yin, R. Fang, M. Li, E. I. Altman, Q. Fan, F. Li, H.-M. Cheng, H. Wang, *Nano Lett.* **2015**, *15*, 7704.

[215] M. Gong, W. Zhou, M.-C. Tsai, J. Zhou, M. Guan, M.-C. Lin, B. Zhang, Y. Hu, D.-Y. Wang, J. Yang, S. J. Pennycook, B.-J. Hwang, H. Dai, *Nat. Commun.* **2014**, *5*, 4695.

[216] Y. Jin, H. Wang, J. Li, X. Yue, Y. Han, P. K. Shen, Y. Cui, *Adv. Mater.* **2016**, *28*, 3785.

[217] J. Y. Huot, M. L. Trudeau, R. Schulz, *J. Electrochem. Soc.* **1991**, *138*, 1316.

[218] J. R. McKone, B. F. Sadtler, C. A. Werlang, N. S. Lewis, H. B. Gray, *ACS Catal.* **2013**, *3*, 166.

[219] J. Rossmeisl, Z.-W. Qu, H. Zhu, G.-J. Kroes, J. K. Nørskov, *J. Electroanal. Chem.* **2007**, *607*, 83.

[220] M. T. M. Koper, *Chem. Sci.* **2013**, *4*, 2710.

[221] H. Dau, C. Limberg, T. Reier, M. Risch, S. Roggan, P. Strasser, *ChemCatChem* **2010**, *2*, 724.

[222] Z. W. She, J. Kibsgaard, C. F. Dickens, I. Chorkendorff, J. K. Nørskov, T. F. Jaramillo, *Science (80-.).* **2017**, *355*, DOI 10.1126/science.aad4998.

[223] V. I. Birss, A. Damjanovic, P. G. Hudson, *J. Electrochem. Soc.* **1986**, *133*, 1621.

[224] M. E. G. Lyons, R. L. Doyle, I. Godwin, M. O'Brien, L. Russell, *J. Electrochem. Soc.* **2012**, *159*, H932.

[225] Y. Yan, B. Y. Xia, B. Zhao, X. Wang, *J. Mater. Chem. A* **2016**, *4*, 17587.

[226] W. T. Hong, M. Risch, K. A. Stoerzinger, A. Grimaud, J. Suntivich, Y. Shao-Horn, *Energy Environ. Sci.* **2015**, *8*, 1404.

[227] J. O. Bockris, T. Otagawa, *J. Phys. Chem.* **1983**, *87*, 2960.

[228] R. Frydendal, M. Busch, N. B. Halck, E. A. Paoli, P. Krtil, I. Chorkendorff, J. Rossmeisl, *ChemCatChem* **2015**, *7*, 149.

[229] D. Pletcher, X. Li, *Int. J. Hydrogen Energy* **2011**, *36*, 15089.

[230] A. Ursua, L. M. Gandia, P. Sanchis, *Proc. IEEE* **2012**, *100*, 410.

[231] Y. Jiao, Y. Zheng, M. Jaroniec, S. Z. Qiao, *Chem. Soc. Rev.* **2015**, *44*, 2060.

[232] J. K. Nørskov, T. Bligaard, J. Rossmeisl, C. H. Christensen, *Nat. Chem.* **2009**, *1*, 37.

[233] J. Greeley, N. M. Markovic, *Energy Environ. Sci.* **2012**, *5*, 9246.

[234] M. Alsabet, M. Grden, G. Jerkiewicz, *Electrocatalysis* **2011**, *2*, 317.

[235] D. S. Hall, C. Bock, B. R. MacDougall, *J. Electrochem. Soc.* **2013**, *160*, F235.

[236] M. Alsabet, M. Grdeń, G. Jerkiewicz, *Electrocatalysis* **2014**, *6*, 60.

[237] D. S. Hall, C. Bock, B. R. MacDougall, *ECS Trans.* **2013**, *50*, 165.

[238] S. L. Medway, C. A. Lucas, A. Kowal, R. J. Nichols, D. Johnson, *J. Electroanal. Chem.* **2006**, *587*, 172.

[239] E. S. Lambers, C. N. Dykstal, J. M. Seo, J. E. Rowe, P. H. Holloway, *Oxid. Met.* **1996**, *45*, 301.

[240] H. Bode, K. Dehmelt, J. Witte, *Electrochim. Acta* **1966**, *11*, 1079.

[241] R. L. Doyle, I. J. Godwin, M. P. Brandon, M. E. G. Lyons, *Phys. Chem. Chem. Phys.* **2013**, *15*, 13737.

[242] F. Dionigi, P. Strasser, *Adv. Energy Mater.* **2016**, *6*, 1600621.

[243] A. G. Oshchepkov, E. R. Savinova, *Kinet. Catal.* **2022**, *63*, 12.

[244] M. B. Stevens, C. D. M. Trang, L. J. Enman, J. Deng, S. W. Boettcher, *J. Am. Chem. Soc.* **2017**, *139*, 11361.

[245] Z. Da He, R. Tesch, M. J. Eslamibidgoli, M. H. Eikerling, P. M. Kowalski, *Nat. Commun.* **2023**, *14*, 3498.

[246] M. W. Louie, A. T. Bell, *J. Am. Chem. Soc.* **2013**, *135*, 12329.

[247] N. U. Hassan, M. Mandal, B. Zulevi, P. A. Kohl, W. E. Mustain, *Electrochim. Acta* **2022**, *409*, 140001.

[248] Y. Chen, K. Rui, J. Zhu, S. X. Dou, W. Sun, *Chem. - A Eur. J.* **2019**, *25*, 703.

[249] S. Klaus, Y. Cai, M. W. Louie, L. Trotochaud, A. T. Bell, *J. Phys. Chem. C* **2015**, *119*, 7243.

[250] A. M. Smith, L. Trotochaud, M. S. Burke, S. W. Boettcher, *Chem. Commun.* **2015**, *51*, 5261.

[251] D. A. Corrigan, *J. Electrochem. Soc.* **1987**, *134*, 377.

[252] M. Görlin, P. Chernev, J. F. De Araújo, T. Reier, S. Dresp, B. Paul, R. Krähnert, H. Dau, P. Strasser, J. Ferreira de Araújo, T. Reier, S. Dresp, B. Paul, R. Krähnert, H. Dau, P. Strasser, *J. Am. Chem. Soc.* **2016**, *138*, 5603.

[253] D. Friebel, M. W. Louie, M. Bajdich, K. E. Sanwald, Y. Cai, A. M. Wise, M.-J. J. Cheng, D. Sokaras, T.-C. C. Weng, R. Alonso-Mori, R. C. Davis, J. R. Bargar, J. K. Nørskov, A. Nilsson, A. T. Bell, *J. Am. Chem. Soc.* **2015**, *137*, 1305.

[254] L. J. Enman, M. S. Burke, A. S. Batchellor, S. W. Boettcher, *ACS Catal.* **2016**, *6*, 2416.

[255] R. D. L. Smith, C. Pasquini, S. Loos, P. Chernev, K. Klingan, P. Kubella, M. R. Mohammadi, D. González-Flores, H. Dau, *Energy Environ. Sci.* **2018**, *11*, 2476.

[256] M. S. Burke, M. G. Kast, L. Trotochaud, A. M. Smith, S. W. Boettcher, *J. Am. Chem. Soc.* **2015**, *137*, 3638.

[257] S. Lee, L. Bai, X. Hu, *Angew. Chemie Int. Ed.* **2020**, *59*, 8072.

[258] S. Lee, K. Banjac, M. Lingenfelder, X. Hu, *Angew. Chemie - Int. Ed.* **2019**, *58*, 10295.

[259] Z. K. Goldsmith, A. K. Harshan, J. B. Gerken, M. Vörös, G. Galli, S. S. Stahl, S. Hammes-Schiffer, *Proc. Natl. Acad. Sci.* **2017**, *114*, 3050.

[260] K. Zhu, X. Zhu, W. Yang, *Angew. Chemie Int. Ed.* **2019**, *58*, 1252.

[261] J. Wang, A. G. Kalinichev, J. E. Amonette, R. J. Kirkpatrick, *Am. Mineral.* **2003**, *88*, 398.

[262] Q. Wang, D. Ohare, *Chem. Rev.* **2012**, *112*, 4124.

[263] L. Lv, Z. Yang, K. Chen, C. Wang, Y. Xiong, *Adv. Energy Mater.* **2019**, *9*, DOI 10.1002/aenm.201803358.

[264] F. Dionigi, Z. Zeng, I. Sinev, T. Merzdorf, S. Deshpande, M. B. Lopez, S. Kunze, I. Zegkinoglou, H. Sarodnik, D. Fan, A. Bergmann, J. Drnec, J. F. de Araujo, M. Gliech, D. Teschner, J. Zhu, W.-X. X. Li, J. Greeley, B. R. Cuenya, P. Strasser, B. Roldan Cuenya,, P. Strasser, *Nat. Commun.* **2020**, *11*, 2522.

[265] F. Song, X. Hu, *Nat. Commun.* **2014**, *5*, 4477.

[266] N. Han, F. Zhao, Y. Li, *J. Mater. Chem. A* **2015**, *3*, 16348.

[267] R. Chen, S. F. Hung, D. Zhou, J. Gao, C. Yang, H. Tao, H. B. Yang, L. Zhang, L. Zhang, Q. Xiong, H. M. Chen, B. Liu, *Adv Mater* **2019**, *31*, e1903909.

[268] and G. S. Xiaowen Yu, Miao Zhang, Wenjing Yuan, *J. Mater. Chem. A* **2015**, 6921.

[269] Q. Wang, L. Shang, R. Shi, X. Zhang, Y. Zhao, G. I. N. Waterhouse, L. Z. Wu, C. H. Tung, T. Zhang, *Adv. Energy Mater.* **2017**, *7*, 1.

[270] B. M. Hunter, W. Hieringer, J. R. Winkler, H. B. Gray, A. M. Müller, *Energy Environ. Sci.* **2016**, *9*, 1734.

[271] X. Li, X. Hao, Z. Wang, A. Abudula, G. Guan, *J. Power Sources* **2017**, *347*, 193.

[272] H. Lei, L. Ma, Q. Wan, S. Tan, B. Yang, Z. Wang, W. Mai, H. J. Fan, *Adv. Energy Mater.* **2022**, *12*, DOI 10.1002/aenm.202202522.

[273] Z. He, J. Zhang, Z. Gong, H. Lei, D. Zhou, N. Zhang, W. Mai, S. Zhao, Y. Chen, *Nat. Commun.* **2022**, *13*, 2191.

[274] J. Xing, Z. Zeng, W. Best, Z. Liu, L. Bonville, R. Maric, S. Bliznakov, *J. Power Sources* **2023**, *558*, 232564.

[275] T. Malkow, A. Pilenga, G. Tsotridis, G. De Marco, *EU Harmonised Polarisation Curve Test Method for Low- Temperature Water Electrolysis*, **2018**.

[276] J. R. Varcoe, R. C. T. Slade, *Fuel Cells* **2005**, *5*, 187.

[277] M. G. Marino, K. D. Kreuer, *ChemSusChem* **2015**, *8*, 513.

[278] J. B. Edson, C. S. Macomber, B. S. Pivovar, J. M. Boncella, *J. Memb. Sci.* **2012**, *399–400*, 49.

[279] C. G. Arges, V. Ramani, *Proc. Natl. Acad. Sci.* **2013**, *110*, 2490.

[280] D. Henkensmeier, H. Kim, H. Lee, D. H. Lee, I. Oh, S. Hong, S. Nam, T. Lim, *Macromol. Mater. Eng.* **2011**, *296*, 899.

[281] D. Li, I. Matanovic, A. S. Lee, E. J. Park, C. Fujimoto, H. T. Chung, Y. S. Kim, *ACS Appl. Mater. Interfaces* **2019**, *11*, 9696.

[282] F. D. Speck, A. Zagalskaya, V. Alexandrov, S. Cherevko, *Angew. Chemie Int. Ed.* **2021**, *60*, 13343.

[283] A. Moysiadou, X. Hu, *J. Mater. Chem. A* **2019**, *7*, 25865.

[284] G. Cao, *Nanostructures and Nanomaterials: Synthesis, Properties and Applications*, Imperial College Press, London, **2004**.

[285] M. M. Mench, E. C. Kumbur, T. N. Veziroglu, *Polymer Electrolyte Fuel Cell Degradation*, Academic Press, **2011**.

[286] R. Vinodh, S. S. Kalanur, S. K. Natarajan, B. G. Pollet, *Polymers (Basel).* **2023**, *15*, DOI 10.3390/polym15092144.

[287] L. Zhang, Q. Xu, Y. Hu, L. Chen, H. Jiang, *ACS Sustain. Chem. Eng.* **2023**, *11*, 13251.

[288] K. Zeng, D. Zhang, *Prog. Energy Combust. Sci.* **2010**, *36*, 307.

[289] J. Zhao, X. Li, Z. sheng Liu, *Int. J. Energy Res.* **2019**, *43*, 6799.

[290] Y. Guo, D. Yang, B. Li, D. Yang, P. Ming, C. Zhang, *ACS Appl. Mater. Interfaces* **2021**, *13*, 27119.

[291] S. Khandavalli, J. H. Park, N. N. Kariuki, S. F. Zaccarine, S. Pylypenko, D. J. Myers, M. Ulsh, S. A. Mauger, *ACS Appl. Mater. Interfaces* **2019**, *11*, 45068.

[292] S. Shukla, S. Bhattacharjee, A. Z. Weber, M. Secanell, *J. Electrochem. Soc.* **2017**, *164*, F600.

[293] J. Mewis, N. J. Wagner, *Colloid. Suspens. Rheol.* **2011**, *9780521515*, 1.

[294] V. I. Kuchuk, I. Y. Shirokova, E. V. Golikova, *Glas. Phys. Chem.* **2012**, *38*, 460.

[295] J. Wyman, *J. Am. Chem. Soc.* **1931**, *53*, 3292.

[296] C. Bellmann, A. Caspari, C. Moitzi, F. Babick, *Dynamische Un Elektrophoretische Lichtstreuung*, **2018**.

[297] M. J. Weber, *Handbook of Optical Materials*, CRC Press LLC, Boca Raton, **2003**.

[298] M. J. Da Silva, *Impedance Sensors for Fast Multiphase Flow Measurement and Imaging*, **2008**.

[299] G. Ritzoulis, A. Fidantsi, *J. Chem. Eng. Data* **2000**, *45*, 207.

[300] T. Weissbach, A. G. Wright, T. J. Peckham, A. Sadeghi Alavijeh, V. Pan, E. Kjeang, S. Holdcroft, *Chem. Mater.* **2016**, *28*, 8060.

[301] L. Ritz, T. Pütz, M. Müller, F. Lohmann-Richters, "FZJ alkaline electrolysis test cell," DOI 10.26165/JUELICH-DATA/A3JB9Ocan be found under https://doi.org/10.26165/JUELICH-DATA/A3JB9, **2025**.

[302] T. Audichon, E. Mayousse, S. Morisset, C. Morais, C. Comminges, T. W. Napporn, K. B. Kokoh, *Int. J. Hydrogen Energy* **2014**, *39*, 16785.

[303] P. Lettenmeier, R. Wang, R. Abouatallah, S. Helmly, T. Morawietz, R. Hiesgen, S. Kolb, F. Burggraf, J. Kallo, A. S. Gago, K. A. Friedrich, *Electrochim. Acta* **2016**, *210*, 502.

[304] E. López-Fernández, J. Gil-Rostra, J. P. Espinós, A. R. González-Elipe, A. De Lucas Consuegra, F. Yubero, *ACS Catal.* **2020**, *10*, 6159.

[305] J. O. Majasan, F. Iacoviello, J. I. S. Cho, M. Maier, X. Lu, T. P. Neville, I. Dedigama, P. R. Shearing,

D. J. L. Brett, *Int. J. Hydrogen Energy* **2019**, *44*, 19519.

[306] J. Wei, M. Zhou, A. Long, Y. Xue, H. Liao, C. Wei, Z. J. Xu, *Nano-Micro Lett.* **2018**, *10*, 75.

[307] F. Razmjooei, T. Morawietz, E. Taghizadeh, E. Hadjixenophontos, L. Mues, M. Gerle, B. D. Wood, C. Harms, A. S. Gago, S. A. Ansar, K. A. Friedrich, *Joule* **2021**, *5*, 1776.

[308] S. Siracusano, S. Trocino, N. Briguglio, V. Baglio, A. S. Aricò, *Materials (Basel).* **2018**, *11*, 1368.

[309] M. A. Travassos, V. V. Lopes, R. A. Silva, A. Q. Novais, C. M. Rangel, *Int. J. Hydrogen Energy* **2013**, *38*, 7684.

[310] D. Malevich, E. Halliop, B. A. Peppley, J. G. Pharoah, K. Karan, *J. Electrochem. Soc.* **2009**, *156*, B216.

[311] J. T. Mueller, P. M. Urban, *J. Power Sources* **1998**, *75*, 139.

[312] O. Antoine, Y. Bultel, R. Durand, *J. Electroanal. Chem.* **2001**, *499*, 85.

[313] M. Eikerling, A. . Kornyshev, *J. Electroanal. Chem.* **1999**, *475*, 107.

[314] I. Dedigama, P. Angeli, K. Ayers, J. B. Robinson, P. R. Shearing, D. Tsaoulidis, D. J. L. Brett, *Int. J. Hydrogen Energy* **2014**, *39*, 4468.

[315] C. Liu, K. Wippermann, M. Rasinski, Y. Suo, M. Shviro, M. Carmo, W. Lehnert, *ACS Appl. Mater. Interfaces* **2021**, *13*, 16182.

[316] C. Spöri, J. T. H. Kwan, A. Bonakdarpour, D. P. Wilkinson, P. Strasser, *Angew. Chemie Int. Ed.* **2017**, *56*, 5994.

[317] V. Natarajan, S. Basu, *Int. J. Hydrogen Energy* **2015**, *40*, 16702.

[318] A. Thust, J. Barthel, K. Tillmann, *J. large-scale Res. Facil. JLSRF* **2016**, *2*, 3.

[319] A. Kovács, R. Schierholz, K. Tillmann, *J. large-scale Res. Facil. JLSRF* **2016**, *2*, A43.

[320] K. Kameyama, K. Tsukada, K. Yahikozawa, Y. Takasu, *J. Electrochem. Soc.* **1994**, *141*, 643.

[321] B. Johnson, F. Girgsdies, G. Weinberg, D. Rosenthal, A. Knop-Gericke, R. Schlögl, T. Reier, P. Strasser, *J. Phys. Chem. C* **2013**, *117*, 25443.

[322] B. D. Cullity, R. Smoluchowski, *Phys. Today* **1957**, *10*, 50.

[323] T. Luxbacher, A. P. GmbH, *The Zeta Potential for Solid Surface Analysis : A Practical Guide to Streaming Potential Measurement*, Anton Paar GmbH, **2014**.

[324] C. Bellmann, A. Caspari, C. Moitzi, F. Babick, *Dynamische Und Elektrophoretische Lichtstreuung-Leitfaden Zur Partikelgrößenanalyse Und Zetapotenzialbestimmung*, Anton Paar GmbH, Graz, **2018**.

[325] H. Noack, C. Moitzi, *Modulator Monitoring during Measuring Electromobility*, **2014**, EP 2 735 870 A1.

[326] W. Jiang, NiFe Layered Double Hydroxide Catalysts for Oxygen Evolution Reaction in Alkaline Water Electrolysis = Geschichtete NiFe Doppelhydroxid Katalysatoren Für Die Sauerstoffentwicklungsreaktion in Der Alkalischen Wasserelektrolyse, RWTH Aachen, **2022**.

[327] Z. W. Gao, J. Y. Liu, X. M. Chen, X. L. Zheng, J. Mao, H. Liu, T. Ma, L. Li, W. C. Wang, X. W. Du, *Adv. Mater.* **2019**, *31*, 1.

[328] Y. Han, Z. H. Liu, Z. Yang, Z. Wang, X. Tang, T. Wang, L. Fan, K. Ooi, *Chem. Mater.* **2008**, *20*, 360.

[329] J. Zhang, L. Yu, Y. Chen, X. F. Lu, S. Gao, X. W. D. Lou, *Adv Mater* **2020**, e1906432.

[330] M. Inaba, Y. Kamitaka, K. Kodama, *J. Electroanal. Chem.* **2021**, *886*, 115115.

[331] T. Lazaridis, B. M. Stühmeier, H. A. Gasteiger, H. A. El-Sayed, *Nat. Catal.* **2022**, *5*, 363.

[332] C. Du, Q. Tan, G. Yin, J. Zhang, in *Rotating Electrode Methods Oxyg. Reduct. Electrocatal.*, Elsevier, **2014**, pp. 171–198.

[333] M. Maazallahi, R. Bagheri, S. Nandy, K. H. Chae, M. M. Najafpour, *ACS Appl. Energy Mater.* **2023**, DOI 10.1021/acsaem.3c00629.

[334] B. J. M. Etzold, U. Krewer, S. Thiele, A. Dreizler, E. Klemm, T. Turek, *Chem. Eng. J.* **2021**, *424*, 130501.

[335] M. P. Arcot, M. Cronin, M. Fowler, M. Pritzker, *Electrochem* **2023**, *4*, 1.

[336] N. Kumano, K. Kudo, A. Suda, Y. Akimoto, M. Ishii, H. Nakamura, *J. Power Sources* **2019**, *419*, 219.

[337] G. Gupta, K. Scott, M. Mamlouk, *J. Power Sources* **2018**, *375*, 387.

[338] M. Mamlouk, K. Scott, J. A. Horsfall, C. Williams, *Int. J. Hydrogen Energy* **2011**, *36*, 7191.

[339] D. Xu, M. B. Stevens, M. R. Cosby, S. Z. Oener, A. M. Smith, L. J. Enman, K. E. Ayers, C. B. Capuano, J. N. Renner, N. Danilovic, Y. Li, H. Wang, Q. Zhang, S. W. Boettcher, *ACS Catal.* **2019**, *9*, 7.

[340] Q. Li, R. He, J. O. Jensen, N. J. Bjerrum, *Chem. Mater.* **2003**, *15*, 4896.

[341] S. Koch, J. Disch, S. K. Kilian, Y. Han, L. Metzler, A. Tengattini, L. Helfen, M. Schulz, M. Breitwieser, S. Vierrath, *RSC Adv.* **2022**, *12*, 20778.

[342] W. Xu, K. Scott, *Int. J. Hydrogen Energy* **2010**, *35*, 12029.

[343] Y. Jang, C. Seol, S. M. Kim, S. Jang, *Int. J. Hydrogen Energy* **2022**, *47*, 18229.

[344] E. Cossar, A. O. Barnett, F. Seland, R. Safari, G. A. Botton, E. A. Baranova, *J. Power Sources* **2021**, *514*, 230563.

[345] R. Phillips, A. Edwards, B. Rome, D. R. Jones, C. W. Dunnill, *Int. J. Hydrogen Energy* **2017**, *42*, 23986.

[346] A. Buttler, H. Spliethoff, *Renew. Sustain. Energy Rev.* **2018**, *82*, 2440.

[347] C. Chen, Y. L. S. Tse, G. E. Lindberg, C. Knight, G. A. Voth, *J. Am. Chem. Soc.* **2016**, *138*, 991.

[348] R. J. Gilliam, J. W. Graydon, D. W. Kirk, S. J. Thorpe, *Int. J. Hydrogen Energy* **2007**, *32*, 359.

[349] F. Allebrod, C. Chatzichristodoulou, P. L. Mollerup, M. B. Mogensen, *Int. J. Hydrogen Energy* **2012**, *37*, 16505.

[350] A. Hodges, S. Renz, F. Lohmann-Richters, A. Al-Musawi, A. Jupke, W. Lehnert, G. F. Swiegers, G. G. Wallace, *J. Chem. Eng. Data* **2023**, *68*, 1485.

[351] K. N. Grew, X. Ren, D. Chu, *Electrochem. Solid-State Lett.* **2011**, *14*, DOI 10.1149/2.011112esl.

[352] D. Marx, *ChemPhysChem* **2006**, *7*, 1848.

[353] S. J. Paddison, R. Paul, *Phys. Chem. Chem. Phys.* **2002**, *4*, 1158.

[354] P. Choi, N. H. Jalani, R. Datta, *J. Electrochem. Soc.* **2005**, *152*, E84.

[355] D. Hellwinkel, H. Seifert, *Justus Liebigs Ann. Chem.* **1972**, *762*, 29.

[356] C. Vogel, H. Komber, J. Meier-Haack, *React. Funct. Polym.* **2017**, *117*, 34.

[357] T. H. Pham, J. S. Olsson, P. Jannasch, *J. Am. Chem. Soc.* **2017**, *139*, 2888.

[358] G. Merle, M. Wessling, K. Nijmeijer, *J. Memb. Sci.* **2011**, *377*, 1.

[359] J. Ran, L. Wu, Y. He, Z. Yang, Y. Wang, C. Jiang, L. Ge, E. Bakangura, T. Xu, *J. Memb. Sci.* **2017**, *522*, 267.

[360] M. A. Hickner, A. M. Herring, E. B. Coughlin, *J. Polym. Sci. Part B Polym. Phys.* **2013**, *51*, 1727.

[361] R. A. Krivina, G. A. Lindquist, S. R. Beaudoin, T. N. Stovall, W. L. Thompson, L. P. Twight, D. Marsh, J. Grzyb, K. Fabrizio, J. E. Hutchison, S. W. Boettcher, *Adv. Mater.* **2022**, *2203033*, 2203033.

[362] J. Hnát, M. Plevová, J. Žitka, M. Paidar, K. Bouzek, *Electrochim. Acta* **2017**, *248*, 547.

[363] H. Qi, P. Zhang, H. Wang, Y. Cui, X. Liu, X. She, Y. Wen, T. Zhan, *J. Colloid Interface Sci.* **2021**, *599*, 370.

[364] C. Zhang, M. Shao, L. Zhou, Z. Li, K. Xiao, M. Wei, *ACS Appl. Mater. Interfaces* **2016**, *8*, 33697.

[365] C. Andronescu, S. Barwe, E. Ventosa, J. Masa, E. Vasile, B. Konkena, S. Möller, W. Schuhmann, *Angew. Chemie - Int. Ed.* **2017**, *56*, 11258.

[366] R. Li, J. Xu, Q. Pan, J. Ba, T. Tang, W. Luo, *ChemistryOpen* **2019**, *8*, 1027.

[367] Z. Zhang, D. Zhou, J. Liao, X. Bao, H. Yu, *Int. J. Energy Res.* **2019**, *43*, 1460.

[368] X. Li, F. C. Walsh, D. Pletcher, *Phys. Chem. Chem. Phys.* **2011**, *13*, 1162.

[369] A. Khataee, A. Shirole, P. Jannasch, A. Krüger, A. Cornell, *J. Mater. Chem. A* **2022**, *10*, 16061.

[370] Z. Liu, S. D. Sajjad, Y. Gao, H. Yang, J. J. Kaczur, R. I. Masel, *Int. J. Hydrogen Energy* **2017**, *42*, 29661.

[371] N. Ul Hassan, M. Mandal, G. Huang, H. A. Firouzjaie, P. A. Kohl, W. E. Mustain, *Adv. Energy Mater.* **2020**, *10*, 1.

[372] S. Siracusano, V. Baglio, S. A. Grigoriev, L. Merlo, V. N. Fateev, A. S. Aricò, *J. Power Sources* **2017**, *366*, 105.

[373] V. Gatard, I. M. Marin, D. De Masi, T. Encinas, F. Charlot, V. Martin, M. Aouine, C. Geantet, S. Faure, J. Deseure, J. Carrey, B. Chaudret, M. Chatenet, *ACS Appl. Energy Mater.* **2022**, *5*, 7034.

[374] J. Larminie, A. Dicks, *Fuel Cell Systems Explained*, Wiley, **2003**.

[375] R. A. Krivina, G. A. Lindquist, M. C. Yang, A. K. Cook, C. H. Hendon, A. R. Motz, C. Capuano, K. E. Ayers, J. E. Hutchison, S. W. Boettcher, *ACS Appl. Mater. Interfaces* **2022**, *14*, 18261.

[376] B. Mayerhöfer, K. Ehelebe, F. D. Speck, M. Bierling, J. Bender, J. A. Kerres, K. J. J. Mayrhofer, S. Cherevko, R. Peach, S. Thiele, *J. Mater. Chem. A* **2021**, *9*, 14285.

[377] P. Oliva, J. Leonardi, J. F. Laurent, C. Delmas, J. J. Braconnier, M. Figlarz, F. Fievet, A. de Guibert, *J. Power Sources* **1982**, *8*, 229.

[378] L. A. Stern, L. Feng, F. Song, X. Hu, *Energy Environ. Sci.* **2015**, *8*, 2347.

[379] M. B. Stevens, L. J. Enman, E. H. Korkus, J. Zaffran, C. D. M. Trang, J. Asbury, M. G. Kast, M. C. Toroker, S. W. Boettcher, *Nano Res.* **2019**, *12*, 2288.

[380] W. Chen, H. Wang, Y. Li, Y. Liu, J. Sun, S. Lee, J. S. Lee, Y. Cui, *ACS Cent. Sci.* **2015**, *1*, 244.

[381] J. Liu, J. Zhou, S. Liu, G. Chen, W. Wu, Y. Li, P. Jin, C. Xu, *Electrochim. Acta* **2020**, *356*, 136827.

[382] Y. Tang, Q. Liu, L. Dong, H. Bin Wu, X. Y. Yu, *Appl. Catal. B Environ.* **2020**, *266*, 118627.

[383] M. Casas-Cabanas, J. Canales-Vázquez, J. Rodríguez-Carvajal, M. R. Palacín, *J. Am. Chem. Soc.* **2007**, *129*, 5840.

[384] D. S. Hall, D. J. Lockwood, S. Poirier, C. Bock, B. R. MacDougall, *J. Phys. Chem. A* **2012**, *116*, 6771.

[385] B. Sriram, J. N. Baby, S. F. Wang, R. Ranjitha M., M. Govindasamy, M. George, *ACS Sustain. Chem. Eng.* **2020**, *8*, 17772.

[386] J. T. Kloprogge, D. Wharton, L. Hickey, R. L. Frost, *Am. Mineral.* **2002**, *87*, 623.

[387] O. Diaz-Morales, D. Ferrus-Suspedra, M. T. M. Koper, *Chem. Sci.* **2016**, *7*, 2639.

[388] H. Yin, L. Jiang, P. Liu, M. Al-Mamun, Y. Wang, Y. L. Zhong, H. Yang, D. Wang, Z. Tang, H. Zhao, *Nano Res.* **2018**, *11*, 3959.

[389] F. Song, M. M. Busch, B. Lassalle-Kaiser, C. S. Hsu, E. Petkucheva, M. Bensimon, H. M. Chen, C. Corminboeuf, X. Hu, *ACS Cent. Sci.* **2019**, *5*, 558.

[390] J. Chen, F. Zheng, S. J. Zhang, A. Fisher, Y. Zhou, Z. Wang, Y. Li, B. Bin Xu, J. T. Li, S. G. Sun, *ACS Catal.* **2018**, *8*, 11342.

[391] D. C. Huang, P. J. Yu, F. J. Liu, S. L. Huang, K. L. Hsueh, Y. C. Chen, C. H. Wu, W. C. Chang, F. H. Tsau, *Int. J. Electrochem. Sci.* **2011**, *6*, 2551.

[392] C.-H. Song, J.-S. Park, *Energies* **2019**, *12*, 549.

[393] M. Wang, J. H. Park, S. Kabir, K. C. Neyerlin, N. N. Kariuki, H. Lv, V. R. Stamenkovic, D. J. Myers, M. Ulsh, S. A. Mauger, *ACS Appl. Energy Mater.* **2019**, *2*, 6417.

[394] V. Chandrasekharan Nair, P. Gupta, J. S. Sangwai, *Energy & Fuels* **2019**, *33*, 3108.

[395] H. He, J. Gu, X. Liu, D. Yang, Y. Zhu, R. Yao, Q. Fan, R. Huang, *Catalysts* **2020**, *10*, DOI 10.3390/catal10040431.

[396] L. Li, Y. Feng, Y. Li, W. Zhao, J. Shi, *Angew. Chemie - Int. Ed.* **2009**, *48*, 5888.

[397] J. Pérez-Ramírez, S. Abelló, N. M. Van Der Pers, *Chem. - A Eur. J.* **2007**, *13*, 870.

[398] M. R. Gauna, M. S. Conconi, S. Gomez, G. Suárez, E. F. Aglietti, N. M. Rendtorff, *Ceram. - Silikaty* **2015**, *50*, 318.

[399] J. L. Bantignies, S. Deabate, A. Righi, S. Rols, P. Hermet, J. L. Sauvajol, F. Henn, *J. Phys. Chem. C* **2008**, *112*, 2193.

[400] L. Bai, S. Lee, X. Hu, *Angew. Chemie - Int. Ed.* **2021**, *60*, 3095.

[401] H. Zhang, J. Pan, X. He, M. Pan, *J. Appl. Polym. Sci.* **2008**, *107*, 3306.

[402] J. A. Elliott, S. Hanna, A. M. S. Elliott, G. E. Cooley, *Polymer (Guildf).* **2001**, *42*, 2251.

[403] P. J. James, J. A. Elliott, J. McMaster, J. M. Newton, A. M. S. Elliott, S. Hanna, M. J. Miles, *J. Mater. Sci.* **2000**, *35*, 5111.

[404] M. Larsson, A. Hill, J. Duffy, *Annu. Trans. Nord. Rheol. Soc.* **2012**, *20*, 1999.

[405] ASTM Standard D 4187-82, *Am. Soc. Test. Mater.* **1985**.

[406] D. Q. Lin, P. J. Brixius, J. J. Hubbuch, J. Thömmes, M. R. Kula, *Biotechnol. Bioeng.* **2003**, *83*, 149.

[407] S. A. Berlinger, B. D. McCloskey, A. Z. Weber, *J. Phys. Chem. B* **2018**, *122*, 7790.

[408] G. F. Li, D. Yang, P. Y. Abel Chuang, *ACS Catal.* **2018**, *8*, 11688.

[409] I. Ostolska, M. Wišniewska, *Colloid Polym. Sci.* **2014**, *292*, 2453.

[410] S. Tsushima, S. Hirai, *J. Therm. Sci. Technol.* **2015**, *10*, 1.

[411] R. Jiang, C. K. Mittelsteadt, C. S. Gittleman, *J. Electrochem. Soc.* **2009**, *156*, B1440.

[412] Z. Kang, J. Mo, G. Yang, Y. Li, D. A. Talley, S. T. Retterer, D. A. Cullen, T. J. Toops, M. P. Brady, G. Bender, B. S. Pivovar, J. B. Green, F. Y. Zhang, *Appl. Energy* **2017**, *206*, 983.

[413] Y. Qiu, H. Zhang, H. Zhong, F. Zhang, *Int. J. Hydrogen Energy* **2013**, *38*, 5836.

[414] X. Yuan, J. C. Sun, M. Blanco, H. Wang, J. Zhang, D. P. Wilkinson, *J. Power Sources* **2006**, *161*, 920.

[415] M. Breitwieser, M. Klingele, S. Vierrath, R. Zengerle, S. Thiele, *Adv. Energy Mater.* **2018**, *8*, DOI 10.1002/aenm.201701257.

[416] J. Polonský, R. Kodým, P. Vágner, M. Paidar, B. Bensmann, K. Bouzek, *J. Appl. Electrochem.* **2017**, *47*, 1137.

[417] P. Lettenmeier, S. Kolb, F. Burggraf, A. S. Gago, K. A. Friedrich, *J. Power Sources* **2016**, *311*, 153.

[418] J. Lopata, Z. Kang, J. Young, G. Bender, J. W. Weidner, S. Shimpalee, *J. Electrochem. Soc.* **2020**, *167*, 064507.

[419] I. Ieropoulos, J. Winfield, J. Greenman, *Bioresour. Technol.* **2010**, *101*, 3520.

[420] T. Schuler, J. M. Ciccone, B. Krentscher, F. Marone, C. Peter, T. J. Schmidt, F. N. Büchi, *Adv. Energy Mater.* **2020**, *10*, 1.

[421] Z. Li, M. Shao, H. An, Z. Wang, S. Xu, M. Wei, D. G. Evans, X. Duan, *Chem. Sci.* **2015**, *6*, 6624.

[422] M. Plevová, J. Hnat, M. Paidar, K. Bouzek, J. Žitka, *ECS Meet. Abstr.* **2022**, *MA2022-01*, 1226.

[423] M. Plevová, J. Hnát, J. Žitka, L. Pavlovec, M. Otmar, K. Bouzek, *J. Power Sources* **2022**, *539*, DOI 10.1016/j.jpowsour.2022.231476.

[424] K. H. Kim, K. Y. Lee, H. J. Kim, E. A. Cho, S. Y. Lee, T. H. Lim, S. P. Yoon, I. C. Hwang, J. H. Jang, *Int. J. Hydrogen Energy* **2010**, *35*, 2119.

[425] G. A. Lindquist, S. Z. Oener, R. Krivina, A. R. Motz, A. Keane, C. Capuano, K. E. Ayers, S. W. Boettcher, *ACS Appl. Mater. Interfaces* **2021**, DOI 10.1021/acsami.1c06053.

[426] L. Wang, T. Weissbach, R. Reissner, A. Ansar, A. S. Gago, S. Holdcroft, K. A. Friedrich, *ACS Appl. Energy Mater.* **2019**, *2*, 7903.

[427] B. Chen, P. Mardle, S. Holdcroft, *J. Power Sources* **2022**, *550*, 232134.

[428] T. Bayer, B. V. Cunning, R. Selyanchyn, T. Daio, M. Nishihara, S. Fujikawa, K. Sasaki, S. M. Lyth, *J. Memb. Sci.* **2016**, *508*, 51.

[429] F. Sun, G. Wang, Y. Ding, C. Wang, B. Yuan, Y. Lin, *Adv. Energy Mater.* **2018**, *8*, 1.

[430] M. R. Kraglund, M. Carmo, G. Schiller, S. A. Ansar, D. Aili, E. Christensen, J. O. Jensen, *Energy Environ. Sci.* **2019**, *12*, 3313.

[431] M. Rossini, B. Koyutürk, B. Eriksson, A. Khataee, G. Lindbergh, A. Cornell, *J. Power Sources* **2024**, *614*, 235062.

[432] J. Zhao, S. Shahgaldi, A. Ozden, I. E. Alaefour, X. Li, F. Hamdullahpur, *Appl. Energy* **2019**, *255*, 113802.

[433] E. O. Balogun, N. Hussain, J. Chamier, P. Barendse, *Int. J. Hydrogen Energy* **2019**, *44*, 32219.

[434] T. Lickert, S. Fischer, J. L. Young, S. Klose, I. Franzetti, D. Hahn, Z. Kang, M. Shviro, F. Scheepers, M. Carmo, T. Smolinka, G. Bender, S. Metz, *Appl. Energy* **2023**, *352*, 121898.

[435] F. Y. Chen, Z. Y. Wu, Z. Adler, H. Wang, *Joule* **2021**, *5*, 1704.

9 DIRECTORIES

9.1 LIST OF ABBREVIATIONS

1-PrOH	1-propanol
2-PrOH	2-propanol
AEI	anion-exchange ionomer
AEMWE	anion exchange membrane water electrolyzers
aPTE	anodic porous transport electrode
AWE	alkaline water electrolyzers
BET	Brunauer-Emmett-Teller
BoT	begin-of-test
CCM	catalyst-coated membrane
CCS	catalyst-coated substrate
CL	catalyst layer
DFT	density functional theory
DI	deionized
DLS	dynamic light scattering
DM	dispersion media
DMSO	dimethyl sulfoxide
EDX or EDS	energy-dispersive X-ray spectroscopy
EEC	equivalent electrical circuit
EIS	electrochemical impedance spectroscopy
ELS	electrophoretic light scattering
EoT	End-of-Test
EPDM	ethylene propylene diene monomer rubber
ETFE	poly(ethylene-co-tetrafluoroethylene)
EtOH	ethanol
FC	fuel cell
FIB-SEM	focused ion beam SEM
GEIS	galvanostatic electrochemical impedance spectroscopy
H_2	hydrogen
HAADF	high angle annular dark field
HER	hydrogen evolution reaction
HHV	higher heating value

HR-TEM	high-resolution transmission electron microscopy
i	initial
ICP-MS	inductively coupled plasma mass spectrometry
ICP-OES	inductively coupled plasma optical emission spectroscopy
JRC	Joint Research Centre
LDH	layered double hydroxides
LHV	lower heating value
MEA	membrane-electrode assemblies
MeOH	methanol
mRB	milled (on) roller bench
mTM	milled (by) tumbler mixer
O_2	oxygen
OER	oxygen evolution reaction
PAEK	polyaryletherketone
PBI	polybenzimidazole
PCCEL	proton-conducting ceramic electrolysis
PE	polyethylene
PEEK	polyetherketone
PEM	proton exchange membrane
PGM	platinum group metal
PPO	poly(p-phenylene oxide)
PS	polystyrene
PSU	polysulfone
PTFE	polytetrafluorethylen
PTL	porous transport layers
QA	quaternary ammoniums
RDE	rotating disk electrode
redox	reduction-oxidation
RHE	reference hydrogen electrode
rpm	rounds per minute
SEM	scanning electron microscopy
SOEC	solid oxide electrolysis
SS	stainless steel
STEM	scanning transmission electron microscopy
ToF-SIMS	time-of-flight secondary ion mass spectrometry

TPB	triple-phase boundaries
WE	water electrolysis
XPS	X-Ray photoelectron spectroscopy
XRD	X-Ray diffraction

9.2 LIST OF SYMBOLS

E_0	equilibrium potential
E_{cell}	cell potential
E_{rev}	theoretical reversible cell voltage
E_{rev}^0	reversible equilibrium potential
E_{th}^0	thermoneutral potential
H_2	hydrogen
H_2O	water
O_2	oxygen
R_{el}	electronic resistance
R_{mem}	membrane resistance
R_{Ohm}	ohmic resistance
e^-	electron
j_0	exchange current density
η_{F}	faradaic efficiency
η_{HHV}	voltage efficiency reffered to highest heating value
η_{kin}	kinetic overpotential
η_{mt}	mass transport overpotential
η_{Ohm}	ohmic overpotential
η_{v}	voltage efficiency
ΔG^0	change of Gibbs free energy
ΔH^0	enthalpy
ΔS^0	entropy
b	Tafel slope
F	Faradey constant
R	gas constant
T	temperature
a	relative activities of the reactants

i	current (of the electrolyzer)
j	current density
n	number of electrons
p	partial pressure
β	symmetry factor or transfer coefficient

9.3 LIST OF FIGURES

Figures in the Appendix

9.4 LIST OF TABLES

Tables in the Appendix

10 APPENDIX

10.1 APPENDIX: IMPLEMENTATION OF Ni_3Fe-LDH ANODES

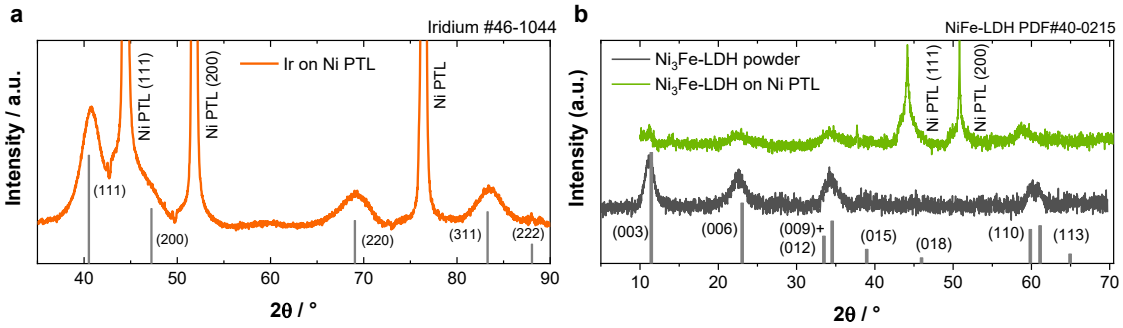

Figure-A 1. Successful deposition of (a) Ir and (b) Ni_3Fe-LDH onto Ni PTLs confirmed by XRD analysis.

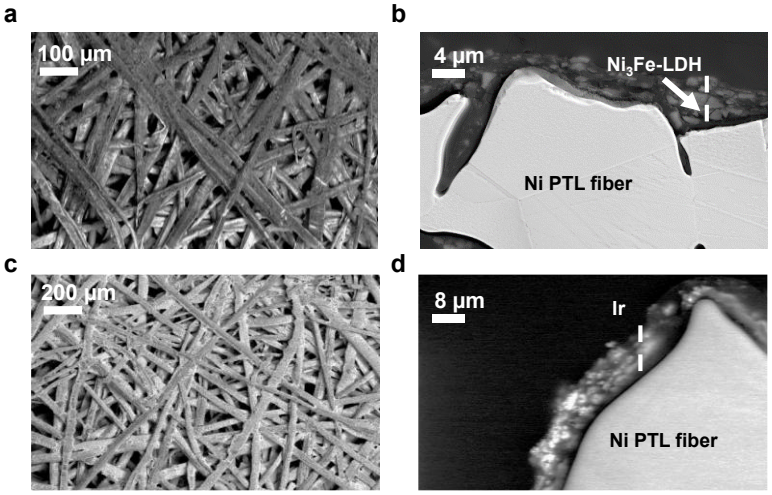

Figure-A 2. SEM images of catalysts coated on Ni fiber PTL: (a) top-view and (b) cross-sectional view of Ir coated PTL, (c) top-view and (d) cross-sectional view of Ni coated PTL. Both catalyst layers have a loading of 1 mg cm^{-2} and 20 wt% binder.

SEM characterization of the electrodes from top-view and cross-sectional view showed a full coverage of the Ni PTL fibers, as well as similar catalyst layer thicknesses for both the Ir and Ni_3Fe-LDH of about 6–10 µm at loadings of 1 mg cm^{-2}.

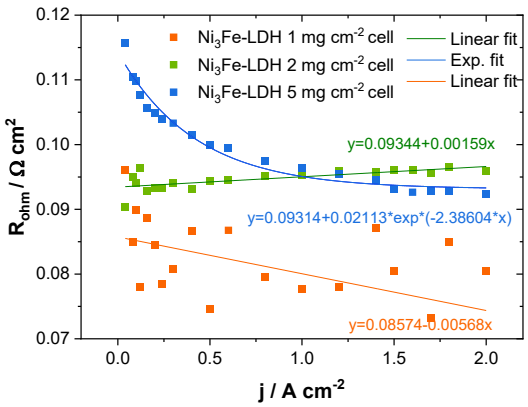

Figure-A 3. Current density dependent R_{Ohm} values for all three single-cells: 1 mg cm^{-2} catalyst loaded cell (orange), 2 mg cm^{-2} catalyst loaded cell (green) and 5 mg cm^{-2} catalyst loaded cell (blue), including the linear fits for the first two, and an exponential fit for the 5 mg cm^{-2} cell's trend.

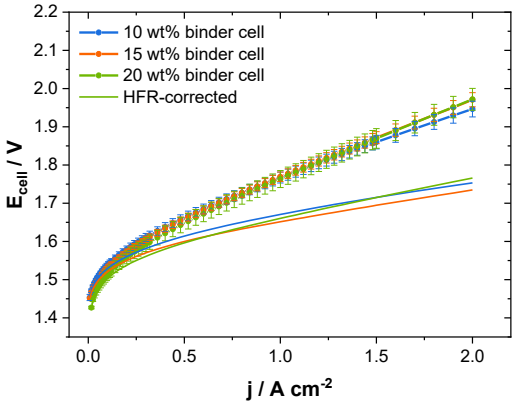

Figure-A 4. Comparison of single-cells with different binder contents in the initial catalyst dispersion (10, 15, 20 wt%): Polarization curves with error bars, incl. iR-corrected curves. All components, except the anodes are identical. Cathode: Pt/C 0.6 mg cm^{-2} (25 wt%). Testing conditions: 1 M KOH, 60 °C.

Table-A 1. Fitted R_{ct} and R_{Ohm} values for the Ni_3Fe-LDH single-cell with varying catalyst loadings in the anode.

	1 mg cm^{-2} catalyst loading	**2 mg cm^{-2} catalyst loading**	**5 mg cm^{-2} catalyst loading**
R_{Ohm} / Ω cm^2	0.082±0.005	0.089±0.006	0.103±0.005
R_{ct} / Ω cm^2	0.184±0.004	0.156±0.009	0.154±0.006

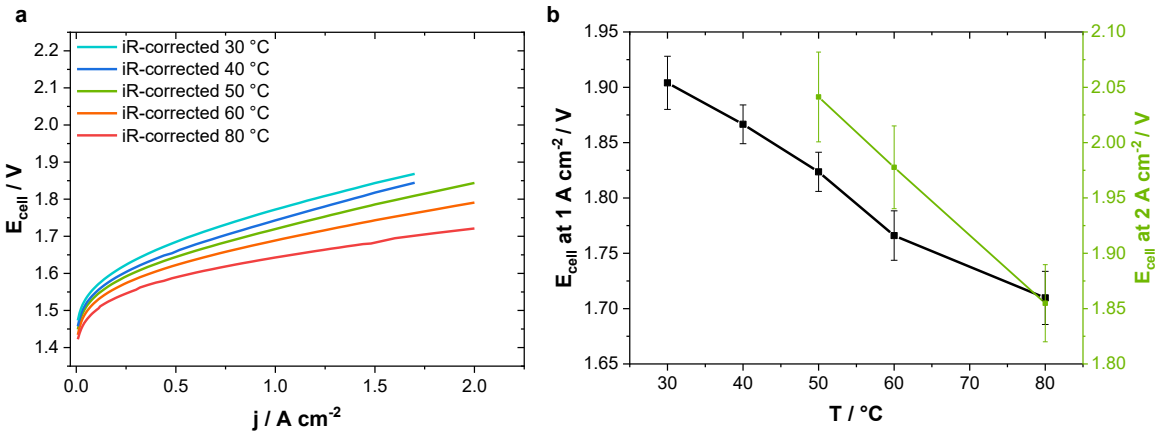

Figure-A 5. Comparison of Ni_3Fe-LDH-based single-cell performance at different operation temperatures: 30 °C (light blue), 40 °C (blue), 50 °C (green), 60 °C (orange) and 80 °C (red). (a) Polarization curves including iR-corrected curves, (b) E_{cell} achieved at different operating temperatures at 1 (black) and 2 (green) A cm^{-2}. For all cells the cathode is Pt/C-based (0.6 mg cm^{-2}, 25 % binder), the electrolyte is 1 M KOH.

Table-A 2. Fitted R_{ct} and R_{Ohm} values for the Ni_3Fe-LDH single-cell with varying binder contents in the anode.

	10 wt% binder content	**15 wt% binder content**	**20 wt% binder content**
R_{Ohm} **/ Ω cm²**	0.096±0.007	0.118±0.080	0.103±0.002
R_{ct} **/ Ω cm²**	0.149±0.004	0.109±0.006	0.150±0.002

Table-A 3. Voltages reached at 1 or 2 A cm^{-2} by the Ni_3Fe-LDH single-cell (2 mg cm^{-2}, 20 wt% binder) at different operating temperatures (30-80 °C). Cathode: Pt/C (0.6 mg cm^{-2}, 25 wt% binder). Tested in 1 M KOH.

Operation temperature vs. cell voltage	**30 °C**	**40 °C**	**50 °C**	**60 °C**	**80 °C**
E_{cell} **at 1 A cm^{-2} / V**	1.904±0.024	1.852±0.013	1.813±0.021	1.776±0.015	1.701±0.023
E_{cell} **at 2 A cm^{-2} / V**	Did not reach <2.1 V	Did not reach <2.1 V	2.041±0.041	1.977±0.037	1.855±0.034

Table-A 4. Fitted R_{ct} and R_{Ohm} values for the Ni_3Fe-LDH single-cell operated at different temperatures.

	30 °C	40 °C	50 °C	60 °C	80 °C
R_{Ohm} / Ω cm²	0.132±0.004	0.108±0.009	0.093±0.009	0.088±0.002	0.067±0.009
R_{ct} / Ω cm²	0.216±0.006	0.183±0.013	0.168±0.008	0.156±0.004	0.119±0.014

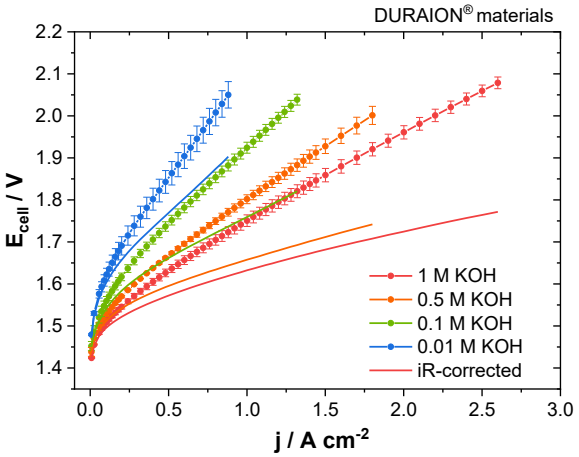

Figure-A 6. Comparison of Ni_3Fe-LDH-based single-cell performance at different electrolyte concentrations: 1 M KOH (red), 0.5 M KOH (orange), 0.1 M KOH (green), 0.01 M KOH (blue): iR-corrected polarization curves. For all cells the cathode is Pt/C-based (0.6 mg cm^{-2}, 25 % binder), the operating temperature is 60 °C.

Table-A 5. Fitted R_{ct} and R_{Ohm} values for the Ni_3Fe-LDH single-cell operated in different electrolyte concentrations.

	1 M KOH	0.5 M KOH	0.1 M KOH	0.01 M KOH
R_{Ohm} / Ω cm²	0.118±0.007	0.144±0.011	0.165±0.009	0.167±0.015
R_{ct} / Ω cm²	0.129±0.006	0.169±0.012	0.242±0.011	0.382±0.020

10.2 APPENDIX: DURABILITY ASSESSMENT AND DEGRADATION MECHANISMS IN Ni_3Fe-LDH ANODES

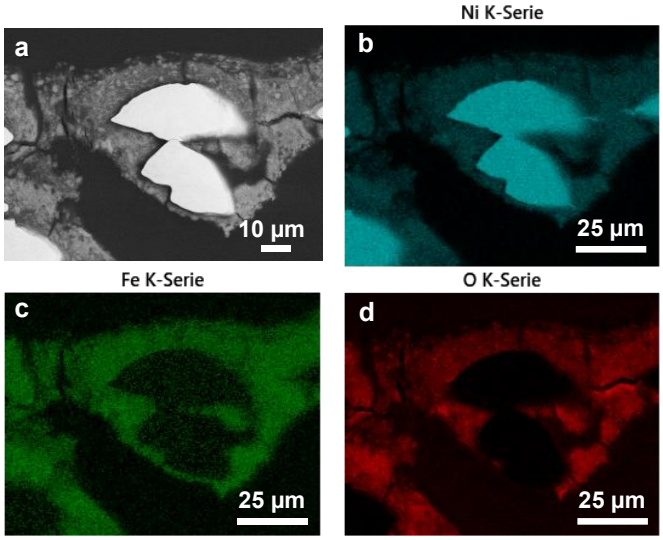

Figure-A 7. Ni_3Fe-LDH coated Ni fiber from cross-sectional view: (a) SEM image, (b) EDS element mapping for Ni, (c) for Fe, (d) for O, proving homogenous distribution of the catalyst.

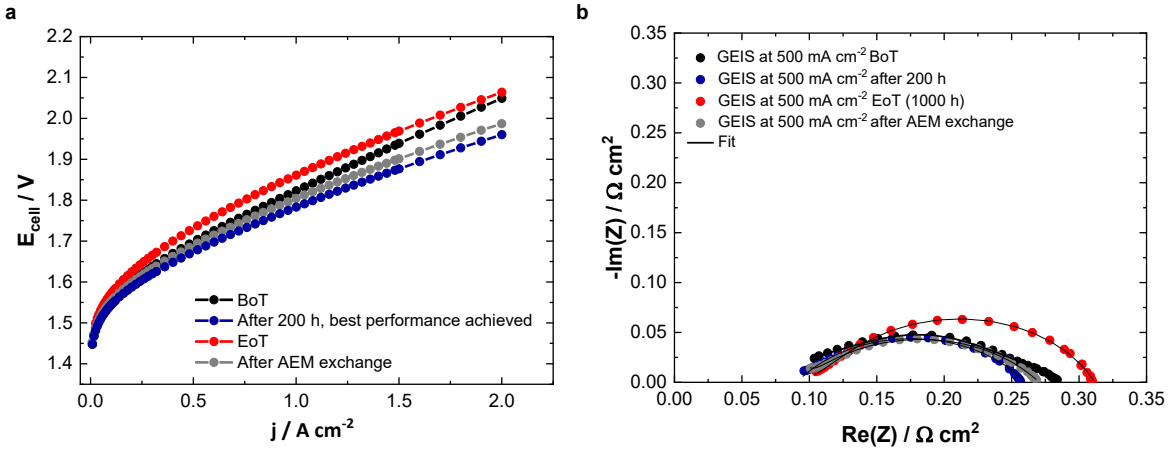

Figure-A 8. (a) Polarization curves and (b) Nyquist plots obtained by impedance spectroscopy for the Ni_3Fe-LDH cell at BoT, EoT, after AEM exchange and after 200 h (lowest E_{cell} achieved). Cathode: Pt/C 0.6 mg cm^{-2} (25 wt% binder). Testing conditions: 1 M KOH, 60 °C.

Table-A 6. Fitted R_{ct} and R_{Ohm} values for the Ni_3Fe-LDH single-cell at BoT, EoT, at every other 100 h of operation and after exchange of membrane.

	BoT	100 h	200 h	300 h	400 h	500 h
R_{Ohm} / Ω cm²	0.064±0.009	0.070±0.010	0.090±0.001	0.100±0.001	0.099±0.002	0.105±0.004
R_{Ohm} / Ω cm²	0.202±0.005	0.177±0.004	0.169±0.001	0.169±0.001	0.184±0.007	0.189±0.006
	600 h	**700 h**	**800 h**	**900 h**	**EoT**	**After AEM exchange**
R_{Ohm} / Ω cm²	0.101±0.001	0.104±0.001	0.105±0.002	0.099±0.003	0.096±0.001	0.055±0.001
R_{Ohm} / Ω cm²	0.196±0.002	0.199±0.001	0.200±0.001	0.200±0.001	0.198±0.003	0.175±0.002

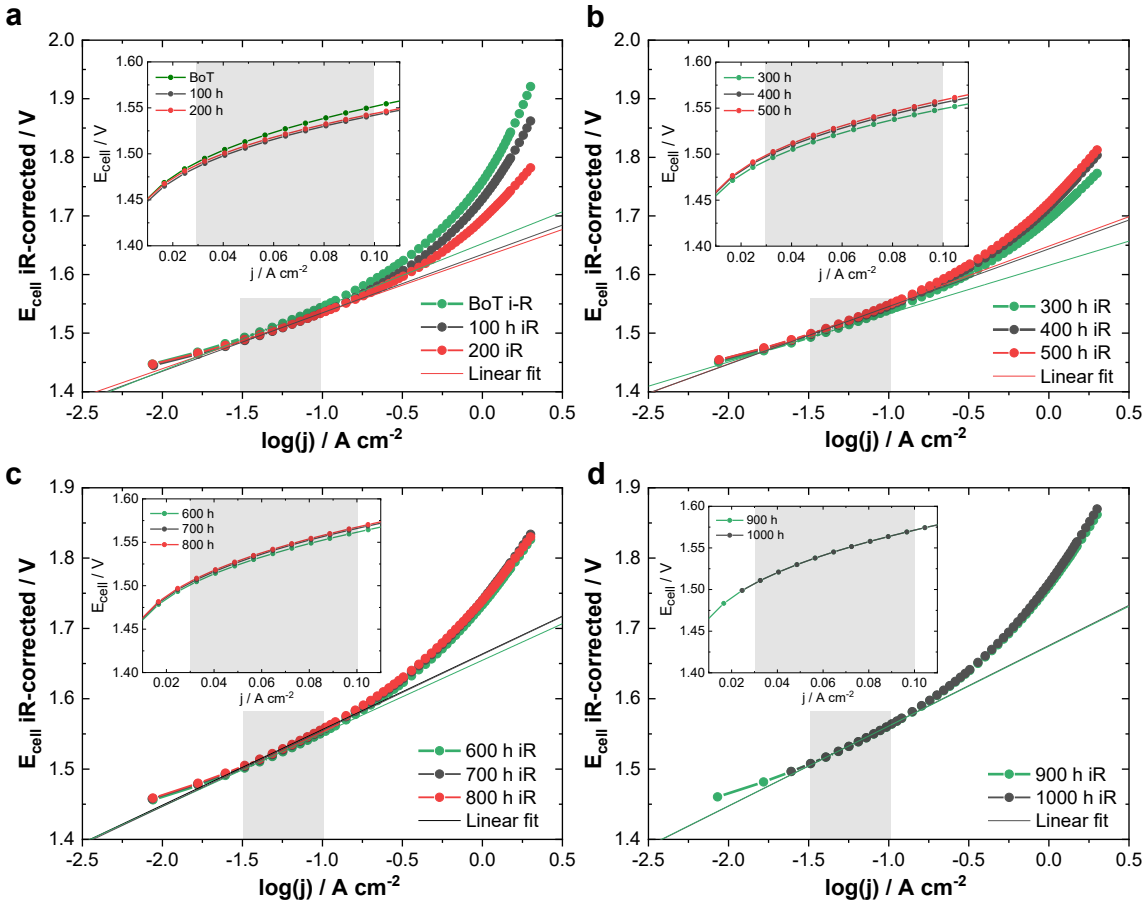

Figure-A 9. dE/dlogj slopes evaluation from the polarization curves, corrected for Ohmic losses and fitted from the linear trend of the polarization curve in the current density intervals from 0.03 to 0.1 A cm^{-2}; (a) for BoT, 100 h, 200 h polarization curves, (b) for 300 h, 400 h, 500 h polarization curves, (c) for 600 h, 700 h, 800 h polarization curves, (d) for 900 h and 1000 h (EoT) polarization curves.

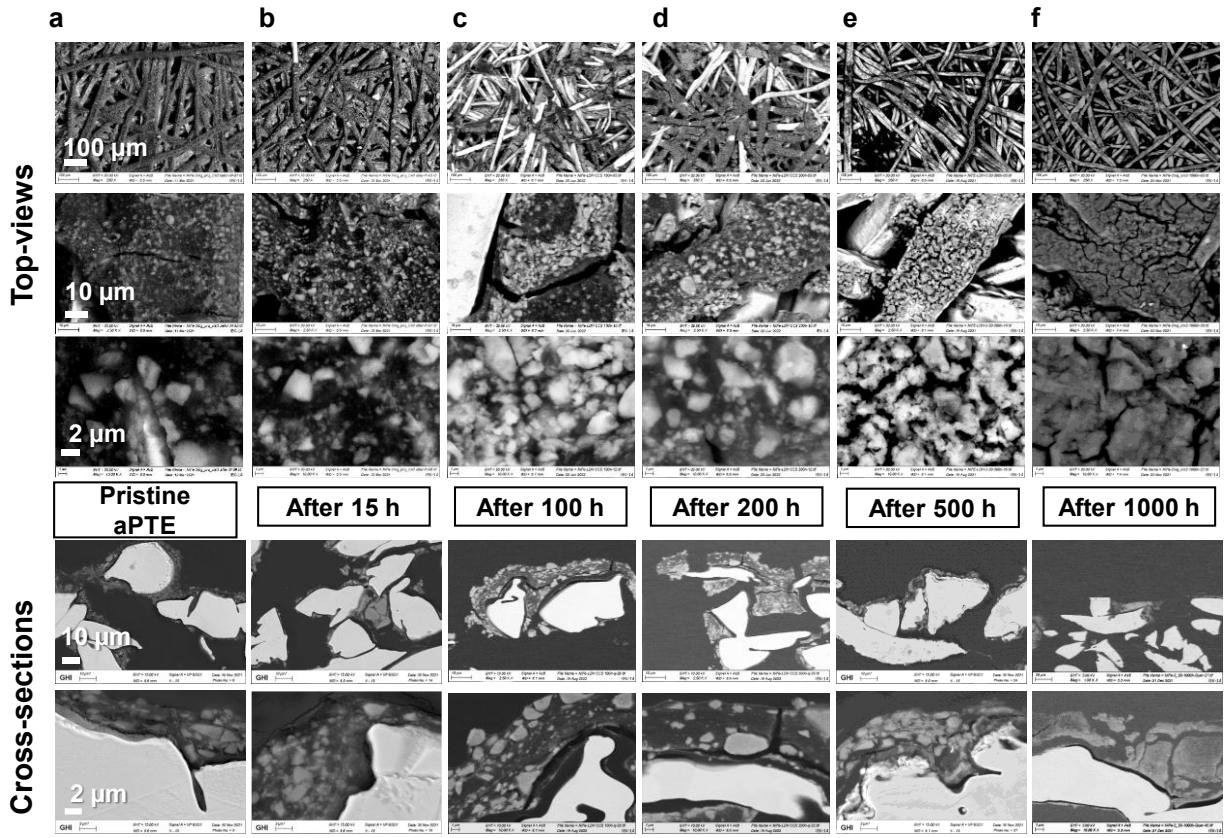

Figure-A 10. Top-view (top three rows) and cross-section (bottom two rows) SEM images of the aPTE (a) direct after fabrication, (b) after 15 h, (c) 100 h, (d) 200 h, (e) 500 h and (f) 1000 h of single-cell operation.

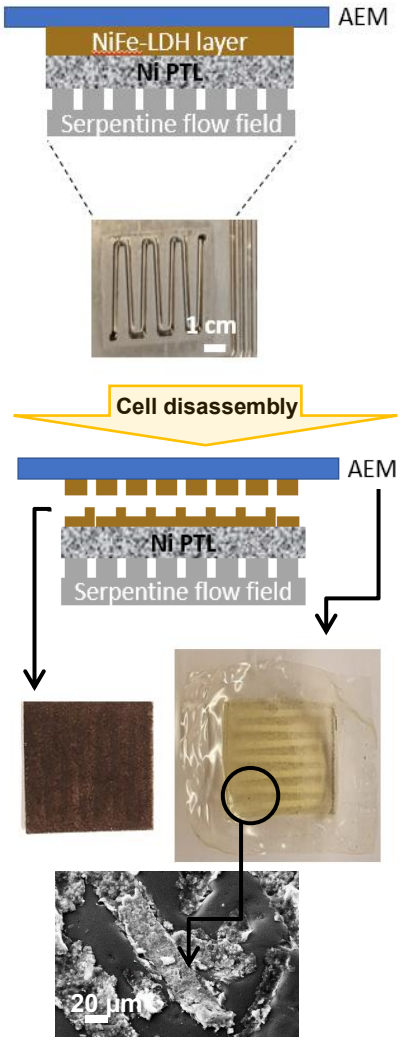

Figure-A 11. Mechanical harm explanation occurring during single-cell disassembly incl. SEM images of catalyst leftovers on the AEM after 1000 h of single-cell operation.

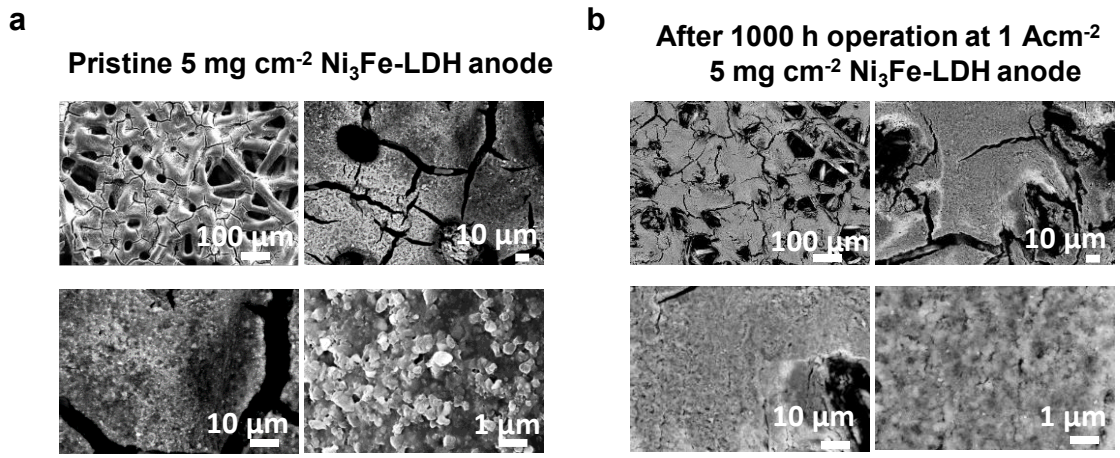

Figure-A 12. SEM images of (a) pristine Ni_3Fe-LDH aPTE with a higher loading of 5 mg cm^{-2}; (b) same aPTE after 1000 h of single-cell operation.

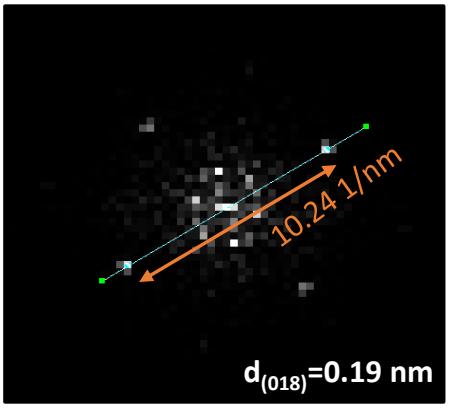

Figure-A 13. Fourier transformed image of the region with basal spacing of 0.19 nm.

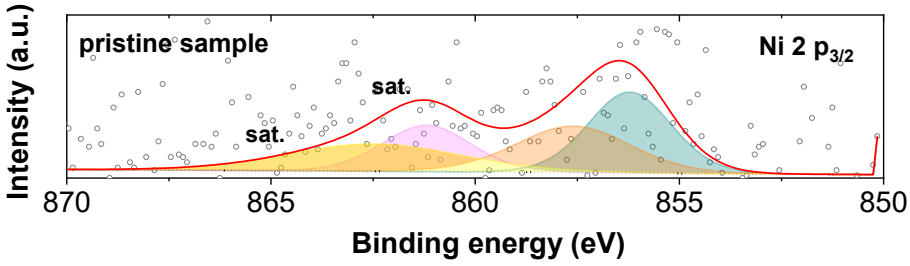

Figure-A 14. The XPS high resolution spectra of Ni 2p of the Ni_3Fe-LDH aPTE with catalyst loading of 2 mg cm^{-2}.

Table-A 7. Main peak position, area, area%, FWHW of the fitted XPS peaks and corresponding specie, found by peak positions and literature.

Ni 2 p3/2	Main peaks in graph	Position (eV)	Area	Area %	FWHM	Specie, peak position (eV), literature
pristine	Black	854.71	393.73	7.36	1.46	NiO 854.70 [*1]
	Blue	855.73	2362.38	44.17	2.05	Ni(OH)2 855.70 [*2,3]
	Orange	857.38	226.13	4.23	2.05	
15 h	Black	854.52	1649.51	7.36	1.99	Clear NiO 855.50 [*1]
	Blue	855.29	9897.05	44.17	2.78	In between NiO and Ni(OH)2 peaks
	Orange	857.31	947.38	4.23	2.78	
100 h	Black	855.16	611.88	6.49	1.36	NiO 855.0 [*4], 855.50 [*1]
	Blue	855.93	4160.75	44.11	2.73	Ni(OH)2 855.90 [*5]
	Orange	857.95	293.70	3.11	1.91	β-NiOOH(2+) 857.7 [*3]
200 h	Black	855.24	1229.47	6.49	1.37	NiO 855.0 [*4], 855.50 [*1]
	Blue	856.01	8360.41	44.11	2.74	Ni(OH)2 856.00 [*6,7,8,9,10]

	Orange	858.03	590.14	3.11	1.92	β-NiOOH(2+) 857.7 [*3]
500 h	Black	855.23	341.21	7.37	1.95	NiO 855.0 [*4], 855.50 [*1] Contribution Ni(OH)2 855.88 [*11]
	Blue	856.00	2047.23	44.22	2.73	Clearer observation of compound Ni(OH)2 [*6,7,8,9,10]
	Orange	858.02	195.97	4.23	2.73	β-NiOOH(2+) 857.7 [*3]
1000 h	Black	855.19	2089.04	7.37	1.82	Close to Ni(OH)2 peaks
	Blue	855.96	12534.25	44.21	2.55	β-NiOOH(2+) 855.7 [*3] Mixed NiOOH 855.92 [*12]
	Orange	857.96	1199.82	4.23	2.55	β-NiOOH(2+) 857.7 [*3]

References used in Table-A 7:

[*1] G. Ertl, R. Hierl, H. Knozinger, N. Thiele, and H. P. Urbach, Appl. Surf. Sci., 5, 49 (1980).

[*2] A. M. Venezia, R. Bertoncello ', and G. Deganello, Surf. Interface Anal., 23, 239 (1995).

[*3] http://www.xpsfitting.com/

[*4] S. O. Grim, L. J. Matienzo, and W. E. Swartz, J. Am. Chem. Soc., 94, 5116 (1972).

[*5] L. Salvati, L. E. Makovsky, J. M. Stencel, F. R. BrownlS, D. M. Hercules, J. Phys. Chem., 85, 3700 (1981).

[*6] A. N. Mansour, Surf. Sci. Spectra, 3, 211 (1994).

[*7] C. E. Dubé, B. Workie, S. P. Kounaves, A. Robbat, Jr., M. Levant Aksu, and G. Davies, J. Electrochem. Soc., 142, 3357 (1995).

[*8] B. P. Lochel and H. H. Strehblow, J. Electrochem. Soc., 131, 713 (1984).

[*9] J. C. Klein and D. M. Hercules, J. Catal., 82, 424 (1983).

[*10] C. P. Li, A. Proctor, and D. M. Hercules, Appl. Spectrosc., 38, 880 (1984).

[*11] K. Lian, S. J. Thorpe, and D. W. Kirk, Electrochim. Acta, 37, 2029 (1992).

[*12] K. K. Lian, D. W. Kirk, and S. J. Thorpe, J. Electrochem. Soc., 142, 3704 (1995).

10.3 APPENDIX: ENHANCED AEMWE PERFORMANCE THROUGH CATALYST MILLING AND LAYER DESIGN

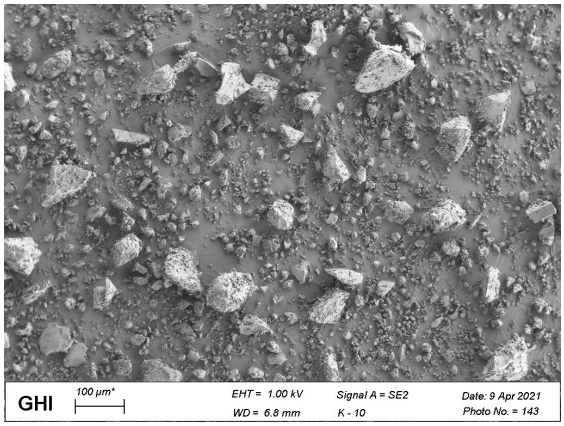

Figure-A 15. SEM image of the loose initial Ni_3Fe-LDH catalyst powder (i-NiFe-LDH): agglomerate or cluster size is inhomogeneous and reaches from 1 µm up to 100 µm.

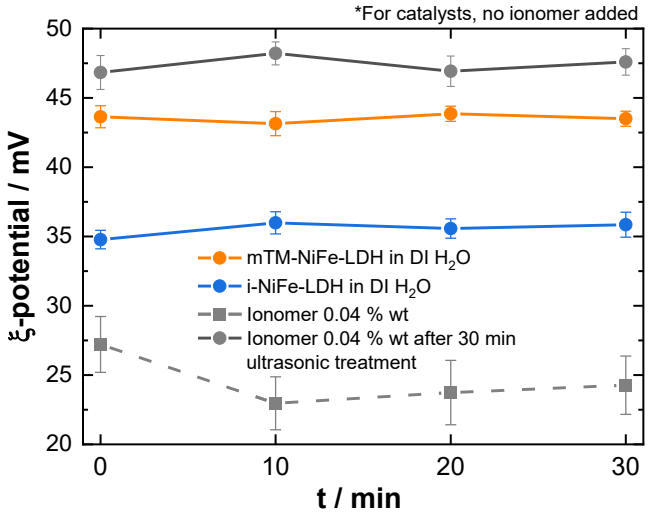

Figure-A 16. Dispersion control on i-NiFe-LDH (blue) and mTM-NiFe-LDH (orange) catalysts: ζ-potential values of the catalysts in pure water after 30 min of dispersion and within 30 min without additional dispersing afterwards, and of the anion-conducting binder dispersion after being dissolved and after 30 min of additional ultrasonic dispersing.

Table-A 8. ζ-potential values for all catalyst dispersions, including ionomer and different solvents and dispersing times of 10 or 30 min. Some dispersion compositions were analyzed just once, as these were directly excluded for further experiments due to the low stability of the inks.

	i-NiFe-LDH		**mRB-NiFe-LDH**		**mTM-NiFe-LDH**	
Dispersion media (DM), ultranosic (US) dispersing time	Average value	Standard deviation	Average value	Standard deviation	Average value	Standard deviation
pure EtOH, 10 min US	33.1	1.6	35.3	2.4	36.4	1.9
pure EtOH, 30 min US	20.2	1.5	38.1	1.8	37.9	1.2
3:1 EtOH:H_2O, 10 min US	29.4	0.9	32.3	1.6	32.0	2.3
3:1 EtOH:H_2O, 30 min US	31.1	1.1	34.2	1.2	33.6	2.9
1:1 EtOH:H_2O, 10 min US	37.1	1.1	45.8	2.3	45.5	Not repeated
1:1 EtOH:H_2O, 30 min US	39.1	1.3	46.2	1.7	47.8	1
3:1 2-PrOH:H_2O, 10 min US	21.2	1.9	22.4	Not repeated	32.1	Not repeated
3:1 2-PrOH:H_2O, 30 min US	23.2	1.5	33.1	Not repeated	34.8	Not repeated
1:1 2-PrOH:H_2O, 10 min US	30.5	1.7	40.6	2.4	48.8	Not repeated
1:1 2-PrOH:H_2O, 30 min US	33.1	2.3	41.3	1.5	58.4	Not repeated
3:1 1-PrOH:H_2O, 10 min US	50.8	Not repeated	48.5	4.1	57.1	Not repeated
3:1 1-PrOH:H_2O, 30 min US	53.4	Not repeated	49.9	1.7	63.2	Not repeated
1:1 1-PrOH:H_2O, 10 min US	57.8	2.0	63.0	2.6	67.0	3.1
1:1 1-PrOH:H_2O, 30 min US	58.9	0.9	69.1	3.4	70.1	3.4

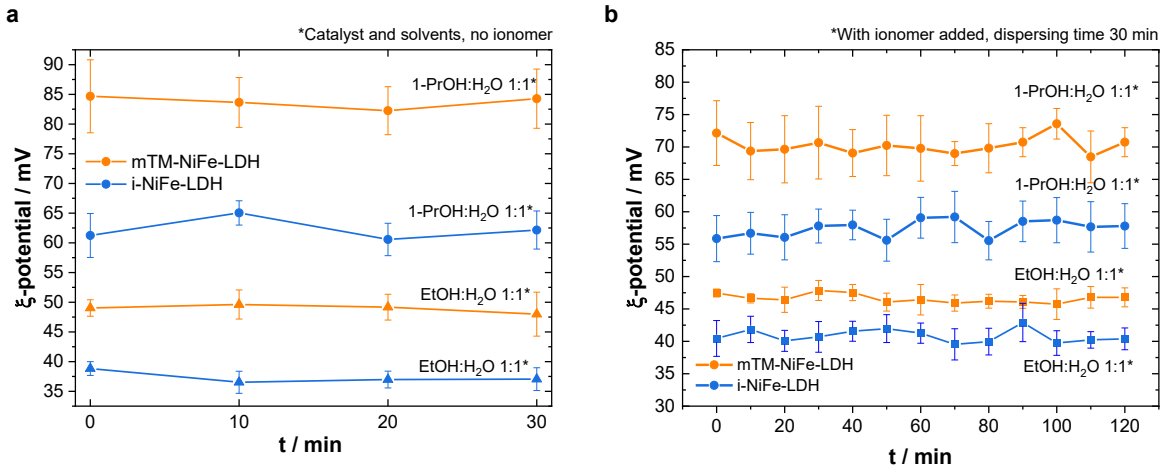

Figure-A 17. ζ-potential values of the four chosen catalyst inks based on EtOH:H_2O 1:1 and 1-PrOH:H_2O 1:1: (a) tracked during 30 min of being kept on the bench without additional dispersing, without the binder added; (b) with binder added, during 120 min of being kept on the bench without additional dispersing.

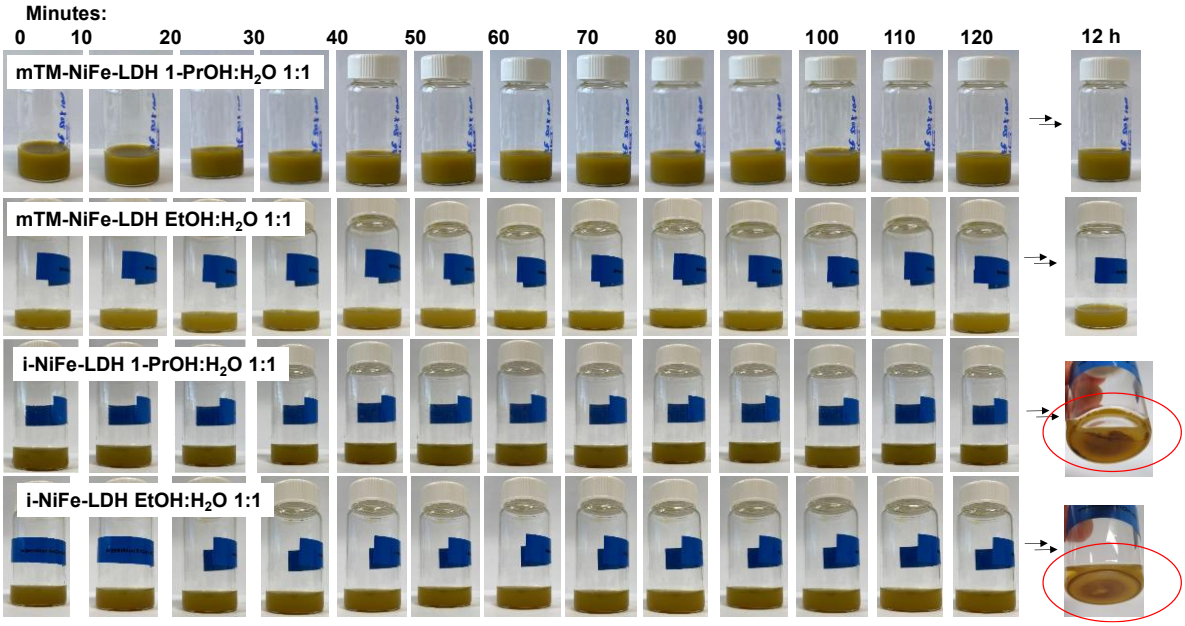

Figure-A 18. Time-lapse photographic analysis of stability in selected catalyst ink compositions: every 10 min up to 2 h, and additionally after 12 h.

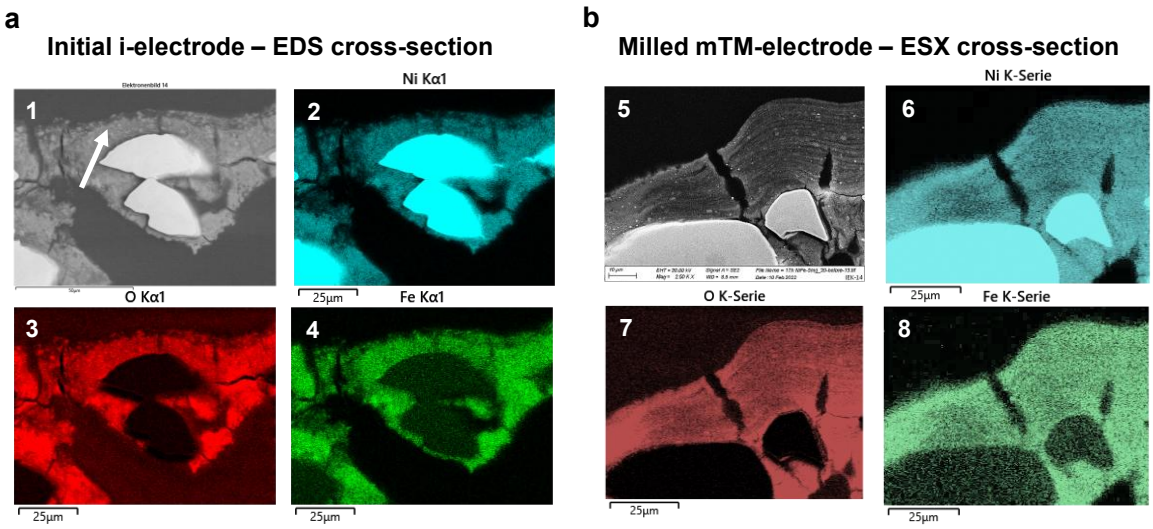

Figure-A 19. Ni_3Fe-LDH coated on Ni fiber PTL: EDS mapping for Ni, Fe and O, (a) for i-electrode and (b) mTM-electrode; cross-section view. White arrays indicate the formation of multiple layers within the CL with varying particle densities, likely a result from catalyst particle sedimentation occurring during electrode fabrication.

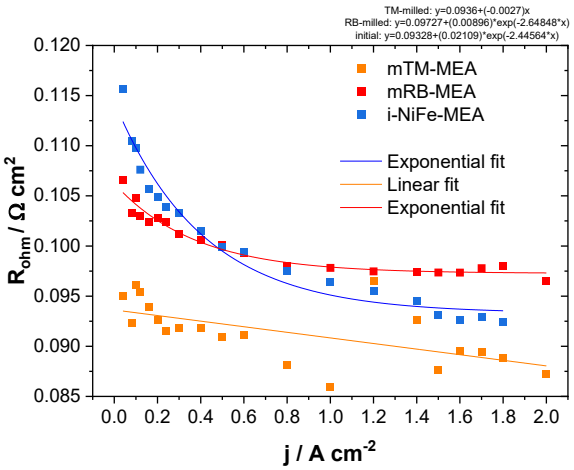

Figure-A 20. Current density dependent Ohmic resistance (R_{Ohm}) values for all three single-cells: i-NiFe-LDH (blue), mRB-NiFe-LDH (red), mTM-NiFe-LDH (orange), including the exponential fits for the first two, and a linear fit for the mTM-NiFe-LDH MEA's trend.

Table-A 9. Fitted R_{ct} and R_{Ohm} values for the Ni_3Fe-LDH single-cell with varying catalysts: the initial NiFe-LDH (i-cell), milled mRB-NiFe-LDH and milled mTM-NiFe-LDH (mTM-cell).

	i-cell	**mRB-cell**	**mTM-cell**
R_{Ohm} / Ω cm²	0.102	0.099	0.092
R_{ct} / Ω cm²	0.157	0.128	0.113

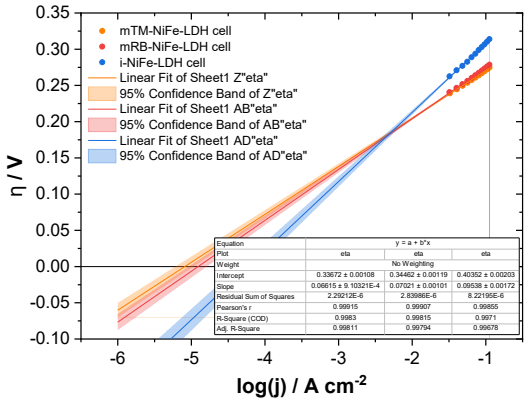

Figure-A 21. Linear fits for *dE*/*d*log*j* with R-squares of 0.998 for both milled-cells and 0.997 for the i-cell.

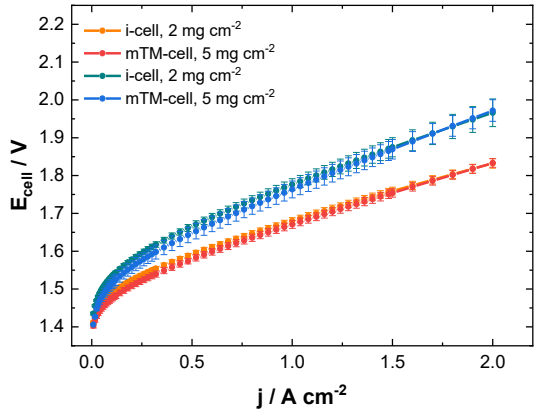

Figure-A 22. Comparative single-cell performance tests for i-cell and mTM-cell catalyts with loadings of 2 and 5 mg cm^{-2} on the anode electrodes. Cathode: Pt/C 0.6 mg cm^{-2} (25 wt% binder). Testing conditions: 1 M KOH, 60 °C.

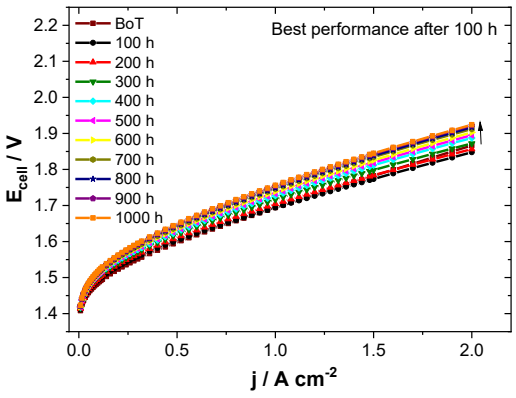

Figure-A 23. Polarization curves for the mTM-cell, recorded at BoT, EoT (1000 h) and every 100 h in between during long-term durability test. Cathode: Pt/C 0.6 mg cm^{-2} (25 wt% binder). Testing conditions: 1 M KOH, 60 °C.

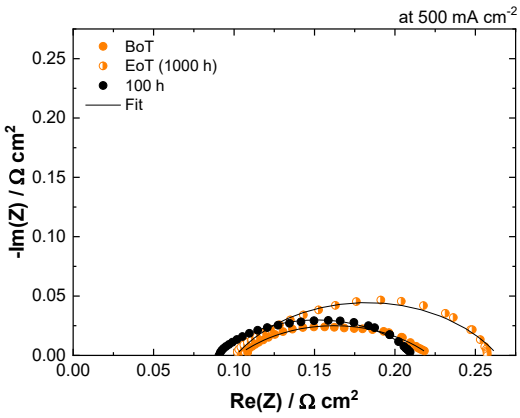

Figure-A 24. Nyquist plots obtained by impedance spectroscopy at 500 mA cm^{-2} with simulated fit curves for the milled-cell at BoT, EoT and after 100 h of operation. Cathode: Pt/C 0.6 mg cm^{-2} (25 wt% binder). Testing conditions: 1 M KOH, 60 °C.

10.4 APPENDIX: STRUCTURAL AND ELECTROCHEMICAL INSIGHTS INTO ANODE CONFIGURATIONS

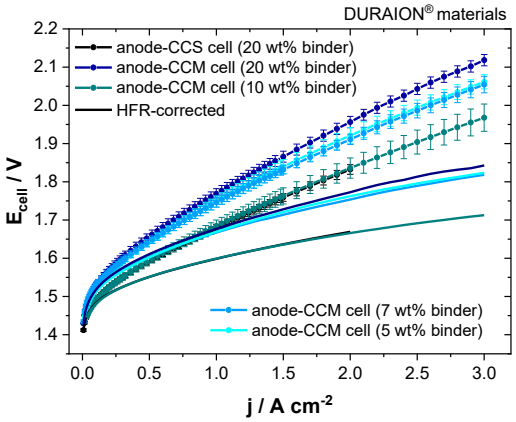

Figure-A 25. Polarization curves with error bars incl. iR-corrected curves. Performance of anode-CCM single-cells with different binder contents in the initial catalyst dispersion (5, 7, 10, 20 wt%) and the anode-CCS cell (20 wt% binder). The MEAs are fabricated based on DURAION® materials. All components, except the MEA are identical. Cathode: Pt/C 0.6 mg cm^{-2} (25 wt% binder). Testing conditions: 1 M KOH, 60 °C.

Table-A 10. R_{Ohm} and R_{ct} values of the analysed cells, obtained by fitting the corresponding Nyquist plots at 500 mA cm^{-2}.

Single-cell	Anode-CCS (20 wt% binder) or full CCS cell	Anode-CCM (20 wt% binder) cell	Anode-CCM (10 wt% binder) cell	Anode-CCM (7 wt% binder) cell	Anode-CCM (5 wt% binder) cell
R_{Ohm} / Ω cm^2	0.079	0.095	0.086	0.077	0.078
R_{ct} / Ω cm^2	0.124	0.154	0.128	0.155	0.153

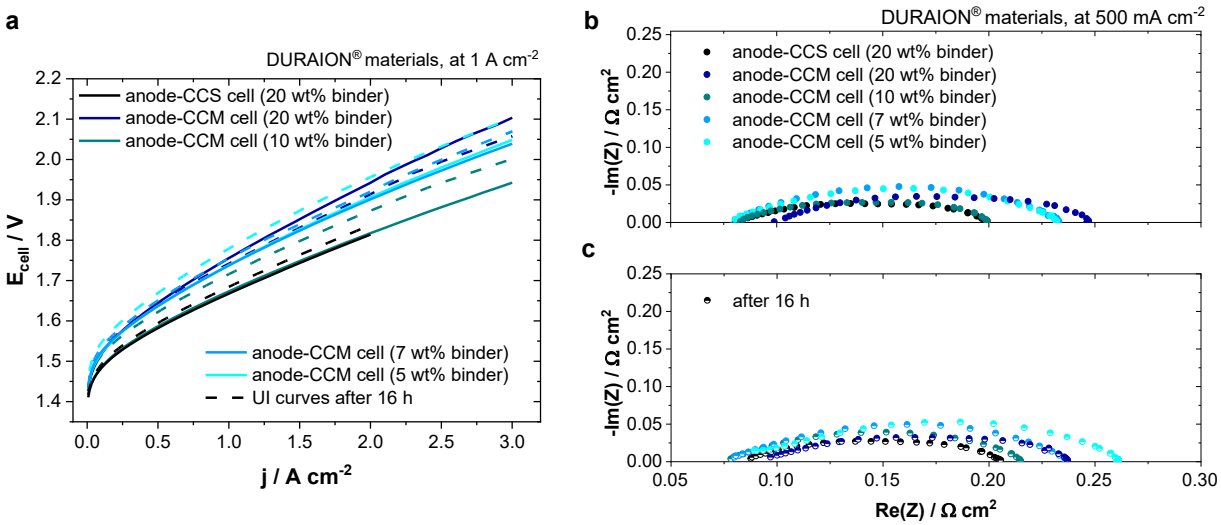

Figure-A 26. (a) Polarization curves before and after 16 h stability test and corresponding, Nyquist plots obtained by impedance spectroscopy at 500 mA cm^{-2} for the anode-CCS cell (20 wt% binder) and the anode-CCMs cell with varying binder content (5, 7, 10, 20 wt%) (b) before and (c) after 16 h. Cathode: Pt/C 0.6 mg cm^{-2} (25 wt% binder). Testing conditions: 1 M KOH, 60 °C.

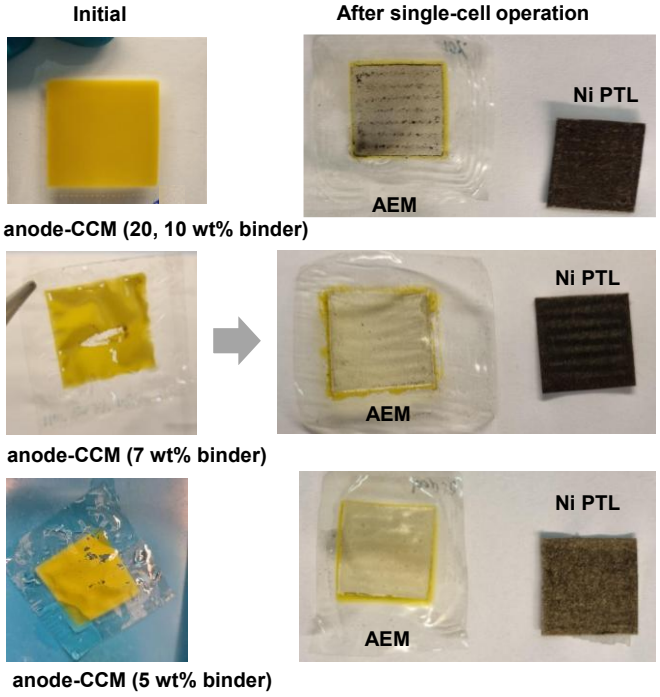

Figure-A 27. Anode-CCMs based on DURAION® AEM with varying ionomer content before single-cell assembly (left) and after single-cell operation and disassembly (right), the transferring of the CL from AEM to the Ni PTL is shown.

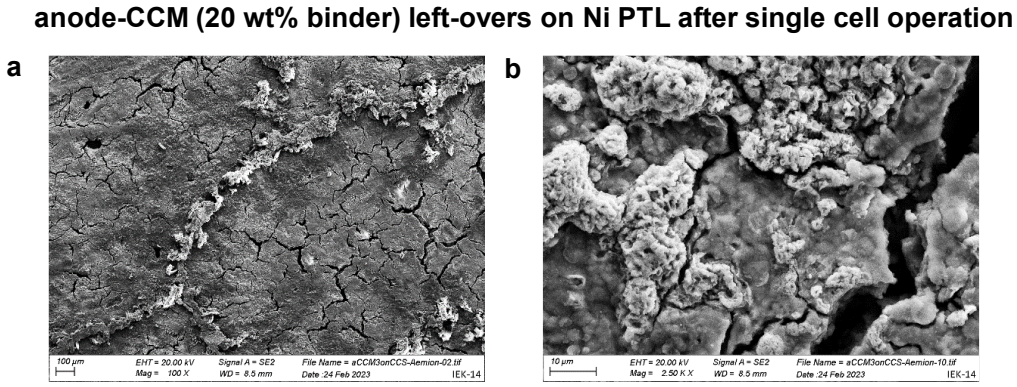

Figure-A 28. Top-view SEM images at a magnification of (a) x100 and (b) x2500 of Ni PTLs covered with the CL printed from the anode-CCM (20 wt% binder) based on DURAION® AEM after single-cell operation. The transferred CL creates a nearly continuous layer, markedly different from the initial anode-CCS, which displayed coated individual fibers.

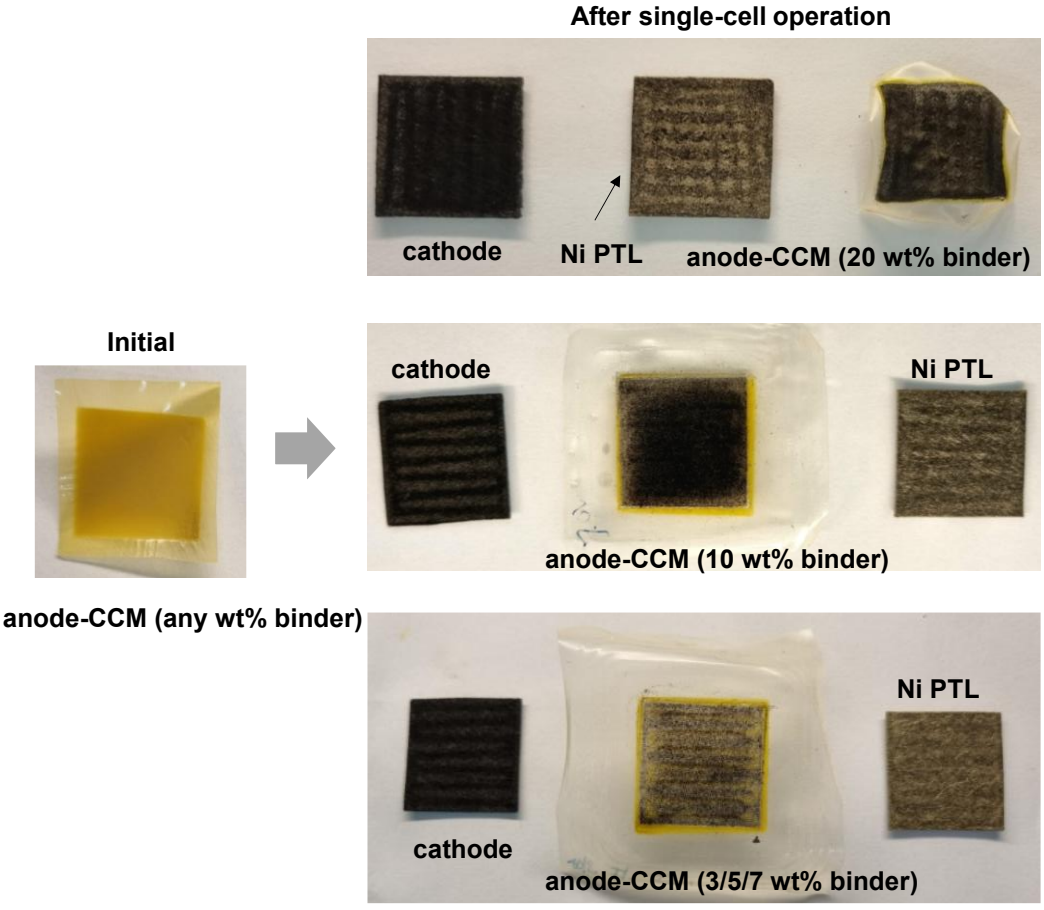

Figure-A 29. Anode-CCMs based on Aemion+™ materials with varying ionomer content before single-cell assembly (left) and after single-cell operation and disassembly (right), the transferring of the CL from AEM to the Ni PTL is shown.

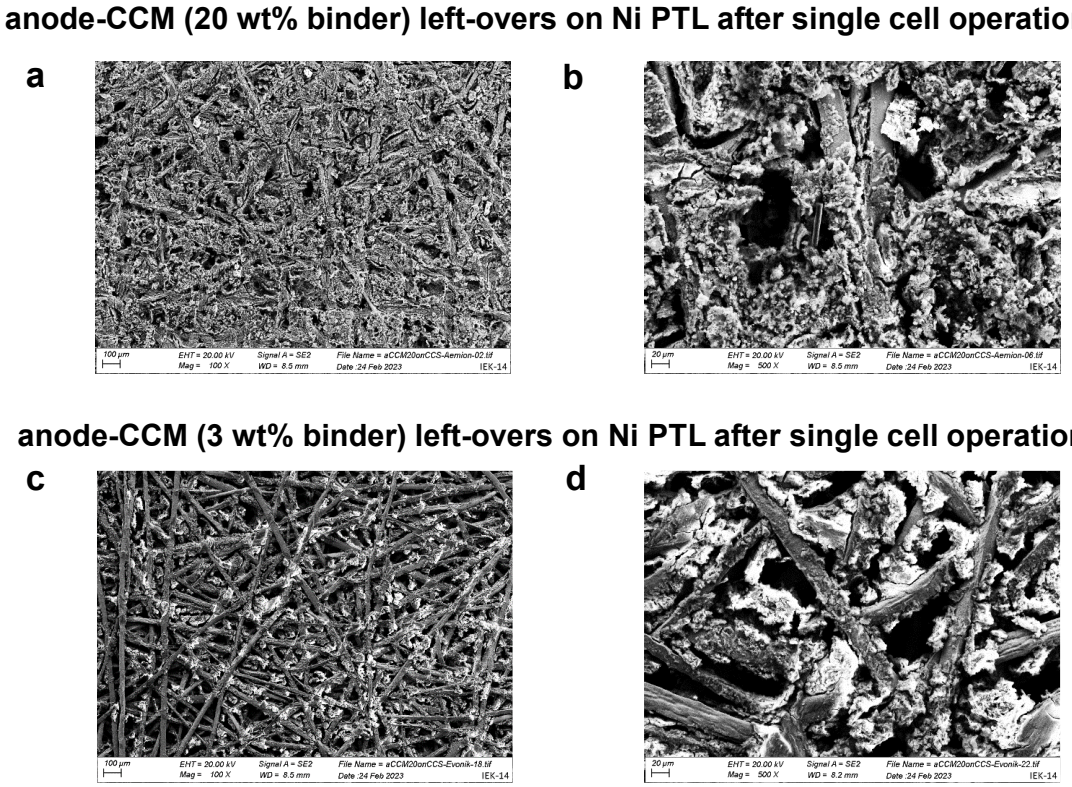

Figure-A 30. Top-view SEM images of Ni PTLs covered with the CL left-overs printed from the anode-CCM (20 wt% binder) at a magnification of (a) x100, (b) x500 and from anode-CCM (3 wt% binder) at a magnification of (c) x100 and (d) x500 based on Aemion+™ AEMs after single-cell operation. The transferred CL is less pronounced than in the case of DURAION® AEM-based anode-CCMs.

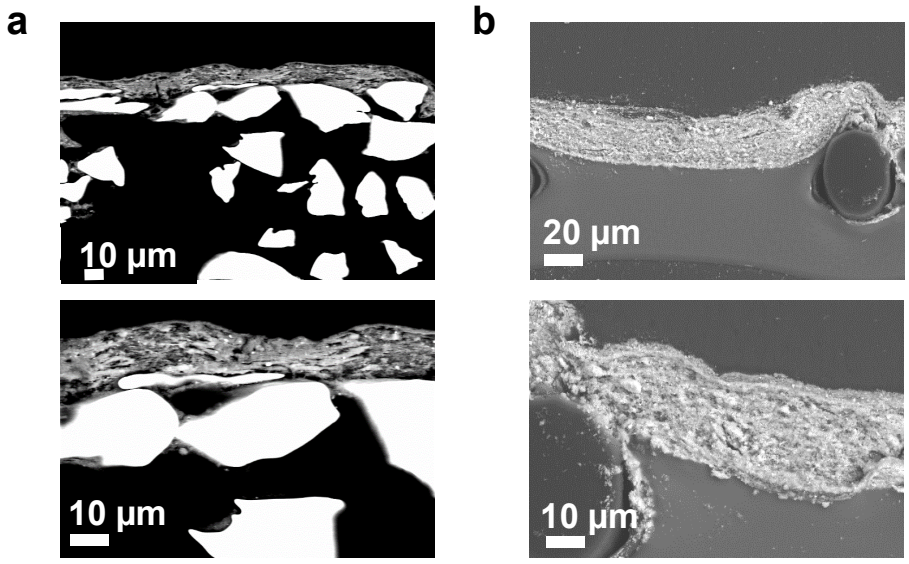

Figure-A 31. SEM images of the (a) anode-CCS and (b) anode-CCM from cross-sectional view at magnifications x1000, x2500 (from top to bottom). Both CL were prepared with 20 wt% binder. The AEM and binder are commercial Aemion+™ materials by Ionomr.

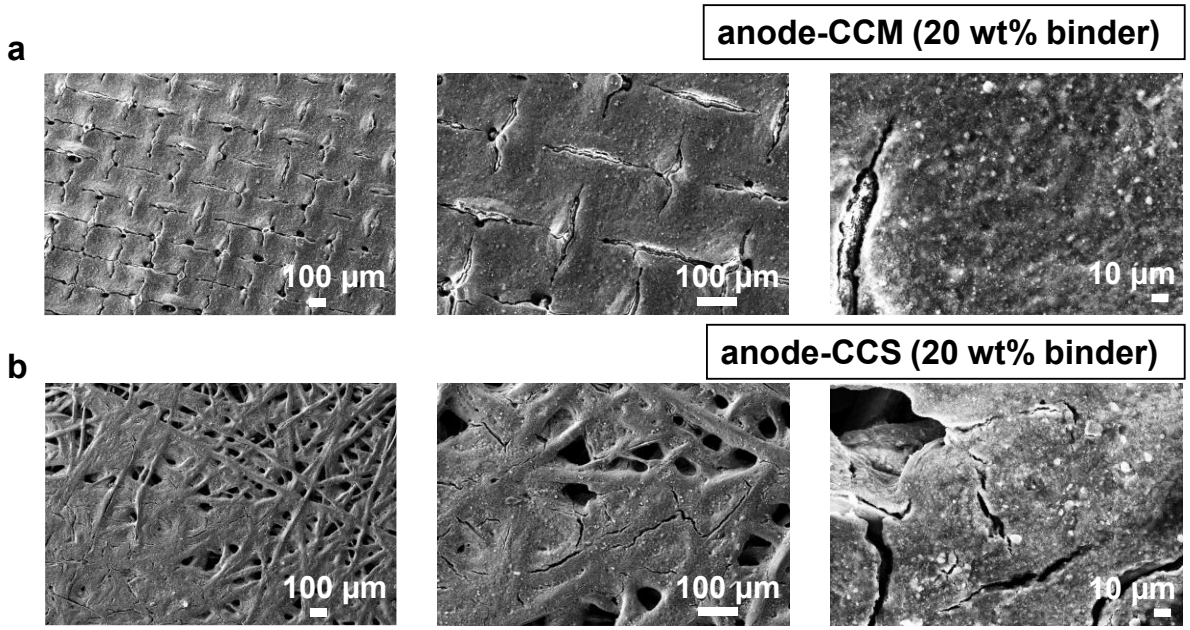

Figure-A 32. SEM images of the (a) anode-CCM and (b) anode-CCS from top-view at magnifications x100, x250, x1000 (from left to right). Both CL were prepared with 20 wt% binder in dispersion; the catalyst loadings are 2 mg cm^{-2} for the presented CLs. The AEM and binder are commercial Aemion+™ materials by Ionomr.

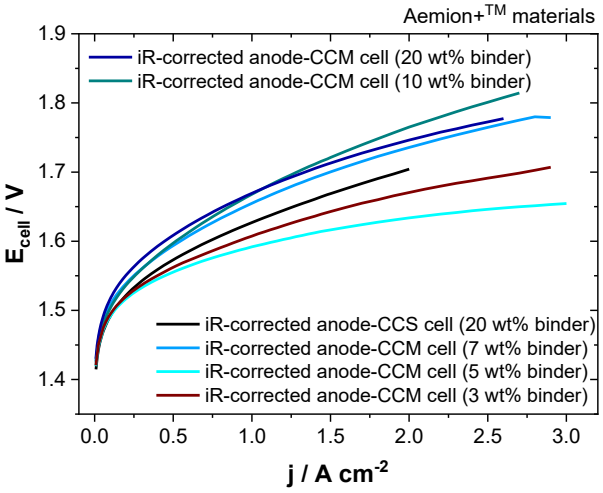

Figure-A 33. Comparison of anode-CCM single-cells with different binder contents (3, 5, 7, 10, 20 wt%) with the anode-CCS cell (20 wt% binder) and among each other: iR-corrected polarization curves. The MEAs are fabricated based on Aemion+™ materials. All components, except the MEAs are identical. Cathode: Pt/C 0.6 mg cm^{-2} (25 wt% binder). Testing conditions: 1 M KOH, 60 °C.

Table-A 11. R_{Ohm} and R_{ct} (mΩ cm^2) values extracted from Nyquist plot fits for the single-cells, based on Aemion+™ materials with varying binder content in the initial catalyst dispersion.

Single-cell	**Anode-CCS (20 wt% binder)**	**Anode-CCM (20 wt% binder)**	**Anode-CCM (10 wt% binder)**	**Anode-CCM (7 wt% binder)**	**Anode-CCM (5 wt% binder)**	**Anode-CCM (3 wt% binder)**
R_{Ohm} / mΩ cm^2	095	118	104	108	095	101
R_{ct} / mΩ cm^2	152	155	180	155	124	125

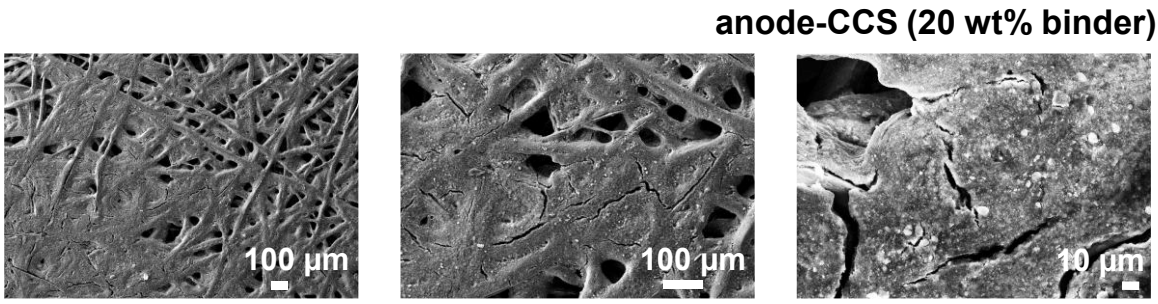

Figure-A 34. SEM images of the anode-CCSs (20 wt% binder) from top-view at magnifications x100, x250, x1000 (from left to right. The catalyst loading is 2 mg cm^{-2}. The AEM and binder are commercial Aemion+™ materials by Ionomr.

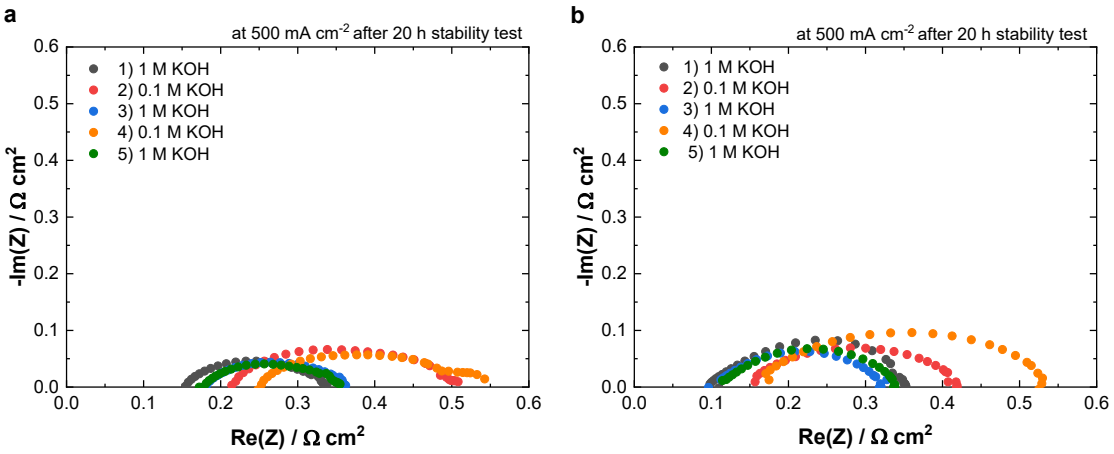

Figure-A 35. Nyquist plots from impedance spectroscopy data recorded at 500 mA cm^{-2} after each 20 h stability test (a) for the full-CCS single-cell, corresponding to Figure 5.56, (b) for the anode-CCM (cathode-CCS) single-cell, corresponding to Figure 5.57.

Table-A 12. R_{Ohm} and R_{ct} (Ω cm^2) values extracted from Nyquist plot fits recorded at 500 mA cm^{-2} for the single-cells, based on anode-CCMs or anode-CCS with DURAION® materials in varying electrolyte concentrations.

Test number	Electrolyte concentration / M	anode-CCM cell R_{Ohm} / Ω cm^2	anode-CCM cell R_{ct} / Ω cm^2	anode-CCS cell R_{Ohm} / Ω cm^2	anode-CCS cell R_{ct} / Ω cm^2
1	1	0.099	0.200	0.112	0.253
2	0.5	0.110	0.199	0.127	0.247
3	0.1	0.144	0.276	0.165	0.334
4	0.01	0.166	0.383	0.191	0.373
5	1	0.091	0.198	0.102	0.195
6	0.5	0.113	0.206	0.115	0.251
7	0.1	0.142	0.347	0.161	0.378
8	0.01	0.210	0.589	0.23	0.535
9	1	0.095	0.200	0.101	0.198
10	0.5	0.108	0.209	0.115	0.232
11	0.1	0.140	0.289	0.153	0.338
12	0.01	0.155	0.371	0.163	0.442
13	1	0.104	0.207	0.106	0.238

10.5 APPENDIX: REPRODUCIBILITY CHALLENGES AND THEIR IMPACT ON RESEARCH OUTCOMES

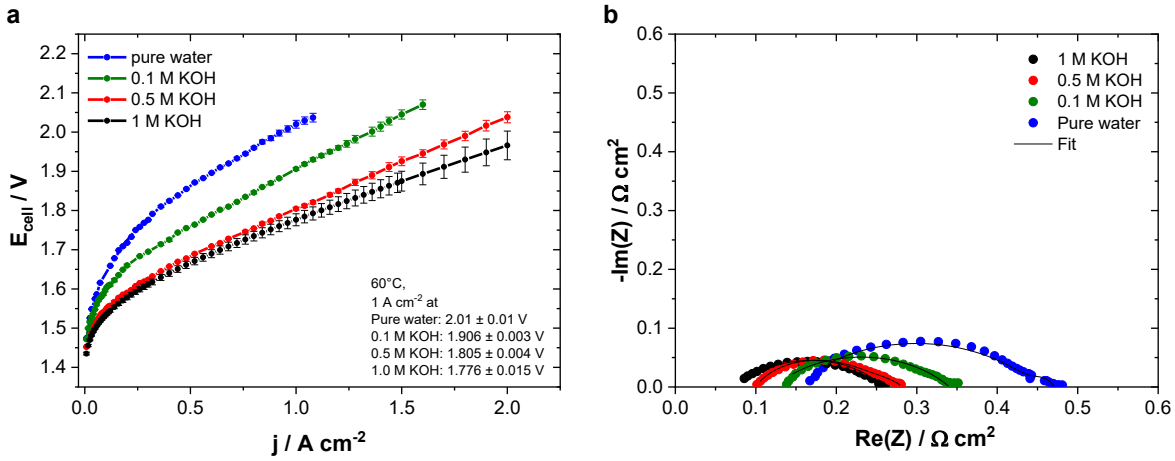

Figure-A 36. Single-cell performance of a full-CCS single-cell evaluated in varying electrolytes (a) Polarization curves, (b) corresponding Nyquist plots recorded at a current density of 500 mA cm^{-2}. Anode: Ni_3Fe-LDH 2 mg cm^{-2} (20% binder), Cathode: Pt/C 0.6 mg cm^{-2} (25 wt% binder), DURAION® materials. Testing conditions: 1 M KOH, 60 °C.

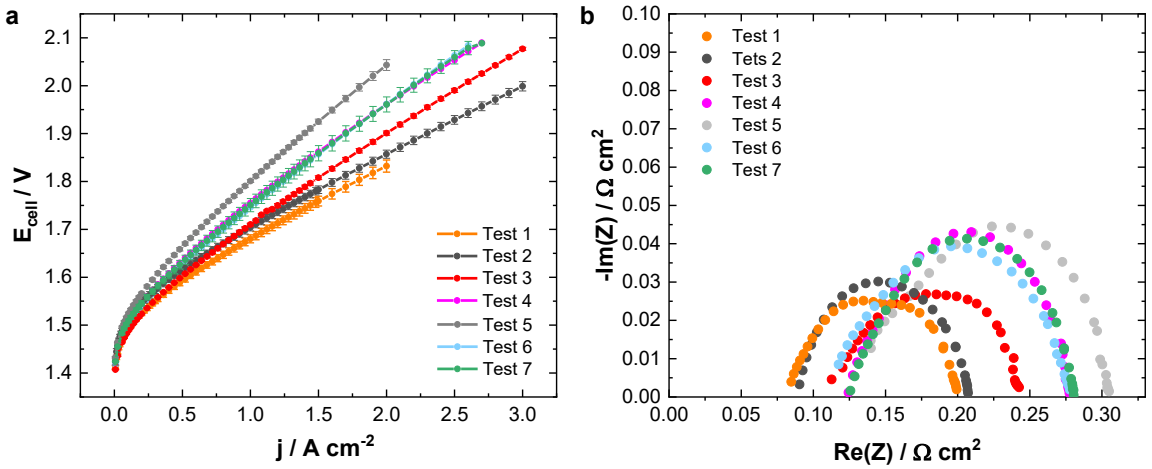

Figure-A 37. Electrochemical performance comparison of single-cells using different material batches, emphasizing the reproducibility challenges. The CL layer parameters as well as the testing conditions remain consistent. (a) Polarization curves, (b) corresponding Nyquist plots recorded at 500 mA cm^{-2}. Anode: milled (mTM-NiFe-LDH) Ni_3Fe-LDH 2 mg cm^{-2} (20 wt% binder), Cathode: Pt/C 0.6 mg cm^{-2} (25 wt% binder). Testing conditions: 1 M KOH, 60 °C.

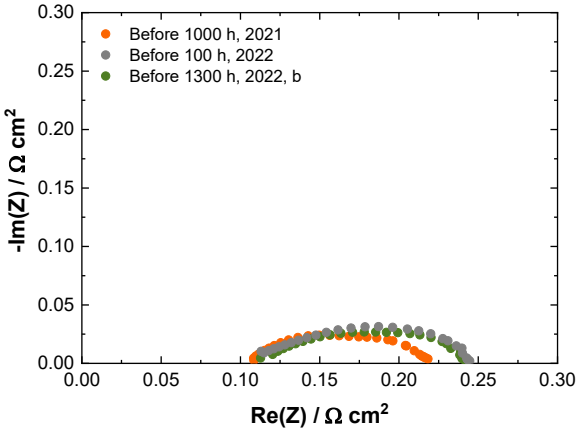

Figure-A 38. Nyquist plots recorded at a current density of 500 mA cm^{-2} before each of the durability tests (Figure 5.63Figure 5.62) Anode: milled Ni_3Fe-LDH 2 mg cm^{-2} (20 wt% binder), Cathode: Pt/C 0.6 mg cm^{-2} (25 wt% binder), DURAION® materials. Testing conditions: 1 M KOH, 60 °C.

ACKNOWLEDGEMENTS

This thesis would not have been possible without the support of many people, and I would like to thank everyone who contributed to it in different ways-scientifically, technically, and personally.

First, I would like to express my gratitude to **Prof. Anna K. Mechler** for her supervision and guidance throughout the work. I especially appreciate that she took over my supervision after I had already been working on my PhD for about two years. Her support made a major difference for the continuation and successful completion of this thesis. Her feedback helped me sharpen the scientific focus and keep the overall direction clear. I also sincerely thank **Prof. Ralf Peters** for reviewing this thesis and for taking on the role of second examiner for my defense.

I would like to thank **Dr. Fabian Scheepers** for his continuous scientific support and for helping to structure and keep the work on track throughout the project. I especially appreciate his support during periods of change, and his ability to encourage progress not only in the good phases, but also during times when things felt difficult. His constructive feedback, reliability, and positive team spirit were a major support for me over the time of this thesis. A special thank you goes to **Prof. Werner Lehnert** for his scientific and personal support and mentoring, especially during the early phase of this project, when his input helped set a strong foundation of the work.

I am also very grateful to **Dr. Martin Müller**, **Dr. Marcelo Carmo** and **Dr. Meital Shviro** for their support at the start of my work and for helping me get the research off the ground. I would like to sincerely thank **Dr. Wulyu Jiang** for the synthesis of the Ni_3Fe-LDH OER catalyst, which was essential for this thesis. I also gratefully acknowledge Dr. Felix Lohmann-Richters for his contributions to results-related discussions and for project support.

I would like to thank my **colleagues** and **fellow PhD students** for the supportive working environment, great teamwork, and many memorable moments, both in and outside the lab. The daily exchange of ideas, spontaneous problem-solving, and the shared motivation during intense phases made a real difference and helped keep the work moving forward, especially when experiments became challenging. In particular, I would like to thank **Ilias Stamatelos, Worawee Saei and Hakim Kerroumi** (who all brought the best personal, genuinely funny moments into the daily work and made even long days feel lighter)**, Dr. Niko Utsch** (who was not only my colleague throughout my time at RWTH but supported the BET measurements), **Dr. Edward Rauls and Dr. Ali Karaca** (who first encouraged me to seriously consider pursuing a PhD and helped spark the confidence to take that step)**, Dr. Cinar Karacan** (who gave me my first introduction to alkaline water electrolysis and the test station operation)**, Stefan Hess, Dr. Stefanie Renz, Felix Benz, Dominik Sachse, Lukas Ritz, Dr. Sarah Zerressen, Sharon Pape, Johanna Güttler, and Dr. Seongeun Park**.

A large part of this thesis relies on advanced characterization methods, and I am very grateful to everyone who supported these measurements. **Andreas Everwand** (IET-4, Forschungszentrum Jülich) performed most **SEM/EDX** measurements and carried out the **XRD** analysis. **Lea Risters** conducted

FIB-SEM at the **Ernst Ruska-Centrum (ER-C)**, Forschungszentrum Jülich. **Dr. Meital Shviro** recorded **TEM and STEM** images at Forschungszentrum Jülich. **Dr. Heinrich Hartmann** (ZEA-3, Forschungszentrum Jülich) conducted the main **XPS** measurements, with additional XPS support from **Dr**. **Alaa Y. Faid** (NTNU, Trondheim). Alaa Y. Faid also carried out the **Raman spectroscopy** measurements and provided mentoring and scientific support. **Volker Nischwitz** supported **ICP-MS and ICP-OES** measurements (former ZEA-3, Forschungszentrum Jülich), **Uwe Breuer** assisted with **ToF-SIMS** (ZEA-3), and **Astrid Besmehn** supported further **ZEA-3 measurements**. I also thank **Denise Günther, Thomas Pütz, Daniel Holtz, Norbert Commerscheidt** for their excellent technical support and practical help during the experimental work. In particular, I am grateful to **Katja Klafki** and **Andreas Everwand** for their support with sample preparation and cross-sections, as well as for conducting key characterization measurements, including **SEM, EDS, and XRD**.

This thesis was completed within the **CHANNEL project**, funded by the **Fuel Cells and Hydrogen 2 Joint Undertaking** under grant agreement **No 875088**, supported by the **European Union's Horizon 2020 programme**, **Hydrogen Europe**, and **Hydrogen Europe Research**. I sincerely thank all project partners for the collaboration, and in particular **Prof. Svein Sunde** and **Dr. Alaa Y. Faid** for their support within the project. I also thank **Evonik**, especially **Patrick Borowski** and **Artjom Maljusch**, for providing the anion-conducting materials.

Finally, and most importantly, I would like to thank my **family and closest friends**. Your constant support, patience, and understanding carried me through the entire PhD time, especially during the stressful phases when progress felt slow or uncertain. Thank you for always believing in me, for keeping me grounded, and for reminding me that there is more than work when I needed it most. Your encouragement and trust meant more than I can express.

I would also like to add a very personal thank you to **Dr. Nikita Grigorev**, my husband, for his support far beyond technical and scientific contributions. Alongside his input on the catalyst milling work, his constant encouragement, honest feedback, and everyday support made a real difference throughout this thesis.

Schriften des Forschungszentrums Jülich
Reihe Energie & Umwelt / Energy & Environment

Band / Volume 716
Process Optimization and Scale-Up for Ba(Zr,Ce,Y)$O_{3-\delta}$-Based Proton-Conducting Electrolysis Half-Cells
L.-A. Schäfer (2026), iv, 141 pp
ISBN: 978-3-95806-940-4 (Print)
ISBN: 978-3-95806-941-1 (E-Book)

Band / Volume 717
Kostenoptimale Energieausfälle in erneuerbaren Energiesystemen
D. Franzmann (2026), xix, 235 pp
ISBN: 978-3-95806-942-8 (Print)
ISBN: 978-3-95806-943-5 (E-Book)

Band / Volume 718
***Semiclassical Thermodynamics* of Metal-Solution Interfaces: A Density-Potential Functional Theory Study**
Z. Zhang (2026), 143 pp
ISBN: 978-3-95806-946-6 (Print)
ISBN: 978-3-95806-947-3 (E-Book)

Band / Volume 719
Development and Characterization of the Airborne Chemical Ionization Mass Spectrometer FunMass-C for Atmospheric Trace Gas Measurements
S. Alber (2026), xli, 265 pp
ISBN: 978-3-95806-948-0 (Print)
ISBN: 978-3-95806-949-7 (E-Book)

Band / Volume 720
Material design and stability of All-Solid-State Lithium batteries
F. H. Al-Jaljouli (2026), xv, 174 pp
ISBN: 978-3-95806-950-3 (Print)
ISBN: 978-3-95806-951-0 (E-Book)

Band / Volume 721
Towards improved representation of the hydrological cycle by assimilating multi-source remotely sensed soil moisture data in terrestrial system models
H. Zhao (2026), XVI, 139 pp
ISBN: 978-3-95806-952-7 (Print)
ISBN: 978-3-95806-953-4 (E-Book)

Schriften des Forschungszentrums Jülich
Reihe Energie & Umwelt / Energy & Environment

Band / Volume 722
Combining Lattice Boltzmann Simulation and Synchrotron Imaging to Study Bubble Dynamics in Electrodes of Vanadium Redox Flow Batteries
K. Duan (2026), xxiii, 116 pp
ISBN: 978-3-95806-954-1 (Print)
ISBN: 978-3-95806-955-8 (E-Book)

Band / Volume 723
Geophysical characterization of landscapes along a climate and vegetation gradient in the Chilean coastal cordillera
I. Dal Bo (2026), 138 pp
ISBN: 978-3-95806-956-5 (Print)
ISBN: 978-3-95806-957-2 (E-Book)

Band / Volume 724
Model informed assessment of observation impact for emission rate optimization using four-dimensional variational data assimilation
A. Hermanns (2026), xvi, 109 Seiten
ISBN: 978-3-95806-958-9 (Print)
ISBN: 978-3-95806-959-6 (E-Book)

Band / Volume 725
Synthese und Bewertung hochaktiver Katalysatoren zur Herstellung höherer Alkohole aus Methanol als Kraftstoff
J. Häusler (2026), xiii, 265 Seiten
ISBN: 978-3-95806-962-6 (Print)
ISBN: 978-3-95806-963-3 (E-Book)

Band / Volume 726
Development and Characterization of Ni_3Fe Layered Double Hydroxide-Based Oxygen-Evolution Electrodes for Anion Exchange Membrane Water Electrolysis
I.Galkina (2026), vii, 173, xxxiii Seiten
ISBN: 978-3-95806-966-4 (Print)
ISBN: 978-3-95806-967-1 (E-Book)

Weitere ***Schriften des Verlags im Forschungszentrum Jülich*** unter
http://wwwzb1.fz-juelich.de/verlagextern1/index.asp

Energie & Umwelt / Energy & Environment
Band / Volume 726
ISBN 978-3-95806-967-1

Mitglied der Helmholtz-Gemeinschaft

JÜLICH
Forschungszentrum